Development and application of a ground-based fully polarimetric microwave radiometer for temperature sounding in the middle atmosphere

Inaugural dissertation
of the Faculty of Science,
University of Bern

presented by

Witali Krochin

from Utzenstorf BE

Supervisor of the doctoral thesis: PD. Dr. Gunter Stober

Development and application of a ground-based fully polarimetric microwave radiometer for temperature sounding in the middle atmosphere

Inaugural dissertation
of the Faculty of Science,
University of Bern

presented by

Witali Krochin

from Utzenstorf BE

Supervisor of the doctoral thesis: PD. Dr. Gunter Stober

Accepted by the Faculty of Science.

The Dean:

Bern, den November 14, 2024 Prof. Dr. Jean-Louis Reymond

Preface

The main motivation behind this dissertation is the rising climate crisis, which has been a constant companion of ice-cold fear and great danger. I am convinced, that watching nature slowly die in front of our eyes, helpless and unable to intervene, changes us as persons. When I started the PhD position in 2020 the critical voices, unwilling to believe in what we as mankind have done, were still loud—spreading their misinformation over the media. By now, 4 years later these voices have fallen silent. Partly because the evidence for an anthropogenic CO_2 footprint is inarguable after the 2021 IPCC report, partly because the predicted consequences can not be overseen anymore. The last meteorological summer was the hottest since records, while this summer is dominated by heavy thunderstorms and flooding. Regarding these circumstances, it is personally important for me to be part of the solution, however, it might look, and stand on the right side of history.

Contents

1. Objective and structure of this thesis

The studies presented in this thesis involve two big fields of research: atmospheric dynamics and remote sensing. Studying the atmospheric circulation in the middle atmosphere raised the question of which atmospheric effects can be measured with ground-based microwave radiometry. As a result, we have developed a procedure to measure the amplitude and phase of solar thermal tides.

On the technical side, the goal was to improve the temperature radiometer TEMPERA. A temperature radiometer measures atmospheric microwave radiation. From these measurements, atmospheric temperature profiles can be retrieved. As part of the doctoral dissertation, a newly implemented inversion algorithm increases the altitude range for temperature retrievals from TEMPERA measurements and facilitates the study of the middle atmosphere by ground-based radiometry.

The main achievement is the development of the instrument TEMPERA-C. TEMPERA-C is measuring fully polarimetric, which results in an even more increased altitude range and improved temporal resolution. Furthermore, it is supposed to resolve magnetic field features due to the Zeeman line splitting. Compared to single polarization measurements, the calibration of a fully polarimetric instrument is challenging and the state-of-the-art calibration process requires materials with complex properties, which in addition have to be measured precisely beforehand. Therefore the simplified calibration process, developed as part of this dissertation, is of great relevance.

Reflecting the dual nature of the topic, this manuscript consists of two parts. The first part is covered by **Section 2** - **Section 6** and treats atmospheric dynamics, composition, and radiation. The basics of atmospheric composition and circulation are summarized in **Section 2**. In **Section 3** the theory of solar tides as well as suitable measurement techniques are discussed and the results of solar tide measurements are presented. In **Section 4** - **Section 6** the physics of radiation propagation through the atmosphere and the retrieval of atmospheric temperature from microwave observations is described.

The second part **Section 7** - **Section 9** is more technical and focuses on ground-based microwave radiometry and instrument development. **Section 7** provides an introduction to the topic of atmospheric microwave remote sensing and calibration of radiometer instruments. In **Section 8** a recently implemented inversion algorithm for the older instrument TEMPERA is described. The newly developed instrument TEMPERA-C together with the post-process correction and first results are presented in **Section 9**.

Since the work for this dissertation was done at the interface between the theory of atmospheric physics and the technical application of microwave radiometers, this manuscript is neither a purely theoretical nor a technical report, but can be seen as a synthesis of both fields.

2. The atmosphere: basics overview

2.1. The layers and composition of the atmosphere

The layers of the atmosphere can be characterized by their temperature gradient and composition. The lowest layer is the troposphere with a height of up to 20 km at the equator, around 6 km at the poles, and approximately 12 km in the mid-latitudes. Except for local anomalies near the surface, hydro-static equilibrium (**Eq. 2.1**) can be assumed in the troposphere. In thermal equilibrium, the tropospheric temperature is determined by the exponential decrease of pressure and density with altitude and the ideal gas law (**Eq. 2.2**), where p is the pressure, z the altitude, ρ the density, T the temperature, $g = 9.81$ ms^{-2} earth's gravity constant, and R the specific gas constant. The resulting temperature profile is, to a good approximation, linear with a negative gradient, which is referred to as the lapse rate:

$$\frac{\partial p}{\partial z} = -\rho g, \tag{2.1}$$

$$p = \rho R T. \tag{2.2}$$

The troposphere contains about 70% of the total mass of the atmosphere and 99% of the atmospheric water content. The presence of water vapour and liquid water locally affects the temperature gradient through heating by absorption of solar radiation. Also, all of the weather and cloud formation happens in the troposphere. The transition region to the next higher layer is the tropopause, characterized by a constant temperature profile. As the sign of the temperature gradient changes from negative to positive during the layer transition, convective layer mixing is suppressed. Since most of the water also forms ice crystals before it reaches the tropopause due to its low temperature, the tropopause also acts as an effective water barrier.

The layer above the tropopause is the stratosphere. Most of the water content is blocked by the tropopause due to freeze drying and therefore, the stratosphere remains very dry. The stratospheric temperature profile is dominated by heating due to absorption of solar radiation by Ozone. As a result of the radiative energy budget, the temperature gradient is positive. One consequence of the positive temperature gradient is that convection is prevented and vertical mixing is dominated by turbulent eddies. The transition region above the stratosphere, the stratopause is located at an altitude of about 50 km and is again characterised by an inversion of the temperature gradient to a negative lapse rate.

The layer between 50 and 85 up to 100 km is the mesosphere, in which the temperature gradient is again negative, mainly due to the very low density, low pressure, and decreasing solar heating with altitude. The stratosphere and the mesosphere together are referred to as the middle atmosphere. An example of a temperature profile up to an altitude of 70 km, is shown in **Fig. 2.1**. The atmospheric temperature was retrieved from TEMPERA measurements (see **Section 8**) operating at MeteoSwiss technical station in Payerne CH.

Above the middle atmosphere, there is the thermosphere, which reaches an altitude of about 600 km. The transition between the mesosphere and the thermosphere is the mesopause. The temperature gradient in the thermosphere is dominated by solar radiation and is therefore positive. The density in the thermosphere is so low that molecular mixing dominates over turbulence, i.e. heavier molecules sink while lighter ones rise. The uppermost level is the exosphere, which

extends between 600 km and 10'000 km. In this layer, molecules escape to space.

The main compounds of the atmosphere are molecular nitrogen N_2 with a volume percentage of 78.084% (excluding water vapour), oxygen with a volume percentage of 20.948%, and argon with 0.934%, which are nearly uniformly stratified up to 60 km. Carbon dioxide accounts for only 0.04%, which is nevertheless over 40% above the pre-industrial level. Water vapour, which mainly is found in the troposphere, occurs in varying amounts between 0-4%. Ozone, which is mostly located in the stratosphere, occurs also in varying amounts of about 0-12x10^{-6}% (Liou, 2002).

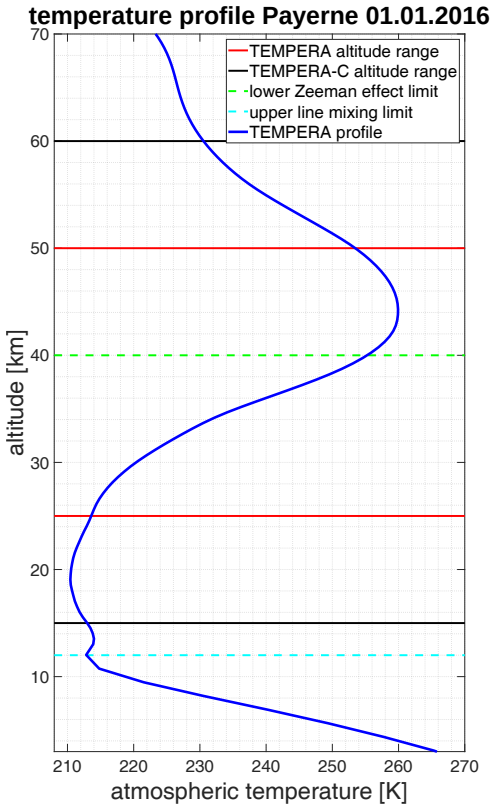

Figure 2.1: Atmospheric temperature profile retrieved from TEMPERA measurements (see **Section 8**). The TEMPERA-C instrument is described in **Section 9**, the Zeeman effect in **Section 6.3**, and line-mixing in **Section 6.2**

2.2. The circulation in the middle atmosphere

The main circulation in the troposphere is described by the General Circulation. A detailed overview of the tropospheric General Circulation can be found in Holton and Hakim (2012). Since the focus of this thesis is on the middle atmosphere, a description of the general circulation is skipped and only the circulation in the middle atmosphere is described.

The zonally averaged temperature field in the stratosphere increases with altitude due to the absorption of solar radiation by ozone as described in **Section 2.1**. It reaches a maximum at about 50 km. In contrast to the troposphere, the meridional temperature distribution in the stratosphere has its minimum in the tropics and increases towards the poles, where the temperature

gradient is higher in the summer hemisphere. The zonally averaged meridional transport is described by the Brewer-Dobson circulation (Brewer (1949), Dobson et al. (1929), Dobson (1949)), which is a stratospheric global scale circulation. On zonal average, tropospheric air rises into the stratosphere in the tropics and descends at high latitudes. Therefore, diabatic cooling occurs in the tropics, while the descending air in the high latitudes is adiabatically heated. Zonally averaged zonal winds in the stratosphere are westward in the summer hemisphere and vice versa during the winter months. This meridional temperature and transport pattern differs from the purely radiation-determined one. The angular momentum balance would also not be conserved without Eddie-forcing, which occurs through equatorial Rossby modes that originate in the troposphere and propagate vertically, where they increase in amplitude until wave breaking occurs, depositing momentum in the stratosphere. This mechanism is also called Extra-tropical-pump (Holton et al., 1995). As mentioned above, the pole-ward flow on the winter hemisphere is eastward. As a consequence, a vortex forms around the pole regions. The polar vortex has been a vital research topic over the past decades (for example Shi et al. (2023)). This is mainly due to the importance of the polar vortex and its mid-winter breakdown in the northern hemisphere Matsuno, 1971; Matthias et al., 2021, which normally occurs in mid-winter by a sudden warming of the stratosphere (Schranz et al. (2019), Schranz et al. (2020), and Shi et al. (2023)) or the final break-down during the transition towards spring Matthias et al., 2021. Disturbances from the polar vortex breakdown, so-called planetary waves, travel even extend over various latitudes from the polar regions down to the latitude of Switzerland (47°N) and can be monitored with ground-based microwave radiometers. **Fig. 2.2** shows a series of temperature profiles retrieved with the ground-based temperature radiometer TEMPERA (see **Section 8**). The characteristic planetary waves are visible as strong oscillations in temperature at 30-50 km altitude. **Fig. 3.2** gives another perspective on this effect. The temperature median over 40-50 km shows the appearance of oscillations with amplitudes around 10 K and periods around 30 days, starting in October and lasting usually until March.

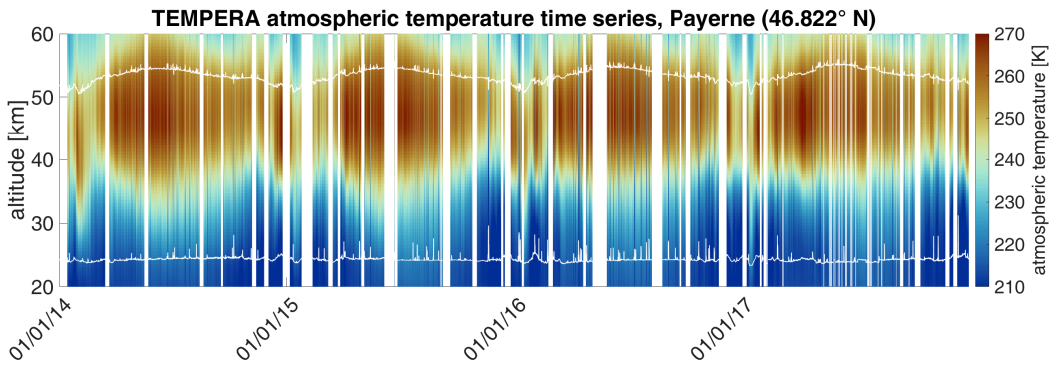

Figure 2.2: Continuous time series of atmospheric temperature profiles for the time period 2014-2017 (Krochin et al., 2024). Increased temperatures are observed during summer months, while planetary waves are present during winter time in the mesosphere. The MR=0.6 is marked with a white line.

The zonally averaged temperature field in the mesosphere is also counter-intuitive as the meridional temperature gradient points from the summer pole to the winter pole. The meridional transport in the mesosphere consists of a single cell, where the air rises at the summer pole and descends at the winter pole. Similar to the case of the Brewer-Dobson circulation, the pole-to-pole flow would not be possible without eddy-forcing, which in the mesosphere is dominated by internal gravity-wave drag. This transport pattern is often called residual circulation R. S. Lindzen, 1981; Becker, 2012. One interesting consequence of the residual circulation is the formation of noctilucent clouds at mid and high latitudes during the hemispheric summer months.

These are mesospheric ice clouds formed by condensation due to rising and cooling air masses in the summer-pole mesosphere. These cloud formations, usually observed at high latitudes, have the characteristic feature to glow in the early night sky. Due to their high altitude, they continue to scatter sunlight after sunset. As a result of the changing climate and resulting reinforced circulation and cooling mesosphere (Bailey et al., 2021), sightings of noctilucent clouds were reported more frequently in the past decades Lübken et al. (2018) and Stevens et al. (2022).

For a more detailed description of middle atmospheric dynamics see, Holton and Hakim (2012), Andrews et al. (1987), Lindzen (1990), and Smith (2012). These textbooks were used for this section and are highly recommended. A general historical and technical overview concerning the Brewer-Dobson circulation can be found in Butchart (2014).

2.3. Basic equations: momentum and mass conservation

The next two sections provide a brief overview of the basic equations that describe the dynamics of the Earth's atmosphere and prepare for the derivation of Laplace's tidal equation (see **Section 3.2**). The so-called primitive equations describe the basic conservation laws of physics for a fluid on a rotating sphere. As in **Section 2.2**, the textbooks Holton and Hakim (2012), Andrews et al. (1987), and Lindzen (1990) were taken into account for this chapter, but the notation was slightly modified.

The atmosphere, as any fluid, can be characterised by the velocity field $\mathbf{U} = (u, v, w)$, which in general will depend on the location and time. The basic momentum conservation equation for a fluid parcel on a rotating sphere has the form:

$$\frac{D\mathbf{U}}{Dt} = -2\Omega \times \mathbf{U} - \frac{1}{\rho}\nabla p + \mathbf{g} + \mathbf{F_r}, \tag{2.3}$$

where $\frac{D}{Dt} = \frac{\partial}{\partial t} + \mathbf{U}\nabla$ is the material derivative. The terms on the right-hand side are the Coriolis force with angular velocity Ω, pressure gradient force with the density ρ, gravitational force, and friction force. In most cases, the atmosphere is assumed to be incompressible, in which case the mass conservation or continuity equation is:

$$\frac{\partial \rho}{\partial t} + \nabla(\rho\mathbf{U}) = 0. \tag{2.4}$$

A suitable coordinate system must be introduced for applications. A commonly used coordinate system is the local Cartesian system, expressed in derivatives of spherical coordinates (r, ϕ, λ). Here r is the sum of the earth's radius and altitude, ϕ the latitude, and λ the longitude. The local coordinate transformation is:

$$u = r\cos\phi\frac{D\lambda}{Dt}, \tag{2.5}$$

$$v = r\frac{D\phi}{Dt}, \tag{2.6}$$

$$w = r\frac{Dz}{Dt}. \tag{2.7}$$

Since the earth's radius a is much larger than any possible altitude in the atmosphere z, the approximation $r = a + z \approx a$ can be used. In these coordinates, the momentum conservation equation is:

$$\frac{Du}{Dt} - \frac{uv\tan\phi}{a} + \frac{uw}{a} = -\frac{1}{\rho}\frac{\partial p}{\partial x} + 2\Omega v\sin\phi - 2\Omega w\cos\phi + F_{rx}, \tag{2.8}$$

$$\frac{Dv}{Dt} - \frac{u^2\tan\phi}{a} + \frac{vw}{a} = -\frac{1}{\rho}\frac{\partial p}{\partial y} - 2\Omega u\sin\phi + F_{ry}, \tag{2.9}$$

$$\frac{Dw}{Dt} - \frac{u^2+v^2}{a} = -\frac{1}{\rho}\frac{\partial p}{\partial z} - g + 2\Omega u\cos\phi + F_{rz}. \tag{2.10}$$

And the continuity equation is transformed to:

$$\frac{1}{\rho}\frac{d\rho}{dt} + \frac{1}{a\cos\phi}\left(\frac{\partial u}{\partial\lambda} + \frac{\partial}{\partial\phi}(v\cos\phi)\right) + \frac{1}{a^2}\frac{\partial}{\partial z}(r^2 w) = 0. \tag{2.11}$$

In preparation for the derivation of Laplace's tidal equation, further simplifications of the above equations can be made. By neglecting wind and assuming very low flow velocities, terms with velocities in powers greater than 1 can be ignored. This process of linearisation is equivalent to treating the velocity field as turbulence and setting the background flow to zero:

$$u = \bar{u} + u' + o(\alpha^2), \tag{2.12}$$

$$v = \bar{v} + v' + o(\alpha^2), \tag{2.13}$$

$$w = \bar{w} + w' + o(\alpha^2), \tag{2.14}$$

$$\tag{2.15}$$

$$\bar{u} = \bar{v} = \bar{w} = 0. \tag{2.16}$$

For the pressure and density, the linearisation is:

$$P = P_0 + P' + o(\alpha^2), \tag{2.17}$$

$$\rho = \rho_0 + \rho' + o(\alpha^2). \tag{2.18}$$

A scale analysis shows that the terms $2\Omega w\cos\phi$ and $2\Omega u\cos\phi$ are orders of magnitude smaller than the leading terms, so they can be neglected. Moreover, it is suitable to assume no change in density $d\rho = 0$, except for the vertical direction (Bussinesq approximation). Finally, friction is also neglected, and the system of momentum and mass conservation becomes:

$$\frac{\partial u'}{\partial t} = -\frac{1}{\rho_0 a\cos\phi}\frac{\partial p'}{\partial\lambda} + 2\Omega v'\sin\phi, \tag{2.19}$$

$$\frac{\partial v'}{\partial t} = -\frac{1}{\rho_0 a}\frac{\partial p'}{\partial\phi} - 2\Omega u'\sin\phi, \tag{2.20}$$

$$\frac{\partial w'}{\partial t} = -\frac{1}{\rho_0}\frac{\partial p'}{\partial z} - g, \tag{2.21}$$

$$0 = \frac{1}{a\cos\phi}\left(\frac{\partial u'}{\partial\lambda} + \frac{\partial}{\partial\phi}(v'\cos\phi)\right) + \frac{\partial w'}{\partial z}. \tag{2.22}$$

By neglecting vertical acceleration $\frac{\partial w'}{\partial t} = 0$, **Eq. 2.21** becomes the hydrostatic equilibrium equation (**Eq. 2.1**).

2.4. Basic equations: energy conservation

The fourth of the main equations is the first law of thermodynamics, describing energy conservation in a closed system:

$$c_v \frac{DT}{Dt} + p\frac{D\alpha_\rho}{Dt} = J. \tag{2.23}$$

Here, c_v is the heat capacity at constant volume, $\alpha_\rho = \frac{1}{\rho}$, and $J = \frac{\delta Q}{dt}$ is the heating rate per unit mass. In tidal theory, the energy equation is described in terms of the geopotential:

$$\Phi(z) = \int_0^z g(z)dz \tag{2.24}$$

and a transformed vertical coordinate:

$$z^* = -H \ln \left({}^{P}/_{P_s} \right), \tag{2.25}$$

where $H = {}^{RT_s}/_{g}$ is the scale height. With the hydro-static-equilibrium (**Eq. 2.1**), the gas law (**Eq. 2.2**), and the assumption of adiabatic motion:

$$\frac{\partial p}{\partial t} + w\frac{\partial p}{\partial z} = 0, \tag{2.26}$$

the energy equation can be written in the log-pressure form:

$$\frac{\kappa J}{H} = \frac{\partial^2 \Phi}{\partial t \partial z^*} + \omega^* N^2, \tag{2.27}$$

where $\omega^* = \frac{dz^*}{dt}$ is a transformed velocity and

$$N^2 = \frac{R}{H}\left(\frac{\partial T}{\partial z^*} + \frac{\kappa T}{H}\right) \tag{2.28}$$

is the square of the Brunt-Vaisala buoyancy frequency with $\kappa = {}^{R}/_{c_p}$, where c_p is the heat capacity at constant pressure.

3. Thermal tides

3.1. What are thermal tides?

Atmospheric solar tides are global-scale oscillations in temperature(R. S. Lindzen and Chapman, 1969; Chapman and R. Lindzen, 1970; R. S. Lindzen, 1979), wind, density, and pressure with periods of a fraction of a day (1d, 1/2d, 1/3d). Solar tides are generated by the absorption of solar radiation by water vapour in the troposphere and ozone in the stratosphere. Different modes of tides are distinguished. Tides propagating zonally with the sun (sun-synchronous) are called migrating. Each other propagating mode is called non-migrating. As internal gravity wave modes, tides also travel vertically and grow in amplitude. In the middle atmosphere, the tidal amplitude increases until nonlinear effects cause wave breaking, depositing momentum in high altitudes, and enforcing turbulent eddy mixing (Becker, 2017). In the past decades, it was recognized that the upward propagation of tides has a significant impact on global- and shorter-scale dynamics in the middle atmosphere (Oberheide et al., 2009; Oberheide et al., 2011). Therefore, the modelling of tides and their vertical propagation was studied theoretically (J. Forbes, 1982; Ortland, 2005) and numerically (Hagan et al., 1995; Hagan et al., 1999; Chang et al., 2008).

Figure 3.1 illustrates diurnal thermal tide oscillations from temperature profiles retrieved from TEMPERA measurements collected in 2014. Panel a) shows the series of unfiltered temperature profiles. Panel b) shows the same but with a 5-day moving window median removed. The daily oscillations become visible at all altitudes. Panel c) shows the temperature median over 40-55 km over a sine fit to illustrate the sinusoidal behaviour. Panel d) shows the thermal tide amplitude profiles calculated with the ASF algorithm (see **Section 3.3**).

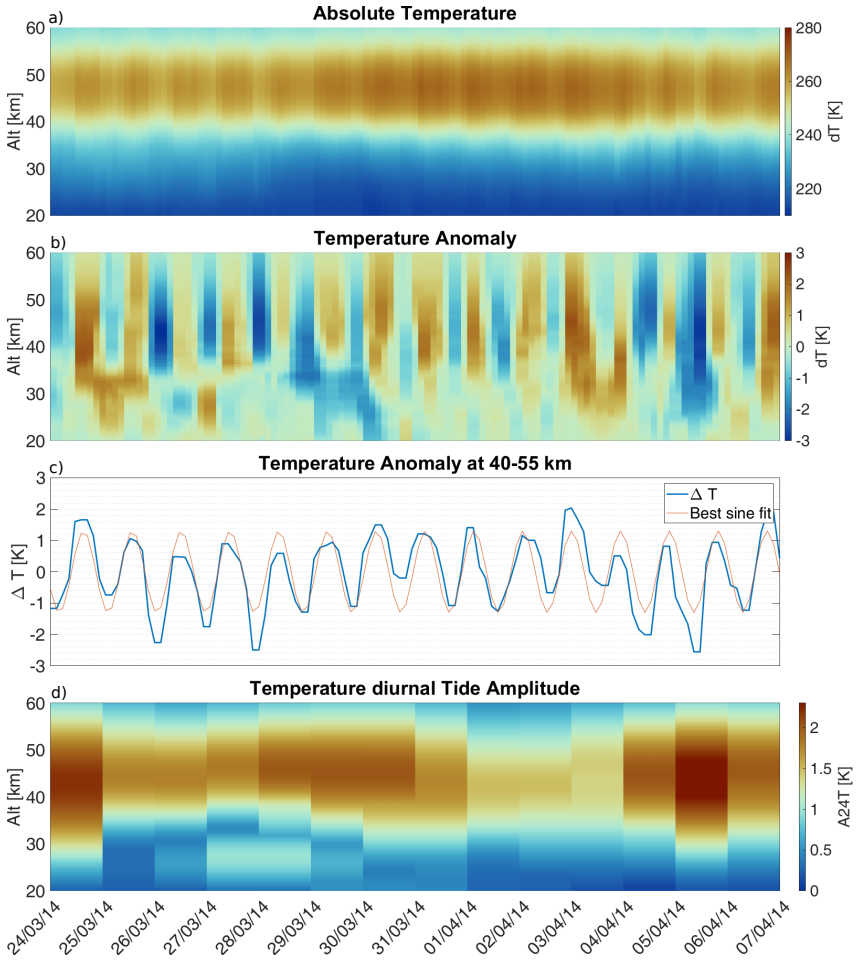

Figure 3.1: Illustration of thermal tides (Krochin et al., 2024). A detailed description of each panel is given in the text.

3.2. Laplace tidal equation

Tidal modes can be expanded in a series of functions that solve Laplace's tidal equation (Hough modes, Hough and Darwin, 1898), which describes oscillation modes in a thin resting layer of atmosphere on a rotating sphere. The derivation of the Laplace's tidal equation in this section is according to Andrews et al., 1987. For this derivation, the primitive equations were simplified (see **Section 2.3**).

The starting point for Laplace's tidal equation is the system of momentum, mass, and energy conservation equations already presented in the previous section:

$$0 = \frac{\partial u'}{\partial t} - fv' + \frac{1}{a\cos\phi}\frac{\partial \Phi'}{\partial \lambda}, \tag{3.1}$$

$$0 = \frac{\partial v'}{\partial t} + fu' + \frac{1}{a}\frac{\partial \Phi'}{\partial \phi'}, \tag{3.2}$$

$$0 = \frac{1}{a\cos\phi}\left(\frac{\partial u'}{\partial \lambda} + \frac{\partial}{\partial \phi}(v'\cos\phi)\right) + \frac{\partial \omega'^*}{\partial z^*}, \tag{3.3}$$

$$\frac{\kappa J'}{H} = \frac{\partial^2 \Phi'}{\partial t \partial z^*} + \omega'^* N^2. \tag{3.4}$$

Where $f = 2\Omega \sin\phi$. Note also that the expression for pressure was replaced by:

$$\frac{1}{\rho_0}\frac{\partial P'}{\partial \lambda} = \frac{\partial \Phi'}{\partial \lambda}, \tag{3.5}$$

$$\frac{1}{\rho_0}\frac{\partial P'}{\partial \phi} = \frac{\partial \Phi'}{\partial \phi}. \tag{3.6}$$

Also the vertical velocity was replaced by:

$$\frac{\partial w'}{\partial z} = \frac{\partial \omega'^*}{\partial z^*}. \tag{3.7}$$

The next step towards the tidal equation is to separate the vertical dependence from the horizontal and time dependence by defining:

$$(u', v', \Phi') = U(z)\left[\tilde{u}(\lambda,\phi,t), \tilde{v}(\lambda,\phi,t), \tilde{\Phi}(\lambda,\phi,t)\right] e^{-z/2H}, \tag{3.8}$$

$$\omega^* = W(z)\tilde{\omega}(\lambda,\phi,t)e^{z/2H}. \tag{3.9}$$

Also, the heating has to be set to zero $J' = 0$, it will be introduced again in a later stage. However, by doing so, the ω^* dependence can be eliminated:

$$0 = \frac{\partial \tilde{u}}{\partial t} - f\tilde{v} + \frac{1}{a\cos\phi}\frac{\partial \tilde{\Phi}}{\partial \lambda}, \tag{3.10}$$

$$0 = \frac{\partial \tilde{v}}{\partial t} + f\tilde{u} + \frac{1}{a}\frac{\partial \tilde{\Phi}}{\partial \phi}, \tag{3.11}$$

$$0 = \frac{1}{a\cos\phi}\left(\frac{\partial \tilde{u}}{\partial \lambda} + \frac{\partial \tilde{v}\cos\phi}{\partial \phi}\right) + \frac{1}{gh}\frac{\partial \tilde{\Phi}}{\partial t}. \tag{3.12}$$

Here, h is the mean depth, which is a separation constant with length dimensions with the condition for a thin atmosphere $a >> h$. The procedure to solve the system of equations is to pose the sinusoidal form:

$$\left(\tilde{u}, \tilde{v}, \tilde{\Phi}\right) = \Re\left\{\left[\bar{u}(\lambda,\phi,t), \bar{v}(\lambda,\phi,t), \bar{\Phi}(\lambda,\phi,t)\right] e^{(s\lambda-\sigma t)i}\right\}, \tag{3.13}$$

where s is the zonal wave number, and $2\pi/\sigma$ is the period. Substituting **Eq. 3.10** and **Eq. 3.11** into **Eq. 3.12** finally leads to the Laplace tidal equation:

$$\mathcal{L}\bar{\Phi} + \gamma\bar{\Phi} = 0. \tag{3.14}$$

The factor:

$$\gamma = \frac{4\Omega^2 a^2}{gh} \tag{3.15}$$

is called Lamb's parameter.

$$\mathcal{L} = \frac{d}{d\mu}\left[\frac{(1-\mu^2)}{(\sigma^2-\mu^2)}\frac{d}{d\mu}\right] - \frac{1}{\sigma^2-\mu^2}\left[\frac{-s(\sigma^2+\mu^2)}{\sigma(\sigma^2-\mu^2)} + \frac{s^2}{1-\mu^2}\right] \tag{3.16}$$

is a second order differential operator and

$$\mu = \sin\phi. \tag{3.17}$$

The eigenfunctions solving the Laplace tidal equation are called Hough functions or Hough modes. For a given set of (s, σ, n) the Hough mode $\Theta_n^{(\sigma,s)}$ of order n fulfills:

$$\mathcal{L}\Theta_n^{(\sigma,s)} + \gamma_n^{(\sigma,s)}\Theta_n^{(\sigma,s)} = 0. \tag{3.18}$$

The solar heating J can now be expanded in a series of Hough modes:

$$J(\phi, z, t) = \Re\left\{\sum_{s=1}^{3} J^{(s)}(\phi, z)e^{is(\lambda+\sigma t)}\right\}, \tag{3.19}$$

$$J^{(s)}(\phi, z) = \sum_n J_n^{(s)}(z)\Theta_n^{(s)}(\mu). \tag{3.20}$$

The response to heat forcing will consist of the same periodicity as for the geopotential:

$$\Phi^{(s)}(\phi, z) = \sum_{n=1}^{\infty} U_n^{(s)}(z)\Theta_n^{(s)}(\mu)e^{z/2H}. \tag{3.21}$$

Or equivalent for the temperature:

$$T(\phi, z, t) = T_0(\phi, z) + \Re\left\{\sum_{s=1}^{3} T^{(s)}(\phi, z)e^{is(\lambda+\sigma t)}\right\}, \tag{3.22}$$

$$T^{(s)}(\phi, z) = \sum_n T_n^{(s)}(z)\Theta_n^{(s)}(\mu). \tag{3.23}$$

3.3. Measuring thermal tides

The measurements of thermal tides in the middle atmosphere published to date have mostly been derived from satellite measurements, which provide a long-term overview of a large part of the globe (Huang et al., 2006; Zhang et al., 2006; Zhang et al., 2010; J. M. Forbes and Wu, 2006; Sakazaki et al., 2012; Dhadly et al., 2018). In this way, the zonally averaged distribution of Hough modes can be studied as a function of latitude. The repetition rate, however, of an orbiting satellite is usually not much larger than one flyby per day for each longitude and local time. Therefore, multiple orbits have to be sampled over long periods to represent one tidal cycle, which also leads to sampling errors in the observed phase (Zhang et al., 2006; Xu et al., 2009; Sakazaki et al., 2012). In contrast, ground-based observations are more suitable to monitor temperature at one location, but with a time resolution of 30-60 min, as this is the case for TEMPERA, a full cycle can be resolved. Ground-based observations of tides were also performed using wind measurements from meteor radar systems (Vincent et al., 1988; Lu et al., 2011; Pokhotelov et al., 2018; Du et al., 2007; Stober et al., 2021; Caspel et al., 2022) and Doppler radars (Riggin et al., 2002). Also, thermal tide measurements signatures from temperature measurements with lidars systems (Gille et al., 1991; Liu et al., 2007; Kopp et al., 2015; Yuan et al., 2008; She et al., 2002; Baumgarten and Stober, 2019a; Yuan et al., 2021; Fong et al., 2022; Yuan et al., 2014) and wind measurements with microwave radiometers (Baumgarten and Stober, 2019b; Hagen et al., 2020) were reported. Lidars offer a temporal resolution in the hourly range but no continuity, as several systems are not able to record data in daylight. Microwave radiometers provide continuous datasets but with lower time resolution (1-12 h) and are affected by cloud coverage and rainfall. A comparison between satellite

measurements, ground-based measurements, and model results can be found in Ward et al., 2010.

The separation of migrating from non-migrating modes is, however, not possible from a single location observation. An additional challenge are interactions with other wave modes. The observed series consists of a superposition of all wave activity present in the atmosphere. Figure 3.2 shows the median of temperature time series over 40-50 km. The dataset was retrieved from TEMPERA measurements on the roof of the ExWi building in 2022. The line in the first panel is unsmoothed but filtered. Out-layer values and missing data were replaced with the mean value of the neighbouring data points. The oscillations highest in frequency (1 day) are thermal tides. The third panel illustrates the same data set after smoothing with a moving window median and a moving window length of 8 days. Oscillations with periods of around 6-10 days become visible in the second half of August. Before that, in May-July, periods around 3-6 days seem to dominate. The curve in the next panel was smoothed with a moving window of 30 days and reveals planetary waves with periods around 30 days, usually starting in October and lasting until March.

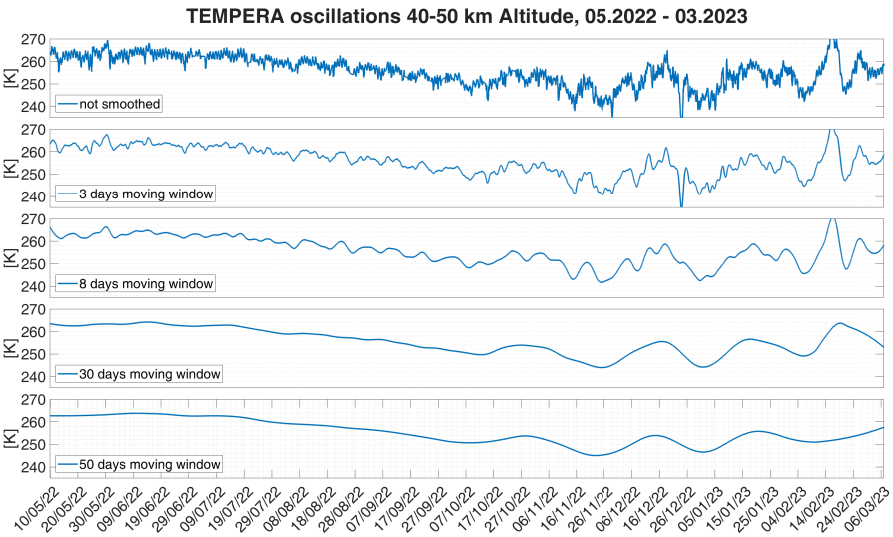

Figure 3.2: Median of atmospheric temperatures over 40-50 km altitude. Several atmospheric oscillation modes are superimposed. Smoothing with moving windows of different sizes has a similar effect as filtering higher frequency modes, periods smaller than the moving window get suppressed.

A first attempt to separate the oscillation modes was to compare well-known spectral decomposition methods. The challenges of decomposing the series above are noise, data gaps, and variable periods and phases. These are aspects that are critical for a classical Fourier transformation. **Fig. 3.3** shows an attempt to decompose the series above with 4 different methods where all the parameters were fine-tuned to illustrate diurnal tides. The first panel was made with a classical moving window FFT with a window length of 10 days. For the FFT, the outlayers were removed, and the remaining data gaps were linearly interpolated. Moreover, for a 10-day window, the background was removed. The FFT filters the diurnal tides in the absence of planetary waves and even gives a tide amplitude, which is in the order as found in Krochin et al., 2024. The Lomb-Scargle power decomposition (Lomb, 1976; Scargle, 1982; Press et al., 1992) was developed to handle data gaps and uneven sampling and does not require interpolation. The performance seems similar to the FFT algorithm, but the output units are not directly transformable into input units. The result of the wavelet analysis algorithm (Torrence and Compo, 1998) shows clearly the diurnal modes even in the presence of planetary waves, but

the exact period becomes blurred. Also, the output units are not directly related to the input units, as in the case of the Lomb-Scargle algorithm. It was also found that a simple sine fit gave reasonable results for time windows where the tidal period remained stable.

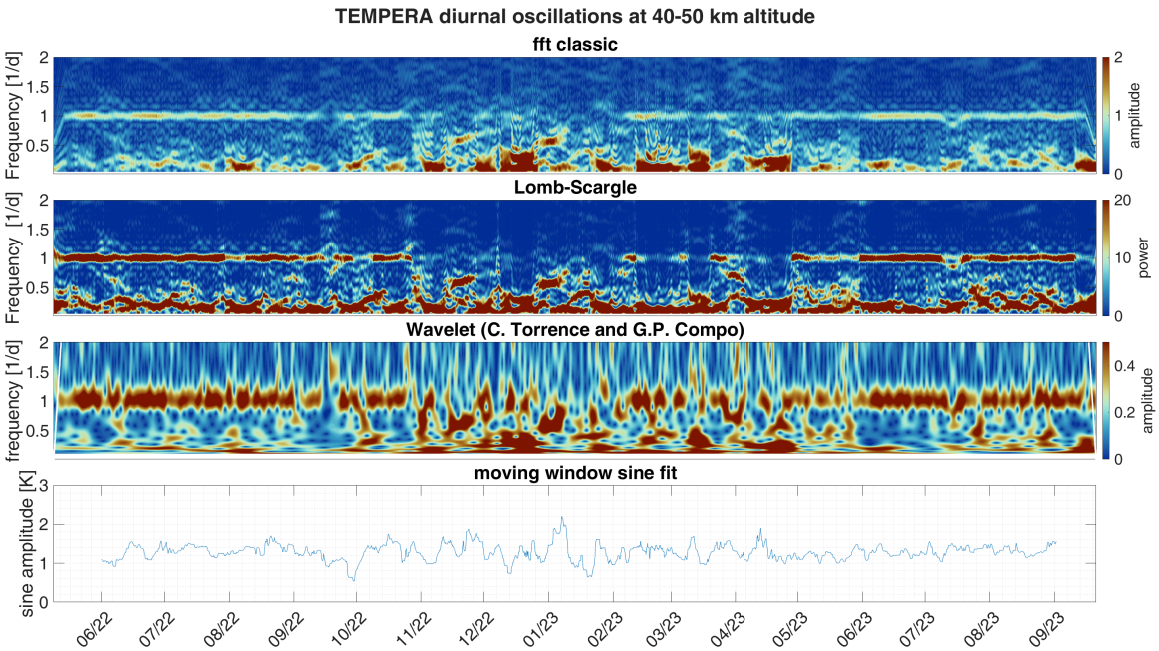

Figure 3.3: Spectral decomposition of the temperature median between 40-50 km. The focus of the illustration are diurnal thermal tides. The classical moving window FFT seems to produce reasonable results where the amplitude is in the range of the one found in Krochin et al., 2022a.

For the publication of thermal tides, we decided to use an algorithm called adaptive-spectral-filter (Baumgarten and Stober, 2019b; Stober et al., 2020). At a given altitude it fits the temperature $T(t_n)$ within a moving window of given length and centre t_n with sine, and cosine functions according to the equation:

$$T(t_n) = T_0(t_n) + \sum_{n=1}^{3} a_n \sin\left(\frac{2\pi}{P_n} t_n\right) + a_n \cos\left(\frac{2\pi}{P_n} t_n\right). \tag{3.24}$$

After fitting the background temperature coefficients a_n, b_n, the tide amplitude A_n is given by:

$$A_n = \sqrt{a_n^2 + b_n^2} \tag{3.25}$$

and the phase $\Delta\phi_n$ can be found by:

$$\frac{a_n}{b_n} = \tan\left(\Delta\phi_n\right). \tag{3.26}$$

The fitting algorithm also handles data gaps and varying phases.

3.4. Comments on publication I

Thermal tides in the middle atmosphere at mid-latitudes measured with a ground-based microwave Radiometer

Cite as:

Krochin, W., Murk, A., and Stober, G.: Thermal tides in the middle atmosphere at mid-latitudes measured with a ground-based microwave Radiometer, Atmos. Meas. Tech. Discuss. [preprint], in review, 2024.

DOI: `https://doi.org/10.5194/amt-2024-42`

Summary

Using temperature time series retrieved from TEMPERA observations above Bern (CH) and Payerne (CH), thermal tide amplitudes and phases were calculated with a moving window adaptive spectral filter (ASF) algorithm. Maxima of thermal tidal amplitudes between 2-3 K were found at altitudes between 38-45 km. The temperature time series indicated downward phase propagation in the lower stratosphere and a constant phase of 18.00 LST at the upper stratosphere.

Author contribution

For this publication, I performed the retrievals, the data analysis, and error calculation. For the tidal analysis, I used the adaptive spectral filter algorithm provided by Gunter Stober and adapted it to the specific case. As first author, I have written the largest part of the manuscript, and Gunter Stober provided the ASF algorithm, as well as expertise knowledge on atmospheric dynamics. All authors contributed to the editing of the manuscript.

4. Radiative transfer

4.1. Schwarzschild's equation

Radiative transfer is a basic tool in microwave radiometry, as it describes the propagation of electromagnetic radiation through a medium, or in this case, the atmosphere. The combined phenomena of absorption, emission, and scattering are captured by the Schwarzschild equation, which is described in this section. A comprehensive description of radiative transfer can be found in the textbooks Liou, 2002; Grant, 2006; Stamnes et al., 2017.

A monochromatic beam with frequency ν and spectral radiance $I(s)$ $(\mathrm{W} \cdot \mathrm{sr}^{-1} \cdot \mathrm{m}^{-2} \cdot \mathrm{Hz}^{-1})$, passing through a homogeneous medium on a path $s \in [s_1, s_2]$ with the absorption coefficient $\beta(s)$, and physical temperature $T(s)$, will be attenuated due to absorption and amplified by thermal emission. At any location s, the change in intensity by absorption dI_a and emission dI_e can be formally written:

$$dI_a = -\beta I ds, \tag{4.1}$$

$$dI_e = \beta B ds. \tag{4.2}$$

In most cases, the medium is idealized as a grey-body emitter where B is the Planck distribution:

$$B(T, \nu) = \frac{2h}{c^2} \frac{\nu^3}{e^{\frac{h\nu}{k_b T}} - 1}. \tag{4.3}$$

Here, h is the Planck constant, c is the speed of light, k_b is the Boltzmann constant, and ν is the frequency. Note also that every quantity is frequency dependent and could be provided with a subscript $\beta(\nu) \equiv \beta_\nu, I(s, \nu) \equiv I_\nu(s)$,... u.s.w. The subscript will be omitted, instead of writing it for each variable. For the total change, the contributions **Eq. 4.1** and **Eq. 4.2** can be summed up, leading to the first-order differential equation:

$$dI = dI_a + dI_e = \beta \left(B - I\right) ds. \tag{4.4}$$

In many references, the solution of this equation is provided in terms of s. A bit more elegant is to introduce the optical depth τ by integrating the absorption coefficient over the propagation path:

$$\tau(s_1, s_2) = \int_{s_1}^{s_2} \beta(s) ds \Rightarrow d\tau = -\beta ds. \tag{4.5}$$

This variable transformation transforms the differential equation to:

$$\frac{dI}{d\tau} = B - I. \tag{4.6}$$

With the solution, known as the Schwarzschild equation:

$$I(\tau) = I(0)e^{-\tau} + \int_0^\tau B e^{-\tau'} d\tau'. \tag{4.7}$$

As the radiation in the microwave frequency range is not affected by scattering from atmospheric molecules, it is skipped in this discussion, as well as the effects of refraction and diffraction. When scattering is taken into account, the scattering source function S is added on the right-hand side of **Eq. 4.7**. The total attenuation from absorption and scattering is then called extinction.

4.2. Line profiles

The relevant physics is carried by the absorption coefficient β. In general, for a specific atmospheric absorption species and frequency β will depend on the temperature, pressure, and density:

$$\beta \equiv \beta(T, P, \rho). \tag{4.8}$$

Next to continuum absorption or emission, molecules undergo several quantum mechanical energy transitions. At a frequency that matches the energy difference of the transition by $E_T = |E_2 - E_1| = h\nu$, a sharp jump in the absorption and emission spectrum will be found. In this manuscript, this will be called emission line. In general, different transition mechanisms have their frequency band. For example, emitted radiation caused by electron transitions in single atoms or molecular orbits is in the UV range, and molecular vibrations have energy transitions in the IR range. In our case, we are interested in rotational transitions, which absorb and emit in the microwave range. Due to energy conservation, the absorption and emission coefficient of a certain transition are identical, and both phenomena will be referred to as emission further on.

An emission line has a shape that depends on the transition, the temperature, density, and pressure of the emitting gas. It is the shape, that allows to retrieve atmospheric quantities from the measured spectra. The gas absorption coefficient β is related to the absorption cross-section per molecule σ_N by:

$$\beta = \sigma_N n, \tag{4.9}$$

where n is the number of molecules within the field of view of our radiometric antenna beam. The cross-section is also often expressed per mass or path length. For a rotational transition, the cross-section in the frequency domain is given by a lineshape $f(\nu)$ and a line-strength S:

$$\sigma_\nu = Sf(\nu). \tag{4.10}$$

Since a quantum-mechanical transition has one clearly defined energy E_T, one would expect an emission line to behave like a δ-function, for example, $\sigma_\nu = S\delta(\nu - {}^{E_T}/_{h})$. The line-shape $f(\nu)$ results from various broadening mechanisms, blurring the transition energy and, therefore, the observed frequency. For example, every emission line is affected by natural broadening, which is due to the uncertainty relation $\Delta E_T \Delta t_S \geq {}^{h}/_{4\pi}$. Since the lifetime t_S of the rotational state is comparably short, its uncertainty Δt_S is small. The energy uncertainty ΔE_T has to take a value large enough to compensate for the uncertainty relation. The observed line shape will be Lorentz distributed.

Since molecules of any gas with a temperature greater than zero $T > 0$K have a non-vanishing velocity, observed emissions will be Doppler shifted accordingly. The Doppler line shape $f_D(\nu)$, therefore reflects the Boltzmann distribution of the thermal velocities:

$$f_D(\nu) = \frac{1}{\alpha_D\sqrt{\pi}} e^{-\left(\frac{\nu-\nu_0}{\alpha_D}\right)^2}, \tag{4.11}$$

$$\alpha_D = \nu_0 \sqrt{\frac{2k_B T}{mc^2}}. \tag{4.12}$$

The most important broadening effect for our purposes is induced by collisions between particles, the pressure broadening. Pressure broadening is not fully understood theoretically yet. A

simplified explanation is that collisions between particles can lead to collision-induced emission, reducing the lifetime of a rotational state and, therefore, increasing the uncertainty of the emitted energy. The pressure-broadened line shape is approximately given by the Lorentz profile:

$$f_L(\nu) = \frac{1}{\pi} \frac{\alpha_L}{(\nu - \nu_0)^2 + \alpha_L^2}, \tag{4.13}$$

$$\alpha_L = \alpha_0 \frac{p}{p_0} \left(\frac{T}{T_0} \right)^n . \tag{4.14}$$

Which describes and approximates the line shape as it is observed in the atmosphere around the line center. However, at the line wings, larger deviations might be present. Here n is a constant ranging from $1/2$ to 1, depending on the molecule. A profile that behaves better around the line wings is the Van-Vleck-Weisskopf profile (Van Vleck and Weisskopf, 1945):

$$f_{VVW}(\nu) = \frac{1}{\pi} \left(\frac{\nu}{\nu_0} \right)^2 \left(\frac{\alpha_L}{(\nu - \nu_0)^2 + \alpha_L^2} + \frac{\alpha_L}{(\nu + \nu_0)^2 + \alpha_L^2} \right) . \tag{4.15}$$

A combined Doppler and Lorentz profile is given by the convolution of both profiles:

$$f_V = \int f_D(\nu') f_L(\nu - \nu') d\nu' \tag{4.16}$$

and is called the Voigt profile.

5. Inversion of atmospheric spectra

5.1. Forward model simulations

To retrieve a profile of any atmospheric quantity $x(z)$ from measurements of microwave emissions, it is crucial to know the relationship between the desired variable and the emitted radiation. The Lorentz profile has a strong temperature dependence, which can be used to estimate the atmospheric temperature at the location of emission. However, the spectrum y measured on the ground is a superposition of emissions from all radiating species within the antenna beam from the surface to the highest altitudes. The retrieval or inversion process is to disentangle the altitude dependence such that for each altitude grid point, a single emission spectrum can be determined, which afterwards is solved for the temperature. The retrieval theory in this thesis follows Rodgers, 2000, which to this day is the state-of-the-art formulation of retrieval theory.

The first step is to set up a model atmosphere and simulate the measurement y for a given profile x, additional atmospheric quantities b, and a corresponding error ϵ. This is called the forward model F:

$$y = F(x, b) + \epsilon. \tag{5.1}$$

The error ϵ consists of a normal distributed measurement error. The forward model Jacobian also called the weighting function, is defined as:

$$\mathbf{K}_{ij} = \frac{\partial F_i(x)}{\partial x_j}. \tag{5.2}$$

5.2. Optimal estimation

The goal of the inversion process is to find an optimal state $\hat{x}$ and $\hat{b}$, such that the inversion R of F fulfills:

$$\hat{x} = R(y, \hat{b}, x_a, c). \tag{5.3}$$

The main challenge is that the problem of finding $\hat{x}$ is ill-posed because the solution is not unique. The basic idea behind the procedure presented in Rodgers, 2000, is to assume that the measurement vector y and the atmospheric state vector x are normal distributed with covariance matrices $\mathbf{S}_\epsilon$ and $\mathbf{S}_a$, and expectation values $\bar{y}(x) = F(x, b)$ and x_a, respectively:

$$P\left(y\left(x\right)\right) = \frac{1}{\left(2\pi\right)^{n/2} \left|\mathbf{S}_\epsilon\right|^{1/2}} e^{-\frac{1}{2}(y-\bar{y})^T \mathbf{S}_\epsilon^{-1}(y-\bar{y})}, \tag{5.4}$$

$$P(x) = \frac{1}{\left(2\pi\right)^{n/2} \left|\mathbf{S}_a\right|^{1/2}} e^{-\frac{1}{2}(x-x_a)^T \mathbf{S}_a^{-1}(x-x_a)}. \tag{5.5}$$

The mean atmospheric state x_a is called apriori state and can be obtained, for example, by a climatological average from satellite data. The normal distribution allows to find $P(x|y)$ (probability of x under the condition that y is known) by using Bayes' Theorem:

$$P(x|y) = \frac{P(y|x)P(x)}{P(y)}. \tag{5.6}$$

The distribution $P(y)$ itself does not depend on x and can simply be thought of as a normalization factor. Maximising $P(x|y)$ becomes equivalent to minimising the cost function $J(x) = -2\ln\{P(y|x)P(x)\}$:

$$J(x) = [y - F(x)]^T \mathbf{S}_\epsilon^{-1} [y - F(x)] + [x - x_a]^T \mathbf{S}_a^{-1} [x - x_a] . \tag{5.7}$$

The derivative of the cost function is given by:

$$\nabla_x J(x) = -\mathbf{K}(x)^T \mathbf{S}_\epsilon^{-1} [y - F(x)] + \mathbf{S}_a^{-1} (x - x_a) . \tag{5.8}$$

A state vector x is a local extremum if:

$$\nabla_x J(x) = 0. \tag{5.9}$$

To find a local minimum $\hat{x}$, the Levenberg-Marquardt algorithm is used. It iteratively minimizes the cost function by:

$$x_{i+1} = x_i + \left(\mathbf{S}_a^{-1} + \mathbf{K}_i^T \mathbf{S}_\epsilon^{-1} \mathbf{K}_i + \gamma D\right)^{-1} \left[\mathbf{K}_i^T \mathbf{S}_\epsilon^{-1} (y - F(x_i)) - \mathbf{S}_a^{-1} (x_i - x_a)\right] . \tag{5.10}$$

In the Levenberg-Marquardt algorithm, γ is a factor that must be chosen carefully to enforce convergence, and D is usually the unit matrix. For $\gamma = 0$, the Levenberg-Marquardt algorithm is equivalent to the Gauss-Newton iteration. The assumption of a normal distributed measurement and state vector is necessary to find an analytical expression for the cost function.

While the measurement error is usually instrument noise, which in general is described well by a normal distribution, the atmospheric state in nature is not randomly distributed over a long-term expectation value but instead follows cyclical patterns. On the other hand, when the apriori state is known so well that remaining offsets to reality follow a normal distribution, there is no need to perform the inversion. A further issue is that systematical errors in the forward model, for example, a bias in the vmr of an emission species, can not be handled. This is where the inversion theory of Gaussian distributed errors finds its limits.

5.3. Error analysis

The apriori covariance matrix is constructed by assuming an exponentially decreasing correlation between the altitude grid points z_i with z_{ac} as the distance over which the correlations decreases by e^{-1}:

$$(\mathbf{S}_a)_{ij} = \sigma_a(z_i)\sigma_a(z_j) \exp\left(-\frac{|z_i - z_j|}{z_{ac}}\right) . \tag{5.11}$$

The Jacobian of the inversion is called the gain matrix and is given by:

$$\mathbf{G}_{ij} = \frac{\partial R_i}{\partial y_j}. \tag{5.12}$$

After multiplying the gain matrix by the weighting function, the averaging kernel matrix A is obtained, an estimate of the sensitivity of the retrieved state to changes in the true state:

$$\mathbf{A} = \mathbf{GK}. \tag{5.13}$$

The i-th row of the averaging kernel describes how much a value at the altitude grid point z_i depends on the other grid points. The full width at half maximum can be interpreted as altitude resolution. The weighted sum of the rows results in the measurement response vector mr:

$$mr_i = \frac{\mathbf{A}_i x_a}{x_{ai}}. \tag{5.14}$$

The measurement response vector provides an estimate of how strongly a value of the retrieved state vector at a particular grid point depends on the measurement or the apriori profile. A mr value of about 1 indicates that the grid point depends mainly on the measurement, whereas grid points with mr values below 0.6 contain over 40% apriori information.

The observational error covariance matrix $\mathbf{S}_o$ is defined by mapping the measurement covariance matrix $\mathbf{S}_\epsilon$ into the state space:

$$\mathbf{S}_o = \mathbf{G}\mathbf{S}_\epsilon\mathbf{G}^T. \tag{5.15}$$

Weighting the apriori covariance matrix $\mathbf{S}_a$ with the averaging kernel gives the smoothing error caused by the finite resolution of the observation system:

$$\mathbf{S}_s = (\mathbf{A} - \mathbf{I})\,\mathbf{S}_a\,(\mathbf{A} - \mathbf{I})^T\,. \tag{5.16}$$

By mapping the residuum $\left[y - F(\hat{x}, \hat{b})\right]$ into the state space, one gets an estimate of the error caused by idealizing the atmosphere by the forward model. The modelling error or forward model error is defined as:

$$s_M = \mathbf{G}\left[y - F(\hat{x}, \hat{b})\right]. \tag{5.17}$$

In theory, this vector should be evaluated in the true state instead of $\hat{x}$ and $\hat{b}$, which is, in general, not known. According to Rodgers, however, the deviation from the true forward model error will be in negligible order.

5.4. The atmospheric radiative transfer simulator (ARTS)

The atmospheric radiative transfer simulator (ARTS, S. Buehler et al., 2005; Eriksson et al., 2011; S. A. Buehler et al., 2018) is probably the most important tool for atmospheric research in the microwave group. The software is designed to perform forward model simulations with absolute freedom in setting the model atmosphere. With implemented surface properties, it's possible to design ground-based as well as space-born observation systems. Moreover, it facilitates the synthetic setup of sensor and back-end properties tuned on the system at hand. Several OEM options allow us to perform inversions of atmospheric spectra into atmospheric profiles. The OEM computations are based on the terminology of Rodgers, 2000.

The source code of ARTS is written in C++, and the basic version acts as its own scripting language. Up to version ARTS 2.5, a MATLAB interface Qpack (Eriksson et al., 2005) is available but not supported anymore. The TEMPERA instrument performs its operational retrievals with ARTS 2.5 and Qpack. An interface is also available for Python, called Pyarts. TEMPERA-C uses ARTS 2.6 with the Pyarts interface.

6. The oxygen microwave emission band

6.1. The oxygen emission spectrum at 60GHz

The 60GHz oxygen emission band is widely used for temperature retrievals in the troposphere and the middle atmosphere. It consists of the superposition of a total of 73 fine structure lines from rotational transitions (Vleck, 1934; Vleck, 1947; Rosenkranz, 1975; Liebe et al., 1992; Tretyakov et al., 2005; Makarov et al., 2011). This frequency range is weakly affected by other atmospheric species, so interactions with most of the atmospheric compounds and also scattering can be neglected. In addition, the oxygen vmr remains nearly constant up to an altitude of around 80 km. For tropospheric temperature profiles, the slope of the left wing is measured, usually in several broad bands. TEMPERA was used to measure the left wing of the complex with 9 filter banks with a bandwidth of 250 MHz and 3 filter banks with 1000 MHz with different azimuth angles to determine the tropospheric opacity (Stähli et al., 2013).

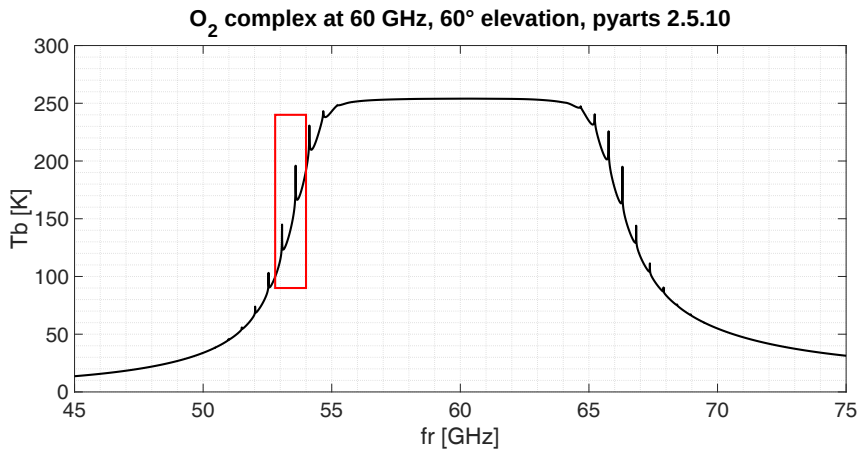

Figure 6.1: The oxygen emission complex as observed with a ground-based instrument at an elevation angle of 60°(Krochin et al., 2022b). The forward model simulation was performed with ARTS for standard atmosphere winter conditions. The band measured with TEMPERA is marked with a red box.

By using a high-resolution spectrometer, narrow line features can be resolved to retrieve middle atmospheric profiles. The fine structure lines originate mainly from regions above the tropopause because, under tropospheric conditions, these lines get broadened into the continuum. Therefore, the fine structure line-centers are nearly unaffected by the troposphere.

However, some challenges remain regarding using this complex for temperature retrievals. Since molecular oxygen has a magnetic dipole, its emission is affected by the Zeeman effect, which dominates the lineshape of emission lines above 40 km. Line mixing affects the physics of emission at higher pressures and alters the emission spectra in the troposphere. Furthermore, air humidity and liquid water influence the observed spectra by thermal emission (Bernet et al., 2017).

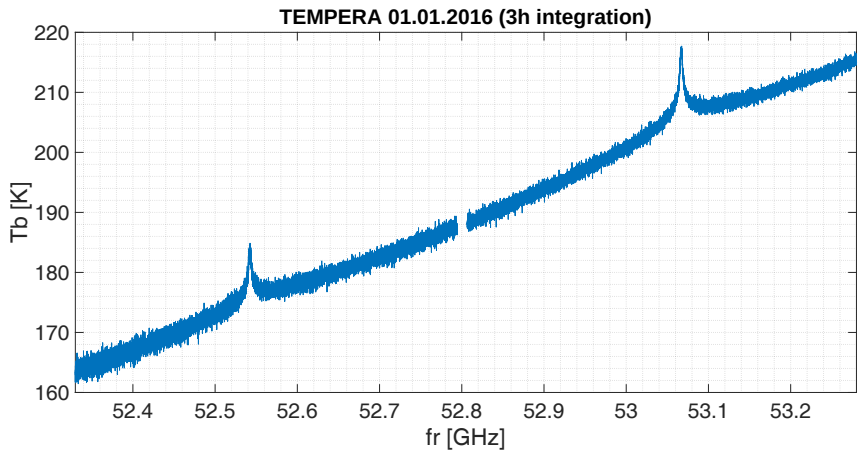

Figure 6.2: Fine structure spectra (see red box in **Fig. 6.1**) measured with TEMPERA after two point calibration with the noise diode.

6.2. Line mixing

For ground-based observations, line mixing has a strong influence on the spectrum of the oxygen emission complex. Line mixing occurs at high pressures as present in the troposphere. Collisions of oxygen with the broadening gas repopulate the rotational quantum states, such that their distribution deviates from the Boltzmann statistic, which is assumed for calculating the energy state population. The effect at the frequency range of interest can lead to a deviation of up to 50K, compared to simulations where line mixing was not taken into account (see **Fig. 6.3**).

Line mixing was not implemented in the inversion algorithm for temperature retrievals from TEMPERA measurements. To compensate for that effect, a tropospherical correction and baseline retrieval were performed (Krochin et al., 2022a; Krochin et al., 2024). Since ARTS 2.5.10 line mixing computations are performed automatically.

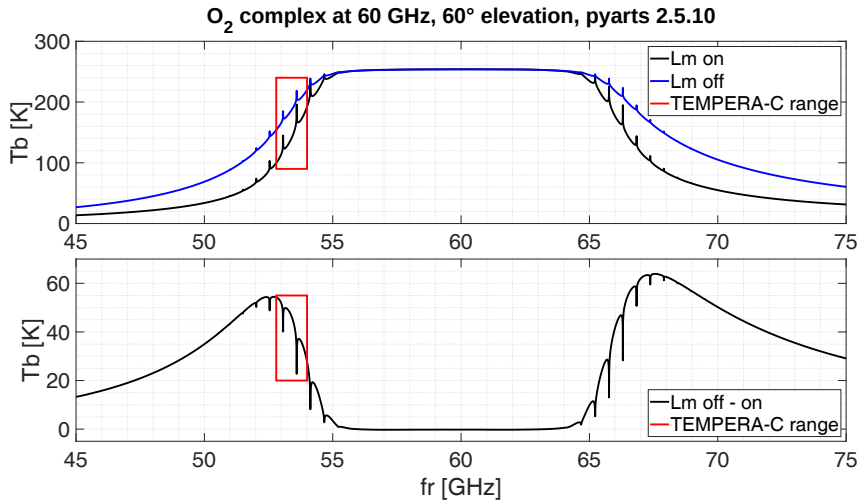

Figure 6.3: The oxygen emission complex was simulated twice with activated and deactivated line mixing modules. The difference is shown in the bottom panel.

6.3. The Zeeman effect in atmospheric oxygen

As a linear and symmetric compound, molecular oxygen (O_2) has no electrical dipole moment. As other neutral compounds can not couple to the electrical field due to the lack of electrical dipole moment and, therefore, have no rotational emission spectra, the oxygen molecule must have something else. A closer look at the bonding orbital reveals that there are indeed two unpaired electrons leading to a permanent magnetic dipole. It is this magnetic dipole that enables molecular oxygen to couple to the EM field and emit and absorb EM radiation. Since the dipole is magnetic, it couples to the Earth's magnetic field, leading to a Zeeman splitting effect in single emission lines. The Zeeman splitting affects the line profile dramatically by splitting a single line into several hundred ones. The Zeeman splitting or Zeeman broadening dominates above 40km where atmospheric pressure is low. Below 40 km, pressure broadening is still the dominating broadening effect.

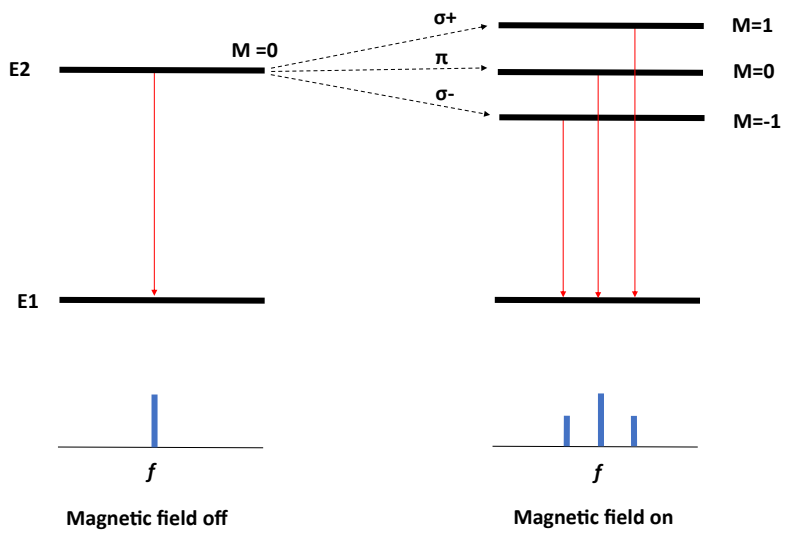

Figure 6.4: Simplified chart to illustrate the Zeeman effect. The B-field splits the energy level E2 into three sub-levels $\sigma^+, \pi,$ and σ^-.

The theoretical overview in this section is taken from Larsson et al., 2014; Larsson et al., 2019. The energy shift ΔE due to coupling to the magnetic field $\vec{B}$ of a rotational state with rotational quantum number N, and total angular momentum quantum number $J \in [|N-S|, |N-S+1|, ..., |N+S|]$ (where S is the spin quantum number) is given by:

$$\Delta E = -g_{J_N} M_J |\vec{B}| \mu_b, \tag{6.1}$$

where $M_J \in [-J, -J+1, ..., J]$ is the projection of the total angular momentum quantum number J on $\vec{B}$, μ_b is the Bohr magneton, and g_{J_N} is called the Landé factor which depends on the emitting particle and the specific state J_N. The frequency shift from the transition $J''_N - J'_N$, where the double prime denotes the higher state and the prime denotes the lower state is:

$$\Delta\nu_Z = \frac{H\mu_b}{h}\left(g''_{J''_N} M'' - g'_{J'_N} M'\right) \tag{6.2}$$

and the line shape of one specific Zeeman line f_Z is given by:

$$f_Z = \frac{1}{\alpha_D\sqrt{\pi}} w(z),\ z(\nu) = \frac{\nu - \nu_0 - \Delta\nu_Z + i\alpha_L}{\alpha_D}. \tag{6.3}$$

Here, $w(z)$ is the Faddeeva function. It has the properties that for $z = x+yi$, one has $\Re\{w(z)\} = f_V(x)$. Summing over all Z of the possible transitions $M'' - M'$, every Zeeman line Z will have its strength S_Z. For fully polarimetric treatment, f_Z is multiplied with the Müller matrix Φ_Z, which describes the polarization state of the radiation:

$$\mathbf{K}_P = nS_{J''_N J'_N} \sum_Z S_Z f_Z \Phi_Z. \tag{6.4}$$

Furthermore, $S_{J''_N J'_N}$ is the line strength of the un-split line, and $\mathbf{K}_P$ is the propagation matrix. It's an analogue to the absorption cross-section (**Eq. 4.9**) but in 3-dimensions and accounting for polarization.

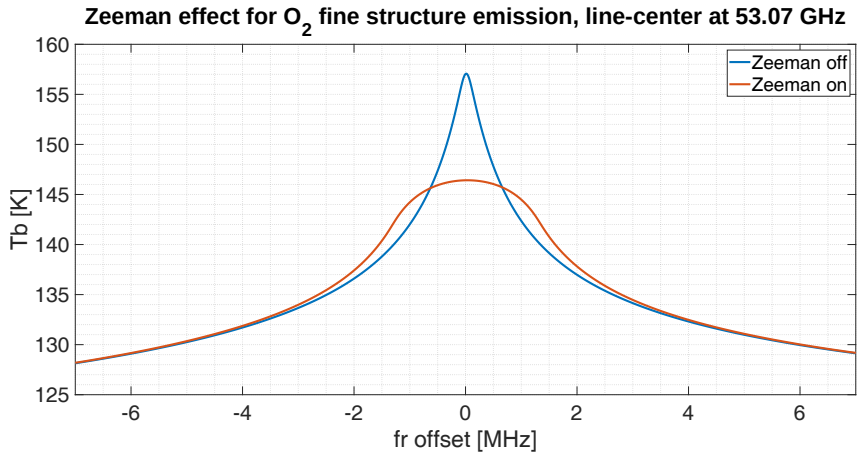

Figure 6.5: The B-field splits one rotational transition in hundreds of transitions (depending of J'_N and J''_N) with slightly different energy differences ΔE. The superposition of the Zeeman split emission lines Eq. 6.4 appears as one broadened line. This illustration was simulated with ARTS 2.6

6.4. The Stokes vector

In the absence of coupling to a magnetic field, rotational emission lines, in general, are unpolarized because the polarization cancels out due to rotational symmetry. However, the coupling to the Earth's magnetic field breaks this symmetry, and the observed radiation gets a polarization signature. When the magnetic field lines of $\vec{B}$ are perpendicular to the observed beam, the radiation will be linearly polarized, and a beam along $\vec{B}$, will lead to circularly polarized radiation. Therefore, radiation along a line of sight, which is tilted concerning $\vec{B}$ will carry both components. For observations of all of the polarization components, the Stokes formalism is suitable. The Stokes vector $S = (I, Q, U, V)$ is a four-component vector carrying information about the polarization state of the radiation. The following is a summary of the Stokes formalism.

A local E-field $\mathbf{E}(\mathbf{t})$ in front of the antenna is of the form:

$$\mathbf{E}(\mathbf{t}) = \left(\mathbf{E}_x + \mathbf{E}_y e^{i\Delta\phi}\right) e^{i\omega t}. \tag{6.5}$$

The coordinate system is chosen, such that the z direction is along the antenna beam and the x, y-plane is perpendicular to it (antenna plane), the subscripts denote that the corresponding

field component is linearly polarized along this axis, $\Delta\phi$ is the phase difference between the x and y polarization, and $\omega = 2\pi\nu$ is the angular frequency of the radiation. The Stokes components are defined as

$$I = |\mathbf{E}_x|^2 + |\mathbf{E}_y|^2, \tag{6.6}$$
$$Q = |\mathbf{E}_x|^2 - |\mathbf{E}_y|^2, \tag{6.7}$$
$$U = 2\Re\left\{\left\langle \mathbf{E}_x\mathbf{E}_y^*\right\rangle\right\}, \tag{6.8}$$
$$V = -2\Im\left\{\left\langle \mathbf{E}_x\mathbf{E}_y^*\right\rangle\right\}, \tag{6.9}$$

where the auto-correlation $\langle ... \rangle$ is defined as:

$$\left\langle \mathbf{E}_x\mathbf{E}_y^*\right\rangle = \frac{1}{T}\int_T \mathbf{E}_x\mathbf{E}_y^* e^{-i\Delta\phi} dt, \tag{6.10}$$

for integration times much higher than the period of the radiation:

$$T \gg \frac{2\pi}{\omega}. \tag{6.11}$$

Note also that:

$$\langle \mathbf{E}_x\mathbf{E}_x^* \rangle = |\mathbf{E}_x|^2. \tag{6.12}$$

In the basis of circular polarization $(\mathbf{E}_{RCP}, \mathbf{E}_{LCP})$, the I and V components are:

$$I = |\mathbf{E}_{RCP}|^2 + |\mathbf{E}_{LCP}|^2, \tag{6.13}$$
$$V = |\mathbf{E}_{RCP}|^2 - |\mathbf{E}_{LCP}|^2. \tag{6.14}$$

The 4 Stokes components of the Oxygen fine structure emission line at 53.07GHz are shown in **Fig. 6.6**.

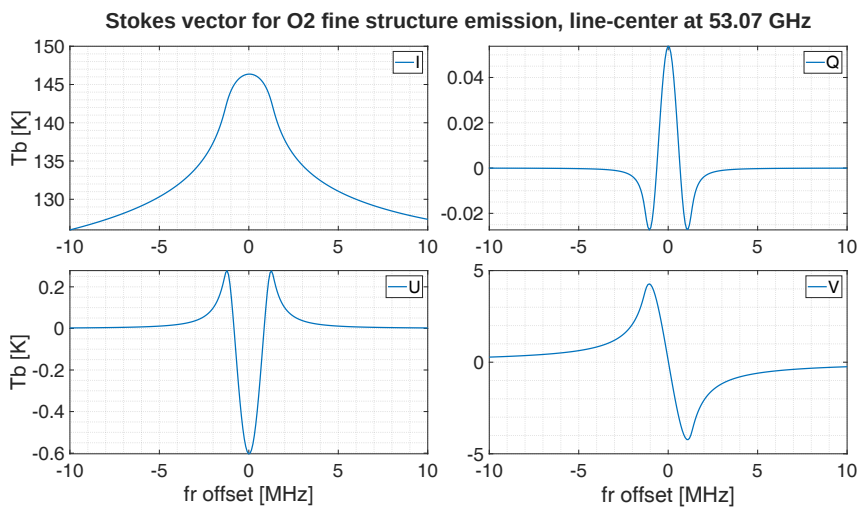

Figure 6.6: The components of the Stokes vector for a fine structure oxygen emission line.

7. Ground-based microwave radiometry

7.1. Basics

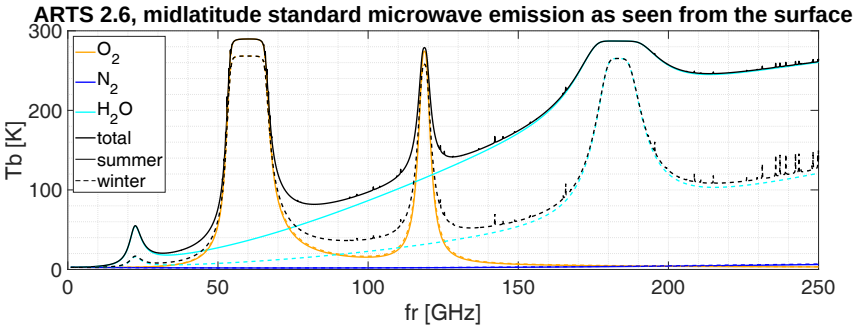

Figure 7.1: Atmospheric microwave emission spectra for zenith view on ground at mid-latitudes.

Several atmospheric compounds such as water, nitrogen, oxygen, or ozone molecules emit microwave radiation by undergoing rotational energy transitions (see **Fig. 7.1**). The emission spectra form natural line shapes, which are formed by pressure, Doppler and Zeeman broadening, and line mixing (see **Section 4.2**). A microwave radiometer is an instrument designed to measure the emission spectra in the microwave band to retrieve profiles of atmospheric quantities (see **Section 5.2**). Next to ground-based instruments, microwave radiometers on board satellites are widely used for climate studies and weather monitoring and predictions (Livesey et al., 2006; Waters et al., 2006; Russell III et al., 1999; Parkinson, 2022, and many more). Ground-based radiometers offer a high time resolution in the range of hours, where the time resolution for space-born instruments is limited by the orbital geometry to one or two overflights per day for each longitude and latitude. On the other hand, satellite observations cover a wide area of the globe, while a ground-based instrument measures at one location. Compared to active remote sensing techniques such as LIDARs and RADARs, microwave radiometers consume less power and are not affected by sunlight. However, in terms of time resolution of a few hours and altitude resolution in the range of meters, LIDAR systems are unmatched by any other technique (the altitude resolution of TEMPERA is about 15km).

The main parts all radiometers share are the feed horn or antenna, which collects the atmospheric radiation. Rotating mirrors guide the signal from the atmosphere or the calibration target into the antenna. A low noise amplifier amplifies the received signal before a bandpass filter reduces it to the frequency band of interest. Since microwave frequencies are too high to be resolved digitally, the frequency of the signal is downsized by mixing with a well-known frequency, which is generated in a local oscillator. The amplified and downsized signal is afterwards analyzed by an FFT spectrometer. The challenge in microwave radiometry is the weak atmospheric signal intended to be observed, which demands high precision in manufacturing the single components and a well-performed calibration. A wide overview of microwave remote sensing theory and application is given in Mätzler, 2006.

7.2. Sub-harmonic mixing

The observed frequency range of TEMPERA and TEMPERA-C is between 52-54 GHz. These frequencies are too high to be analyzed with the FFT spectrometer and need to be downsized.

With the instruments mentioned above, this is done with an electronic device known as a subharmonic mixer. The frequency of the signal entering the antenna is called radio frequency RF. A second signal of known frequency is generated in the local oscillator (LO). A sub-harmonic mixer has two inputs for signals of frequency RF and LO. The output is a down-mixed signal with frequency IF = |RF-LO| but consists of an overlay of two bands with center frequencies f_{lower} = LO-IF and f_{upper}= LO+IF. The overlapping lower sideband is suppressed with a bandpass filter before entering the mixer. In the case of TEMPERA-C, one emission line of interest is at 53.07 GHz, and the LO frequency is 50 GHz. The mixer generates a signal which at IF = 3 GHz contains the overlap of the spectra, which before mixing were at LO-IF = 47 GHz and LO+IF = 53 GHz. The bandpass filter suppresses the signal below 50 GHz and is coupled in front of the mixer. The backend center frequency is tuned to 3 GHz to resolve the emission line of interest.

7.3. Calibration

The output power of the backend is usually in voltage [V] or counts [u]. To determine instrumental noise and convert the backend output into units of incoming radiation, the system needs to be calibrated. The common unit in microwave radiometry is brightness temperature T_B. Brightness temperature is defined as the temperature a blackbody would have radiating with the same power. Since microwave frequencies are very low and the temperatures in the atmosphere are between 200-300 K, one has the condition $\frac{h\nu}{k_b T} \ll 1$, which justifies using the Rayleigh-Jeans approximation:

$$B(T) = \frac{2k_b T}{c^2}\nu^2 \tag{7.1}$$

and the assumption that the brightness temperature is proportional to the radiation power entering the antenna. A slight deviation is only notable when the antenna beam is directed at a liquid nitrogen surface with a physical temperature of 77 K (ΔT = 1.2 K at 50 GHz).
Both instruments in this thesis are at least partially calibrated with the two-point calibration. In the two-point calibration, two distinct signals of known brightness temperature are coupled into the receiver chain T_{Hot} and T_{Cold}. For ground-based applications, the hot source is an absorbing target having the properties of a black body. The brightness temperature is determined by measuring its physical temperature $T_{Hot} = T_{Ambient}$. The cold source is a surface of liquid nitrogen whose surface temperature (boiling temperature) depends on the ambient pressure through the Clausius-Clapeyron equation:

$$\ln \frac{P_2}{P_0} = \frac{\Delta H_{vap}}{R}\left(\frac{1}{T_0} - \frac{1}{T_2}\right). \tag{7.2}$$

The coefficient $\Delta H_{vap} = 5.57^{\mathrm{KJ}}/_{\mathrm{mol}}$ is the vaporization enthalpy per mol, and $T_0 = 77.35K$ at $P_0 = 101.325$kPa. For example, the surface temperature of liquid nitrogen on the Jungfrau Joch high altitude (3571m a.s.l) research station is 73 K.

The calibration equation for the two-point calibration is:

$$V = gT_A + V_N, \tag{7.3}$$

where V is the output signal, usually in voltage or counts [u], g is the receiver gain, T_A is the antenna temperature, which is the power in [K] in front of the Antenna, and T_N is the instrument noise temperature. The instrument noise depends on the components and their temperature and is not reduced by increasing the integration time. Note that the linear approach is only possible

since the Raleigh-Jeans approximation is applied. The measurements of the hot and cold sources form the system of equations:

$$V_{Hot} = g\left(T_{Hot} + T_N\right), \tag{7.4}$$
$$V_{Cold} = g\left(T_{Cold} + T_N\right). \tag{7.5}$$

Which can be solved for g and T_N:

$$g = \frac{V_{Hot} - V_{Cold}}{T_{Hot} - T_{Cold}}, \tag{7.6}$$
$$T_N = \frac{T_{Hot}V_{Cold} - T_{Cold}V_{Hot}}{V_{Hot} - V_{Cold}}. \tag{7.7}$$

The sum of the antenna temperature T_A and the noise temperature T_N is the system temperature $T_{sys} = T_A + T_N$. The statistical accuracy is given by the radiometer equation:

$$\Delta T = \frac{T_{sys}}{\sqrt{\Delta\nu\Delta\tau}}, \tag{7.8}$$

where $\Delta\nu$ is the measured band width and $\Delta\tau$ the integration time. In our case, a noise diode, generating white noise of known temperature T_{ND}, is coupled into the receiver. For calibration, the noise diode is switched on while looking at the ambient load. In equation (7.6) and (7.7), substitute T_{cold} with the ambient load temperature, and T_{hot} with the sum of the ambient temperature and noise temperature $T_{cold} = T_{Ambient}$ and $T_{hot} = T_{Ambient} + T_{ND}$.

Standing waves will form between the calibration loads and the antenna (see **Fig. 7.2**). Therefore, the loads have to be positioned with a slight angle off the antenna plane. For the case that standing waves form between the nitrogen surface and the antenna, a full cycle should be chosen for integration. A periodic shift of the distance between the mirror and the surface of a quarter of the wavelength (wobbling) is suitable to reduce standing waves.

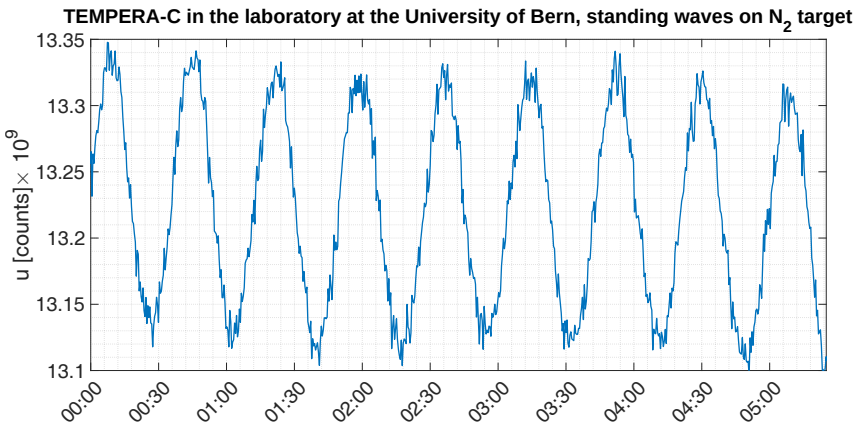

Figure 7.2: Standing waves between the antenna and the liquid nitrogen surface. As the surface sinks over time, the distance to the antenna increases. A peak forms when the distance is equal to an even number times 1/4 of the wavelength, while sinks correspond to an odd number. For calibration, integration should be performed only over full cycles.

8. TEMPERA

8.1. Summary

TEMPERA (TEMPerature RAdiometer) was built in the microwave group in 2013 (Stähli et al., 2013). With a high-resolution spectrometer (30.5 kHz resolution with 2× 500 MHz bandwidth) and 12 broadband channels, it was designed to observe tropospheric and stratospheric temperature spectra. In the initial measurement mode, TEMPERA performed a tipping curve, observing the left wing of the 60 GHz oxygen complex to retrieve the tropospheric temperature profile. To retrieve the stratospheric profile, the observation at 60°elevation was used, resolving the fine structure emission lines at 52.54 and 53.07 GHz. In this measurement mode, the integration time necessary for fine structure spectra was around 3 h, resulting in 8 profiles per day. TEMPERA measured operational from 2014 at the MeteoSwiss technical station in Payerne and was moved to the roof of the ExWi building in 2022.

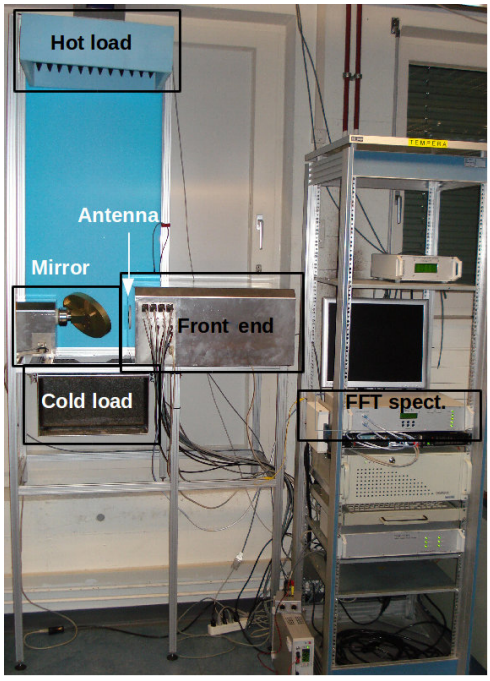

Figure 8.1: TEMPERA in the laboratory at the University of Bern (Navas-Guzmán et al., 2015)

Bandwidth	2× 500 MHz
Frequency resolution	30.5 kHz
line-center 1	52.54 GHz
line-center 2	53.07 GHz
Elevation angle	60°
Integration time	1-3 h

Table 8.1: TEMPERA stratospheric spectra specifictions overwiev.

8.2. Optimal elevation angle

There are seven stratospheric fine structure lines on the left oxygen complex (see **Fig. 8.2**). To decide which line is optimal for observation at which elevation, the spectrum was simulated at different elevation angles. From the simulations, the line amplitudes and their ratio to the tropospheric baseline were computed (see **Fig. 8.3**). TEMPERA operates currently with an elevation angle of 60°. The backend is tuned on the lines at 52.54 and 53.07 GHz.

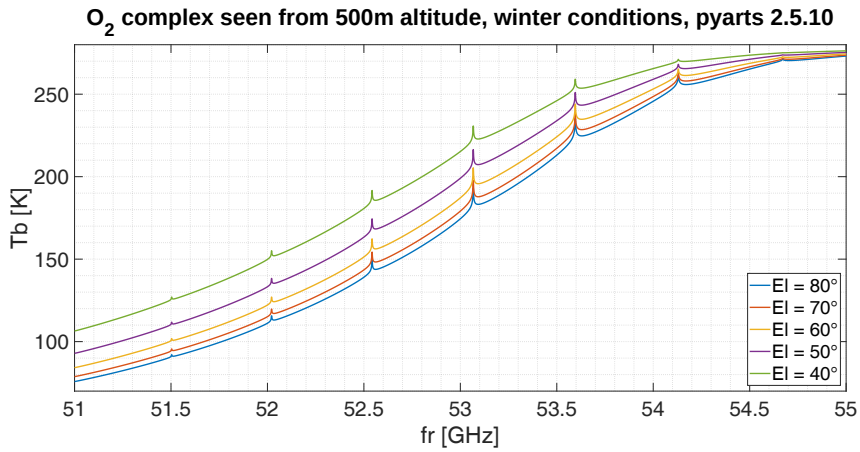

Figure 8.2: Simulation of the oxygen emission complex for different elevation angles. For lower elevations, the antenna beam covers more air mass in the troposphere. Therefore, the tropospheric brightness temperature is higher.

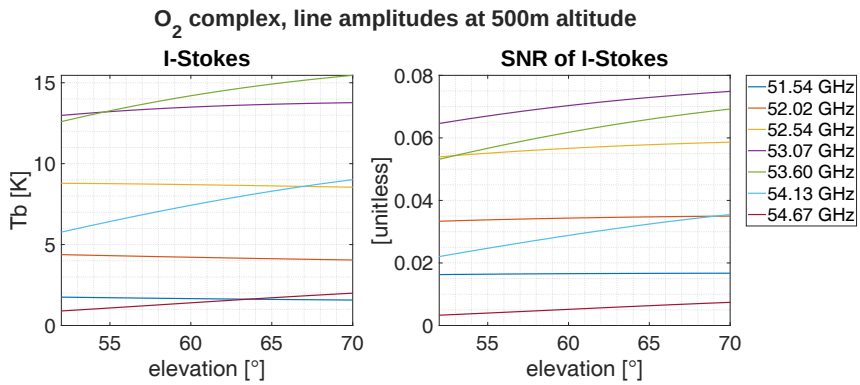

Figure 8.3: The amplitudes of the fine structure lines and their ratio to the tropospheric background increase with the elevation angle. The maximal elevation is, however, limited by the microwave window in the laboratory to 60°.

8.3. Updated retrieval algorithm

The ARTS Zeeman module was released in 2014 and was not implemented in the retrieval routine until 2022. The first inversions were performed by cutting off 1MHz around the line centre of the spectra to avoid contamination of the temperature retrieval by the Zeeman line splitting. Even though TEMPERA retrieved the tropospheric temperature profile, the tropospherical correction for stratospheric profiles was done according to Ingold and Kämpfer, 1998 assuming the troposphere as a homogeneous layer and using only the surface temperature to estimate a mean weighted opacity.

The current setup for the forward model atmosphere is as follows. The model atmosphere is 3 dimensional, having a 5×5 grid in 1.125° steps in latitude and 1.125° steps in longitude. The sensor is placed in the middle grid square. Depending on the tropospherical correction, the sensor altitude is 12 km or 500m. The atmospheric apriori profiles were generated with a long-time running mean over ECMWF (European Centre for Medium-Range Weather Forecasts `https://www.ecmwf.int`) profiles and are constant through the grid. Next to O_2 the species H_2O and N_2 are included in the ensemble, which is required by ARTS. The vmr profiles for the atmospheric species are provided by ARTS, the magnetic field taken from IGRF (Thébault et al., 2015). Line data for rotational transitions was downloaded from the HITRAN database

(Gordon et al., 2017). Next to the atmospheric temperature profile, a linear baseline correction, frequency shift, and frequency stretch are retrieved.

The Zeeman module was implemented in Krochin et al., 2022a, which increased the upper altitude limit to 50 km. **Fig. 8.4** shows a comparison of the scaled AVK matrices with the corresponding measurement response. Version 1, as it was published in Krochin et al., 2022a, had the Zeeman module implemented and used the tropospheric correction according to Ingold and Kämpfer, 1998. The sudden jump in the AVK above 40 km is most likely due to the use of two different species of O_2 in the algorithm. The species below 40 km were affected only by pressure broadening, while the broadening of the species above 40 km was calculated with the Zeeman module. The apriori error in versions 1 and 2 was chosen slightly to increase with altitude, enforcing higher measurement response values. The retrievals of Version 2 and 3 were made without tropospheric correction. Here, the algorithm retrieves the temperature profile down to the surface instead of correcting for the troposphere. This method improves the computation of tropospheric signals in the algorithm, but the tropospheric profiles retrieved in this way are not recommended for scientific analysis. As in Version 1, two O_2 species were implemented. In version 3, the cutoff for the pure pressure broadened species was at 12 km. The line wings were used for the tropospheric profile, but measurement and apriori error were chosen such that the retrieved tropospheric profile deviated only by a few Kelvin from the apriori. In Version 3, the measurement and apriori error were adapted for the troposphere, which lowered the altitude limit and the altitude resolution. **Tab. 8.2** shows the altitude range and the bandwidth used for the retrieval. Even though a MR>0.6 denotes that over 60% of information at the respective altitude is from the spectrum, the profile does not necessarily reflect reality. Without considering the Zeeman effect, an upper altitude limit of 48km, as in Stähli et al., 2013, seems unlikely.

8.4. Current status

Currently, TEMPERA is operating at the roof of the ExWi Building at a constant elevation of 60°, where the backend is tuned on the fine structure lines at 52.54 and 53.07 GHz. The level 0 data are stored daily on the research storage. An automated shell script runs the calibration and retrievals on a daily basis. The calibration scripts are made in Matlab. For inversion, the Atmospheric Radiative Transfer Simulator (ARTS version 2.2) is used with the Qpack interface. The scripts are uploaded to git (`https://git.iap.unibe.ch/wk20h916/TEMPERA_operational_2022`). Data during cloudy or rainy conditions are filtered out, using the fact that the brightness temperature of the baseline increases significantly due to liquid water thermal emission. The current cycle is performed without a tipping curve to maximize stratospheric measurement time. The integration time is fixed to exactly one hour instead of integrating up to a given signal-to-noise ratio. This choice is made because equal sampled data is better for spectral decomposition, even though the actual noise can vary.
In the year 2022, an unevenness in the baseline was found, most probably caused by the built-in attenuator between the oscillator multiplier and the sub-harmonic mixer, which happens to be of a very old model. The issue was fixed by changing the LO frequency by a few MHz.

Version	Tph correction	Used bandwidth	MR>0.6 range [km]
0 - 2013	yes	500MHz (15 MHz in full resolution)	19-48
1 - 2021	yes	200MHZ (20 MHz in full resolution)	21-57
2 - 2022	none	120 MHz in full resolution	24-51
3 - 2023	none	160 MHz in full resolution	18-51

Table 8.2: Overview of the used bandwidth and altitude range for the different retrieval versions.

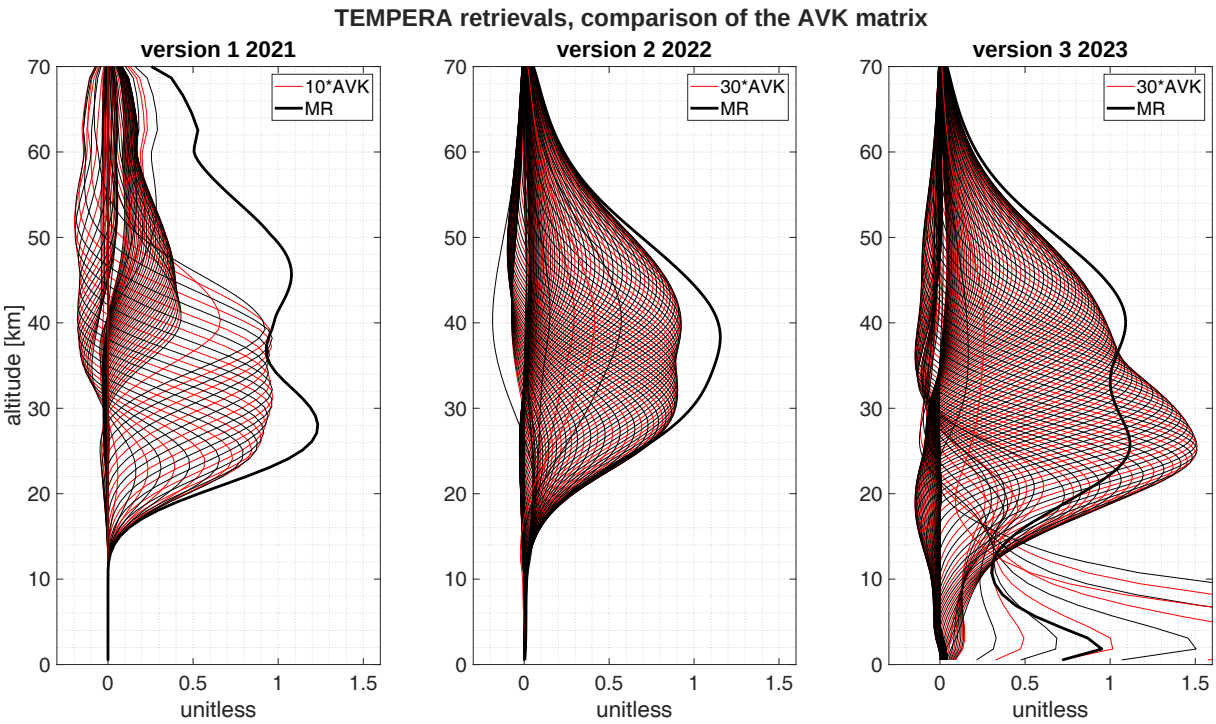

Figure 8.4: Comparison of the AVK matrix of the different retrieval versions. The rows of the AVK matrix are scaled to illustrate them together with the MR.

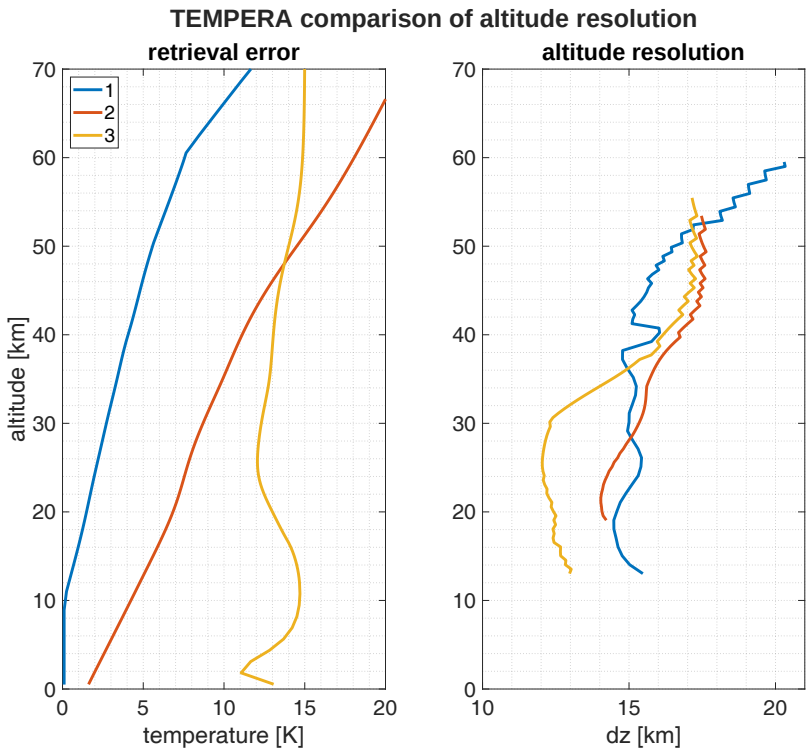

Figure 8.5: Left panel: The total retrieval error ($\mathbf{S}_{tot} = \mathbf{S}_s + \mathbf{S}_o$) for the different retrieval versions. Right panel: FWHM value of the rows of the AVK matrix for the different retrieval versions illustrates the altitude resolution.

8.5. Comments on publication II

Continuous temperature soundings at the stratosphere and lower mesosphere with a ground-based radiometer considering the Zeeman effect

Cite as:

Krochin, W., Navas-Guzmán, F., Kuhl, D., Murk, A., and Stober, G.: Continuous temperature soundings at the stratosphere and lower mesosphere with a ground-based radiometer considering the Zeeman effect, Atmos. Meas. Tech., 15, 2231–2249, https://doi.org/10.5194/amt-15-2231-2022, 2022.

DOI: `https://doi.org/10.5194/amt-15-2231-2022`

Summary

This manuscript shows 4 years of continuous temperature sounding with TEMPERA at the location of the MeteoSwiss technical station in Payerne (CH). The innovation is the implementation of the Zeeman effect in the retrieval algorithm. For validation, the data set is compared with MERRA2 and NAVGEM-HA. The comparison showed a good agreement on time scales of one month with correlation coefficients of 0.9 ± 0,1. However, a systematic overestimation in the lower stratosphere and an underestimation in the upper stratosphere of the retrieved temperatures from TEMPERA compared to the reanalysis data was found.

Author contribution

For this publication, I rewrote the calibration algorithm for TEMPERA from scratch, implemented the Zeeman splitting module in the retrieval algorithm, and performed the validation. To calculate the Zeeman effect, the forward model had to be extended from a 1D to a 3D atmosphere, and the retrieval parameters had to be adjusted and optimized accordingly. As the first author, I have written most of the manuscript. Gunter Stober provided background information, and Axel Murk provided expert knowledge on instrument calibration. All authors were involved in revising the text.

9. TEMPERA-C

9.1. Towards a new state of art for temperature retrievals

As TEMPERA, TEMPERA-C is designed for ground-based temperature sounding in the middle atmosphere. The innovation is to separate the incoming microwave radiation into its orthogonal polarized components. A digital correlator allows for measuring the self and cross-correlation of the orthogonally polarized signals. The self-correlation output gives the linear polarizations and the cross-correlation of the 3rd and 4th components of the Stokes vector. This allows us to observe all 4 Stokes components of the Zeeman-affected oxygen microwave emission spectrum and, with them, the circularly polarized components. Instrument noise is highly reduced compared to the older instrument because better components are used, and simultaneous measurement of two (independent) polarizations doubles the information content. The goal of TEMPERA-C is, in the first place, to expand the altitude range for temperature retrievals. The improved performance also increases the time resolution of the atmospheric temperature profiles. By using the circularly polarized component, the orientation of the polarization axis and its rotation due to reflection on the mirror does not matter. Moreover, the U and V-Stokes components of atmospheric oxygen were never measured before. The calibration of the Stokes components is, however, more challenging compared to the two-point calibration of the full-intensity spectrum of TEMPERA.

9.2. Component description

The calibration optic is illustrated in **Fig. 9.2**. Incoming microwave radiation is currently guided by two mirrors (1,2) into the corrugated horn antenna (3). The flat mirror (1) is controlled by two motors. A circular motor allows to scan vertically between -90°to 90°. A linear motor is installed for wobbling. The parabolic mirror (2) focuses the radiation in the antenna (3). The antenna guides the signal through the orthomode transducer ((4) in **Fig. 9.1** and **Fig. 9.3**), which splits it into the two orthogonal polarized components and guides it into two identical receiver channels. The two independent signals are amplified (7), and a bandpass filter (8) suppresses the lower sideband before the signal is mixed with the local oscillator frequency (9). The amplified, filtered, and down-mixed signals enter the two inputs of the digital correlator, which has 4 outputs. Two outputs are for the self-correlated spectra, and the other two carry the real and complex part of the cross-correlated spectra. Waveguides and electronic components are optimized for a frequency range between 53-54 GHz.

For the operational instrument calibration, noise diodes (6) are coupled into both receiver channels in front of the amplifier. For the ambient temperature source, a microwave absorber is placed at -90°elevation. The remaining parts of the calibration optic in **Fig. 9.2** are currently under construction and will be installed at the beginning of 2025. The calibration optic was designed by the microwave group and manufactured by the mechanics workshop of the Institute of Applied Physics. Further component specifications are given in the following overview, **Tab. 9.1** and Krochin et al., 2022b.

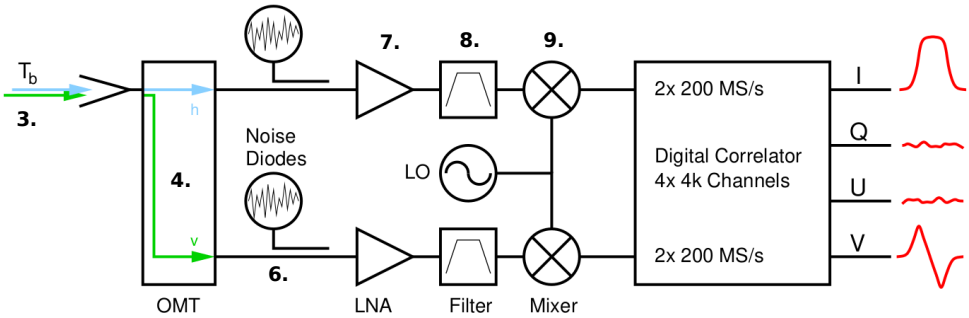

Figure 9.1: Simplified chart of the TEMPERA-C front-end (Krochin et al., 2022b).

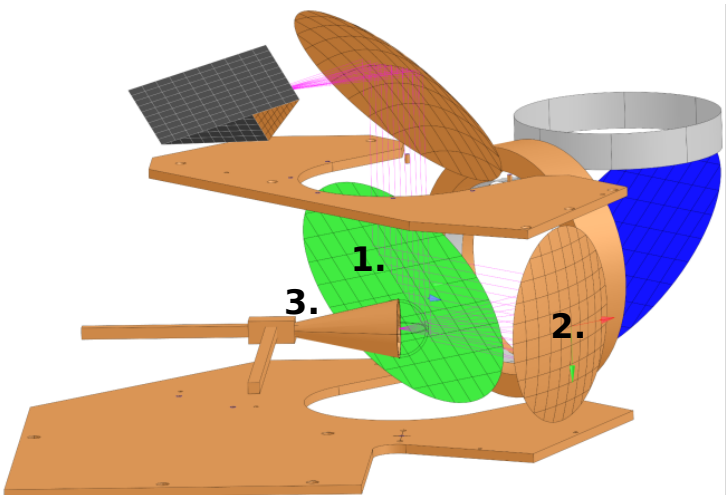

Figure 9.2: Grasp model of the TEMPERA-C optic

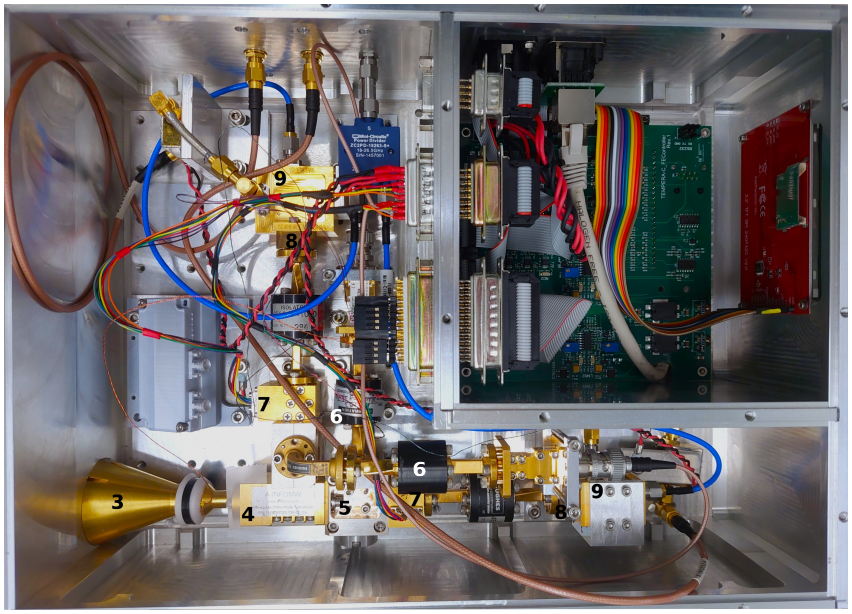

Figure 9.3: Interior of the TEMPERA-C front-end.

1. **Rotating Mirror**
   A flat aluminum honeycomb structured mirror. A rotating motor covers the elevation angles -90°to 90°. A linear motor allows for wobbling.

2. **Parabolic Mirror**
   The internal parabolic mirror is designed to shape the antenna beam to 3.2°opening angle (FWHM of the final beam). The diameter is as large as possible to minimize spillover, and the shape is optimized to minimize cross-polarization. A small reflection angle of 60°also reduces polarization effects compared to larger reflection angles. The remaining cross-polarization was negligible in the simulations.

3. **Horn**
   The corrugated horn was designed specifically for polarimetric observations of frequencies between 52-54 GHz. The Antenna co-polar beam is highly symmetric for both orthogonal axes, which are normal to the antenna plane (H and E plane), the side lobes are below -50dB, and the cross-polar lobes are below -40dB (see Figure A.4). The full width at half maximum was measured to 18.8°for the E- and H-plane. The horn design was performed by the microwave group, and the manufacturing was done by Thomas Keating Ltd.

4. **OMT**
   The OMT (Ortho-mode transducer) is a commercial device from A-INFO. It has one circular input and two rectangular outputs for the orthogonal polarized signals. The Frequency range is 50-70 GHz.

5. **Coupler**
   A directional coupler couples a fraction of the noise power into the receiver channel. Gaussian error calculation showed that the smallest calibration error is reached with a noise diode temperature between 600-800 K.

6. **Noise diodes**
   The noise-generating diodes are a commercial device from noisecom. Their noise power is stable over a long period.

7. **LNA**
   The LNA is a commercial device from Low Noise Factory and is designed for the frequency range 45-77 GHz. The typical noise temperature is 217 K at an amplification of 34dB.

8. **Band pass filter**
   Filters the lower side-band with optimized transmission between 50-54 GHz.

9. **Mixer**
   The subharmonic mixer is a commercial device from Virginia Diodes Inc.

10. **Digital correlator**
    The USRP X310 digital correlator from Ettus has two signal inputs and generates four outputs (2× self-correlated signals and the real and complex part of the cross-correlated signal) of 100MHz bandwidth and 4096 channels, resulting in a resolution of 24.4 kHz.

OMT	
Manufacturer	AINFO
Port to Port Isolation	<-43 dB
Insertion Loss	<0.5 dB
LNA	
Manufacturer	LNF
Gain	>33dB
Noise Figure	2.4 dB
Band pass filter	
Manufacturer	In house
3dB Corner Fr	50.8-54.2 GHz
Insertion loss	<0.6 dB
Mixer	
Type	VDI
DSB conversion Loss	<6 dB
DSB Noise Temperature	<700 K
Digital Correlator	
Manufacturer	Ettus
Type	USRP X310
Daughterboards	2× TwinRX
Bandwidth	4×100 MHz
Channels	4×4096
Resolution	24.4 kHz

Table 9.1: Component description TEMPERA-C. This table was taken from Krochin et al., 2022b

9.3. Comments on publication III

Development of a Polarimetric 50-GHz Spectrometer for Temperature Sounding in the Middle Atmosphere

Cite as:

W. Krochin, G. Stober and A. Murk, "Development of a Polarimetric 50-GHz Spectrometer for Temperature Sounding in the Middle Atmosphere," in IEEE Journal of Selected Topics in Applied Earth Observations and Remote Sensing, vol. 15, pp. 5644-5651, 2022.

DOI: `10.1109/JSTARS.2022.3186796`

Summary

This manuscript contains a detailed component description of TEMPERA-C, the first measurement of circularly polarized microwave spectra of atmospheric oxygen, as well as the first post-process correction procedure. Moreover, it contains retrieval results from simulated spectra and forward model simulations of circularly polarized spectra with varying magnetic fields.

Retrievals with simulated spectra showed that, by using circular polarized spectra, the upper altitude limit for temperature retrievals can be extended from 50 to 60 km, compared to retrieval with one spectrum of total polarization.

Author contribution

I performed and calibrated the TEMPERA-C measurements, developed the post-process correction, set up the forward model simulations, and performed the retrievals. Technical expert knowledge was provided by Axel Murk. All authors were involved in revising the text.

9.4. Polarimetric calibration and correction

For a polarimetric radiometer, a simple two-point or total power calibration is not enough since polarization properties have to be calibrated as well. In this section, the calibration correction algorithm, specifically developed for TEMPERA-C, is described.

The local E-field in front of the antenna has the same form as in **Eq. 6.5**:

$$E(t) = \left(E_a + E_b e^{\Delta\phi i}\right) e^{\omega t i}. \tag{9.1}$$

The a, b-plane is parallel to the antenna plane but can be rotated around the third axis by a random angle. The reason to use the circularly polarized components is that for circular polarization, the rotation angle between the a, b-plane and the x, y-plane is irrelevant. The output of the digital correlator for an ideal receiver is:

$$V_a = |g_a|^2 \langle E_a E_a^* \rangle + V_{Na}, \tag{9.2}$$

$$V_b = |g_b|^2 \langle E_b E_b^* \rangle + V_{Nb}, \tag{9.3}$$

$$V_X = \langle g_a g_b^* E_a E_b^* \rangle + O_X. \tag{9.4}$$

However, due to imperfections of the orthomode transducer, a small fraction of b-polarized radiation will enter the a-channel and vice versa. With the cross-talk coefficients (c_a, c_b), a more realistic receiver has an output signal of the form:

$$\begin{aligned} V_a =& \langle (g_a E_a + g_a c_b E_b)(g_a E_a + g_a c_b E_b)^* \rangle + V_{Na} \\ =& |g_a|^2 \langle E_a E_a^* \rangle + |g_a|^2 |c_b|^2 \langle E_b E_b^* \rangle + \left\langle g_a^2 c_b^* E_a E_b^* + g_a^{2*} c_b E_a^* E_b \right\rangle + V_{Na} \\ =& |g_a|^2 \langle E_a E_a^* \rangle + |g_a|^2 |c_b|^2 \langle E_b E_b^* \rangle + 2\Re\left\{\left\langle g_a^2 c_b^* E_a E_b^* \right\rangle\right\} + V_{Na}, \end{aligned} \tag{9.5}$$

$$V_b = |g_b|^2 \langle E_b E_b^* \rangle + |g_b|^2 |c_a|^2 \langle E_a E_a^* \rangle + 2\Re\left\{\left\langle g_b^2 c_a^* E_b E_a^* \right\rangle\right\} + V_{Nb}, \tag{9.6}$$

$$\begin{aligned} V_X =& \langle (g_a E_a + g_a c_b E_b)(g_b E_b + g_b c_a E_a)^* \rangle + O_X \\ =& \langle g_a g_b^* (1 + c_a^* c_b) E_a E_b^* \rangle + \langle g_a g_b^* c_a^* E_a E_a^* \rangle + \langle g_a g_b^* c_b E_b E_b^* \rangle + O_X. \end{aligned} \tag{9.7}$$

Here, O_X is a constant signal offset, which is distinguished from instrument noise as random noise is, in general, uncorrelated. The goal of the calibration process is to determine the complex gains g_a, g_b along with the complex cross-talk coefficients c_a, c_b. The state of art procedure is to

use a specially prepared calibration target according Gasiewski and Kunkee, 1993. This calibration method uses a rotatable polarization grid. A phase retardation plate can also be added as described in Lahtinen et al., 2003. The plate adds a phase offset to the field, depending on the polarization of the field and the angle of the plate. However, the properties of the polarization grid and the plate have to be precisely measured beforehand. In addition, the digital correlator used for TEMPERA-C has no cross-talk between the channels V_a, V_b, and V_X, which is taken into account in the method described above. To save on costs and materials, we have decided to try a simplified calibration method for TEMPERA-C. The procedure to estimate the parameters c_a, c_b uses only a rotatable polarized grid in combination with an ambient load and a liquid nitrogen load.

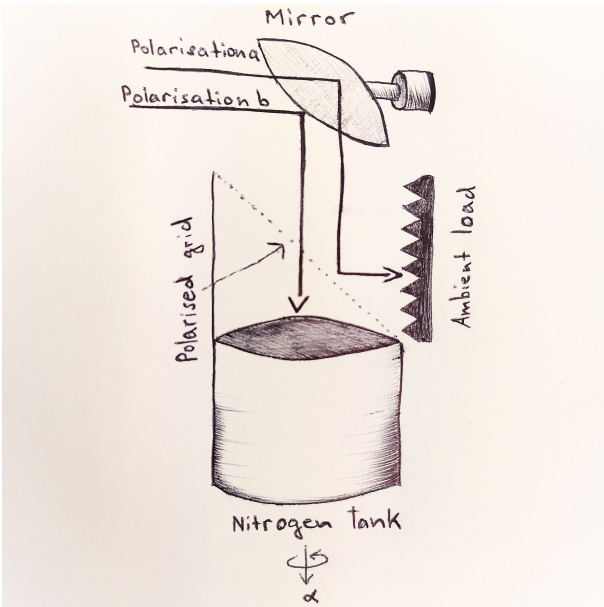

Figure 9.4: Illustration of the instrumental setup. A polarized grid was placed on a rotatable N_2 tank.

The E-field units are chosen to fulfill:

$$T_a \propto \langle E_a E_a^* \rangle \,, \tag{9.8}$$
$$T_b \propto \langle E_b E_b^* \rangle \,, \tag{9.9}$$
$$T_U \propto \Re \left\{ \langle E_a E_b^* \rangle \right\} . \tag{9.10}$$

Also, the ambient and N_2-load radiation is assumed to be unpolarized, and the grid is assumed to be ideal. For the grid rotation angle α, the orientation is as follows:

$$T_U^{(\alpha=0°,90°)} = 0, \tag{9.11}$$
$$T_U^{(\alpha=45°)} = T_H - T_C, \tag{9.12}$$
$$T_U^{(\alpha=135°)} = T_C - T_H. \tag{9.13}$$

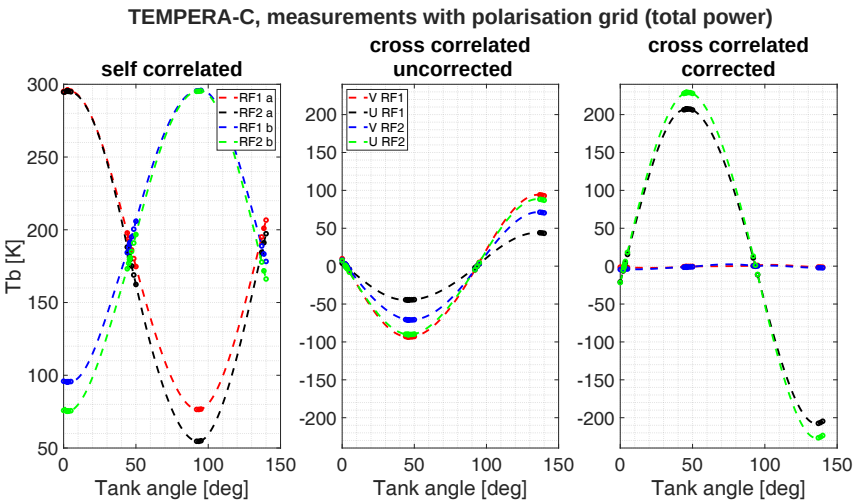

Figure 9.5: Calibrated brightness temperatures for different angles of the polarized grid for the linear polarized components (upper panel), and the U- and V-Stokes components (middle and lower panel).

The measurements taken with the rotating polarization grid are illustrated in **Fig. 9.5**. The gains g_x and cross-talk coefficients c_x are complex numbers but appear in the calibration equation **Eq. 9.5 - Eq. 9.7** only in combinations. Therefore, it is sufficient to define a complex phase δ_x as:

$$g_x^2 c_x = |g_x|^2 |c_x| e^{\delta_x i}. \tag{9.14}$$

Considering the a-polarization chain V_a, multiple measurements V_a^α with specifically chosen angles α, and a pure ambient load measurement V_a^H, were made to produce following system of equations:

$$\begin{aligned}
V_a^{\alpha=0} &= |g_a|^2 T_H + |g_a|^2 |c_b|^2 T_C + V_{Na}, && (9.15)\\
V_a^{\alpha=90} &= |g_a|^2 T_C + |g_a|^2 |c_b|^2 T_H + V_{Na}, && (9.16)\\
V_a^{\alpha=45} &= \frac{1}{2}|g_a|^2 \left(1 + |c_b|^2\right)(T_H + T_C) + 2|g_a|^2 |c_b| (T_H - T_C)\cos(\delta_a) + V_{Na}, && (9.17)\\
V_a^{\alpha=135} &= \frac{1}{2}|g_a|^2 \left(1 + |c_b|^2\right)(T_H + T_C) + 2|g_a|^2 |c_b| (T_C - T_H)\cos(\delta_a) + V_{Na}, && (9.18)\\
V_a^{H} &= |g_a|^2 \left(1 + |c_b|^2\right) T_H + V_{Na}. && (9.19)
\end{aligned}$$

Which can be transformed into:

$$\begin{aligned}
V_a^{\alpha=45} - \frac{1}{2}\left(V_a^{\alpha=0} + V_a^{\alpha=90}\right) &= 2|g_a|^2 |c_b| (T_H - T_C)\cos(\delta_a), && (9.20)\\
V_a^{\alpha=135} - \frac{1}{2}\left(V_a^{\alpha=0} + V_a^{\alpha=90}\right) &= 2|g_a|^2 |c_b| (T_C - T_H)\cos(\delta_a), && (9.21)\\
V_a^{\alpha=0} - V_a^{H} &= |g_a|^2 |c_b|^2 (T_C - T_H), && (9.22)\\
V_a^{\alpha=90} - V_a^{H} &= |g_a|^2 (T_C - T_H). && (9.23)
\end{aligned}$$

With the known ambient load temperature T_H and the N_2 load temperatures equations **Eq. 9.20** to **Eq. 9.23** can be solved for $|g_a|, |g_b|, |c_a|, |c_b|, \delta_a, \delta_b$. This parameters are assumed to stay constant and are used for further calibration.

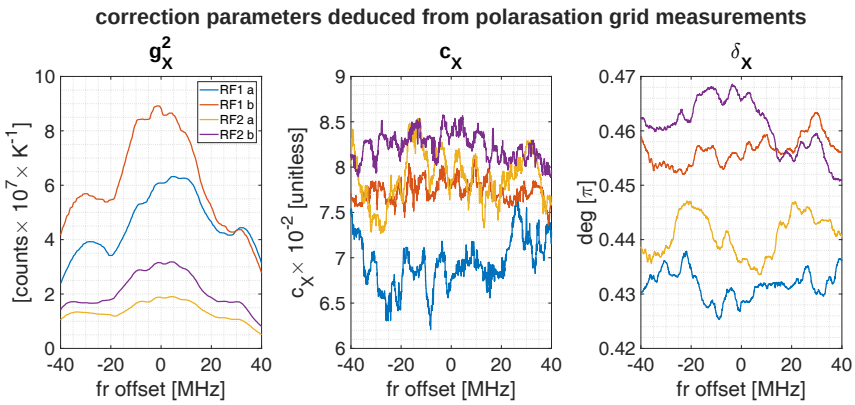

Figure 9.6: Parameters of **Eq. 9.20** - **Eq. 9.23** calculated with the measurements of the rotating polarized grid. polarization 1 corresponds to receiver chain a and polarization 2 corresponds to receiver chain b.

9.5. Correction of linear polarized parameters

For the correction of the linear polarized sky measurement $TB_{(a,b)}$ we consider again **Eq. 9.5**:

$$V_a = |g_a|^2 TB_a + |g_a|^2|c_b|^2 TB_b + 2|g_a|^2|c_b|\Re\left\{\langle E_a E_b^*\rangle\, e^{\delta_a i}\right\} + V_{Na}. \tag{9.24}$$

Since $|c_b|^2 << 1$, the second term on the right-hand side is neglected for simplicity, leading to:

$$\frac{V_a - V_{Na}}{|g_a|^2} - 2|c_b|\Re\left\{\langle E_a E_b^*\rangle\, e^{\delta_a i}\right\} = TB_a. \tag{9.25}$$

The first term on the left-hand side is the uncorrected brightness temperature, and the second term is the correction term. The correlation $\langle E_a E_b^*\rangle$ is given by:

$$\langle E_a E_b^*\rangle = T_U + iT_V. \tag{9.26}$$

Where T_U and T_V were corrected beforehand. The system gain g_a and noise V_{Na} is estimated using a two-point calibration with an internal noise diode:

$$V_a^{HND} = |g_a|^2\left(1 + |c_b|^2\right)(T_H + T_{ND}) + V_{Na}. \tag{9.27}$$

Furthermore, it is possible to neglect the factor considering that $|c_b|^2 << 1$:

$$\frac{V_a^{HND} - V_a^H}{T_{HND}} = |g_a|^2, \tag{9.28}$$

$$\frac{T_H(V_a^H - V_a^{HND})}{T_{HND}} + V_a^H = V_{Na}. \tag{9.29}$$

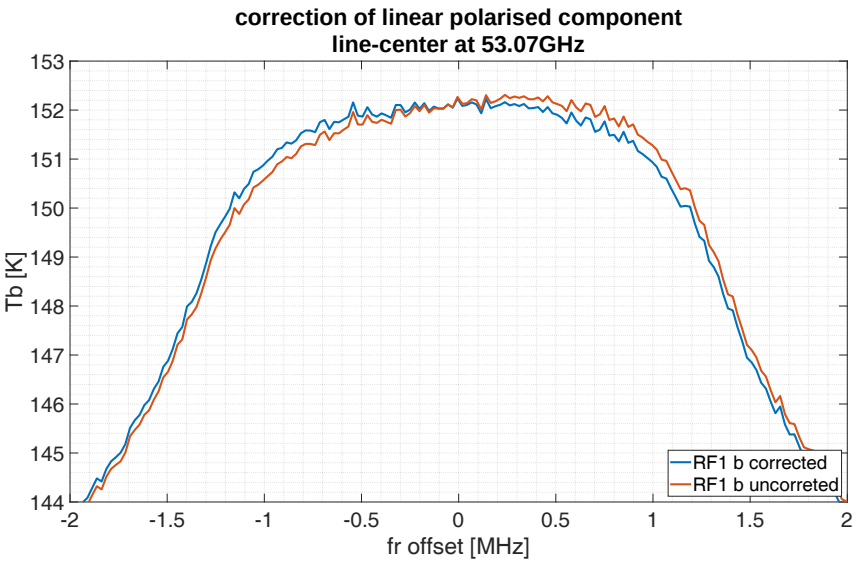

Figure 9.7: Illustration of the linear polarized component RF1 polarization 2 before and after correction according to **Eq. 9.25**.

9.6. Derivation of the correction parameters for Stokes components

Starting from **Eq. 9.7**:

$$V_X = \langle g_a g_b^* \left(1 + c_a^* c_b\right) E_a E_b^* \rangle + \langle g_a g_b^* c_a^* E_a E_a^* \rangle + \langle g_a g_b^* c_b E_b E_b^* \rangle + O_X. \tag{9.30}$$

The factor $c_a^* c_b << 1$ can be neglected for simplicity. As in equation **Eq. 9.14** a complex angle $\Delta\phi$ is introduced where $g_a g_b^* = |g_a||g_b| e^{i\Delta\phi}$. The first term on the right-hand side of **Eq. 9.30** can then be rewritten to:

$$\langle g_a g_b^* E_a E_b^* \rangle = |g_a||g_b| \left\langle e^{i\Delta\phi} E_a E_b^* \right\rangle. \tag{9.31}$$

The hot-load radiation is assumed to be unpolarized, and one has:

$$\left\langle E_a^{Hot} E_b^{Hot} \right\rangle = 0. \tag{9.32}$$

Therefore, the first step leads to:

$$V_X - V_X^H = |g_a||g_b| \left\langle e^{i\Delta\phi} E_a E_b^* \right\rangle + R_X, \tag{9.33}$$

where:

$$R_X = \left\langle g_a g_b^* \left(c_a^* \left[E_a E_a^* - E_a^H E_a^{H*} \right] + c_b \left[E_b E_b^* - E_b^H E_b^{H*} \right] \right) \right\rangle. \tag{9.34}$$

The calibration parameters to estimate are R_X and $\Delta\phi$. The complex angle $\Delta\phi$ was estimated by making use of the relation $T_V = 0$, for radiation passing an ideal polarization grid. The last therm R_x appears to be very small, and to this day, it remains debatable why this term is of such a small order. In the current version of the correction, R_x is simply fitted with the assumption that the V-Stokes is zero outside the line center and afterwards removed from the spectrum.

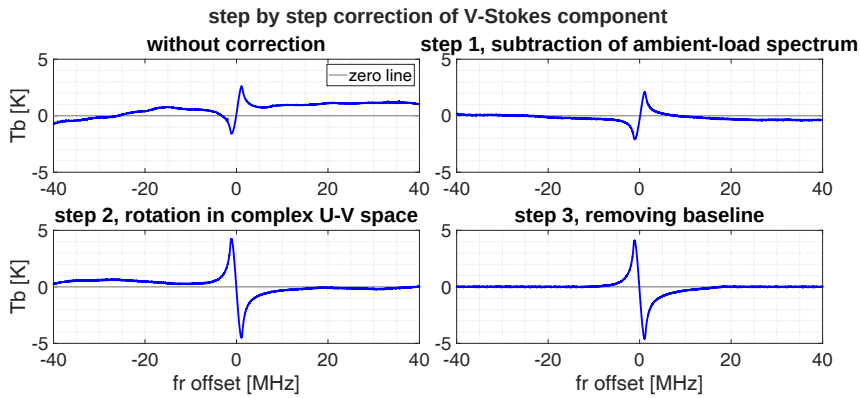

Figure 9.8: Step-by-step correction of the V-Stokes component. The second panel is after subtracting V_H (**Eq. 9.33**), and the third panel is after rotating by $\Delta\phi$. In the last step, R_X is removed by interpolation.

Note that, instead of using the polarized grid, the V-Stokes component can also be corrected using symmetry properties. The V-Stokes is anti-symmetric around the line center, while the U-Stokes is symmetric. The complex angle $\Delta\phi$ separates the two spectra from each other. At the optimum, the U-Stokes reach the highest symmetry, while the V-Stokes reach the highest anti-symmetry. The optimal $\Delta\phi$ can be found by separating the frequency band into two parts through the line-centre frequency ($b1 = [fc, f_c + \Delta f], b2 = [f_c, f_c - \Delta f]$) where $b1$ and $b2$ are of the same length n. Defining a norm N_V:

$$N_V(\Delta\phi) = \sqrt{\sum_n (V(\Delta\phi, b2) - V(\Delta\phi, b1)^2}. \tag{9.35}$$

The angle with the highest anti-symmetry is then at the maximum of N_V. With this method, the optimal angle was $\Delta\phi = 0.65 \pm 0.01\pi$ while the same coefficient estimated with the polarized grid was $\Delta\phi = 0.64 \pm 0.01\pi$.

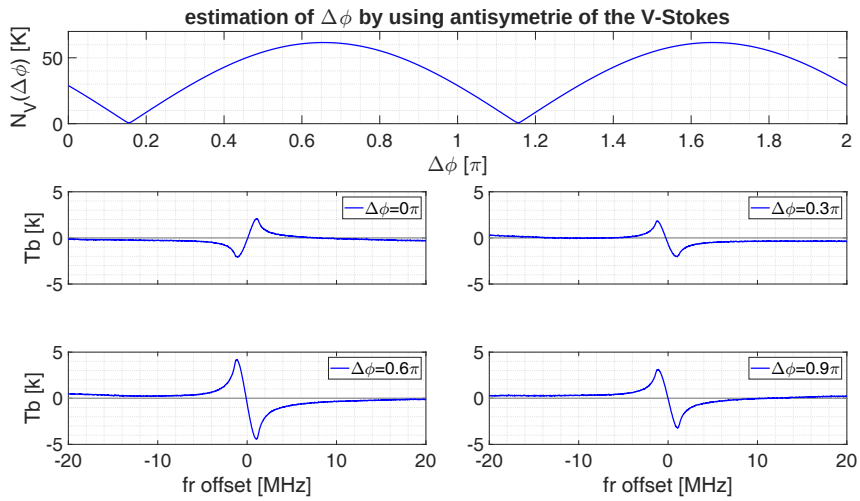

Figure 9.9: Upper panel: N_V as in **Eq. 9.35** as a function of $\Delta\phi$.
Middle and bottom panels: The U- and V- Stokes components mix differently depending on $\Delta\phi$.

A first version of the calibration process was published in Krochin et al., 2022b. However, the calibration process described was further improved, and the current version provides more robust results. The noise diode spectra used for operational calibration are shown in **Fig. A.6**.

An overview of the calibrated orthogonal polarized spectra, the U- and V-Stokes components, and the instrument noise temperature are shown in **Fig. 9.10**.

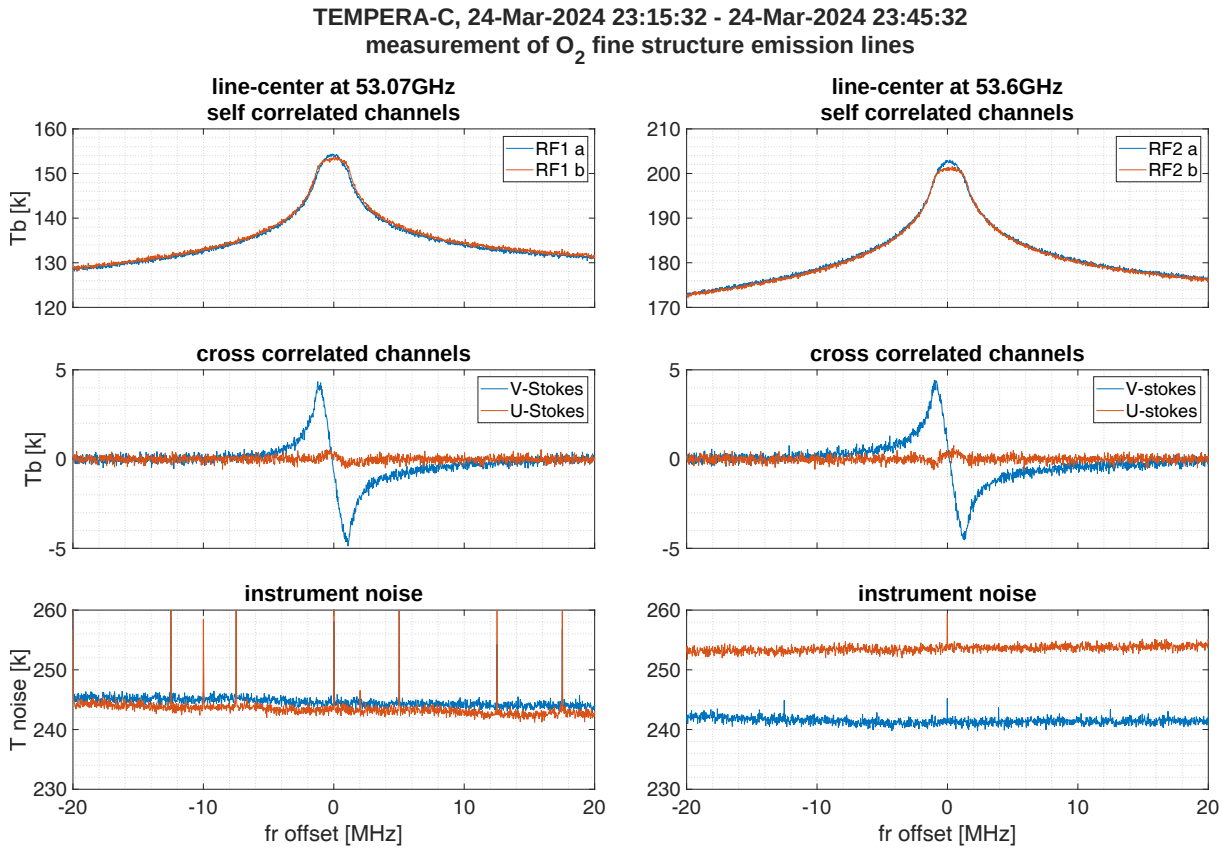

Figure 9.10: TEMPERA-C calibrated and corrected spectra and instrument noise temperatures measured on the JFJ high altitude research station.

9.7. Setup and testing

After years of development and optimization of the TEMPERA-C, a few minor issues remain. One of them is a constant offset of 0.5 K between the polarization chains. It's most likely that this is due to a slightly different behaviour between the two chains. The asymmetries of the linear polarized and V-Stokes spectra are most probably due to cross-talk between the receiver chains, which to varying amounts is produced by the asymmetries of the horn, cross-leakage of the OMT and probably cross-leakage through the LO. Several tests were performed to investigate the performance of the single components. The test setups and results are summarized in this section.

LO sweeping

To get a precise overview of the response of the receiver chains, the frontend was plugged into a spectrum analyzer. For the emission lines at ≈53.07 and 53.60 GHz, different combinations of the local oscillator frequency (LO) and the IF frequency are possible. The receiver channel performance can depend on the LO frequency. We decided to use LO=50 GHz because the spectra of the different channels match best for the combination LO = 50 GHz, IF = 3-4 GHz (see **Fig. A.1**). Note that the nominal frequency at the correlator is the sum RF = LO+IF

where the lower side-band LO-IF is filtered by a band-pass filter.

Band pass filter

Another possibility is that a significant percentage of the lower sideband gets mixed into the output signal. At the observed frequency range, the difference in intensity between the lower and upper sidebands is significant. The lower sideband should be attenuated by the bandpass filter. A method to test the bandpass filter is to induce a CW (continuous wave) signal at LO+IF (upper side-band) and LO-IF (lower side-band) and measure the ratio of the output $CWlower/CWupper$. The result (see **Fig. A.3**) shows a higher difference between the polarized chains at 53.07 GHz as at 53.60 GHz, which is consistent with the offset being higher at 53.07 GHz. However, at an attenuation between 50-60 dB, it remains disputable whether this is enough to explain the offset of 0.5 K.

Cross-talk

The origin of the cross-talk could be introduced by asymmetries of the horn antenna, cross-leakage of the OMT, or being coupled via the local oscillator. To test the leakage of chain a into chain b (and vice versa), the noise diodes were turned on and off separately. In an optimal receiver, the a-chain should be independent of the noise diode in chain b. Taking the ratio:

$$c_{a\rightarrow b} = \frac{V_b^{ND_a on} - V_b^{ND_a off}}{V_{ND_a}} \tag{9.36}$$

gives an upper limit estimation of the leakage (see **Fig. A.2**).

Allan variance

Due to the drifting of the instrument components, the system can be considered stable only for a short period. A calibration cycle (HOT-COLD-SKY) should be performed within this time. The maximal duration over which the instrument is stable can be determined by looking at the Allan variance, which reaches a minimum (see **Fig. A.5**) before the instrument starts to drift significantly. The Allan variance $\sigma_A(\tau)^2$ in our case, is the variance of the differences of $\Delta y(\tau)_i = y(\tau)_i - y(\tau)_{i+1}$ of single measurements $y(\tau)_i$ with an integration time τ:

$$\sigma_A(\tau)^2 = \sigma\left(\Delta y(\tau)\right)^2 = \frac{1}{N-1}\sum_{i=1}^{N-1}\left(\overline{\Delta y(\tau)} - \Delta y(\tau)_i\right)^2. \tag{9.37}$$

Here, N is the number of measurements involved. **Fig. A.5** shows the Allan-Variance (Allan-deviation) for the TEMPERA-C digital correlator outputs. For the test, the single scan time was set to 100ms, and the beam was pointed on the ambient load. The final result is the median over all 4096 channels and shows a minimum of about 20 sec for the self-correlated outputs. The current calibration cycle of TEMPERA-C is 9 seconds, which is within the time the instrument remains stable. Cross-correlated channels have no minimum in Allan-Variance since random noise is uncorrelated.

9.8. Current status

TEMPERA-C was installed on the Jungfraujoch high-altitude research station on 24.03.2024 for a test campaign. Since it performs operational observations. Because of the high altitude of 3454 m, the air humidity is very low, which significantly increases the quality of the data and retrieval results. The optimal fine structure lines were chosen as in **Section 8.2** to the lines at 53.07 GHz and 53.69 GHz (see **Fig. A.8**). The microwave window (see **Fig. 9.12**) restricts the maximal elevation angle to 60°. Heavy precipitation and cloud coverage affect the measurements similar to TEMPERA. Also, snow coverage and wetting of the microwave window can change the polarization properties (see **Fig. 9.11**). The noise diodes were calibrated with liquid N_2 after the installation. The calibration and retrieval routine is not yet operational, as some remaining uncertainties **Fig. 9.15** are still being investigated, and the inversion algorithm is still being optimized. The performance, however, is monitored daily and reveals, as in the case of TEMPERA, high dependence on cloud coverage and precipitation (see **Fig. 9.11**). Currently, weather-proofed housing is developed. In 2025 TEMPERA-C will be mounted on an outside platform of the JFJ high-altitude research station, which is suitable for azimuth scanning.

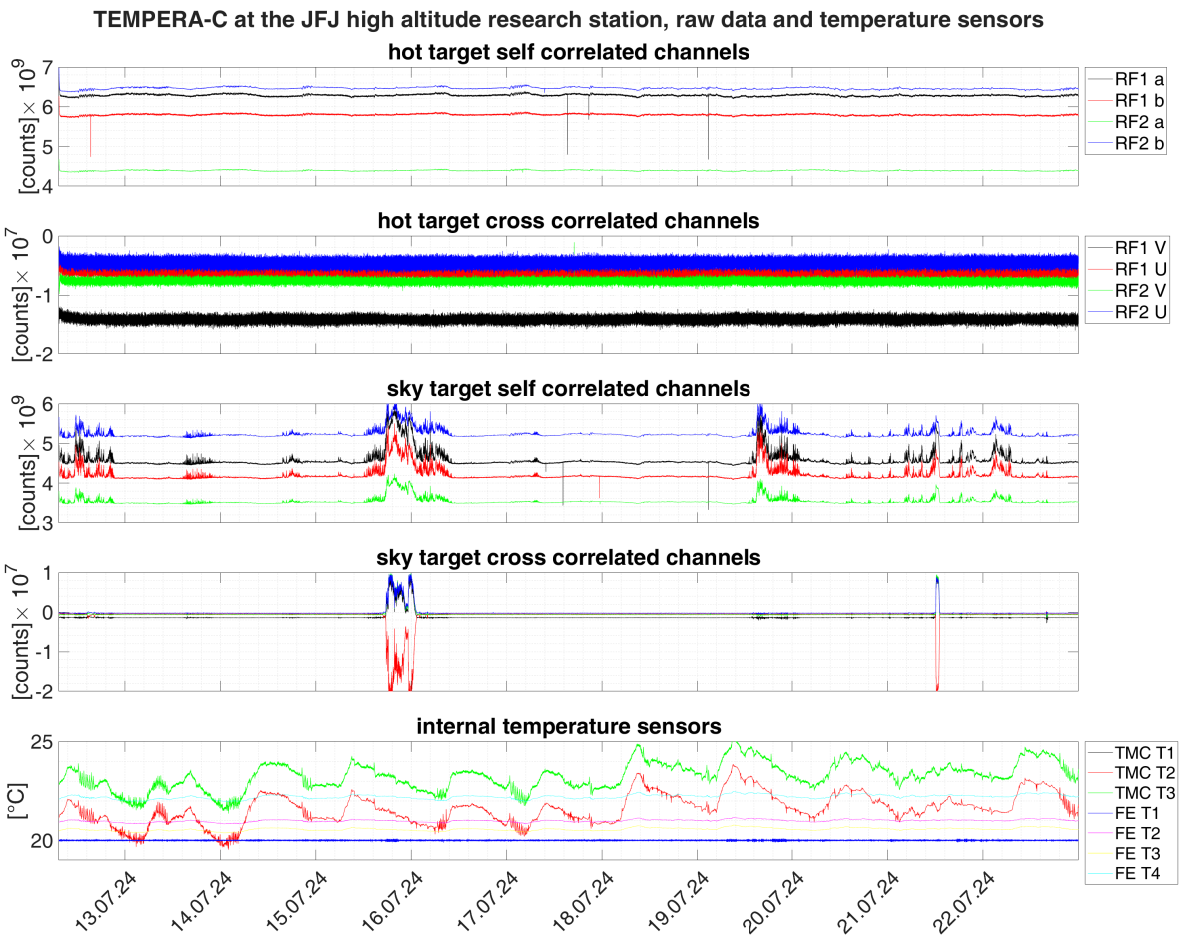

Figure 9.11: Total power of TEMPERA-C measurements and temperature sensor outputs (bottom panel) on the JFJ high altitude research station. A precipitation event is visible on the 15.07 due to an increase of brightness temperature and noise of the self- and cross-correlated channels.

Figure 9.12: TEMPERA-C at the Jungfraujoch high altitude research station.

9.9. Retrieval with Stokes parameters

Unlike the retrievals of TEMPERA, the retrievals of TEMPERA-C are performed with ARTS v.2.6, which is not supported by Qpack. Instead, pyarts, a Python interface for ARTS, is used. The advantage of version 2.6 for our purposes is the implementation of line mixing and modifications, which fixed some bugs in the Zeeman calculations compared to version 2.2.

The setup for the forward model atmosphere for the retrievals was analogous to the setup made for TEMPERA (see **Section 8.3**) except that the sensor is placed at 3571 m a.s.l. No tropospheric correction is required, and the forward model is initialized at the surface. Compared to previous versions of retrievals, the newly implemented line mixing effect improves tropospheric retrievals significantly. A further difference is that two lines of right and left circular polarization are simulated instead of only one linear total intensity spectra at each frequency. First sensitivity studies are shown in **Fig. 9.13** and **Fig. 9.14**. A comparison of the forward model simulation to the observed spectra shows a remaining offset. A sensitivity study reveals which parameters are to pay attention to. The parameters tested were surface temperature, elevation angle, and water vapour vmr. Surface temperature values have to be increased up to an unrealistically high value to match the observations. Increasing the water vapour density, increases the overall brightness temperature but the line shape does not match the observations. Decreasing the elevation from 60°(30 °Zenith) to 53°(37°Zenith) matches best with the observations. Therefore, the elevation angle of the current TEMPERA-C setup needs to be calibrated. A remaining offset could be contributed by the line mixing algorithm.

Figure **Fig. 9.14** shows the effect of the magnetic field strength and direction on the V-Stokes component. The highest V-Stokes amplitude is reached, pointing the antenna beam towards the south. The lowest is in the opposite direction. The magnetic field strength determines the distance between the V-Stokes maximum and minimum. A similar result is shown in figure **Fig. 10.1** and **Fig. 10.2**. Interestingly enough, an increased water vapour mixing ratio seems to decrease the amplitude of the V-Stokes component, most probably through absorption.

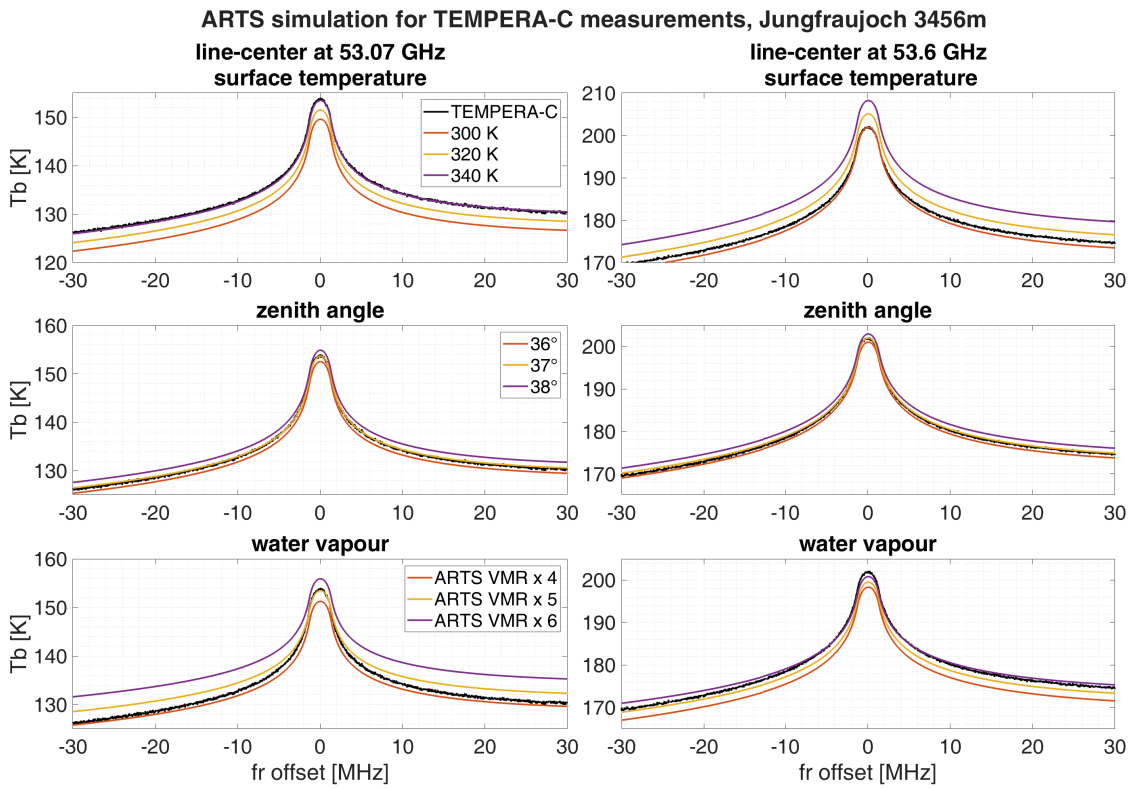

Figure 9.13: Forward simulations of the oxygen fine structure spectra in linear polarization as measured by TEMPERA-C with varying forward model parameters.

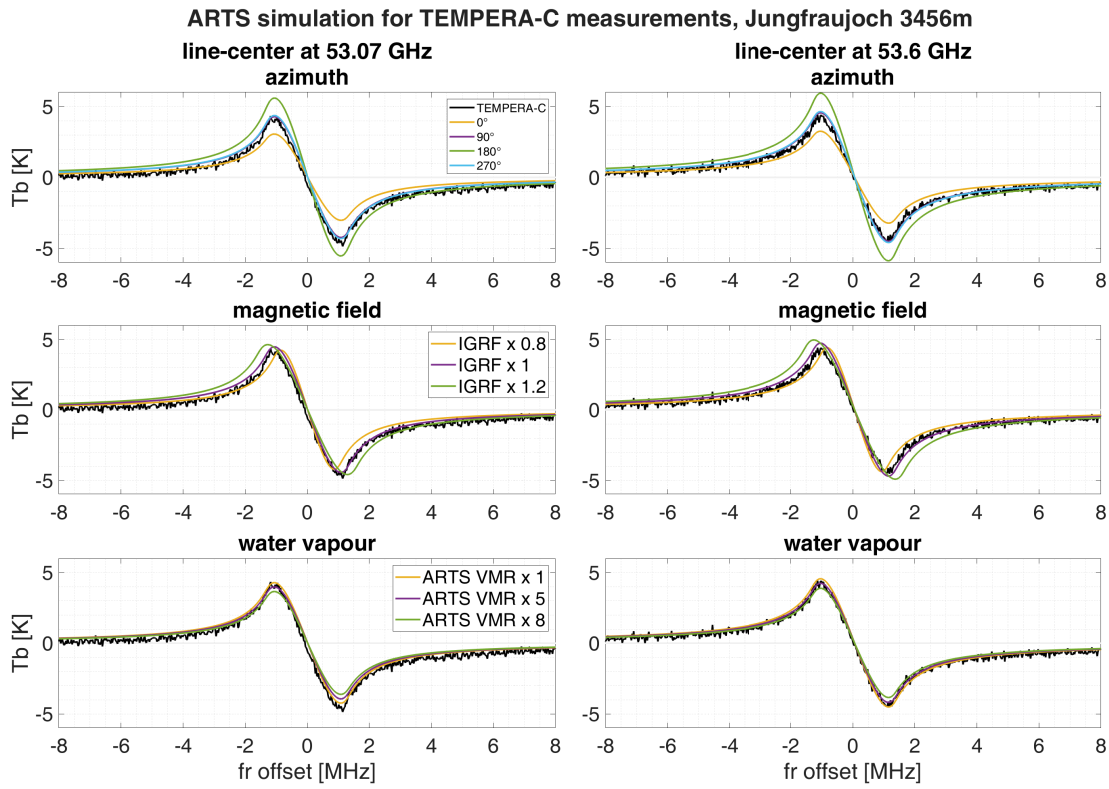

Figure 9.14: Forward simulations of the V-Stokes components of the oxygen fine structure spectra as measured by TEMPERA-C with varying forward model parameters.

9.10. First results

For the first tests, the temperature apriori error was set as constant to 10 K. The measurement error was set to 2 K with exponentially increasing values at the wings. Only 20 MHz around the line centers of the spectra were kept in full resolution, while the line wings were binned with a factor of 10. The results (see Figure **Fig. 9.15**) show remaining residua in the RCP components, which seem to be systematic. The reason for the residua of this form is most probably a combination of uncertainties in the polarimetric correction and fine-tuning of the apriori pressure and temperature grid. A remaining offset in the angle of the line of sight and the magnetic field could also be possible. At around 40 km, a bump in the temperature profile is present. This is most likely a numeric oscillation due to the choice of the apriori and measurement error. Decreasing the apriori error or increasing the measurement error reduces this oscillation but decreases the effective altitude range. The remaining residua and the oscillation in the profile are most likely related. The measurement response exceeds 0.6 in an altitude range between 15-60 km. From the first TEMPERA-C series, thermal tides can be observed. The example presented in Figure 9.16 shows thermal tide amplitudes reaching amplitudes up to 4 K.

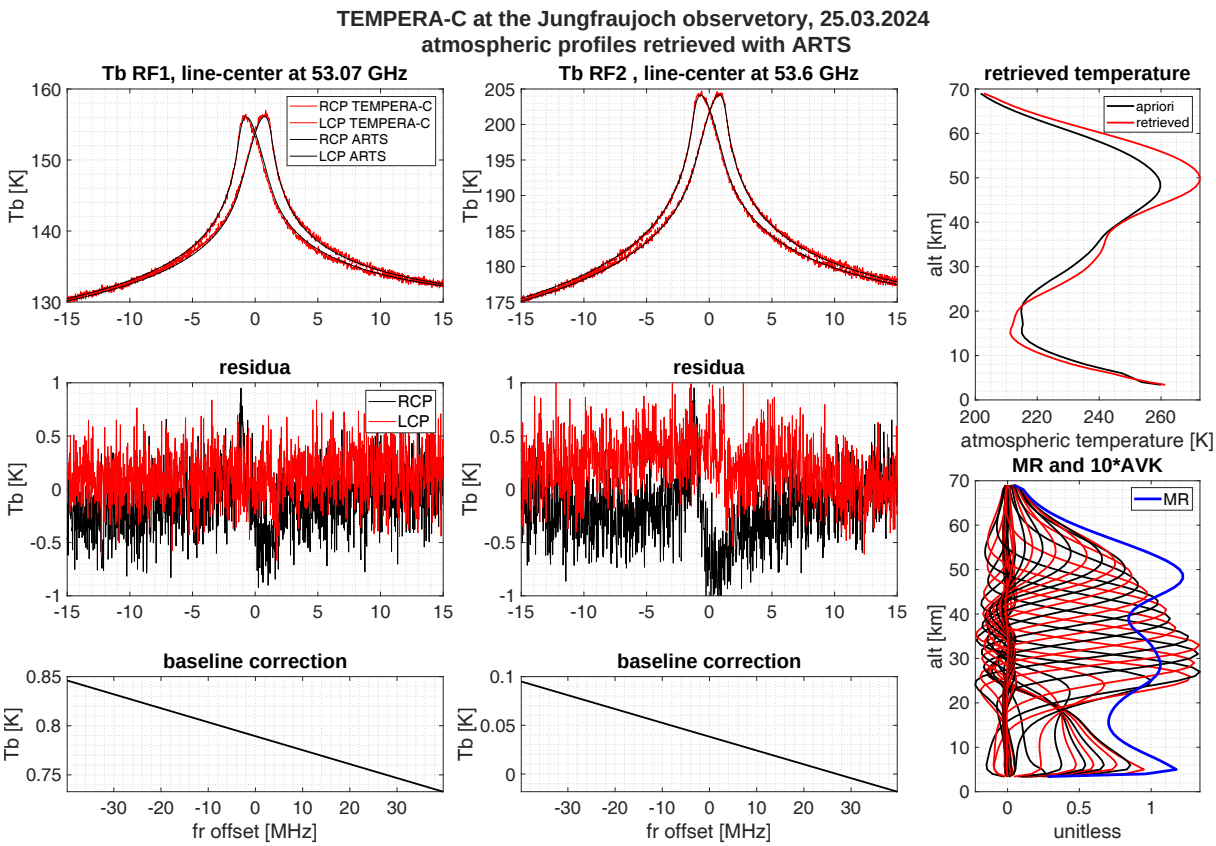

Figure 9.15: First retrieval results of LCP-RCP spectra from TEMPERA-C measurements of the JFJ high altitude research station.

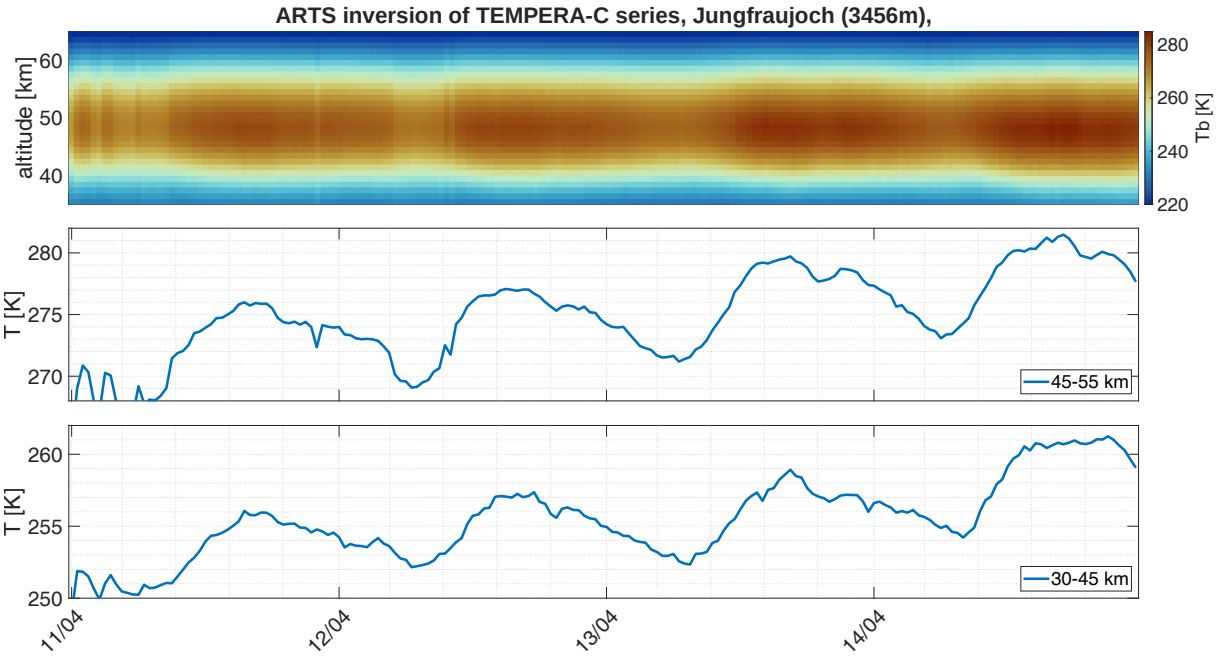

Figure 9.16: Time series of atmospheric temperature profiles, retrieved from TEMPERA-C measurements. Diurnal thermal tides are present in the stratosphere and mesosphere.

10. Conclusions and outlook

10.1. Conclusive remarks

It was shown that the altitude range for ground-based temperature retrievals can be improved by taking the Zeeman effect and line-mixing into account. Using fully polarimetric observations, the altitude range can be further extended. Due to a high temporal resolution and continuity of stratospheric temperature profile series, ground-based radiometry provides a unique dataset to investigate atmospheric waves as thermal tides and planetary waves, which can be separated by spectral decomposition.

It was shown that fully polarimetric observations of atmospheric oxygen emission lines can be calibrated with a simplified setup using symmetry properties. All 4 Stokes components can be simulated in the forward model and, up to deviations of a few Kelvin, show the correct line shape.

However, the forward model and the inversion algorithm can be further optimized. By placing the instrument at a high altitude, the retrieval quality can be improved due to reduced humidity, while cloud coverage and precipitation remain a challenging issue for ground-based microwave observations.

10.2. Suggestions for future work

Influence of water vapour

The humidity of air together with liquid water content, has a significant influence on the observed spectra in the oxygen band, most likely due to thermal emission. Handling humidity and liquid water is crucial to improve the temperature profile at this stage. Unfortunately, it was not feasible yet to investigate this effect in detail. Earlier studies Bernet et al., 2017 showed that including a cloud box in ARTS could improve the retrieval quality by a few Kelvin. However, the issue on hand is not caused by scattering, for which the cloud-box method was designed. Also, cloud properties can not be tuned using this method. The next attempt will include a liquid-water profile in the forward model atmosphere. The liquid water profile is tunable and should account for the observed thermal emission.

Magnetic field retrievals

As mentioned in **Section 6.3**, the Stokes Vector depends on the magnetic field strength and the angle between the line of sight and the magnetic field lines. A future project for TEMPERA-C is to perform 360°scans. From the multi-angle observations, it theoretically should be possible to retrieve magnetic field features. The challenge, however, is that the changes in the Earth's magnetic field are very weak, and so will the signal in the microwave range. **Fig. 10.1** shows the influence of the magnetic field strength on the RCP/LCP components. The magnetic field was multiplied with factors 1-2 to generate this plot. In 2025, the TEMPERA-C instrument will be placed on the outdoor measurement platform of the JFJ high-altitude research station, allowing for scanning at multiple azimuth angles. Measuring at multiple angles, the retrieval of magnetic field features should become possible.

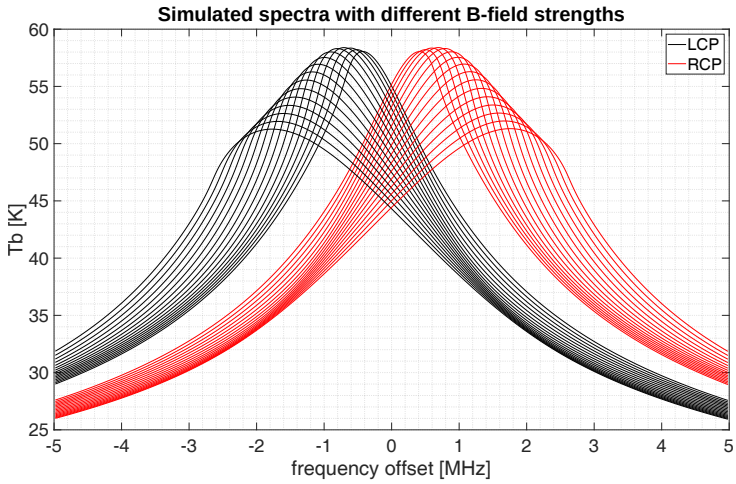

Figure 10.1: LCP and RCP spectra simulated for different B-field strengths. Increasing B-Field strengths increase the separation of the line centers linearly Krochin et al., 2022b. The magnetic field strength variation is plotted against the line-center offset in **Fig. 10.2**

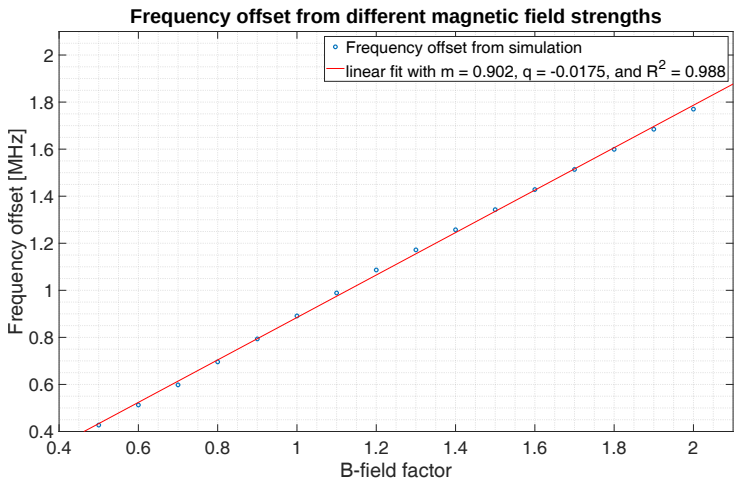

Figure 10.2: Offset of the line center from **Fig. 10.1** are plotted against the overall factor the magnetic field was multiplied with Krochin et al., 2022b.

Spectral decomposition of atmospheric waves

The detection of atmospheric waves is a suitable task for ground-based observations (see **Fig. 3.3**)), mostly because of the continuity of the datasets and the high time resolution. For the detection and classification of the different wave types, suitable spectral decomposition methods should be studied in more detail.

Relation to ozone

The correlation of stratospheric ozone and temperature (see **Fig. 10.3**) was already the topic of several studies (Sauvageat et al., 2023). Due to a change of the chemical balance, the correlation of ozone and temperature changes from positive to negative at altitudes between 30-40 km. Since ozone and temperature radiometers operate simultaneously and with a very short distance in

between, a further study of the short-time variation of the diurnal ozone cycle will open new research aspects for tidal short-term variability.

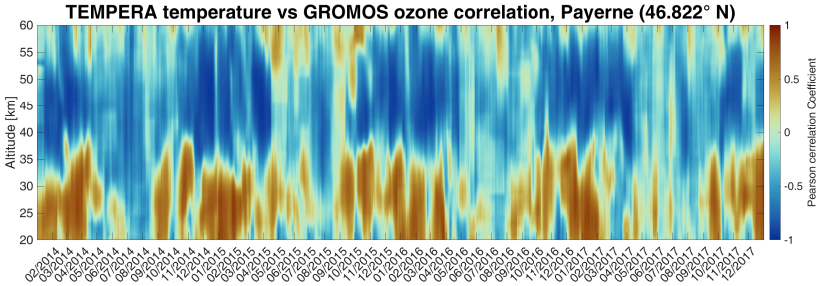

Figure 10.3: TEMPERA and GROMOS °redcitation correlation performed with a 30 day moving-window. The illustration is from Krochin et al., 2024

Apendix A: TEMPERA-C test results

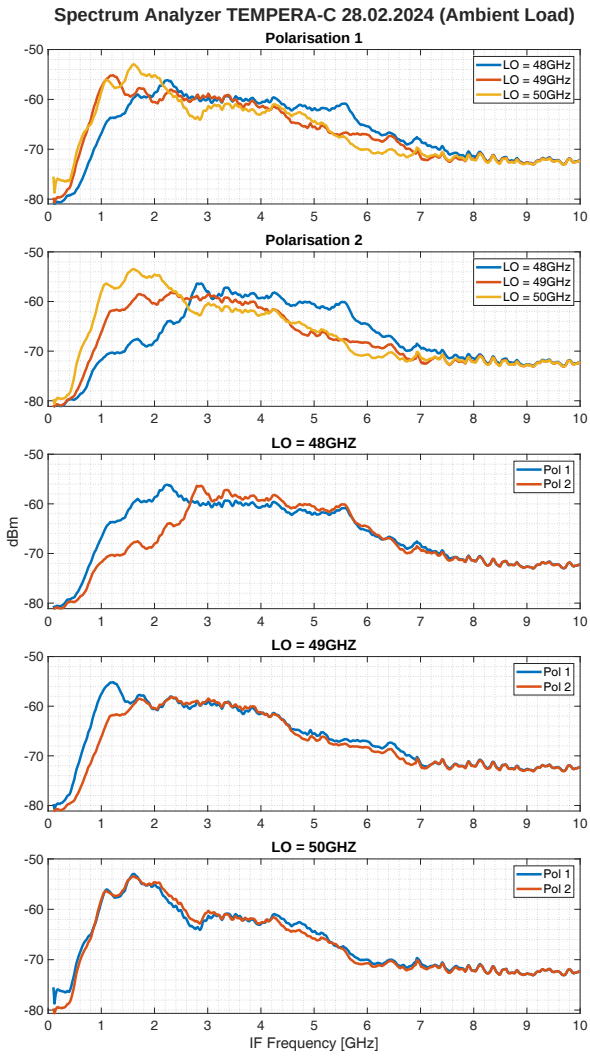

Figure A.1: Test of the receiver chains with different LO settings. The testing procedure is described in detail in **Section 9.7**.

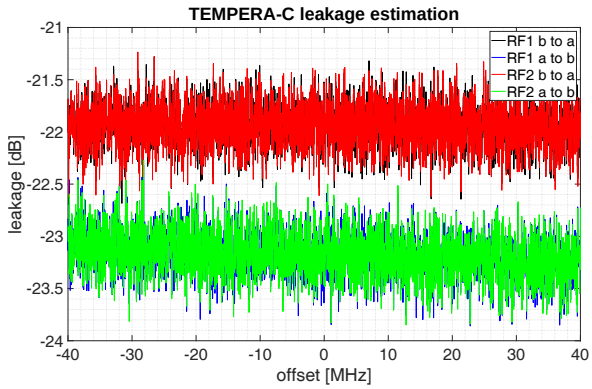

Figure A.2: Leakage coefficients according to **Eq. 9.36**.

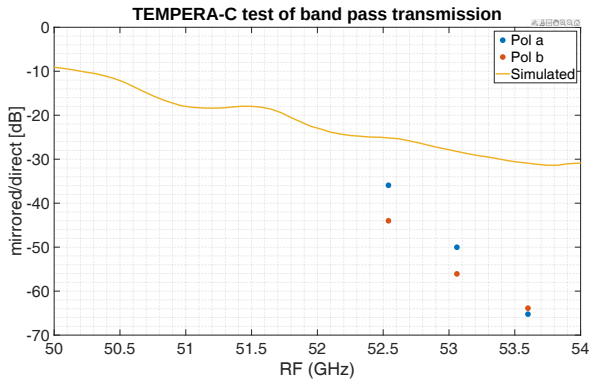

Figure A.3: Test of the bandpass filter transmission. The testing procedure is described in detail in **Section 9.7**.

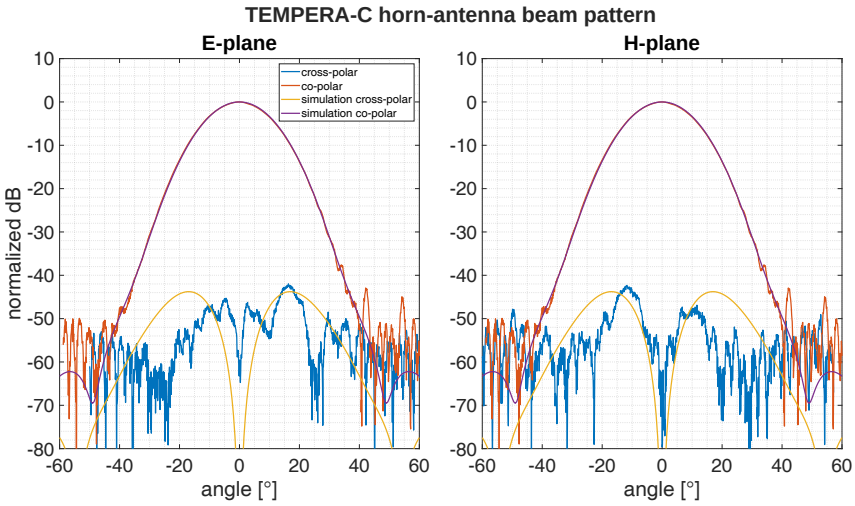

Figure A.4: The beam pattern of the TEMPERA-C horn antenna measured in the laboratory of the microwave group at the University of Bern. The main co-polar beam matches the simulations. Side lobes and cross-polar components are below -40 dB.

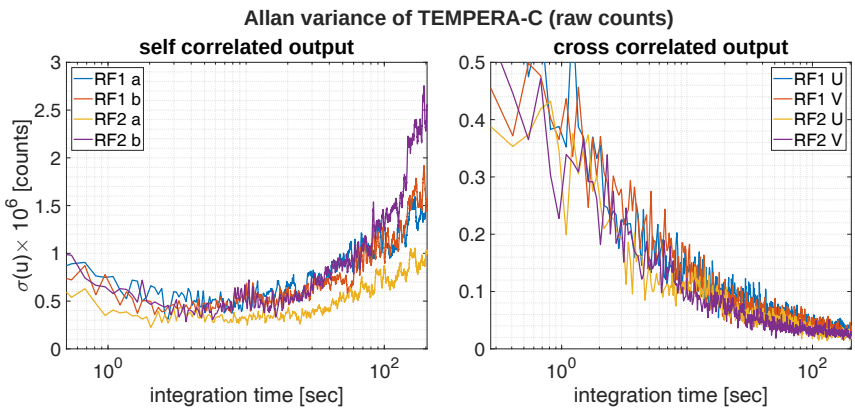

Figure A.5: Allan-Variance test for TEMPERA-C. The minimum for the self-correlated outputs is around 20 sec. Since random noise is uncorrelated, the cross-correlated outputs do not rise in Allan-Variance.

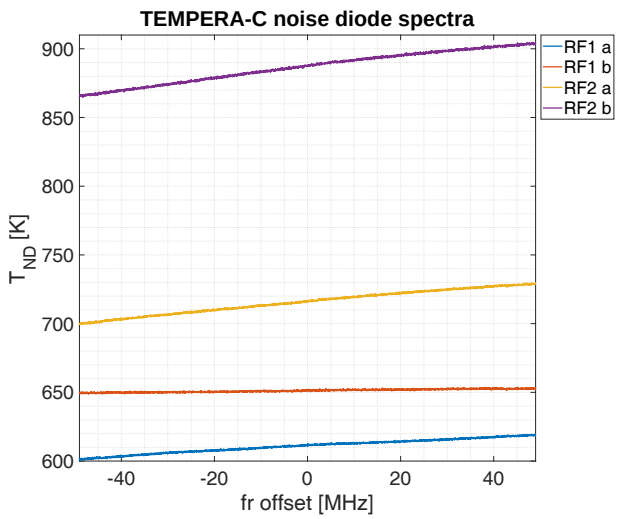

Figure A.6: Noise diode spectra after two-point calibration with an ambient load and liquid nitrogen as used for the operational calibration on the JFJ high altitude research station.

Apendix B: Simulated elevation scan with JFJ conditions

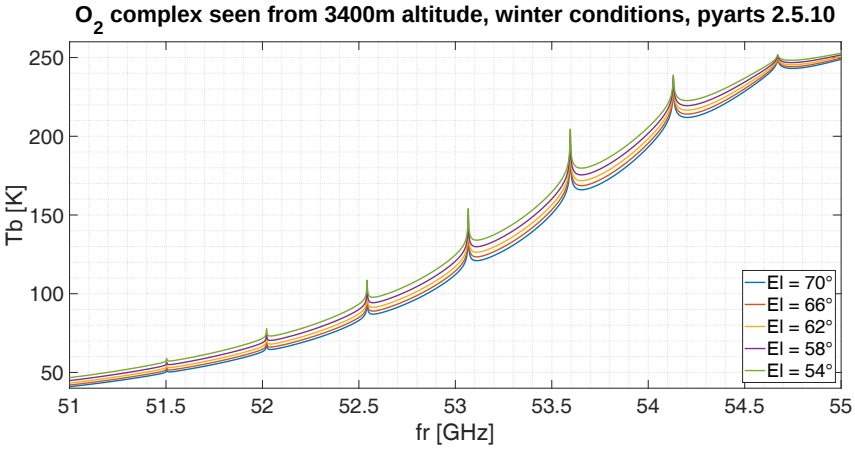

Figure A.7: Simulation of the oxygen emission complex as in Figure 8.2 but with the conditions of the Jungfraujoch high altitude research station.

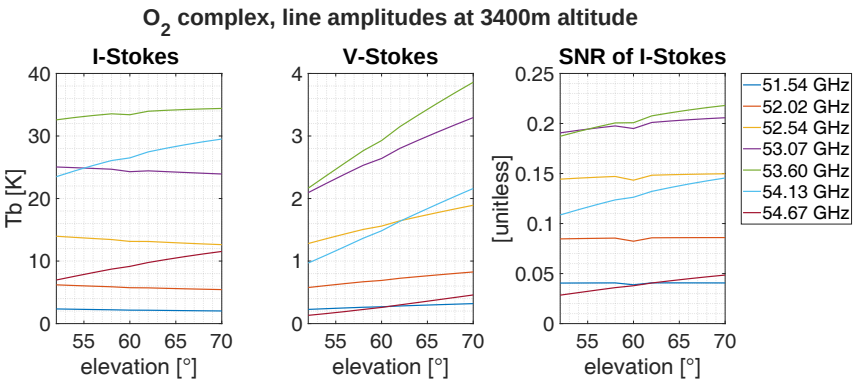

Figure A.8: Amplitudes of the fine structure lines of the oxygen emission complex as in Figure 8.3 but with the conditions of the Jungfraujoch high altitude research station and an additional panel for the V-Stokes component.

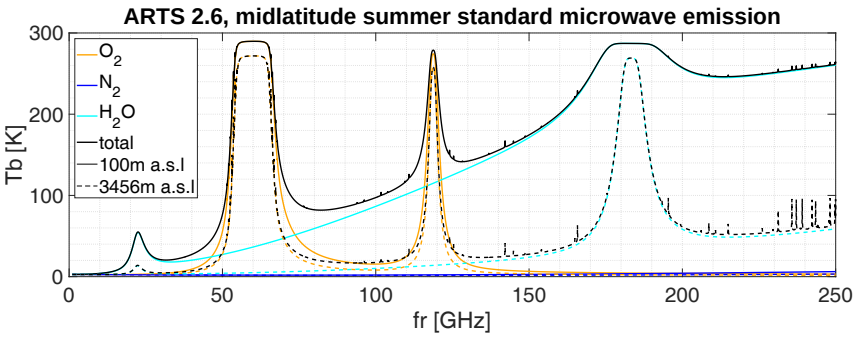

Figure A.9: Comparison of atmospheric microwave emission between the spectra observed at ground level and the altitude of the JFJ high altitude research station.

Apendix C: Publications

Publication I

https://doi.org/10.5194/amt-2024-42
Preprint. Discussion started: 28 March 2024

Atmospheric Measurement Techniques Discussions

Thermal tides in the middle atmosphere at mid-latitudes measured with a ground-based microwave Radiometer

Witali Krochin[1,2], Axel Murk[1,2], and Gunter Stober[1,2]

[1]Institue of Applied Physics, University of Bern
[2] Oeschger Center for Climate Change Research, University of Bern

Correspondence: Witali Krochin (witali.krochin@unibe.ch)

Abstract. In recent decades, theoretical studies and numerical models of thermal tides have gained attention. It has been recognized that tides have a significant influence on the dynamics of the middle and upper atmosphere, as they grow in amplitude and propagate upwards, they transport energy and momentum from the lower to the upper atmosphere, contributing to the vertical coupling between atmospheric layers. The superposition of tides with other atmospheric waves leads to non-linear wave-wave interactions. However, direct measurements of thermal tides in the middle atmosphere are challenging and often are limited to satellite measurements at the tropics and low latitudes. Due to the orbit geometry such observations provide only a reduced insight into the short-term variability of atmospheric tides. In this manuscript, we present tidal analysis from 5 years of continuous observations of middle atmospheric temperatures. The measurements were performed with the ground-based temperature radiometer TEMPERA, which was developed at the University of Bern in 2013 and was located partially in Bern (46.95°N, 7.45°E) and Payerne (46.82°N, 6.94°E). TEMPERA achieves a temporal resolution of 1-3h and covered the altitude range between 25-55 km. Using an adaptive spectral filter with a vertical regularization (ASF2D) for the tidal analysis, we found maximum amplitudes for the diurnal tide of approximately 2.4 K accompanied by seasonal variability. The maximum amplitude was reached on average at an altitude of 43 km, which also reflected some seasonal characteristics. We demonstrate that TEMPERA is suitable to provide continuous temperature soundings at the stratosphere and lower mesosphere with a sufficient cadence to infer tidal amplitudes and phases for the dominating tidal modes. Furthermore, our measurements exhibit a dominating diurnal tide and smaller amplitudes for the semidiurnal and terdiurnal tides at the stratosphere.

1 Introduction

Atmospheric tides are global-scale internal gravity waves forced by solar radiation with periods of an integer fraction of a day (Lindzen and Chapman, 1969; Chapman and Lindzen, 1970; Lindzen, 1979). Thus, tides are classified by the number of oscillations per day as diurnal, semidiurnal, and terdiurnal, respectively. Furthermore, tides can be characterized by their propagation direction and wavenumber. Atmospheric tides that are sun-synchronous are referred to as migrating tides and all other tidal modes are called non-migrating tides. Atmospheric tides are generated by the absorption of solar radiation by water vapor in the troposphere and ozone in the stratosphere (e.g., Sakazaki et al., 2015) and propagate upwards up to the mesosphere/thermosphere. Due to the decreasing density with increasing height, their amplitude grows and they become the

https://doi.org/10.5194/amt-2024-42
Preprint. Discussion started: 28 March 2024

dominating source of variability at the Mesosphere/lower thermosphere (MLT). Atmospheric tides transport energy and momentum in the upper atmospheric layers and enforce layer mixing (Becker, 2017).

During the past decades, there have been many studies on tidal dynamics based on atmospheric modeling (Forbes, 1982; Chang et al., 2008; Hagan et al., 1995, 1999; McCormack et al., 2017; Becker, 2017). Atmospheric tides can be described by normal-mode oscillations in pressure, density, wind, and temperature through Hough-modes (Ortland, 2013). In Sakazaki et al. (2013) seasonal variations of the migrating diurnal thermal tides are discussed, using Hough-mode decomposition of a global reanalysis data set (MERRA). It was found that the latitudinal-vertical structure is well represented by the four lowest-order Hough modes.

Tidal variations inferred from satellite observations (Zeng et al., 2008; Oberheide et al., 2011b, a; Zhang et al., 2010; Sakazaki et al., 2012; Dhadly et al., 2018), provide global observations but are often not suitable to investigate the short-time variability due to their orbit geometry. SABER onboard the TIMED spacecraft drifts in local time and, hence, samples every 60 days all local times at each location. Furthermore, SABER has a yaw cycle, which changes the viewing geometry every 60 days and, thus, observes the mid- and polar latitudes on both hemispheres interleaved. Satellites on sun-synchronous orbits, such as MLS onboard AURA (Livesey et al., 2006; Waters et al., 2006), suffer from even more aliasing effects due to fixed local time sampling (Hocke, 2023). Ideally, a temporal resolution of one hour per day is needed to infer the short-time variability of diurnal or semidiurnal tides. Very often such a high sampling rate is only achieved by ground-based (Baumgarten and Stober, 2019; Krochin et al., 2022a) instruments.

Continuous and high-resolution temperature measurements at the stratosphere and lower mesosphere are sparse. Lidar soundings are often depending on the tropospheric cloud coverage and the daylight capability of the systems. Thus, there are only very limited continuous lidar observations covering several successive days (Baumgarten and Stober, 2019). Furthermore, most studies of thermal tides focused on the tropical and lower latitude region and the upper mesosphere and thermosphere, where tidal amplitudes are much stronger and become the dominating atmospheric wave (She et al., 2016a; Yuan et al., 2008; She et al., 2016b; Yuan et al., 2021). Only a few observations in the middle atmosphere (stratosphere and mesosphere) are documented in the literature (Gille et al., 1991; Kopp et al., 2015; Fong et al., 2022). However, most meteorological reanalysis update the data assimilation every 6 hours, although the model output is provided at a higher cadence (Gelaro et al., 2017). Due to the sparsity of observations at the stratosphere, some observations are only available every 12 hours (e.g., radiosondes), and, thus, measurements that capture the short-term tidal variability at these altitudes are crucial to constrain the tidal amplitudes and phases and also to infer heating rates due to the absorption of solar radiation by ozone and water vapor.

In this manuscript, we present diurnal, semidiurnal, and terdiurnal thermal tide amplitudes at altitudes between 20-55 km, derived from continuous long-term observations of atmospheric microwave spectra by a ground-based microwave radiometer (TEMPERA, Stähli et al. (2013)) located at the Meteo Swiss technical center in Payerne (46°48.0′ N, 6°56.0′ E;) and discuss the seasonal and latitudinal climatology. In sections 2,3 and 4 the instrument, the retrieval method for temperature profiles, and the resulting temperature time series are described in more detail. In sections 5 and 6 the tidal analysis method and the resulting tidal amplitudes are presented and in section 7 the results are discussed.

https://doi.org/10.5194/amt-2024-42
Preprint. Discussion started: 28 March 2024

2 Instrument description

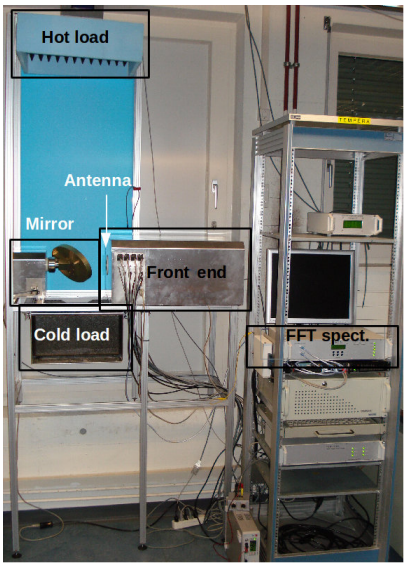

Figure 1. TEMPERA at the Institute of Applied Physics at the University of Bern. Navas-Guzmán et al. (2015)

The TEMperature RAdiometer (TEMPERA) was built at the University of Bern in 2013 (Stähli et al., 2013). TEMPERA measures microwave emission from atmospheric oxygen at the 60 GHz oxygen emission complex (see Figure 2). With a spectral resolution of 30 kHz and a bandwidth of 2× 480 MHz, the fine structure of rotational transitions, used to retrieve temperature in the middle atmosphere, can be resolved (see Figure 3). The original operational mode uses 12 additional filter banks and scans at different zenith angles to retrieve tropospheric temperatures. In this operational mode, the temporal resolution for stratospheric spectra is 3 hours. TEMPERA operated continuously in this measurement mode during the years 2013-2018 at the Meteo Swiss Technical Center in Payerne. Stratospheric spectra are calibrated with a two-point calibration, where an internal noise diode and an ambient load are used. The noise diode is calibrated once a month with liquid nitrogen (LN2) (see Figure 1. The fine structure spectra are inverted using ARTS (Atmospheric Radiative Transfer Simulator, Eriksson et al. (2005)). A more detailed technical description is found in Stähli et al. (2013); Krochin et al. (2022a).

https://doi.org/10.5194/amt-2024-42
Preprint. Discussion started: 28 March 2024

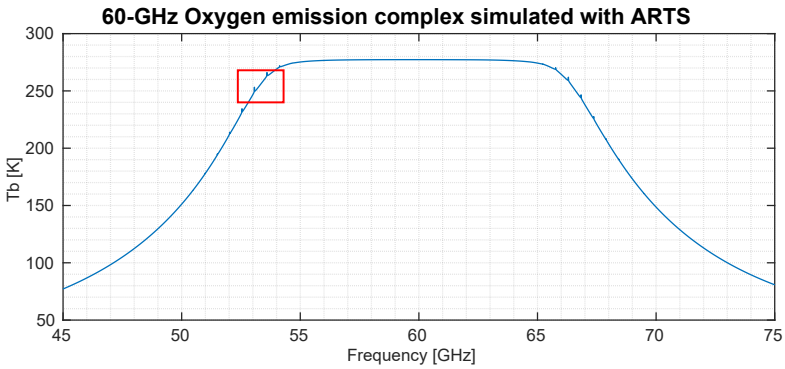

Figure 2. The Oxygen emission complex, simulated with ARTS for the location of Bern during Winter at a zenith angle of 30°. The measurement range of TEMPERA is illustrated with a red rectangle.

In 2022 an updated retrieval algorithm was published (Krochin et al., 2022a), which accounted for the Zeeman-splitting in the line center due to the coupling of atmospheric oxygen to the Earth's magnetic field. The update improved the altitude resolution and increased the upper altitude retrieval limit defined by the measurement response. The basis for this improved retrieval was provided in the ARTS software, which included a module for the Zeeman-Splitting. In the same year, TEMPERA was relocated to the Institute of Applied Physics at the University of Bern. This change was accompanied by a new measurement mode dedicated to stratospheric and lower mesospheric soundings. The new mode relies on noise diode calibration and avoids spending measurement time to perform a tipping curve for tropospheric retrievals, maximizing the measurement time of stratospheric spectra resulting in a temporal resolution of about 1 hour. In addition, several minor updates of the retrieval algorithm were performed, including an improved tropospheric correction, apriori error matrix, baseline correction, retrieval for frequency shift and frequency stretch, and filtering of contaminated spectra (see section 3).

https://doi.org/10.5194/amt-2024-42
Preprint. Discussion started: 28 March 2024

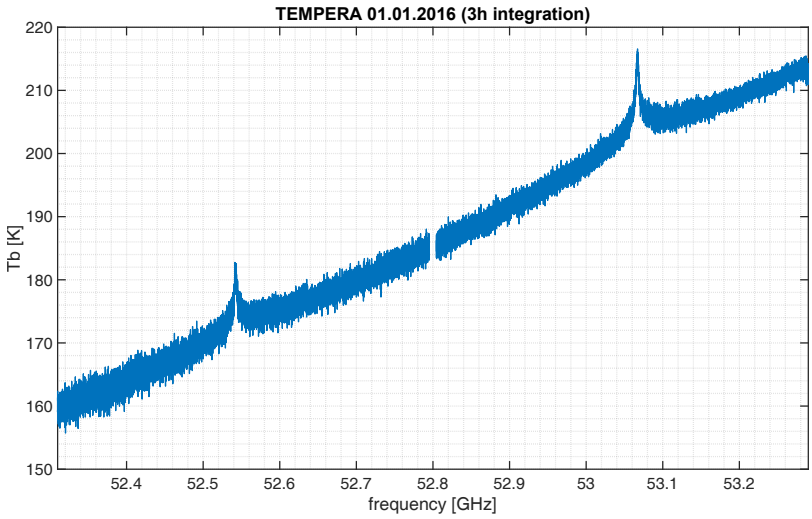

Figure 3. Spectrum of atmospheric Oxygen fine structure emission lines measured with TEMPERA after 3h of integration time (00.00 - 03.00). The ambient load in combination with the integrated noise diode, was used for calibration of this spectrum.

3 Temperature retrievals from atmospheric spectra

The first step is to set up a model atmosphere and simulate the forward radiative transfer.

$$\mathbf{y} = \mathbf{F}(\mathbf{x}) + \epsilon \tag{1}$$

Where $\mathbf{y}$ is the measurement vector, $\mathbf{F}$ the forward model, $\mathbf{x}$ the atmospheric state vector, and ϵ the measurement error. Following the formalism of Rodgers (2000) the forward model is inverted by an optimal estimation method. Assuming that $\mathbf{y}$ and $\mathbf{x}$ have Gaussian probability distributions $P(\mathbf{x})$ and $P(\mathbf{y})$, and using the Bayes' theorem

$$P(\mathbf{x}|\mathbf{y}) = \frac{P(\mathbf{y}|\mathbf{x})P(\mathbf{x})}{P(\mathbf{y})}, \tag{2}$$

a cost function of the following form can be found

$$J(\mathbf{x}) = -2\ln P(\mathbf{x}|\mathbf{y}) = [\mathbf{y} - \mathbf{F}(\mathbf{x})]^T \mathbf{S}_\epsilon^{-1} [\mathbf{y} - \mathbf{F}(\mathbf{x})] + [\mathbf{x} - \mathbf{x}_a]^T \mathbf{S}_a [\mathbf{x} - \mathbf{x}_a] \tag{3}$$

where $J(\mathbf{x})$ is minimized by a Levenberg-Marquardt algorithm. Here $\mathbf{x}_a$ is the apriori state, used as the initial guess to start the iteration, and $\mathbf{S}_a$ and $\mathbf{S}_\epsilon$ are the apriori and measurement covariance matrices. An important quantity for the retrieval analysis is the averaging kernel

$$\mathbf{A} = \mathbf{GK} \tag{4}$$

and the corresponding measurement response

$$\mathbf{MR} = \mathbf{AI}, \tag{5}$$

https://doi.org/10.5194/amt-2024-42
Preprint. Discussion started: 28 March 2024

where $\mathbf{K}$ is the weighting function matrix

$$\mathbf{K} = \frac{\partial \mathbf{F}(\mathbf{x})}{\partial \mathbf{x}}, \tag{6}$$

and $\mathbf{G}$ denotes the gain matrix

$$\mathbf{G} = \left[\mathbf{K}^T \mathbf{S}_\epsilon^{-1} \mathbf{K} + \mathbf{S}_a^{-1}\right]^{-1} \mathbf{K}^T \mathbf{S}_\epsilon^{-1}, \tag{7}$$

and $\mathbf{I}$ denotes the unit matrix. The optimal estimation technique contains several sources of uncertainty, which are the observation error $\mathbf{S}_O$, the smoothing error $\mathbf{S}_S$, which both contribute to the total error S_{tot}

$$\mathbf{S}_O = \mathbf{G}\mathbf{S}_\epsilon \mathbf{G}^T \tag{8}$$

$$\mathbf{S}_S = [\mathbf{A} - \mathbf{I}]\, \mathbf{S}_a\, [\mathbf{A} - \mathbf{I}]^T \tag{9}$$

$$\mathbf{S}_{tot} = \mathbf{S}_O + \mathbf{S}_S \quad . \tag{10}$$

Within ARTS the Zeeman Splitting module (Larsson et al., 2019) was used to account for the Zeeman effect in the forward model. A detailed description of the forward model retrieval algorithm is found in Krochin et al. (2022a). We implemented only a minor change related to the tropospheric correction. Instead of using the method suggested in Ingold and Kämpfer (1998), the tropospheric opacity is retrieved in ARTS using the spectral data of the line wings. Minor improvements were reached by including, frequency shift and frequency stretch in the ensemble of retrieved quantities, and by decreasing the apriori error of the retrieved baseline. The temperature profile apriori error was set constant to a brightness temperature covariance of 15K. Figure 4 illustrates the measurement response (MR), the averaging kernel (AVK), total retrieval error, and the full-width-at-half-maximum of the rows of the AVK matrix, conventionally referred to as altitude resolution. We consider only altitudes with a measurement response of MR>0.6 for all further scientific analyses. A lower measurement response indicates that the solution at these heights is more and more dominated by the apriori state. The forward model formalism, the retrieval algorithm, and the definitions of the retrieval quantities following the formalism from Rodgers (2000).

https://doi.org/10.5194/amt-2024-42
Preprint. Discussion started: 28 March 2024

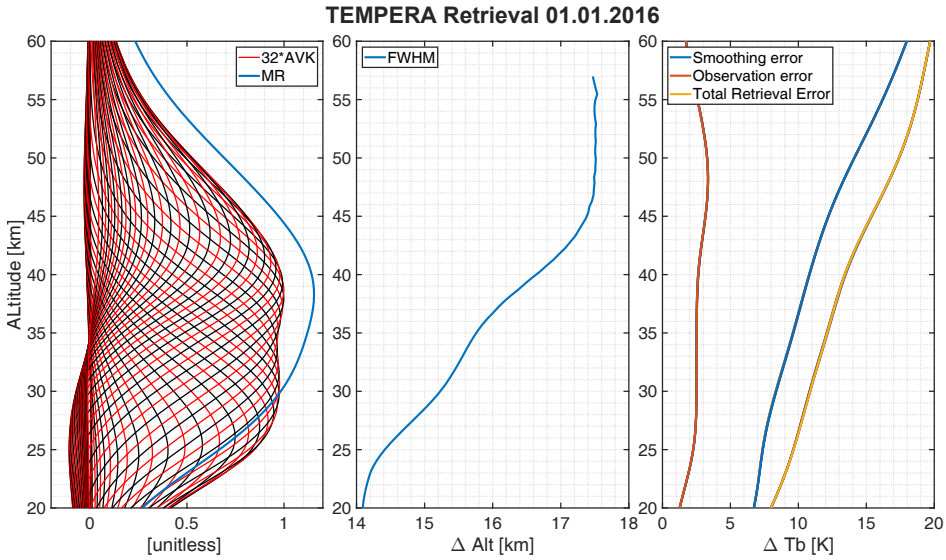

Figure 4. The left panel shows the AVK matrix for each altitude. The AVK values were inflated by 32 to get them to a comparable scale to the MR in the same plot (ARTS output). The middle panel visualizes the FWHM of the AVK matrix for each altitude, which corresponds to the altitude resolution. The right panel exhibits all three retrieval errors as explained in Eq. 8 to 10.

4 TEMPERA observations

In this manuscript, we present measurements of altitude and time-resolved profiles of atmospheric temperatures, retrieved from continuous TEMPERA observations conducted between 2014 to 2023. Two periods are to be distinguished due to a change in the operational mode made in 2022. Between 2014-2017 TEMPERA operated in an interleaved observation mode sharing the measurement time between a tropospheric mode, which scanned several zenith angles to retrieve tropospheric temperatures (Stähli et al., 2013), and a stratospheric/lower mesospheric mode measuring atmospheric spectra at a zenith angle of 30°, which resulted in an effective temporal resolutions of 3 hours. The operational mode implemented in 2022 employs only one zenith angle at 30°, which improves the time resolution of stratospheric spectra to 1 hour. Figure 3 illustrates a calibrated spectrum, observed at the Meteo Swiss Technical Center Payerne in 2016.

The time series of retrieved temperature profiles is shown in Figure 5. The blank times are mainly caused by liquid water clouds or rain that attenuate the stratospheric signal. Under clear sky conditions, the observed frequency range is less affected by the emission/absorption of H_2O molecules and only the effects of line mixing remain. However, liquid water clouds create thermal emission, which increases the brightness temperatures over the entire frequency band at our receiver. An approach to mitigate this problem is to include a cloud box in the forward model of the retrieval algorithm. This method improves tropospheric temperature retrievals (Bernet et al., 2017), but was not tested on stratospheric retrievals and, thus, is not included in the current version of the stratospheric retrieval.

https://doi.org/10.5194/amt-2024-42
Preprint. Discussion started: 28 March 2024

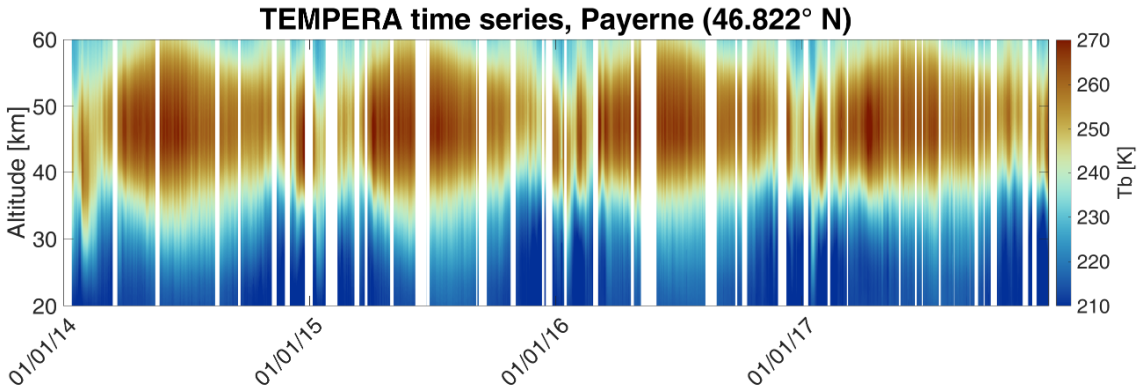

Figure 5. Continuous series of temperature profiles, retrieved from TEMPERA measurements. Data gaps are mainly due to weather conditions. The altitude range is 25-55 km (MR>0.6) but the range in the plot is 20-60 km for illustration.

5 Tidal Analysis - Adaptive Spectral Filter (ASF)

Previous studies have shown that the prevailing tidal modes at mid-latitudes are migrating tides (Stober et al., 2020b; Baumgarten and Stober, 2019; Hibbins et al., 2019). Non-migrating tides have often smaller amplitudes compared to their migrating counterpart. However, satellite observations have demonstrated their presence at the lower latitudes (Oberheide et al., 2011a). TEMPERA observations are only available at one geographic location and, thus, in all further analysis, we refer to the tides as total tides consisting of the migrating and non-migrating modes. Furthermore, we classify the different tidal modes only by their period and discuss diurnal, semidiurnal, and terdiurnal total tidal amplitudes and phases. Local tidal oscillations are often modeled by a mean state and a simple superposition of sinusoidal functions for each included period;

$$T(t_k) = T_{0k} + \sum_{n=1}^{3} \left[a_{nk} \sin\left(\frac{2\pi}{P_n} t_k\right) + b_{nk} \cos\left(\frac{2\pi}{P_n} t_k\right) \right]. \tag{11}$$

Where T_{0k} is the background state (median over k-th window), P_n = [1, $^1/_2$, $^1/_3$]$\times$ day, the period, $A_{nk} = \sqrt{a_{nk}^2 + b_{nk}^2}$ the amplitude, and t_k is the local time of the k-th window. The phase shift $\Delta\phi_{nk}$ (hours from midnight) can be derived by

$$\Delta\phi_{nk} = \arctan\left(\frac{b_{nk}}{a_{nk}}\right) \tag{12}$$

In this study, we applied the adaptive spectral filter (ASF) technique that was already used in many studies and on many different data such as lidar observations, meteor radar winds, EISCAT ion velocity, or GCM winds and temperatures (Stober et al., 2017; Baumgarten and Stober, 2019; Stober et al., 2020b, 2021; Günzkofer et al., 2022).

The ASF also includes a vertical regularization to ensure a smooth phase behavior of each tidal mode, which seems to reduce the contamination due to gravity waves with shorter vertical wavelengths. Furthermore, the algorithm adapts the window length

https://doi.org/10.5194/amt-2024-42
Preprint. Discussion started: 28 March 2024

for each fitted tidal mode to capture transient events that alter the tidal amplitude and phase. Another benefit of this technique is that data gaps or unevenly sampled time series can be analyzed as well. More details can be found in Baumgarten and Stober (2019); Stober et al. (2020b). Here, we implemented the ASF using a 4-day sliding window after the removal of the median. The error propagation for the tidal amplitudes and phases was calculated by weighting the least square error, with the total retrieval error.

6 Results of tidal analysis

Applying ASF on the data set of continuous temperature profiles results in 3 sets of continuous-time and altitude-resolved amplitude and phases (Local Solar Time of maximum). For the period 2014-2017, the time resolution (3h) is not sufficient to resolve semi-diurnal and terdiurnal tides, therefore only one single set of diurnal tides was analyzed. For the period 2022-2023 however, the time resolution (1 h) is sufficient to resolve semi- and terdiurnal tides.

https://doi.org/10.5194/amt-2024-42
Preprint. Discussion started: 28 March 2024

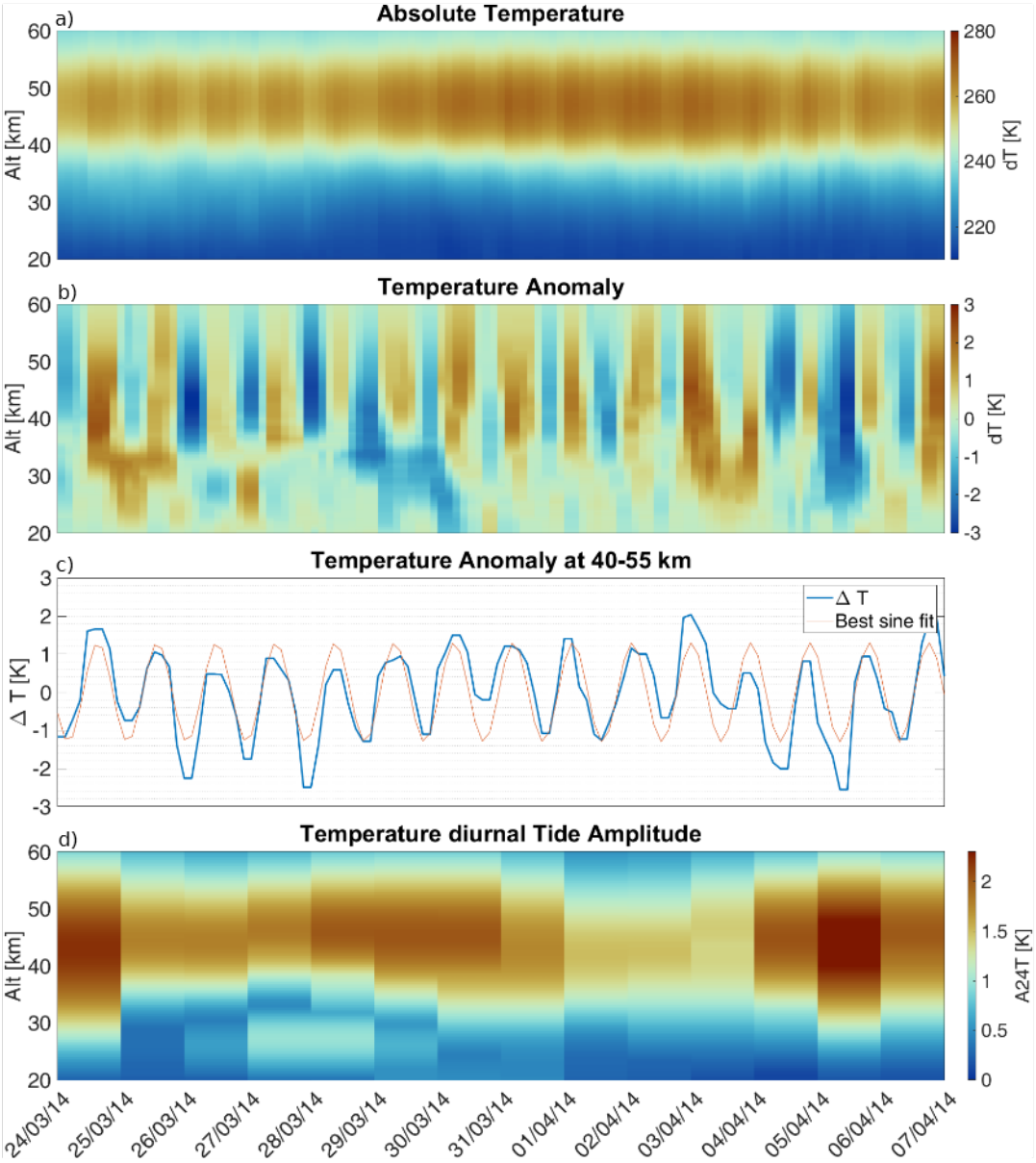

Figure 6. a) Vertical resolved temperature measurements observed with TEMPERA for the period from 24.03.2014-07.04.2014. b) Inferred absolute Temperature anomalies retrieved using a 4-day sliding median to visualize short-scale variations. c) Vertical integrated temperature anomalies calculated from measurements between 40-55 km and a corresponding best-sine-fit. d) Retrieved diurnal tide amplitude profiles calculated from ASF.

Figure 6 shows temperature profiles (top panel) and the corresponding tidal amplitudes (bottom panel) for 14 days during spring 2014. The temperature anomaly (second panel from the top) is the difference between the raw temperature and a background state, smoothed with a 4-day sliding window (median). It shows the complex dynamic at the stratosphere with

https://doi.org/10.5194/amt-2024-42
Preprint. Discussion started: 28 March 2024

Atmospheric Measurement Techniques Discussions

alternating warmer and colder periods at different altitudes. The third plot from the top shows a median over the anomaly profile from 40-55 km. For illustration purposes, a sine function with a period of 24 hours was fitted to the curve. Deviations from the sine fit are assumed to be higher period oscillations caused by gravity waves and planetary waves. Also, the period of thermal tides is not stable and can slightly change from day to day (Baumgarten and Stober, 2019; Stober et al., 2020b; van Caspel et al., 2023).

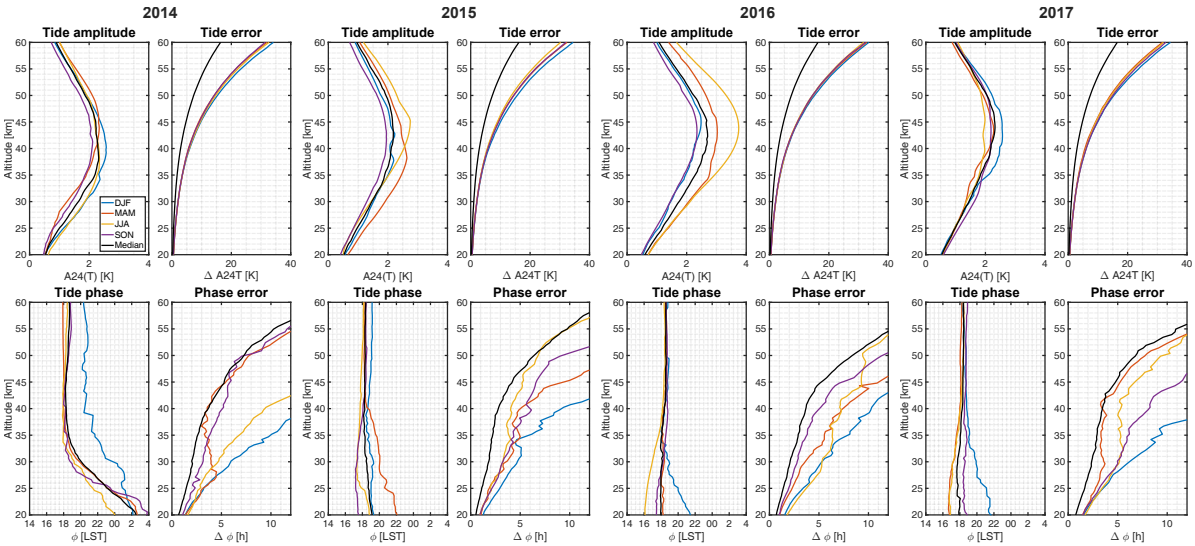

Figure 7. Top: Seasonal averaged diurnal tide profiles with the corresponding error. The black curve represents the median over a whole year. Bottom: Seasonal averaged diurnal tide phase profiles with the corresponding error.

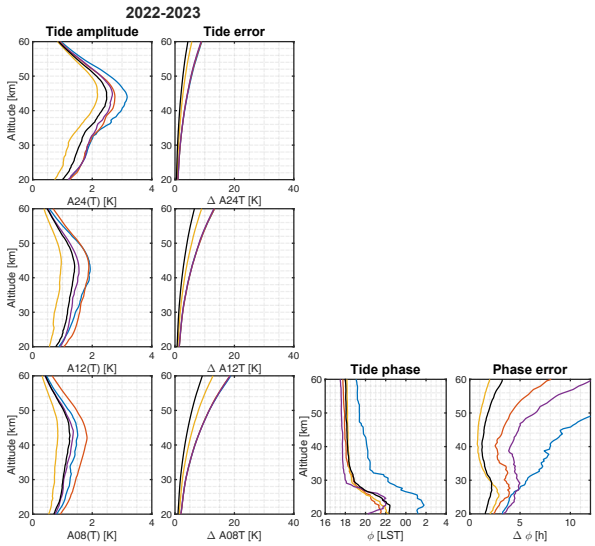

Figure 8. Left: Seasonal averaged diurnal, semi diurnal, and terdiurnal tide profiles with the corresponding error (as in Figure 7). Right: Seasonal averaged diurnal tide phase profiles with the corresponding error (see section 5).

https://doi.org/10.5194/amt-2024-42
Preprint. Discussion started: 28 March 2024

season	2014 Max A24T(@ z [km])	2015 Max A24T(@ z [km])	2016 Max A24T(@ z [km])	2017 Max A24T(@ z [km])
DJF	2.6(40)	2.2(43)	2.5(45)	2.6(42)
MAM	2.3(44)	2.6(38)	3.0(43)	2.3(43)
JJA	2.5(38)	2.8(45)	3.7(44)	2.0(40)
SON	2.1(41)	2.0(42)	2.3(43)	2.2(43)
full median	2.4(38)	2.4(43)	2.8(42)	2.3(44)

Table 1. Maxima and corresponding altitudes of seasonal averaged diurnal tidal amplitudes between 2014-2017.

season	diurnal Max A24T(@ z [km])	semidiurnal Max A12T(@ z [km])	terdiurnal Max A8T(@ z [km])
DJF	3.1(45)	1.9(44)	1.5(43)
MAM	2.8(44)	1.9(43)	1.7(42)
JJA	2.2(45)	1.0(45)	0.8(43)
SON	2.6(44)	1.4(41)	1.2(44)
full median	2.4(44)	1.4(43)	1.2(44)

Table 2. Maxima and corresponding altitudes of seasonal averaged diurnal, semidiurnal, and terdiurnal tidal amplitudes.

Yearly and seasonal averaged amplitude profiles for the period 2014-2017 are illustrated in Figure 7 (upper panels). The black line shows the median for an entire year and colored lines represent medians over the corresponding seasons (December-January-February (DJF) (blue), March-April-May (MAM)(red), June-July-August (JJA)(orange), and September-October-November (SON)(purple)). The mean tide amplitude profile has a maximum between 2.0-3.7 K at 38-45 km (see also Table 1). The seasonal averages show an increased tidal activity in the spring months for the years 2015, and 2016, whereas in 2014 and 2017 the highest tidal activity was found during winter. The absolute difference between summer and winter tide amplitudes is, however, much smaller than the corresponding standard deviation and, thus, is insignificant. The lower panels show the tide phases, which in this case are the local solar times of the tide peak. From 20-30 km, a downward phase propagation can be seen in 2014 with an estimated phase speed of -1.6 km/h. At 30-35 km the phase propagation turns to a constant value of 18 LST. The reversal of the phase propagation seems to be related to the ozone diurnal cycle and will be discussed later. Figure 8 (left panel) shows averaged tidal amplitudes for the period 2022-2023. The maximum for diurnal tide amplitudes (upper panel) occurs between 41-45km where the amplitude reaches values between 2.2-3.2 K. Due to the instrument updates between 2017 and 2022, we analyzed also the semidiurnal (middle panel) and terdiurnal (lower panel) tidal amplitudes for these observations. The profiles show maximum values of 1-1.9 K around 41-45 km for semidiurnal and 0.8-1.5 around 42-44km for terdiurnal tide (see Table 2). Diurnal and semidiurnal tides have the highest amplitudes during winter time, while the terdiurnal tide exhibits maximum amplitudes in spring. The phases for the diurnal tides are shown in Figure 8 (right panel). Semidiurnal and terdiurnal

https://doi.org/10.5194/amt-2024-42
Preprint. Discussion started: 28 March 2024

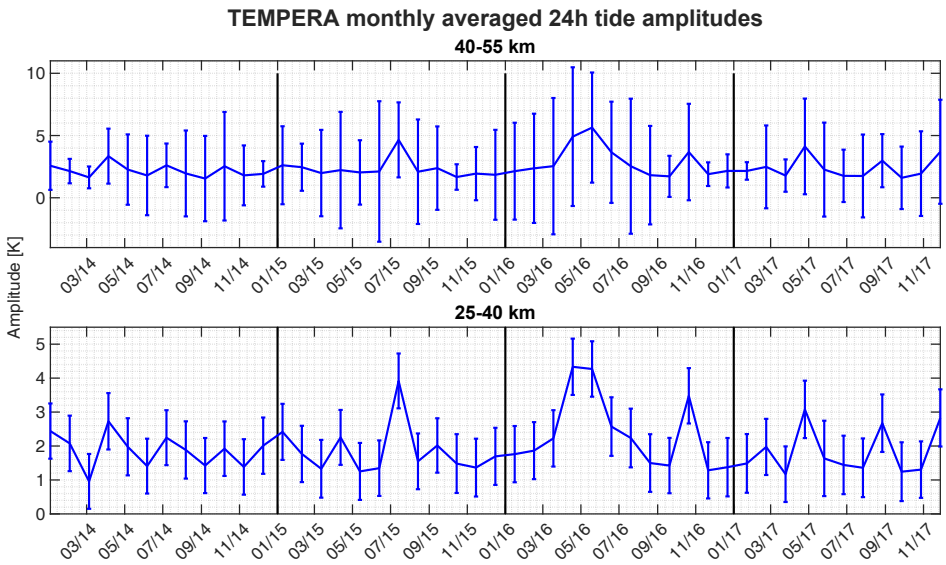

Figure 9. Monthly (31-day window) and altitude (15 km) averaged diurnal tide series with corresponding atmospheric variability (see section 7).

phases are not shown. These appeared to be very variable, which is partly attributed to the much smaller amplitudes and also due to other geophysical effects, which mask the tidal signature such as gravity waves. The phase propagation of diurnal tides shows a reversal from upward to downward at 22 km, a downward propagating phase with a phase speed of -1.8 km/h between 22-28 km, and a constant phase above 30 km.

To illustrate the seasonal climatology, the tide amplitudes were averaged over two altitude regions. The lower region is between 25-40 km and the upper region is between 40-55 km. Figure 9 shows the time series of the period 2014-2017 for both altitude regions. A significantly increased tidal activity appeared during the spring for the years 2016, 2017, and summer 2015, whereas for the year 2014 no significant seasonal pattern was found. The years 2016 and 2017 exhibit also a second maximum in autumn. Figure 10 shows the same plot for the period 2022-2023. All tidal amplitudes show increased activity in September, December, and April.

7 Discussion

Continuous temperature measurements at the stratosphere and lower mesosphere are crucial for benchmarking of reanalysis models or meteorological analysis. Such observations are beneficial for cross-comparison and also for data assimilation. Understanding the short-term tidal variability and vertical propagation requires higher cadence observations and more data assimilation (Liu, 2016; McCormack et al., 2017; Stober et al., 2020b; Dhadly et al., 2018; van Caspel et al., 2023). Currently, MERRA2 meteorological analysis is provided with hourly or three-hourly temporal resolution. However, the 3DVAR data as-

https://doi.org/10.5194/amt-2024-42
Preprint. Discussion started: 28 March 2024

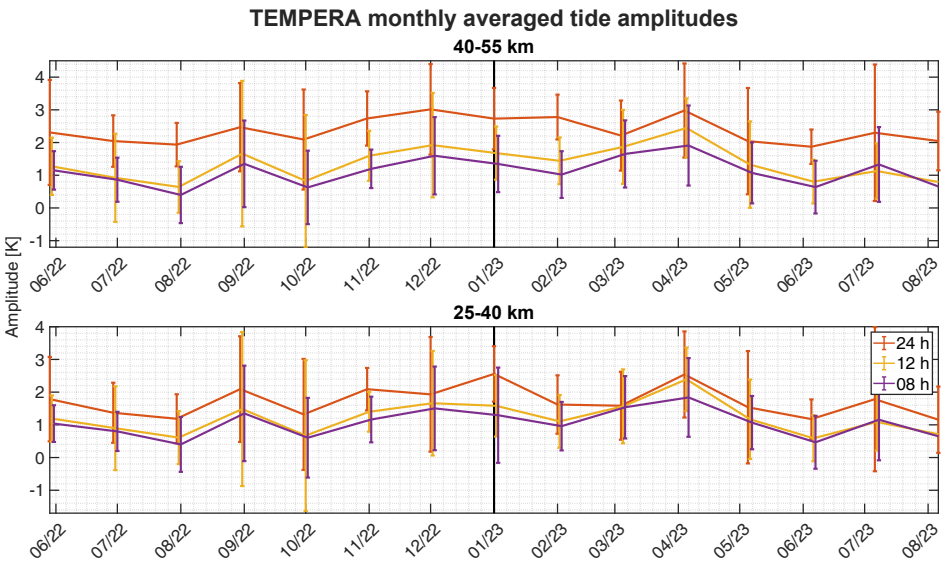

Figure 10. Monthly (31 day window) and altitude (15 km) averaged diurnal, semi diurnal, and terdiurnal tide series.

similation is performed every 6 hours (Gelaro et al., 2017). Furthermore, some measurements that are assimilated in MERRA2 at the stratosphere and the lower mesosphere are only available every 12 hours (e.g., radiosondes). The sparsity of measurements at the stratosphere and lower mesosphere will further increase due to the end-of-life-time of some satellite instruments such as MLS (Waters et al., 2006; Livesey et al., 2006).

Previous studies of atmospheric temperature tides at the stratosphere and lower mesosphere at mid-latitudes were based on lidar observations having full daylight capabilities. However, lidar observations depend on tropospheric cloud coverage, and, thus, the obtained lidar monthly climatologies were inferred by constructing multiyear composites of a day. Measurements acquired from different years and of various lengths covering full days or only a few hours were stacked together and analyzed to estimate tidal amplitudes from the obtained mean composite day (Kopp et al., 2015). So far, there was only one study that covered a 10-day continuous lidar measurement, which showed some tidal intermittency at the stratosphere (Baumgarten et al., 2018; Baumgarten and Stober, 2019). Hence, the shown TEMPERA measurements of stratospheric and lower mesospheric temperatures are valuable to investigate and continuously monitor the source variability of tides.

Diurnal tide profiles reach their seasonal maxima at an altitude around 38-45 km with values around 2-3.7 K, semidiurnal tides at an altitude around 42-45 km with maximum amplitudes of 1-1.9 K, and terdiurnal tides become maximal at 42-43 km with an amplitude of 0.8-1.5 K. This corresponds well to the results from Kopp et al. (2015), where the measurements were performed with a Lidar located in Kühlungsborn (Germany, 54.1469° N, 11.7420° E). However, the seasonal pattern in Kopp et al. (2015) shows a maximum of the diurnal tide at 45-55 km altitude in March and October with significantly lower amplitudes during summer. The results in our study show partially a similar behavior, but not for all years. We found the largest tidal amplitudes in May and October 2016, May and September 2017, September 2022, and April 2023. This follows roughly the pattern of maximal tidal activity in Spring and Autumn, where the spring maximum appears between the end of April and the end of May,

https://doi.org/10.5194/amt-2024-42
Preprint. Discussion started: 28 March 2024

and the autumn maximum appears between the beginning of September and the end of October. However, the tidal activity in the years 2014 and 2015 deviates from this climatological pattern. We attribute these differences in the first years 2014-2017 of TEMPERA measurements to instrumental effects and many changes in the measurement mode. Since 2022 TEMPERA has operated in a dedicated stratospheric and lower mesospheric measurement mode and improved retrievals are implemented (Krochin et al., 2022a), which solved most of the potential problems of the first light observations during the development phase of the prototype.

Classical tidal theory predicts an increased diurnal tidal amplitude during the summer months due to the increased solar heating (Lindzen and Chapman, 1969; Lindzen, 1979). However, this was only confirmed for the year 2015. Figure 9 and 10 show the standard deviation of the corresponding tide amplitudes in the error bars. The standard deviation of the tidal amplitudes is a measure of their geophysical variability and intermittency. Our observations were conducted in Bern and Payerne at the Swiss Plateau, which is next to the Alpine main ridge, a region that is often affected by strong summer convective instabilities due to thunderstorms. These convective cells excite gravity waves, which propagate into the stratosphere and alter the circulation by depositing their energy and momentum likely triggering multistep vertical coupling processes (Becker and Vadas, 2018; Vadas and Becker, 2018; Vadas et al., 2023). Although the averaged tide amplitudes exhibit only partially the expected pattern for the entire period, the geophysical variability indicates good agreement with the tidal theory. This variability reaches a minimum around winter time (March 2014, December 2015, October 2016, February 2017, February 2023). Also, it appears that there are two periods per year (around Mai and October) where it is likely to find increased tidal variation. In general, the variation in summer is 2-3 K higher than the tidal variability found during the winter months.

Observations of tidal phases at the stratosphere are rare. Due to the small tidal amplitudes phases appear to be very noisy and variable. This is also the case for TEMPERA measurements. The vertical profiles of the phases exhibit two regions. Above an altitude of 35 km the phase turns to a constant value of about 18 LST. Below 35 km the phases are much more variable and sometimes tend to reflect clear signs of a phase progression. A constant phase with altitude suggests that the tides are forced at these altitudes, whereas a changing phase indicates tidal propagation from below.

The increased phase variability and inversion of the phase progression at 35 km appear to be coupled to the ozone diurnal cycle. At this altitude, the relationship between ozone and temperature changes from a positive to a negative correlation due to a change in the chemical balance. We illustrate this effect by calculating a correlation between the ozone volume mixing ratio (VMR) and our temperature tidal amplitudes. Leveraging the ozone VMR measurements retrieved from the GROMOS radiometer (Sauvageat et al., 2022), which is located next to TEMPERA, we investigate their altitude-dependent relationship. Figure 11 shows Pearson Correlation coefficients, estimated over a 30-day sliding window, after re-gridding on a generic altitude grid. Since heating due to the absorption of solar radiation by ozone is the main tidal forcing mechanism at these altitudes, changes in ozone VMR are expected to be reflected in our tidal amplitude measurements. A similar calculation as in Figure 11 was also shown in (Sauvageat et al., 2023). A more detailed analysis of the ozone diurnal cycle was already performed in Schranz et al. (2018) and provides a pathway to future analysis.

https://doi.org/10.5194/amt-2024-42
Preprint. Discussion started: 28 March 2024

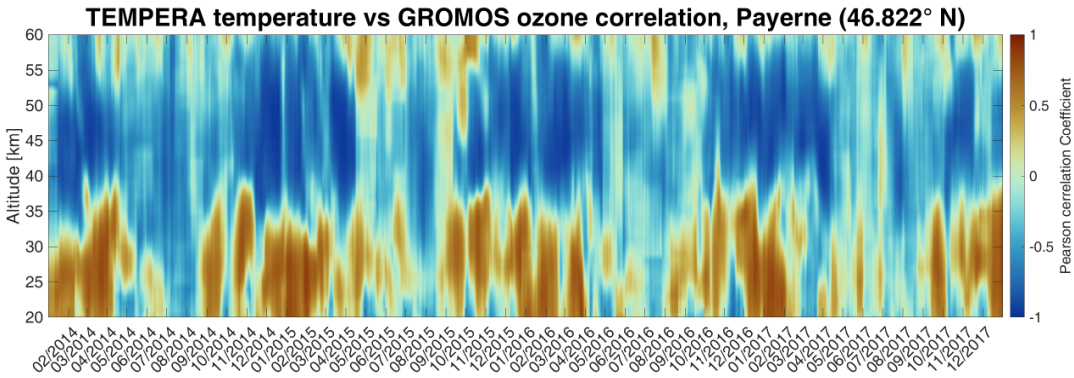

Figure 11. Pearson Correlation coefficients between TEMPERA temperatures and GROMOS Ozone measurements. Correlation Coefficients were calculated over a 30-day sliding window after interpolation on a generic altitude grid.

The main challenges for this type of analysis are related to instrument noise and data gaps, which complicate the spectral analysis and influence the phase information. In addition, there is some tidal intermittency due to planetary wave activity or strong gravity wave excitations (e.g., thunderstorms), which can lead to data gaps rendering classical Fourier transform or Wavelet techniques for the spectral analysis not applicable, or even useless. The ASF2D implemented for the TEMPERA tidal analysis, is designed to provide a decomposition of time series with data gaps or unevenly sampled measurements including error propagation and even a vertical regularization (see Stober et al. (2020a) and Baumgarten and Stober (2019)). Therefore, this technique seems to be adequate to be applied for radiometric high temporal resolution tidal studies.

8 Conclusions

We demonstrated the new capabilities of TEMPERA, the University Bern temperature radiometer, to perform continuous temperature soundings at the stratosphere and lower mesosphere. A recently implemented observational mode dedicated to stratospheric and mesospheric measurements together with updated retrievals (Krochin et al., 2022a) permit temperature measurements between 20-60 km altitude with a temporal resolution of 1 hour. The instrument operates autonomously and requires only occasional LN2 calibrations. The radiometer performs nominally also under tropospheric cloud cover conditions and only precipitation or thick liquid water clouds can lead to a loss of the stratospheric signal from both spectral lines.

Based on these continuous temperature soundings, we derived diurnal, semidiurnal, and terdiurnal tidal amplitude profiles between 20-55 km between 2014-2023. Amplitude profiles reach the maximum at an altitude range from 40-45 km with amplitudes of 2-3.7 K. The obtained tidal amplitudes agree with previous results from multiyear composite lidar observations at mid-latitudes Kopp et al. (2015). Our continuous temperature soundings indicate a notable year-to-year variability of the seasonal tidal activity, which only partially reflects the predictions from the classical tide theory (maximum amplitudes during summer). However, the amplitude geophysical variability appears to be increased by 2-3 K during the summer compared to the winter season, which is likely caused by summer tropospheric convection above the Swiss Plateau and the corresponding

https://doi.org/10.5194/amt-2024-42
Preprint. Discussion started: 28 March 2024

multistep vertical coupling due to gravity waves inducing changes in the stratospheric circulation due to the deposition of the transported energy and momentum.

The retrieved tidal phase also exhibits a characteristic vertical structure. Above 35 km, diurnal tidal phases appear to be constant suggesting a direct excitation of the tide due to the ozone absorption. Below 35 km, we observed an increased variability and in some years a vertical phase progression indicating a vertical propagation of a tide that was forced below. This is confirmed by the Pearson correlation of ozone-temperature measurements, which indicates a change from positive to negative correlation at this altitude.

Another big advantage of TEMPERA is the instrument cost compared to lidars with full daylight capability. The lower unit costs provide an opportunity to install larger observational networks. A larger network of ground-based radiometers would greatly improve the tidal analysis. By deploying TEMPERAs at four different measurement locations, wavefront direction, orientation, and propagation velocity could be resolved. Such an observational network could be complemented with wind observations from the wind radiometers WIRA (Hagen et al., 2018, 2020). Furthermore, the Microwave Group of the University of Bern is currently developing a new fully polarimetric temperature radiometer (TEMPERA-C, Krochin et al. (2022b)). The new instrument will have an increased altitude range (up to 60km) and an even better time resolution of about 30 min.

Data availability. MERRA-2 data are available at MDISC, managed by the NASA Goddard Earth Sciences (GES) Data and Information Services Center (DISC) DOI:10.5067/QBZ6MG944HW0. TEMPERA temperatures are shared on request (gunter.stober@unibe.ch).

https://doi.org/10.5194/amt-2024-42
Preprint. Discussion started: 28 March 2024

Atmospheric Measurement Techniques Discussions

Appendix A: MERRA2 Comparison

For the location of Payerne (46°49'N 6°56'E) MERRA2 temperature profiles for the period 2014-2017 were analyzed with the method described in section 5. The results are illustrated in Figure A1. The amplitude profiles have maximal values of 2-3.4 K at altitudes 47-53 km. Diurnal tide amplitudes and variations also show maximal activity during winter months (Figures A1 and A2).

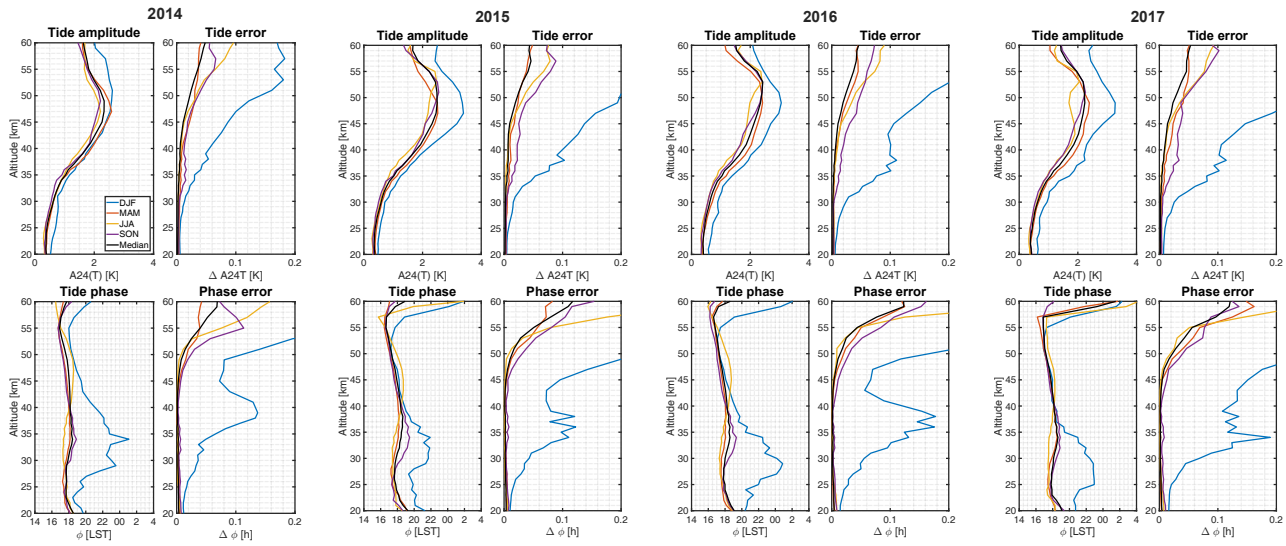

Figure A1.

Top: Seasonal averaged diurnal tide profiles with the corresponding error (same as Figure. 7) derived from MERRA2 data. The black curve represents the median over a whole year.

Bottom: Seasonal averaged diurnal tide phase profiles with the corresponding error.

While MERRA2 tide profile maxima match well with our results, the altitude where the maxima are reached is roughly 6 km higher as in our case. Phase profiles show anomalous behaviour between 25-35 km mostly in winter months. Downward phase propagation was found in all years, but only up to 25km. Above 35 km the phase is not constant but rather shows downward propagation and turns sharply upward above 55 km. However, up to 55 km the phase remains roughly around 18 LST, except in winter months.

The seasonal pattern of MERRA2 diurnal tide amplitudes deviates from our results and classical tide theory. The highest amplitude and variation appear from December to February, while the lowest activity was found in summer. We assume that the main reason for this discrepancy is the implementation of the ozone diurnal cycle in the reanalysis. However, MERRA2 is a meteorological reanalysis and thus the quality of the obtained wind and temperature fields depends crucially on the data to be assimilated. Above 35 km altitude, the data coverage becomes more sparse, and the temporal resolution of the assimilated data products is no longer sufficient to constrain tidal amplitudes and phases on a global scale.

https://doi.org/10.5194/amt-2024-42
Preprint. Discussion started: 28 March 2024

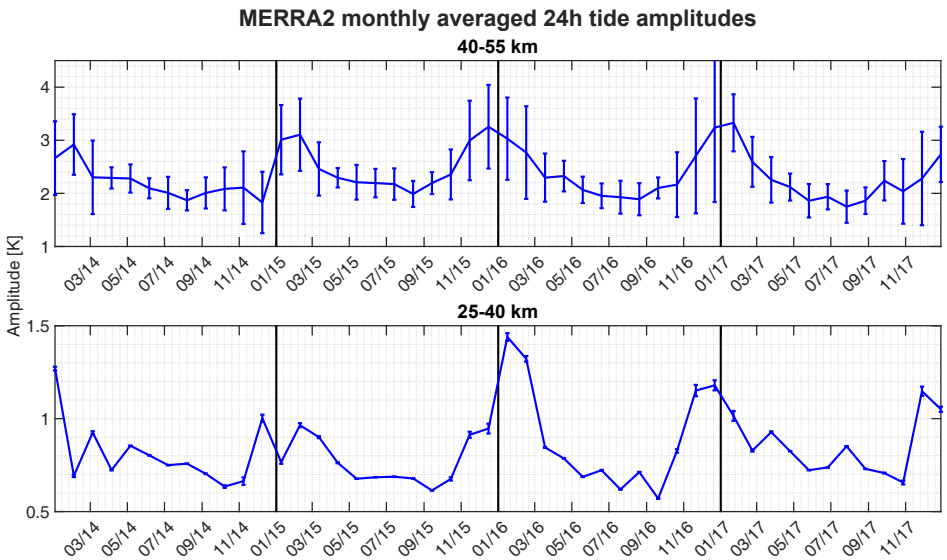

Figure A2. Monthly (31 day window) and altitude (15 km) averaged diurnal tide series (same as Figure. 9), derived from MERRA2 data.

season	2014	2015	2016	2017
	Max A24T(@ z [km])	Max A24T(@ z [km])	Max A24T(@ z [km])	Max A24T(@ z [km])
DJF	2.6(51)	3.4(47)	3.1(49)	3.3(49)
MAM	2.6(47)	2.5(47)	2.4(49)	2.4(49)
JJA	2.2(47)	2.5(53)	2.4(53)	2.0(53)
SON	2.2(49)	2.5(51)	2.4(53)	2.3(51)
full median	2.4(49)	2.7(49)	2.6(53)	2.5(49)

Table A1. Maxima and corresponding altitudes of seasonal averaged diurnal tide profiles derived from MERRA2 data.

Author contributions. WK and GS conceptualized the content of the manuscript. WK implemented the retrieval and performed the data analysis of TEMPERA observations. GS reduced the MERRA2 data for the validation. All authors contributed to the editing of the manuscript.

Competing interests. The authors declare that they have no competing interests.

Acknowledgements. This research has been supported by the Schweizerischer Nationalfonds zur Förderung der Wissenschaftlichen Forschung (grant no. 200021-200517 / 1), and the Swiss Polar Institute (SPI) supports the development of the TEMPERA-C radiometer. We thank the ARTS developer team for their support and Richard Larsson for implementing the Zeeman effect in ARTS. We also thank Francisco Navas-Guzmán and MeteoSwiss for hosting the instrument and calibrating the noise diode, during the period when TEMPERA was located at the

https://doi.org/10.5194/amt-2024-42
Preprint. Discussion started: 28 March 2024

Atmospheric Measurement Techniques Discussions

MeteoSwiss technical centre in Payerne. Scientific color maps (Crameri et al., 2020) are used in this study to prevent visual distortion of the data and exclusion of readers with colour-vision deficiencies.

https://doi.org/10.5194/amt-2024-42
Preprint. Discussion started: 28 March 2024

References

Baumgarten, K. and Stober, G.: On the evaluation of the phase relation between temperature and wind tides based on ground-based measurements and reanalysis data in the middle atmosphere, Annales Geophysicae, 37, 581–602, https://doi.org/10.5194/angeo-37-581-2019, 2019.

Baumgarten, K., Gerding, M., Baumgarten, G., and Lübken, F.-J.: Temporal variability of tidal and gravity waves during a record long 10-day continuous lidar sounding, Atmospheric Chemistry and Physics, 18, 371–384, https://doi.org/10.5194/acp-18-371-2018, 2018.

Becker, E.: Mean-Flow Effects of Thermal Tides in the Mesosphere and Lower Thermosphere, Journal of the Atmospheric Sciences, 74, 2043 – 2063, https://doi.org/10.1175/JAS-D-16-0194.1, 2017.

Becker, E. and Vadas, S. L.: Secondary Gravity Waves in the Winter Mesosphere: Results From a High-Resolution Global Circulation Model, Journal of Geophysical Research: Atmospheres, 123, 2605–2627, https://doi.org/10.1002/2017JD027460, 2018.

Bernet, L., Navas Guzmán, F., and N, K.: The effect of cloud liquid water on tropospheric temperature retrievals from microwave measurements, Atmospheric Measurement Techniques, 10, 4421–4437, https://doi.org/10.5194/amt-10-4421-2017, 2017.

Chang, L., Palo, S., Hagan, M., Richter, J., Garcia, R., Riggin, D., and Fritts, D.: Structure of the migrating diurnal tide in the Whole Atmosphere Community Climate Model (WACCM), Advances in Space Research, 41, 1398–1407, https://doi.org/10.1016/j.asr.2007.03.035, 2008.

Chapman, S. and Lindzen, R.: Atmospheric Tides: Thermal and Gravitational, D. Reidel Publishing company, New York, https://doi.org/10.1007/ 978-94-010-3399-2, 1970.

Crameri, F., Shephard, G. E., and Heron, P.: The misuse of colour in science communication, Nature Communications, 11, https://doi.org/10.1038/s41467-020-19160-7, 2020.

Dhadly, M. S., Emmert, J. T., Drob, D. P., McCormack, J. P., and Niciejewski, R. J.: Short-Term and Interannual Variations of Migrating Diurnal and Semidiurnal Tides in the Mesosphere and Lower Thermosphere, Journal of Geophysical Research: Space Physics, 123, 7106–7123, https://doi.org/https://doi.org/10.1029/2018JA025748, 2018.

Eriksson, P., c. Jiménez, and Buehler, S.: Qpack, a general tool for instrument simulation and retrieval work, Journal of Quantitative Spectroscopy & Radiative Transfer, 91, 47–64, 2005.

Fong, W., Lu, X., Chu, X., Fuller-Rowell, T., Yu, Z., Roberts, B., Chen, C., Gardner, C., and A.J, M.: Winter temperature tides from 30 to 110 km at McMurdo (77.8°S, 166.7°E), Antarctica: Lidar observations and comparisons with WAM, Journal of Geophysical Research: Atmospheres, 119, 2846–2863, https://doi.org/doi:10.1002/2013JD020784, 2022.

Forbes, J.: Atmospheric Tides 1. Model Description and Results for the Solar Diurnal Componen, Journal of Geophysical Research, 87, 5222–5240, https://doi.org/doi:10.1029/2007JD008725, 1982.

Gelaro, R., McCarty, W., Suárez, M. J., Todling, R., Molod, A., Takacs, L., Randles, C. A., Darmenov, A., Bosilovich, M. G., Reichle, R., Wargan, K., Coy, L., R., C., C., D., S., A., V., B., A., C., da Silva A. M., Gu, W., Kim, G., Koster, R., Lucchesi, R., Merkova, D., Nielsen, J. E., Partyka, G., Pawson, S., Putman, W., Rienecker, M., Schubert, S. D., Sienkiewicz, M., and Zhao, B.: The Modern-Era Retrospective Analysis for Research and Applications, Version 2 (MERRA-2), Journal of Climate, 30, 5419–5454, https://doi.org/doi.org/10.1175/JCLI-D-16-0758.1, 2017.

Gille, S., Hauchecorne, A., and Chanin, M.: Semidiurnal and Diurnal Tidal Effects in the Middle Atmosphere as Seen by Rayleigh Lidar, Journal of Geophysical Research, 96, 7579–7587, https://doi.org/10.1029/90JD02570, 1991.

https://doi.org/10.5194/amt-2024-42
Preprint. Discussion started: 28 March 2024

Günzkofer, F., Pokhotelov, D., Stober, G., Liu, H., Liu, H.-L., Mitchell, N. J., Tjulin, A., and Borries, C.: Determining the Origin of Tidal Oscillations in the Ionospheric Transition Region With EISCAT Radar and Global Simulation Data, Journal of Geophysical Research: Space Physics, 127, e2022JA030 861, https://doi.org/https://doi.org/10.1029/2022JA030861, e2022JA030861 2022JA030861, 2022.

Hagan, M., Forbes, J., and F, V.: On modeling migrating solar tides, Geophysical Research Letters, 22, 893–896, https://doi.org/10.1029/95GL00783, 1995.

Hagan, M., Forbes, J., and F, V.: GSWM-98: Results for migrating solar tides, Journal of Geophysical Research: Space Physics, 104, 6813–6827, https://doi.org/10.1029/1998JA900125, 1999.

Hagen, J., Murk, A., Rüfenacht, R., Khaykin, S., Hauchecorne, A., and Kämpfer, N.: WIRA-C: a compact 142-GHz-radiometer for continuous middle-atmospheric wind measurements, Atmospheric Measurement Techniques, 11, 5007–5024, https://doi.org/10.5194/amt-11-5007-2018, 2018.

Hagen, J., Hocke, K., Stober, G., Pfreundschuh, S., Murk, A., and Kämpfer, N.: First measurements of tides in the stratosphere and lower mesosphere by ground-based Doppler microwave wind radiometry, Atmospheric Chemistry and Physics, 20, 2367–2386, https://doi.org/10.5194/acp-20-2367-2020, 2020.

Hibbins, R. E., Espy, P. J., Orsolini, Y. J., Limpasuvan, V., and Barnes, R. J.: SuperDARN Observations of Semidiurnal Tidal Variability in the MLT and the Response to Sudden Stratospheric Warming Events, Journal of Geophysical Research: Atmospheres, 124, 4862–4872, https://doi.org/https://doi.org/10.1029/2018JD030157, 2019.

Hocke, K.: Influence of Sudden Stratospheric Warmings on the Migrating Diurnal Tide in the Equatorial Middle Atmosphere Observed by Aura/Microwave Limb Sounder, Atmosphere, 14, https://doi.org/10.3390/atmos14121743, 2023.

Ingold, T. and Kämpfer, N.: Weighted mean tropospheric temperature and transmittance determination at millimeter-wave frequencies for ground-based applications, Radio Science, 22, 905–918, https://doi.org/10.1029/98RS01000, 1998.

Kopp, M., Gerding, J., and Lübken, F.-J.: Tidal signatures in temperatures derived from daylight lidar soundings above Kühlungsborn, Journal of Atmospheric and Solar-Terrestrial Physics, 127, 37–50, https://doi.org/10.1016/j.jastp.2014.09.002, 2015.

Krochin, W., Navas Guzmán, F., Kuhn, D., Murk, A., and Stober, G.: Continuous temperature soundings at the stratosphere and lower mesosphere with a ground-based radiometer considering the Zeeman effect, Atmospheric Measurement Techniques, 15, 2231–2249, https://doi.org/10.5194/amt-15-2231-2022, 2022a.

Krochin, W., Navas Guzmán, F., Kuhn, D., Murk, A., and Stober, G.: Development of a Polarimetric 50-GHz Spectrometer for Temperature Sounding in the Middle Atmosphere, IEEE Journal of selected topics in applied earth observations and remote sensing, 15, https://doi.org/10.48350/186172, 2022b.

Larsson, R., Lankhaar, B., and Eriksson, P.: Updated Zeeman effect splitting coefficients for molekular oxygen in planetary applications, Geoscientific Model Developement, 224, 431–438, https://doi.org/10.1016/j.jqsrt.2018.12.004, 2019.

Lindzen, R. S.: Atmospheric Tides, Annual Review of Earth and Planetary Sciences, 7, 199–225, https://doi.org/10.1146/annurev.ea.07.050179.001215, 1979.

Lindzen, R. S. and Chapman, S.: Atmospheric Tides, Space Sci. Rev., 10, 3–188, 1969.

Liu, H.-L.: Variability and predictability of the space environment as related to lower atmosphere forcing, Space Weather, 14, 634–658, https://doi.org/10.1002/2016SW001450, 2016.

Livesey, N., Van Snyder, W., Read, W., and Wagner, P.: Retrieval algorithms for the EOS Microwave limb sounder (MLS), IEEE Transactions on Geoscience and Remote Sensing, 44, 1144–1155, https://doi.org/10.1109/TGRS.2006.872327, 2006.

https://doi.org/10.5194/amt-2024-42
Preprint. Discussion started: 28 March 2024

McCormack, J., Hoppel, K., Kuhl, D., de Wit, R., Stober, G., Espy, P., Baker, N., Brown, P., Fritts, D., Jacobi, C., Janches, D., Mitchell, N., Ruston, B., Swadley, S., Viner, K., Whitcomb, T., and Hibbins, R.: Comparison of mesospheric winds from a high-altitude meteorological analysis system and meteor radar observations during the boreal winters of 2009-2010 and 2012-2013, Journal of Atmospheric and Solar-Terrestrial Physics, 154, 132 – 166, https://doi.org/http://dx.doi.org/10.1016/j.jastp.2016.12.007, 2017.

Navas-Guzmán, Kämpfer, N., Murk, A., Larsson, R., Buehler, S. A., and Eriksson, P.: Zeeman effect in atmospheric O_2 measured by ground-based microwave radiometry, Atmospheric Measurement Techniques, 8, 1863–1874, https://doi.org/10.5194/amt-8-1863-2015, 2015.

Oberheide, J., Forbes, J. M., Zhang, X., and Bruinsma, S. L.: Climatology of upward propagating diurnal and semidiurnal tides in the thermosphere, Journal of Geophysical Research: Space Physics, 116, https://doi.org/10.1029/2011JA016784, 2011a.

Oberheide, J., Forbes, J. M., Zhang, X., and Bruinsma, S. L.: Climatology of upward propagating diurnal and semidiurnal tides in the thermosphere, Journal of Geophysical Research: Space Physics, 116, https://doi.org/https://doi.org/10.1029/2011JA016784, 2011b.

Ortland, A. D.: A Study of the Global Structure of the Migrating Diurnal Tide Using Generalized Hough Modes, JOURNAL OF THE ATMOSPHERIC SCIENCES, 62, 2684–2702, https://doi.org/10.1016/j.jastp.2013.07.010, 2013.

Rodgers, C. D.: Inverse Methods for Atmospheric sounding Theory and Practice, World Scientific, https://doi.org/doi.org/10.1142/3171, 2000.

Sakazaki, T., Fujiwara, M., Zhang, X., Hagan, M., and Forbes, J.: Diurnal tides from the troposphere to the lower mesosphere as deduced from TIMED/SABER satellite data and six global reanalysis data sets, Journal of Geophysical Research, 117, https://doi.org/doi:10.1029/2011JD017117, 2012.

Sakazaki, T., Fujiwara, M., and Zhang, X.: Interpretation of the vertical structure and seasonal variation of the diurnal migrating tide from the troposphere to the lower mesosphere, Journal of Atmospheric and Solar-Terrestrial Physics, 105-106, https://doi.org/10.1016/j.jastp.2013.07.010, 2013.

Sakazaki, T., M. Shiotani, M., M. Suzuki, M., D. Kinnison, D., J. M. Zawodny, J. M., M. McHugh, M., and Walker, K. A.: Sunset–sunrise difference in solar occultation ozone measurements (SAGE II, HALOE, and ACE–FTS) and its relationship to tidal vertical winds, Atmospheric Chemistry and Physics, 15, 829–843, https://doi.org/10.1016/j.jastp.2013.07.010, 2015.

Sauvageat, E., Maillard Barras, E., Hoecke, K., Haefele, A., and Murk, A.: Harmonized retrieval of middle atmospheric ozone from two microwave radiometers in Switzerland, Atmospheric Measurement Techniques, 15, https://doi.org/10.5194/amt-15-6395-2022, 2022.

Sauvageat, E., Hoecke, K., Maillard Barras, E., Hou, S., Errera, Q., Haefele, A., and Murk, A.: Microwave radiometer observations of the ozone diurnal cycle and its short-term variability over Switzerland, Atmospheric Chemistry and Physics, 23, 7321–7345, https://doi.org/10.5194/acp-23-7321-2023, 2023.

Schranz, F., Fernandez, S., Kämpfer, N., and Palm, M.: Diurnal variation in middle-atmospheric ozone observed by ground-based microwave radiometry at Ny-Ålesund over 1 year, Atmospheric Chemistry and Physics, 18, 4113–4130, https://doi.org/10.5194/acp-18-4113-2018, 2018.

She, C.-Y., Krueger, D. A., Yuan, T., and Oberheide, J.: On the polarization relations of diurnal and semidiurnal tide in the mesopause region, Journal of Atmospheric and Solar-Terrestrial Physics, 142, 60–71, https://doi.org/https://doi.org/10.1016/j.jastp.2016.02.024, 2016a.

She, C.-Y., Krueger, D. A., Yuan, T., and Oberheide, J.: On the polarization relations of diurnal and semidiurnal tide in the mesopause region, Journal of Atmospheric and Solar-Terrestrial Physics, 142, 60 – 71, https://doi.org/https://doi.org/10.1016/j.jastp.2016.02.024, 2016b.

Stober, G., Matthias, V., Jacobi, C., Wilhelm, S., Hoeffner, J., and Chau, J. L.: Exceptionally strong summer-like zonal wind reversal in the upper mesosphere during winter 2015/16, Annales Geophysicae, 35, 711–720, https://doi.org/10.5194/angeo-35-711-2017, 2017.

Stober, G., Baumgarten, K., McCormack, J., Brown, P., and Czarnecki, J.: Comparative study between ground-based observations and NAVGEM-HA analysis data in the mesosphere and lower thermosphere region, Atmospheric Chemistry and Physics, 20, 11 979–12 010, https://doi.org/10.5194/acp-20-11979-2020, 2020a.

Stober, G., Baumgarten, K., McCormack, J. P., Brown, P., and Czarnecki, J.: Comparative study between ground-based observations and NAVGEM-HA analysis data in the mesosphere and lower thermosphere region, Atmospheric Chemistry and Physics, 20, 11 979–12 010, https://doi.org/10.5194/acp-20-11979-2020, 2020b.

Stober, G., Kuchar, A., Pokhotelov, D., Liu, H., Liu, H.-L., Schmidt, H., Jacobi, C., Baumgarten, K., Brown, P., Janches, D., Murphy, D., Kozlovsky, A., Lester, M., Belova, E., Kero, J., and Mitchell, N.: Interhemispheric differences of mesosphere–lower thermosphere winds and tides investigated from three whole-atmosphere models and meteor radar observations, Atmospheric Chemistry and Physics, 21, 13 855–13 902, https://doi.org/10.5194/acp-21-13855-2021, 2021.

Stähli, O., Murk, A., Kämpfer, N., Mätzler, C., and Eriksson, P.: Microwave radiometer to retrieve temperature profiles from the surface to the stratopause, Atmospheric Measurement Techniques, 6, 2477–2494, https://doi.org/10.5194/amt-6-2477-2013, 2013.

Vadas, S. L. and Becker, E.: Numerical Modeling of the Excitation, Propagation, and Dissipation of Primary and Secondary Gravity Waves during Wintertime at McMurdo Station in the Antarctic, Journal of Geophysical Research: Atmospheres, 123, 9326–9369, https://doi.org/10.1029/2017JD027974, 2018.

Vadas, S. L., Becker, E., Figueiredo, C., Bossert, K., Harding, B. J., and Gasque, L. C.: Primary and Secondary Gravity Waves and Large-Scale Wind Changes Generated by the Tonga Volcanic Eruption on 15 January 2022: Modeling and Comparison With ICON-MIGHTI Winds, Journal of Geophysical Research: Space Physics, 128, e2022JA031 138, https://doi.org/10.1029/2022JA031138, 2023.

van Caspel, W. E., Espy, P., Hibbins, R., Stober, G., Brown, P., Jacobi, C., and Kero, J.: A Case Study of the Solar and Lunar Semidiurnal Tide Response to the 2013 Sudden Stratospheric Warming, Journal of Geophysical Research: Space Physics, 128, e2023JA031 680, https://doi.org/https://doi.org/10.1029/2023JA031680, e2023JA031680 2023JA031680, 2023.

Waters, J., Froidevaux, L., Harwood, R., Jarnot, R., Pickett, H., Read, W., Siegel, P., Cofield, R., Filipiak, M., Flower, D., Holden, J., Lau, G., Livesey, N., Manney, G., Pumphrey, H., Santee, M., Wu, D., Cuddy, D., Lay, R., Loo, M., Perun, V., Schwartz, M., Stek, P., Thurstans, R., Boyles, M., Chandra, K., Chavez, M., Chen, G.-S., Chudasama, B., Dodge, R., Fuller, R., Girard, M., Jiang, J., Jiang, Y., Knosp, B., LaBelle, R., Lam, J., Lee, K., Miller, D., Oswald, J., Patel, N., Pukala, D., Quintero, O., Scaff, D., Van Snyder, W., Tope, M., Wagner, P., and Walch, M.: The Earth observing system microwave limb sounder (EOS MLS) on the aura Satellite, IEEE Transactions on Geoscience and Remote Sensing, 44, 1075–1092, https://doi.org/10.1109/TGRS.2006.873771, 2006.

Yuan, T., Schmidt, H., She, C. Y., Krueger, D. A., and Reising, S.: Seasonal variations of semidiurnal tidal perturbations in mesopause region temperature and zonal and meridional winds above Fort Collins, Colorado (40.6°N, 105.1°W), Journal of Geophysical Research: Atmospheres, 113, https://doi.org/https://doi.org/10.1029/2007JD009687, 2008.

Yuan, T., Stevens, M. H., Englert, C. R., and Immel, T. J.: Temperature Tides Across the Mid-Latitude Summer Turbopause Measured by a Sodium Lidar and MIGHTI/ICON, Journal of Geophysical Research: Atmospheres, 126, e2021JD035 321, https://doi.org/https://doi.org/10.1029/2021JD035321, e2021JD035321 2021JD035321, 2021.

Zeng, Z., Randel, W., Sokolovskiy, S., Deser, C., Kuo, Y., Hagan, M., Du, J., and Ward, W.: Detection of migrating diurnal tide in the tropical upper troposphere and lower stratosphere using the Challenging Minisatellite Payload radio occultation data, Journal of Geophysical Research, 113, 7579–7587, https://doi.org/doi:10.1029/2007JD008725, 2008.

Zhang, X., Forbes, J., and Hagan, M.: Longitudinal variation of tides in the MLT region: 1. Tides driven by tropospheric net radiative heating, Journal of Geophysical Research, 115, https://doi.org/doi:10.1029/2009JA014897, 2010.

Publication II

Atmos. Meas. Tech., 15, 2231–2249, 2022
https://doi.org/10.5194/amt-15-2231-2022

Atmospheric Measurement Techniques
Open Access

Continuous temperature soundings at the stratosphere and lower mesosphere with a ground-based radiometer considering the Zeeman effect

Witali Krochin[1,2], **Francisco Navas-Guzmán**[3,4,5], **David Kuhl**[6], **Axel Murk**[1,2], **and Gunter Stober**[1,2]

[1]Institute of Applied Physics, University of Bern, Hochschulstraße 6, 3012 Bern, Switzerland
[2]Oeschger Center for Climate Change Research, Hochschulstraße 4, 3012 Bern, Switzerland
[3]Applied Physics Department, University of Granada, 18071, Granada, Spain
[4]Andalusian Institute for Earth System Research (IISTA-CEAMA), 18006, Granada, Spain
[5]Federal Office of Meteorology and Climatology MeteoSwiss, Payerne, 1530, Switzerland
[6]Naval Research Laboratory, Washington DC, USA

Correspondence: Witali Krochin (witali.krochin@unibe.ch)

Received: 18 October 2021 – Discussion started: 10 December 2021
Revised: 15 February 2022 – Accepted: 3 March 2022 – Published: 13 April 2022

Abstract. Continuous temperature observations at the stratosphere and lower mesosphere are rare. Radiometry opens the possibility of observing microwave emissions from two oxygen lines to retrieve temperature profiles at all altitudes. In this study, we present observations performed with a temperature radiometer (TEMPERA) at the MeteoSwiss station at Payerne for the period from 2014 to 2017. We reanalyzed these observations with a recently developed and improved retrieval algorithm accounting for the Zeeman line splitting in the line center of both oxygen emission lines at 52.5424 and 53.0669 GHz. The new temperature retrievals were validated against MERRA2 reanalysis and the meteorological analysis NAVGEM-HA. The comparison confirmed that the new algorithm yields an increased measurement response up to an altitude of 53–55 km, which extends the altitude coverage by 8–10 km compared to previous retrievals without the Zeeman effect. Furthermore, we found correlation coefficients comparing the TEMPERA temperatures with MERRA2 and NAVGEM-HA for monthly mean profiles to be in the range of 0.8–0.96. In addition, mean temperature biases of 1 and −2 K were found between TEMPERA and both models (MERRA2 and NAVGEM-HA), respectively. We also identified systematic altitude-dependent cold and warm biases compared to both model data sets.

1 Introduction

Continuous and weather independent temperature soundings with high temporal and vertical resolution at the stratosphere and lower mesosphere are experimentally challenging but desirable to measure continuously the temperature at the stratosphere and lower mesosphere and to assess the intermittent behavior of atmospheric waves, which is important for understanding the day-to-day variability of the forcing from below in the ionosphere and thermosphere for space weather applications (Liu, 2016). Continuous observations of atmospheric temperature in the middle atmosphere are crucial to understand the chemistry (e.g., ozone) (Stolarski et al., 2012; Anderson et al., 2017) and to infer dynamics due to thermal wind balance (Matthias and Ern, 2018).

Satellite observations provide global coverage. SABER (Sounding of the Atmosphere using Broadband Emission Radiometry) on board the TIMED (Thermosphere-Ionosphere-Mesosphere-Energy and Dynamics) satellite measures temperatures from the troposphere up to mesosphere and lower thermosphere. The satellite has an orbit around Earth that permits to cover all local times within 60 d and, thus, provides only limited information on the short-term variability of tides and planetary waves. Furthermore, the latitudinal coverage changes in time due to the yaw cycle of the spacecraft (Russell et al., 1999; Remsberg et al., 2008; Rezac et al., 2015). The Microwave Limb Sounder (MLS) (Waters

et al., 2006) on the AURA satellite (Schoeberl et al., 2006) is on a sun-synchronous orbit and, thus, passes at fixed local times the same geographic locations making a data analysis of tides and their intermittency unfeasible, although MLS obtains temperatures from the stratosphere up to mesosphere covering all latitudes between 82° N and 82° S (Panka et al., 2021).

However, for low- and mid-latitudes SABER observations have been utilized to gain some insight into the climatological seasonal behavior of the migrating and nonmigrating diurnal and semidiurnal tides (Oberheide et al., 2011; Dhadly et al., 2018). Furthermore, these satellite observations have been proven to be valuable for data assimilation purposes into general circulation models (GCMs) such as the Navy Global Environment Model – High Altitude (NAVGEM-HA) (Eckermann et al., 2018). NAVGEM-HA temperature and wind fields show reasonable agreement to ground-based observations and the underlying day-to-day variability due to atmospheric tides and planetary waves (McCormack et al., 2017; Stober et al., 2020). Continuous ground-based temperature observations of the stratosphere and mesosphere are challenging and ambitious. There are only a few Rayleigh lidar measurements that are long enough to infer the tidal variability (Baumgarten et al., 2018; Baumgarten and Stober, 2019). This is mainly due to the fact that lidar observations are weather dependent, which essentially limits the measurement time and data availability. Furthermore, some of these lidars have only nighttime capabilities (Wing et al., 2018; Sica and Haefele, 2015), introducing additional ambiguities to infer mean temperatures and to assess the tidal variability.

Microwave radiometry offers a robust remote sensing technique that is almost weather independent to retrieve atmospheric temperature profiles at the stratosphere and lower mesosphere. A few years ago the University of Bern developed a temperature radiometer TEMPERA (temperature radiometer) to perform continuous soundings including the troposphere (Stähli et al., 2013; Navas-Guzmán et al., 2016). Recently, we developed a new retrieval algorithm due to updates in the radiative transfer model ARTS (Buehler et al., 2018; Eriksson et al., 2005) and revised Quantum numbers of HITRAN. The new retrieval algorithm accounts for the Zeeman effect at the line center in both emission lines at 52.5424 and 53.0669 GHz for routine temperature soundings. The advantage of the new retrieval algorithm is an increased altitude coverage. In this study, we present a validation of the new temperature profiles against MERRA2 and NAVGEM-HA for the location Payerne in Switzerland.

The article is structured as follows. Section 2 contains a brief description of the temperature radiometer TEMPERA, and Sect. 3 summarizes the Zeeman effect on the oxygen emission lines. MERRA2 and NAVGEM-HA data sets are presented in Sect. 4. The retrieval algorithm is outlined in Sect. 5. The TEMPERA temperature soundings and validation are shown in Sects. 6 and 7. The results are discussed in Sect. 8. Our conclusions are summarized in Sect. 9.

2 The TEMPERA radiometer

TEMPERA is a ground-based radiometer that was developed at the University of Bern. It measures atmospheric microwave radiation in the range of the oxygen emission complex at 50–60 GHz. For stratospheric temperature retrievals, two emission lines of the O_2 molecule are observed with a high-resolution digital FFT spectrometer at 52.5424 and 53.0669 GHz with a resolution of 30.5 kHz and a bandwidth of 960 MHz. The instrument was located at the aerological station in Payerne (46.82° N, 6.95° E, 491 m a.s.l.) and was directed westwards with an elevation angle of 60°. The antenna's half-beam-width (HPBW) is 4°. A more detailed technical description of the instrument can be found in Stähli et al. (2013). The measured spectra can be inverted into vertically resolved temperature profiles considering the pressure broadening of the spectral emission lines and their radiative transfer. Retrievals presented in this study make use of the Atmospheric Radiative Transfer Simulator (ARTS) (Buehler et al., 2018) and Qpack, the Matlab interface, for ARTS (Eriksson et al., 2005).

Already in 2015 first observations of the Zeeman effect in the line center for atmospheric Oxygen were reported using TEMPERA (Navas-Guzmán et al., 2015). In 2017 Navas-Guzmán et al. (2017) presented a comparison of almost 3 years of continuous TEMPERA observations with radiosondes, the Microwave Limb Sounder (MLS) on board the AURA spacecraft, and a Rayleigh lidar. These former studies inferred stratospheric temperature profiles up to an altitude of 40–45 km altitude blanking the line center to avoid a contamination of the temperature measurements due to Zeeman line broadening, which was not included at this time in the retrievals due to limitations in the available databases for the radiative transfer and quantum numbers in HITRAN that are required to account for the Zeeman effect in both oxygen lines (Larsson et al., 2019).

The observations presented in this study were performed with the laboratory prototype between 2014–2017 (Stähli et al., 2013). The receiver was upgraded in July 2015, which improved the overall performance of the instrument. The upgrade showed much better suppression of the standing waves. However, the new receiver introduced a small temperature offset in the calibrated and tropospheric corrected spectra of about 0.6 K.

3 The Zeeman effect

The Zeeman effect is a splitting of energy levels in emission and absorption processes due to an interaction of the molecules involved with a magnetic field. Atmospheric oxygen has a permanent magnetic moment that interacts with

Earth's magnetic field. Therefore an emission line, coming from rotational transitions, splits up into several lines. The degree of the line splitting depends on the strength of the magnetic field. Earth's magnetic field is rather weak, compared to stellar magnetic fields often analyzed in astronomy, which leads more to a broadening of the line center rather than a visible separation of individual Zeeman lines for each energy level. At mesospheric altitudes where the atmospheric pressure is already low, Zeeman broadening dominates over pressure broadening. Thus, temperature retrievals above 45 km are no longer feasible without taking into account the Zeeman effect. The change of the line shape due to the Earth's magnetic field for both frequencies is demonstrated in Fig. 1 and underlines the importance to include the magnetic field strength in the inversion. The new retrieval algorithm (Larsson et al., 2019) computes the Zeeman effect for both oxygen emission lines.

4 MERRA2 and NAVGEM-HA

Stratospheric and mesospheric temperatures obtained from the new retrieval algorithm are compared to MERRA2 reanalysis (Gelaro et al., 2017) and to the meteorological analysis NAVGEM-HA (Eckermann et al., 2018). The vertical temperature profiles are extracted for the location of Payerne considering the spatial averaging of the radiometer of about 250 km in diameter keeping the temporal resolution of the model fields of 3 h. Only the vertical resolution of the model data was interpolated to a fixed altitude grid with 2 km vertical resolution to simplify the comparisons. MERRA2 reanalysis utilizes a 3DVAR data assimilation (e.g., Gelaro et al., 2017, and references therein), which updates the state vector every 6 h. A detailed description of the hybrid 4-DVAR data assimilation in NAVGEM-HA is provided in Kuhl et al. (2013) and Eckermann et al. (2018). Similarly to MERRA2 the model state vector is updated every 6 h at the mesosphere.

For the comparison with the temperature observations from TEMPERA, the model data was analyzed at the geographic location of Payerne, and all grid points in a 250 km radius were averaged after they had been interpolated to a geometric vertical altitude grid. Daily mean temperatures and tidal amplitudes were derived by an adaptive spectral filter similarly to Pokhotelov et al. (2018), Baumgarten and Stober (2019), and Stober et al. (2020). The geopotential altitudes from NAVGEM-HA were converted into geometric heights (Stober et al., 2021). The temporal resolution of 3 h for both model data was kept.

5 Temperature retrieval with optimal estimation

5.1 Temperature retrievals

The inversion of the forward model is solved with ARTS 2.4 (Atmospheric Radiative Transfer Simulator; Buehler et al., 2018). The mathematical method follows the formalism from Rodgers (2000) and is briefly explained in this section.

Lets be $\boldsymbol{y}$ the measurement vector and $\boldsymbol{x}$ the state vector. In our case, $\boldsymbol{y}$ is the spectrum with n channels, and $\boldsymbol{x}$ is the temperature profile with m grid points. The forward model $F(\boldsymbol{x},\boldsymbol{b})$ maps the atmospheric state $\boldsymbol{x}$ to an idealized spectrum, this is usually written as

$$\boldsymbol{y} = F(\boldsymbol{x},\boldsymbol{b}) + \boldsymbol{\epsilon}. \tag{1}$$

The vector $\boldsymbol{b}$ contains some other parameters that are not included in the state vector, and $\boldsymbol{\epsilon}$ is the measurement error. The challenge is to find an inversion of the forward model $F(\boldsymbol{x},\boldsymbol{b})$ that presents an optimal estimate to the observations. The problem is that there is often no unique state $\boldsymbol{x}$ for a given measurement $\boldsymbol{y}$, which is classified as ill-posed. The inversion (also called retrieval) can be understood as a mapping R of the measurement vector $\boldsymbol{y}$ onto an optimal state vector $\hat{\boldsymbol{x}}$

$$\hat{\boldsymbol{x}} = R(\boldsymbol{y},\hat{b},\boldsymbol{x}_\mathrm{a},\boldsymbol{c}), \tag{2}$$

where $\hat{b}$ is the best estimate of the forward model parameters, $\boldsymbol{x}_\mathrm{a}$ denotes the a priori knowledge on the state vector, and $\boldsymbol{c}$ are some additional parameters. The optimal estimation method (OEM) provides the most probable solution $\hat{\boldsymbol{x}}$ in the context of the forward model. To apply this method information about the atmospheric state must be added. This information is included in the a priori state $\boldsymbol{x}_\mathrm{a}$, which is a preknowledge background state of the atmosphere. The choice of a certain a priori state is crucial and explained in Sect. 5.2. The error covariance of the a priori state is described in the a priori-covariance matrix $\mathbf{S}_\mathrm{a}$, and the measurements errors are described in the measurement-error covariance matrix $\mathbf{S}_\epsilon$. The optimal solution can be found by maximizing the probability $P(\boldsymbol{x}|\boldsymbol{y})$ of $\boldsymbol{x}$ under the condition that $\boldsymbol{y}$ is known, or in this case equivalent and most common, minimizing the cost function $J(\boldsymbol{x}) = -2\ln P(\boldsymbol{x}|\boldsymbol{y})$, which can be written in the form

$$J(\boldsymbol{x}) = \left[\boldsymbol{y} - F(\boldsymbol{x})\right]^T \mathbf{S}_\epsilon^{-1}\left[\boldsymbol{y} - F(\boldsymbol{x})\right] + \left[\boldsymbol{x} - \boldsymbol{x}_\mathrm{a}\right]^T \mathbf{S}_\mathrm{a}^{-1}\left[\boldsymbol{x} - \boldsymbol{x}_\mathrm{a}\right]. \tag{3}$$

The derivation of this cost function is based on Bayes' probability theorem, and the assumption that the probability distributions for the a priori covariance $\mathbf{S}_\mathrm{a}$ and for $\mathbf{S}_\epsilon$, as well as the posterior distribution $\boldsymbol{x}$, are Gaussian. The minimum of $J(\boldsymbol{x})$ is found by the following condition

$$\nabla_{\boldsymbol{x}} J(\boldsymbol{x}) = 0. \tag{4}$$

This equation is solved using several iterations making use of the Levenberg–Marquardt solver. Thus, successive iterations are computed from

$$\boldsymbol{x}_{i+1} = \boldsymbol{x}_i + \left(\mathbf{S}_\mathrm{a}^{-1} + \mathbf{K}_i^T \mathbf{S}_\epsilon^{-1}\mathbf{K}_i + \gamma D\right)^{-1} \times \left[\mathbf{K}_i^T \mathbf{S}_\epsilon^{-1}\left(\boldsymbol{y} - F(\boldsymbol{x})\right) - \mathbf{S}_\mathrm{a}^{-1}\left(\boldsymbol{x} - \boldsymbol{x}_\mathrm{a}\right)\right], \tag{5}$$

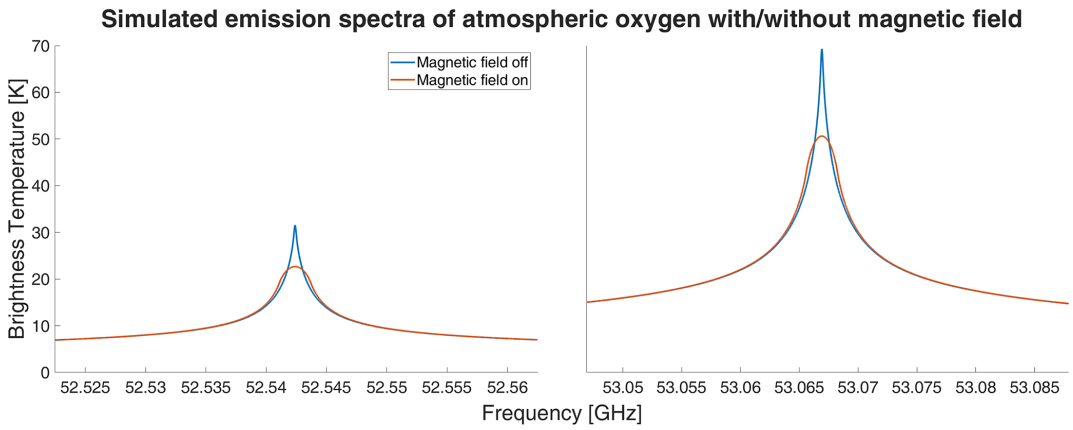

Figure 1. Illustration of the Zeeman effect on the line shape for mid-latitude observations on Earth. The line of sight is directed northwards with a zenith angle of 30°. The tropospheric effect on the brightness temperature has been removed.

where $\mathbf{K} = \partial F/\partial \boldsymbol{x}$ is called the weighting function. The a priori profile was used for the 0th step $\boldsymbol{x}_0 = \boldsymbol{x}_\mathrm{a}$. For $\gamma = 0$, this method is equivalent to the Gauss–Newton method. The damping term γD ensures the iteration to converge, even under poor conditions, making this method more robust but also slower compared to the Gauss–Newton scheme.

5.2 A priori atmospheric information

The retrieval algorithm is initialized using an ECMWF climatology. The climatology was obtained averaging daily mean ECMWF data between 2014–2017 smoothed by a 30 d running window. The resulting seasonal a priori temperature behavior is shown in Fig. 2. Based on this climatological mean atmospheric state, the radiative transfer equations are solved for several molecular species, e.g., O_2, H_2O, O_3, and N_2. However, not all of them contribute significantly to the radiation intensity between 50–60 GHz. Spectroscopic data for O_2 was taken from the HITRAN database (Gordon et al., 2017). These quantum numbers are necessary to account for the Zeeman effect in the radiative transfer model. The magnetic field strength for the location of Bern at the altitude of the mesosphere is taken from ARTS.

5.3 Tropospheric correction

The new retrieval still incorporates a tropospheric correction. The received signal is the integral along the line of sight of all emitted microwave radiation, also including tropospheric altitudes. However, the main goal of the new retrieval is the improvement of the stratospheric and mesospheric temperature soundings, which requires a higher frequency resolution in the line center at the cost of the much broader tropospheric signal, which still dominates the overall brightness temperature in the line wings and the center. Therefore, the tropospheric signal is separated and removed from the stratospheric and mesospheric intensities by implementing a tropospheric correction. The method is based on the assumption that the troposphere can be approximated by a homogeneous layer with a weighted mean brightness temperature

$$T_\mathrm{m}(\nu) = \frac{\int_{z_1}^{z_\mathrm{t}} T(z,\nu)\alpha(z,\nu)e^{-\tau(z,\nu)}\mathrm{d}z}{\int_{z1}^{z_\mathrm{t}} \alpha(z,\nu)e^{-\tau(z,\nu)}\mathrm{d}z}. \tag{6}$$

Where the integral is taken from the ground z_1 to the top of the troposphere z_t, ν is the frequency, α denotes the absorbing coefficient, τ the opacity, and $T(z)$ is the physical thermal equilibrium temperature. The weighted mean temperature is used to estimate a mean tropospheric opacity $\tau_\mathrm{trop}(\nu)$. After estimating all these parameters the brightness temperature on the top of the troposphere is determined by solving the radiative transfer equation. The integrals above are dominated by the lowest altitudes because α is pressure dependent and decreases quickly with increasing altitude. Assuming a linear relationship between the surface temperature T_s and T_m leads to

$$T_\mathrm{m} = aT_\mathrm{s} + b. \tag{7}$$

To determine the coefficients a and b radiosonde measurements at Payerne launched from MeteoSwiss were used. The coefficients for the TEMPERA frequency range are found in Navas-Guzmán et al. (2015) and take values for $a = 0.8159$ and $b = 47.211$. Further details about the method are described in Ingold and Kämpfer (1998). All previous studies based on TEMPERA have applied such a tropospheric correction (Stähli et al., 2013; Navas-Guzmán et al., 2015, 2017). Although, hitherto observations with TEMPERA indicate that the tropospheric correction seems to work well, it represents a coarse approximation that is worth further investigation for various weather conditions. In particular, tropospheric inversion layers might have a more critical impact on the mean tropospheric opacity $\tau_\mathrm{trop}(\nu)$.

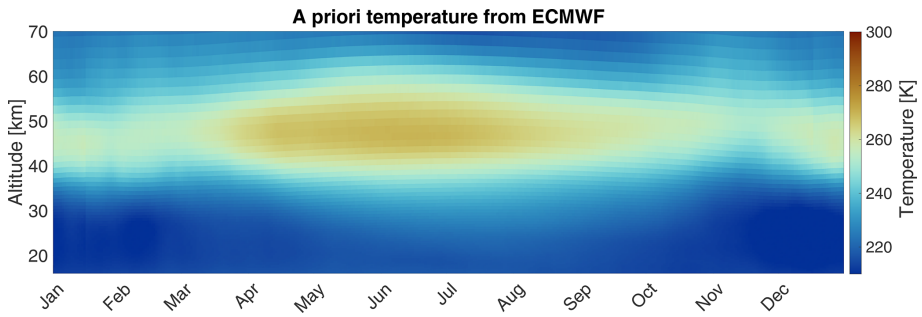

Figure 2. Averaged ECMWF temperature profiles for the geolocation of Payerne (CH). A moving window of 31 d was used for smoothing after the average over the 4 years 2014–2017 was taken.

5.4 Measurement errors

Statistical measurement errors arise from two sources. The first error source is the receiver noise and the second one is atmospheric noise, which originates from fluctuations and turbulent processes in the field of view. Typically, receiver and atmospheric noise are considered as zero-mean Gaussian random processes. Both together, measurement-noise-variance and atmospheric-noise-variance contribute to the measurement-error covariance (Rodgers, 2000). Other systematic errors, such as a systematic frequency shift in the channels, are often hard to identify and, thus, are not taken into account.

In the following, we briefly discuss how the measurement errors are obtained. Considering $y_{ij} = y(\nu_i, t_j)$ as the measurement matrix, ν_i is the frequency of channel number i, and t_j is the time of spectrum number j in a time series with N spectra. The channels are assumed to be uncorrelated with the variance σ_i^2. The final measurement spectrum is the mean of y_{ij} over time $\overline{y}_i = \frac{1}{N}\sum_j y_{ij}$, so that the variance $\overline{\sigma}_i^2$ of $\overline{y}_i$ is related to σ_i^2 as

$$\overline{\sigma}_i^2 = \frac{1}{N}\sigma_i^2. \tag{8}$$

From this, one can calculate $\overline{\sigma}_i^2$ by taking the sample variance of $\overline{y}_i$. A more stable method is to consider the variance $\sigma_{\Delta i}^2$ of the differences $\Delta y_{ij} = y_{ij} - y_{i+1j}$, which is related to σ_i as $\sigma_{\Delta i}^2 = 2\sigma_i^2$ and, hence,

$$\overline{\sigma}_i^2 = \frac{1}{2N}\sigma_{\Delta i}^2. \tag{9}$$

Assuming that all channels are uncorrelated, the measurement error covariance matrix $\mathbf{S}_\epsilon$ takes a diagonal form with entries

$$(\mathbf{S}_\epsilon)_{ii} = \overline{\sigma}_i^2. \tag{10}$$

5.5 A priori covariance

The a priori covariance determines the uncertainty of the a priori state. For temperature profiles, one usually chooses a constant value for each grid point and a with distance exponentially decreasing correlation. However, varying the a priori covariance with altitude can improve the retrieval significantly with respect to the measurement response obtained. Since the platform altitude was set at 12 km (see tropospheric correction), lower altitudes have to be excluded from the inversion. For this purpose, the a priori covariance $\sigma_\mathrm{a}(z_i)$ was set to 0.1 K up to 12 km (z_i is the altitude at the ith grid point). Above the virtual platform altitude, the a priori covariance increases linearly with altitude to a value of 6 K at 50 km, and higher up in the atmosphere, the value increases to 8 K at 60 km and beyond that height, the covariance reaches 12 K at 70 km altitude. A linear increase with altitude avoids numerical oscillations due to sharp "jumps" in the profile, which would occur when a step function is implemented instead. The larger values at the upper altitudes of the retrieval domain are beneficial to optimize the information content of the measurement vector. However, we have to note that this method tends to be more prone to generate some unwanted numerical effects such as spurious oscillations. On the other hand, a smaller choice of the a priori covariance for these altitudes forces the retrieval to stay close to the a priori state, and, thus, information content would be lost. The values described above were optimized through empirical tests prioritizing an optimal balance between numerical stability and high sensitivity of the solution at the stratosphere and lower mesosphere. Considering these aspects, the covariance matrix $\mathbf{S}_\mathrm{a}$ takes the form

$$(\mathbf{S}_\mathrm{a})_{ij} = \sigma_\mathrm{a}(z_i)\sigma_\mathrm{a}(z_j)\exp\left(-\frac{|z_i - z_j|}{h}\right), \tag{11}$$

where h is the correlation length, which was set to be $h = 1$ km.

5.6 Other sources of uncertainty

The advantage of the optimal estimation implementation of the retrieval is the possibility to derive the information gain from the observations (Shannon, 1948; Shannon and Weaver, 1949). An important quantity, which is widely used for error

analysis in information theory, is the gain matrix given by

$$\mathbf{G}_y = \frac{\partial R}{\partial \boldsymbol{y}}. \tag{12}$$

The gain matrix can be interpreted as the sensitivity of the retrieval R to the measurement $\boldsymbol{y}$. Furthermore, the gain matrix can be used to define the averaging kernel matrix by

$$\mathbf{A} = \mathbf{G}_y \mathbf{K}_x. \tag{13}$$

According to Rodgers (2000) the averaging kernel is the sensitivity of the retrieval to the (unknown) true state. The rows of $\mathbf{A}$ provide correlations and a distinct maximum, which defines the altitude of maximum measurement response for a vertical grid point. Their half-width can be regarded as a measure of the effective vertical resolution. The measurement response vector $\boldsymbol{mr}$ is defined as (Rodgers, 2000; Eriksson et al., 2005)

$$\boldsymbol{mr}_i = \frac{\mathbf{A}_i \boldsymbol{x}_\mathrm{a}}{\boldsymbol{x}_{ai}}, \tag{14}$$

where $\mathbf{A}_i$ is row i of the averaging kernel matrix, and $\boldsymbol{x}_{ai}$ is the ith entry of the a priori state. For an ideal retrieval, the value of $\boldsymbol{mr}$ equals 1. The lower the measurement response, the more a priori information is included in the solution. Measurement responses below 0.6 indicate that the retrieved state depends mostly on our a priori information.

Weighting the measurement-error covariance matrix $\mathbf{S}_\epsilon$ with $\mathbf{G}_y$ one obtains the retrieval noise (or observational error) covariance matrix

$$\mathbf{S}_\mathrm{o} = \mathbf{G}_y \mathbf{S}_\epsilon \mathbf{G}_y^\mathsf{T}. \tag{15}$$

Another indicator is the modeling error $\boldsymbol{s}_\mathrm{M}$, obtained by weighting the retrieval residuals with $\mathbf{G}_y$

$$\boldsymbol{s}_\mathrm{M} = \mathbf{G}\left[\boldsymbol{y} - F(\boldsymbol{x}, \boldsymbol{b})\right]. \tag{16}$$

In theory, this vector should be evaluated at the true state $\boldsymbol{x}$ and $\boldsymbol{b}$, which is, of course, not known. Evaluating this quantity at the retrieved state $\hat{\boldsymbol{x}}$ instead will lead to slightly increased values.

As an example, a set of quality control parameters are illustrated in Fig. 3. The modeling error, which is directly related to the forward model residuum, leads to the conclusion that the retrieved profile is underestimated around 30–40 km and overestimated around 45–55 km by about 2 K.

The AVK up to 40 km shows the expected and already documented behavior (Stähli et al., 2013; Navas-Guzmán et al., 2017), where the best performance is reached at an altitude around 30 km. From 40 km upwards the Zeeman calculation leads to a second but lower peak between 40–50 km. The last peak between 60–65 km is due to the increased a priori error in this region. This behavior is also reflected in the measurement response. As a rule of thumb, the altitude range of a retrieved profile is usually defined as the region where the measurement response is above 0.8, which can be found at altitudes between 22–53 km.

6 Temperature retrievals including the Zeeman effect

The revised temperature retrieval was applied to data collected with TEMPERA in Payerne between 2014–2017. The main differences compared to previous work by Navas-Guzmán et al. (2015, 2017) is the inclusion of the Zeeman effect in the center of the oxygen emission lines and the use of updated a priori and measurement covariances to improve numerical stability and the retrieval sensitivity. Furthermore, there is the new retrieval emphasis on stratospheric and mesospheric altitudes to observe tidal waves and their temporal intermittency. The temporal resolution was slightly decreased from 2 h (Navas-Guzmán et al., 2017) to about 2.5 h. The increased integration time resulted in more robust temperature estimates. On average, we obtained 8–9 integrated spectra per day. Each integrated spectra consists of about 150–160 individual atmospheric soundings and spectra obtained from atmospheric observations lasting 0.5 s (mirror pointing towards sky) using the stratospheric and mesospheric measurement mode with the high-resolution FFT-spectrometer.

We also implemented a quality control before the averaged spectra is computed. Some spectra are removed from the averaging due to increased atmospheric noise, mainly caused by tropospheric weather, e.g., strong precipitation or temporary technical issues with the instrument. On average, about 3.6 % of the integrated spectra are removed from the analysis within the 4 years of observations.

Figure 4 shows temperature soundings for TEMPERA, MERRA2, and NAVGEM-HA for the whole period (2014–2017). The seasonal pattern indicates higher temperatures at all retrieved altitudes during the summer season and lower temperatures at the stratosphere during the winter months. The winter months are characterized by an increased planetary wave activity and the frequent occurrence of sudden-stratospheric-warmings (Scherhag, 1952; Matsuno, 1971; Limpasuvan et al., 2016; Matthias et al., 2013). Also, the spring transition is clearly distinguishable from the temperature data (Matthias et al., 2021).

First of all, we investigated how critically the final retrieved temperatures depend on our a priori data. Figure 5 shows a difference between TEMPERA and the ECMWF climatology. The larger the differences at some altitudes, the less critical is the choice of the a priori data, which indicates that at these levels, the solution is only given by the measurements. Furthermore, from 60 km and higher up, the colors become brighter, which points out that these heights depend more on the a priori information. This is also reflected by the lower measurement response and is consistent with the averaging kernels presented in Fig. 3 for these altitudes.

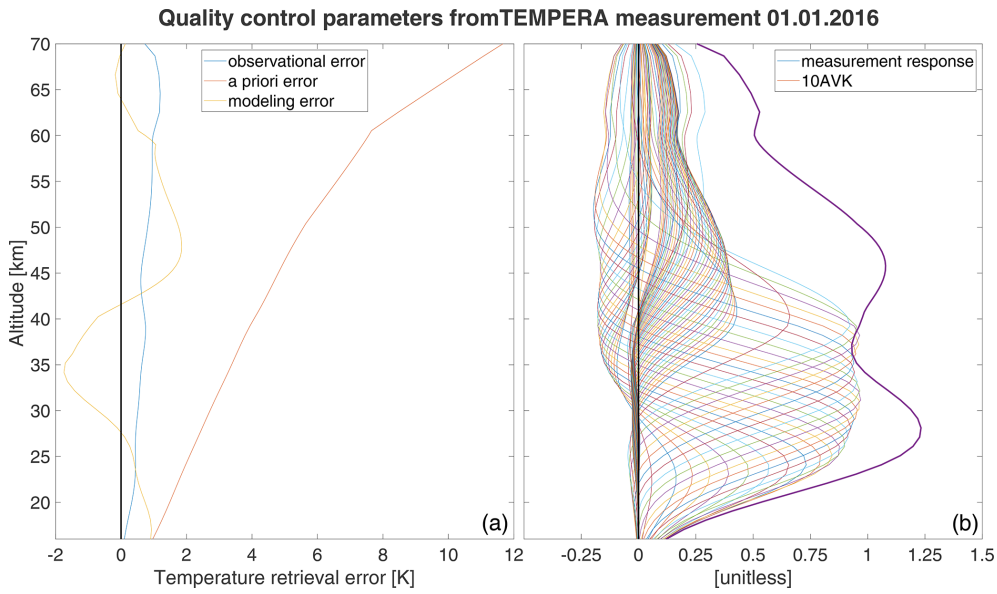

Figure 3. Different error components from the retrieval method **(a)**. Units of errors are always Kelvin here. Measurement response (MR) and averaging kernel matrix (AVK) **(b)**. The AVK is multiplied by a factor of 10 for a facilitated comparison with the MR.

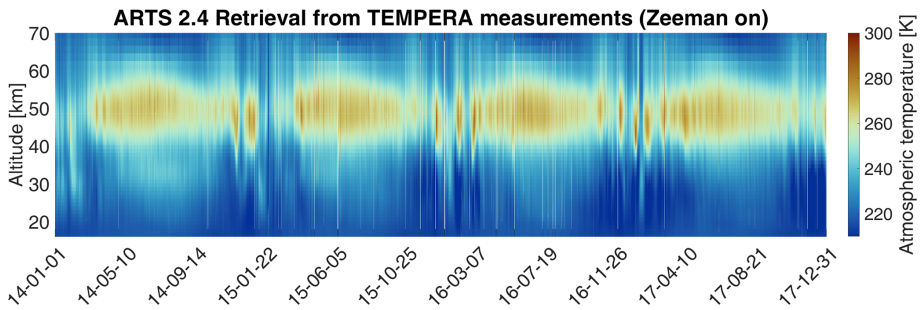

Figure 4. Continuous atmospheric temperature profiles, retrieved from TEMPERA measurements in comparison to MERRA2 and NAVGEM-HA data for the years 2014–2017 over the geolocation of Bern (CH). The altitude range is 53 km. Above 53 km the retrieved profiles are dominated by the a priori profiles.

7 Comparison of temperature retrievals to MERRA2 and NAVGEM-HA

The performance of the new temperature retrievals is assessed by comparing our observations to state-of-art reanalysis data from MERRA2 and the meteorological analysis of NAVGEM-HA. Therefore, we compute correlation coefficients based on monthly medians and corresponding variances for all data sets. These monthly medians essentially remove all atmospheric waves on short timescales, such as tides and gravity waves, from the model fields as well as the temperature soundings. However, we have to note that atmospheric time series cannot necessarily be considered as Gaussian random variables. Often, the atmospheric natural variability exceeds the statistical uncertainty of the observations (e.g., Stober et al., 2017, see Fig. 3), and, thus, an overestimation or inflation of the correlation coefficients is the result. Assuming a linear regression model between the TEMPERA profiles $T_{\mathrm{TMP}}(z)$ and the profile for cross comparison $T_{\mathrm{CCP}}(z)$

$$T_{\mathrm{TMP}}(z) = mT_{\mathrm{CCP}}(z) + q, \tag{17}$$

the coefficients m, q were determined through linear regression. For two statistically identical data sets, we would obtain $m = 1$, and $q = 0$. The coefficient q gives an absolute offset of the two profiles, while a slope m above 1 indicates a higher sensibility of the profile $T_{\mathrm{TMP}}(z)$ (see Sect. 8) relative to the compared profile $T_{\mathrm{CCP}}(z)$. This method gives a quantitative estimation of the absolute offset but provides no information as to at which altitude this occurs. In Figs. 6 and 7 we show linear correlation coefficients of the median monthly temperature profiles for the year 2016 for TEMPERA vs MERRA2 and TEMPERA vs. NAVGEM-HA, respectively. The error bars correspond to the temperature variance for each data set. The correlations are estimated after subtracting the median temperature from each profile, which was estimated to

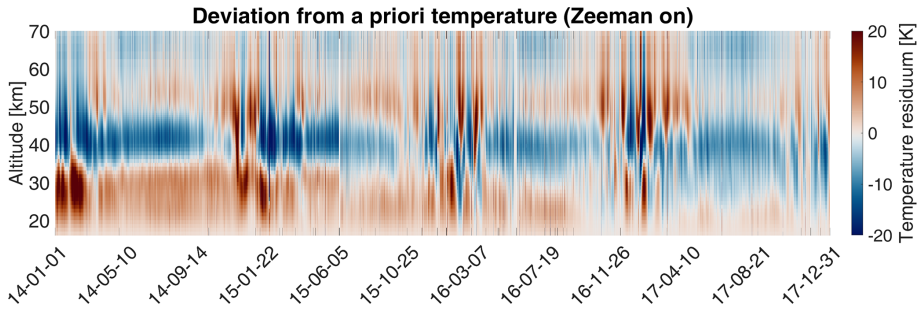

Figure 5. Absolute differences between retrieved TEMPERA profiles and a priori profiles. Reddish regions indicate higher values for the retrieved quantities in comparison to the a priori ones. Bluish areas support colder temperatures concerning the a priori state.

be approximately 250 K

$$T_{\mathrm{TMP}} \rightarrow T_{\mathrm{TMP}} - 250\,\mathrm{K}, \tag{18}$$

$$T_{\mathrm{CCP}} \rightarrow T_{\mathrm{CCP}} - 250\,\mathrm{K}. \tag{19}$$

The shift of the temperature profile to lower values is necessary because the linear regression would otherwise falsely give good values for m. The other years can be found in Appendix A.

The monthly median temperature correlation coefficients exhibit a range between 0.93–0.98 for the comparison with MERRA2 and about 0.94–0.98 for NAVGEM-HA. The highest correlation coefficients are achieved during the summer months from April to September and in December. The lowest correlations are found during January and February and are the result of the increased planetary wave activity and the more variable polar vortex dynamics in 2016 (Matthias et al., 2016; Stober et al., 2017; Matthias and Ern, 2018). NAVGEM-HA indicates a similar seasonal behavior for the year 2016 and occasionally has minimal larger correlations. The mean temperature bias $|q|$ between the new TEMPERA retrievals and MERRA2 is smaller than 1.5 K. The temperature bias relative to NAVGEM-HA takes values between -0.1 up to -2.2 K (excluding the exceptional January 2016). The slopes m of the linear regression with MERRA2 and NAVGEM-HA are in a range between $m = 0.8$ and $m = 0.96$, indicating a lower sensitivity of TEMPERA to the atmospheric variability relative to the model fields. We also estimated yearly median altitude-resolved Pearson correlation coefficients. These are shown in Fig. 8. It is remarkable that the correlation coefficients for retrievals with activated Zeeman effect (upper panels) are most of the time larger than 0.8 and often exceed 0.9 for MERRA2 and NAVGEM-HA, respectively. Furthermore, the seasonal correlation coefficients reveal a sharp drop off at about 53–55 km, which appears to be the limiting altitude for TEMPERA temperatures and the new retrieval. Above this altitude, the solutions of the retrieval are dominated by a priori information. The comparison also indicates that NAVGEM-HA exhibit a slightly higher correlation concerning TEMPERA temperatures relative to MERRA2.

In addition, Fig. 8 (lower panels) show yearly correlation coefficients for TEMPERA retrievals with deactivated Zeeman effect. For calculations without the Zeeman effect, usually the line center is blanked and only the line wings are used. This approach results in retrievals with a limited upper altitude of about 45 km. Above this altitude, the retrieved profile quickly converges towards the a priori profile, because due to the missing line center the measurements do not provide any information beyond these heights. Besides some small effects, the profiles with activated and deactivated Zeeman effect would match up to this altitude. The plots with Zeeman on/off are shown in Figs. 8 and 9. However, we retrieved temperatures keeping the line center but turned off the Zeeman effect by setting the magnetic field essentially to zero to investigate the impact of the Zeeman broadening. Correlation coefficients for retrievals with deactivated Zeeman effect are lower than 0.9 everywhere and even lower than 0.8 for most of the altitudes. This underlines that accounting for the Zeeman effect has not only an impact on the upper altitudes. Due to the energy conservation in the radiative transfer, almost all altitudes are affected with decreasing impact for the lower altitudes.

Another important aspect to compare are altitude-time-dependent systematic differences between MERRA2 and NAVGEM-HA. Therefore, we compute altitude time residuals by subtracting MERRA2 and NAVGEM-HA from the temperatures observed by TEMPERA. Figure 9 shows the resulting temperature residuals for both model data sets and the complete time series. Similarly to the Pearson correlation coefficients MERRA2 and NAVGEM-HA reflect the same characteristic systematic differences. Furthermore, the installation and upgrade of the receiver around 5 June 2015 is clearly visible in the residual comparison. The new receiver reduced the standing wave contamination in the line wings and, thus, mostly affected the data quality below 40 km altitude.

In addition, Fig. 9 shows difference plots for TEMPERA retrievals with deactivated Zeeman effect and the full line center (the same as Fig. 8).

The vertical residuals show some systematic and altitude-dependent differences. Below 35 km there is a tendency

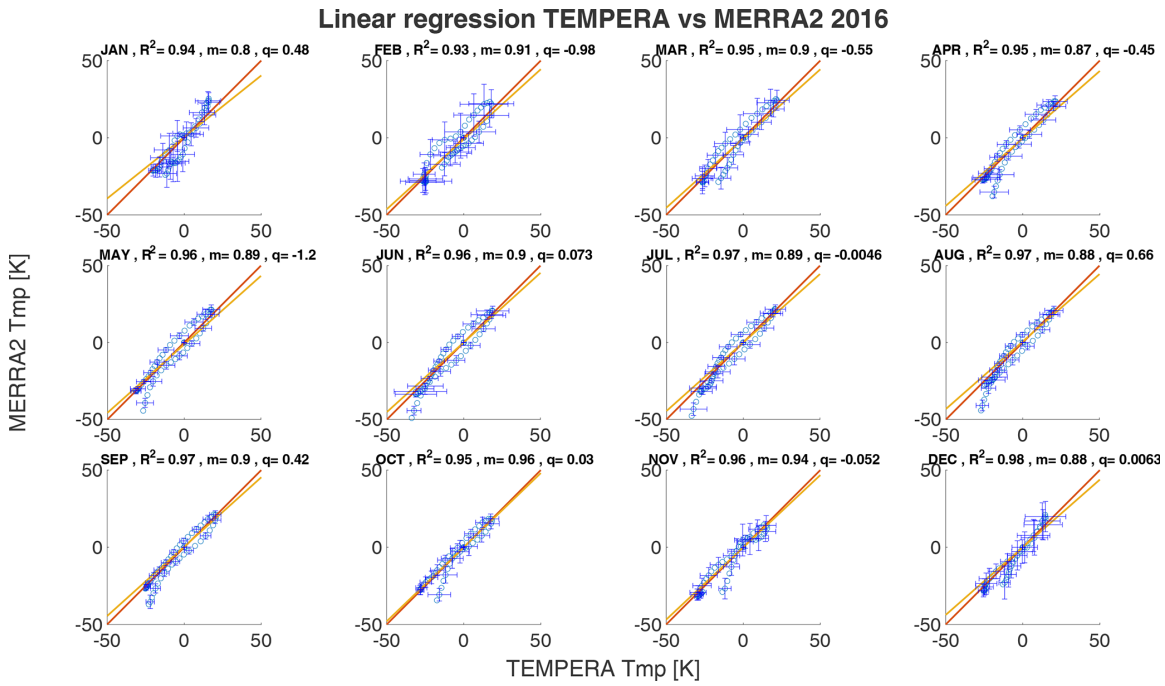

Figure 6. Linear regression of TEMPERA against MERRA2 temperatures.

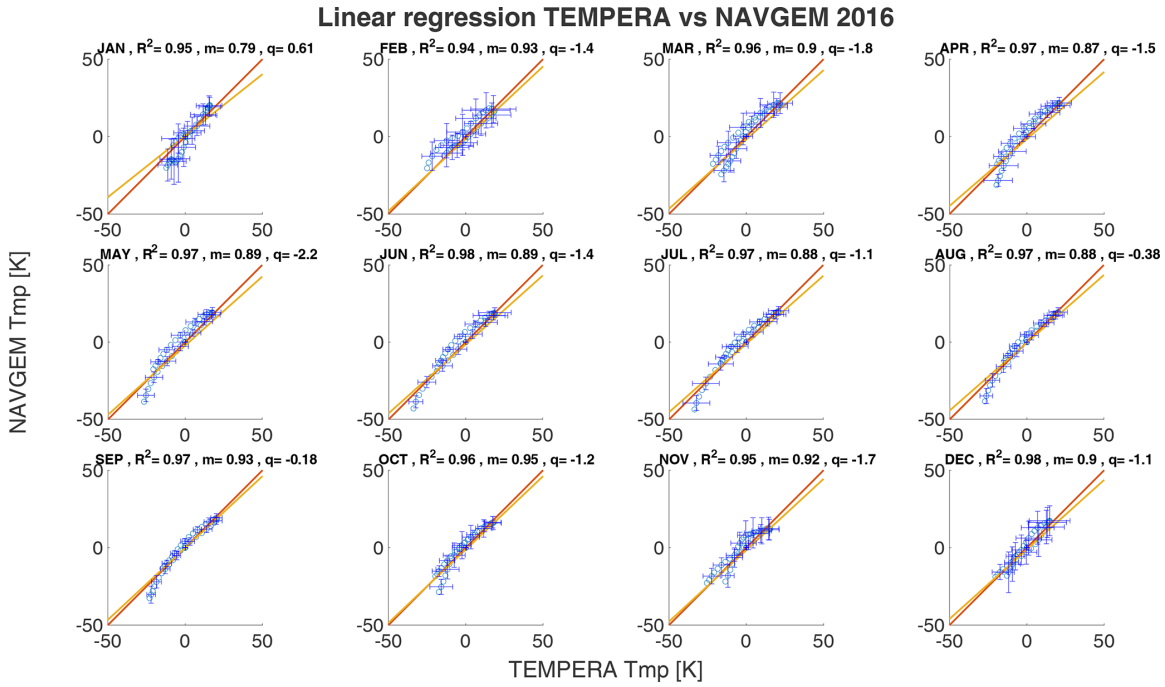

Figure 7. Linear regression of TEMPERA against NAVGEM-HA temperatures.

for TEMPERA to show warmer temperatures compared to MERRA2 and NVAGEM-HA. Between 35–50, the models seem to have a warm bias compared to the radiometric temperature sounding. Above 53 km MERRA2 indicates a clear tendency to underestimate the temperatures relative to TEMPERA, whereas NAVGEM-HA shows a more variable vertical structure of the residual temperature exhibiting times and altitudes with warmer, but also periods and heights with colder temperatures. It is also evident from the residual comparison that during the winter season the increased planetary

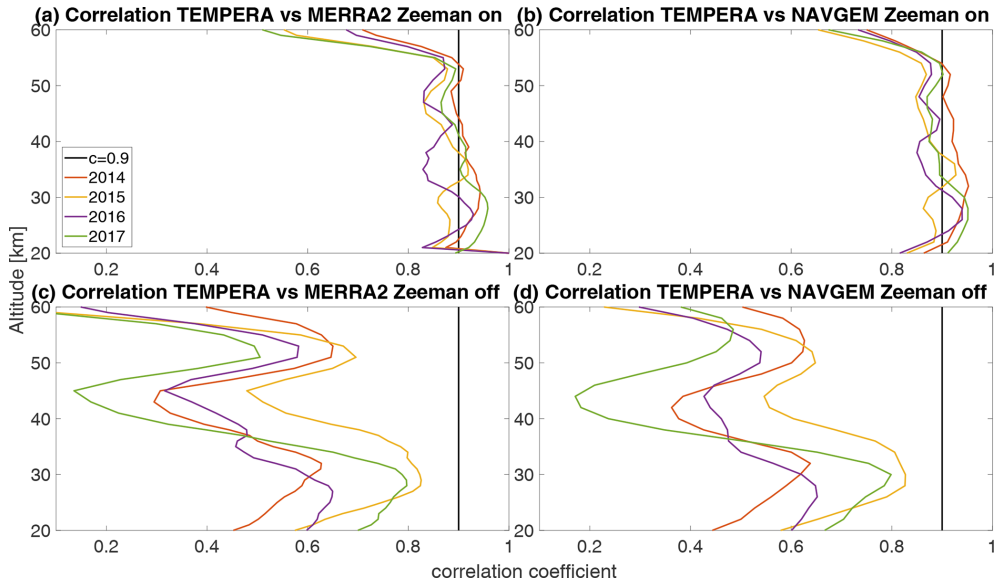

Figure 8. Correlation coefficients over altitude between TEMPERA and MERRA2 data **(a, c)**, and TEMPERA and NAVGEM-HA **(b, d)** data. Calculations were performed with activated Zeeman effect **(a, b)** and deactivated Zeeman effect but with the full line center included **(c, d)**.

wave activity leads to larger differences between our temperature observations and the model data.

The plots with Zeeman effect turned off shows cold biases of 20 K above 45 km and hot biases around 5–20 K below. The cold bias is due to an overestimation of the pressure broadening since the Zeeman broadening is treated as pressure broadening when Zeeman calculations are deactivated. Hot biases occur mainly as an effect of compensation since the total radiation intensity along the beam path has to be preserved.

Finally, Fig. 10 presents a comparison of the 3-hourly resolved temperature time series at 50 km altitude. The comparison underlines that the TEMPERA observations still exhibit such a high measurement response at this height that the temperature amplitude and phase of planetary waves is well captured in comparison to MERRA2 and NAVGEM-HA. There is also a characteristic diurnal tidal oscillation in MERRA2, NAVGEM-HA, and the radiometer data visible. Overall the measurements from TEMPERA and the MERRA2 and NAVGEM-HA temperature agree within a few kelvin (5–10 K). Furthermore, the comparison supports that it is feasible to obtain tidal information from the TEMPERA temperature soundings on a daily basis.

8 Discussion

The main goal of the new retrieval algorithm was the implementation of the Zeeman effect in the temperature retrievals, which was not available in previous versions of the radiative transfer model for both oxygen emission lines. Thus, the new temperature retrieval yields an increased measurement response and altitude coverage up to 55 km compared to former TEMPERA observations where 45–48 km seemed to be the limiting altitude (Stähli et al., 2013; Navas-Guzmán et al., 2015). Furthermore, the new retrieval was optimized concerning the a priori state vector and covariances, which also led to some improvement at the upper stratosphere and lower mesospheric heights. TEMPERA observations offer the possibility to perform continuous temperature measurements at altitudes between 16–55 km.

While implementing a new retrieval method it is always necessary to achieve a balance between numerical stability and sensitivity to the atmospheric state. A small a priori covariance or a too large measurement error results in low sensitivity of the retrieval, although such a retrieval is stable concerning numerical oscillations. On the other hand, such a retrieval likely underestimates the natural or true variability of the estimated parameters, and the solution would stay tied to the a priori state. A large a priori covariance improves the sensitivity of the retrieval, but at the cost of numerical oscillations, which can dominate the whole retrieved profile. The new retrieval is well balanced to achieve the highest possible sensitivity at 50 km while avoiding numerical instabilities and oscillations.

Statistical measurement errors are known with high precision; the final error on the temperature profile is rather a measure of the information content rather than an error in the classical sense. The state-of-the-art method is a cross comparison of different and independent data sets. Calculations of correlation coefficients or goodness-of-fit values (R^2) in a linear regression always requires some information about the uncertainty of the data set. Since this information is missed, usually the sample variation is taken instead. This approach should, however, be used with appropriate caution because

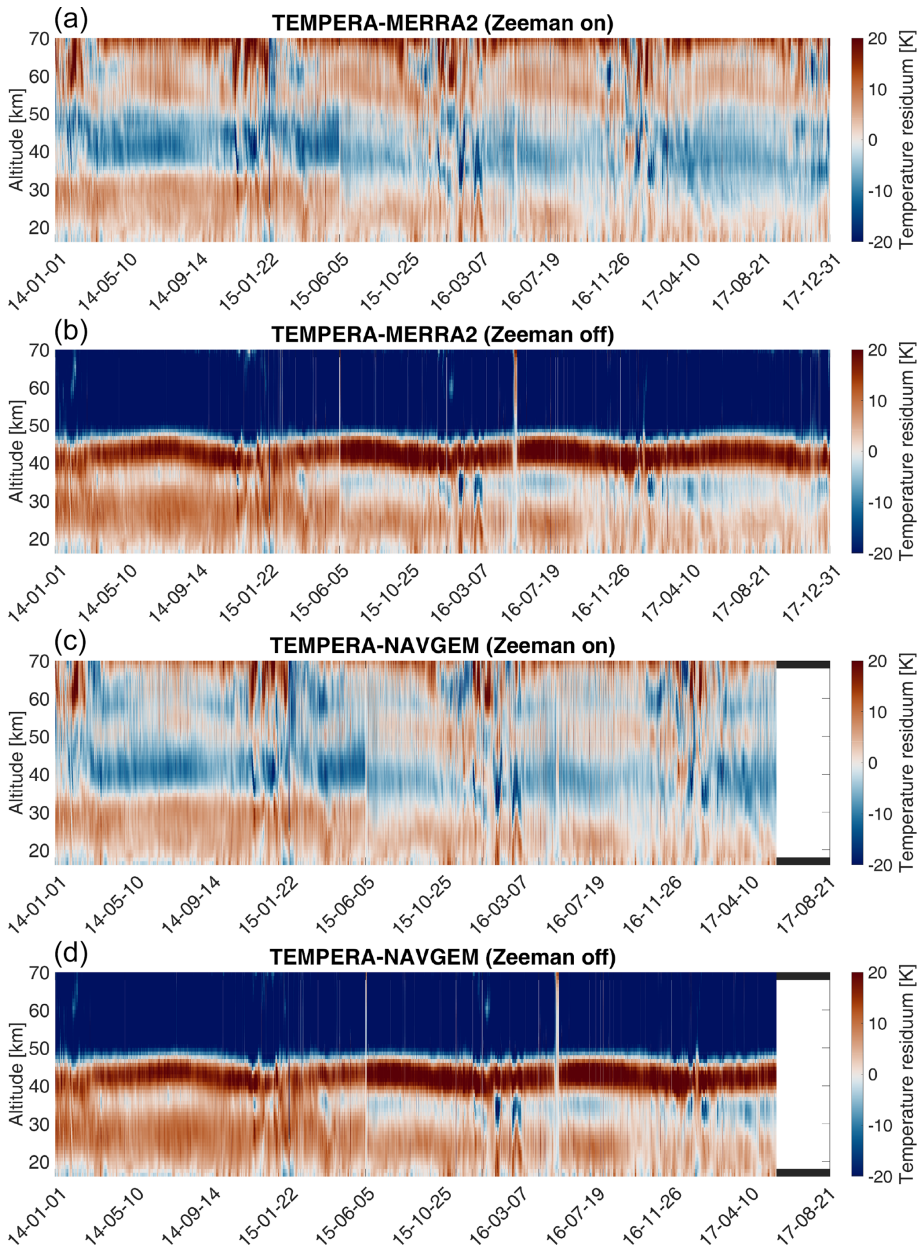

Figure 9. Absolute differences between TEMPERA and MERRA2 **(a, b)**, and NAVGEM-HA **(c, d)**. Calculations with Zeeman off were performed including the line center in order to show the influence of the Zeeman broadening on the retrieved profile. Red regions indicates higher values of TEMPERA.

atmospheric profiles or time series are not random variables, and natural variations could be bigger than the actual errors. This circumstance leads directly to an overestimation of the correlation coefficients of two compared data sets.

Continuous temperature observations at the stratosphere and mesosphere are rare. Lidars are often limited by the tropospheric weather conditions, and only a few long observations are available (e.g., Stober et al., 2017; Baumgarten and Stober, 2019; Eixmann et al., 2020). However, these lidar studies underline that continuous temperature observations are essential to investigate atmospheric wave and their intermittency covering periods from gravity waves, tides, and planetary waves at the source region, to research wave–wave interactions.

Satellite observations from MLS or SABER provide neither the temporal nor the spatial resolution to resolve all atmospheric waves and their intermittent behavior. Due to the spacecraft orbit and viewing geometry very often only one measurement per day is available for a specific geographic location. However, satellite observations are a key

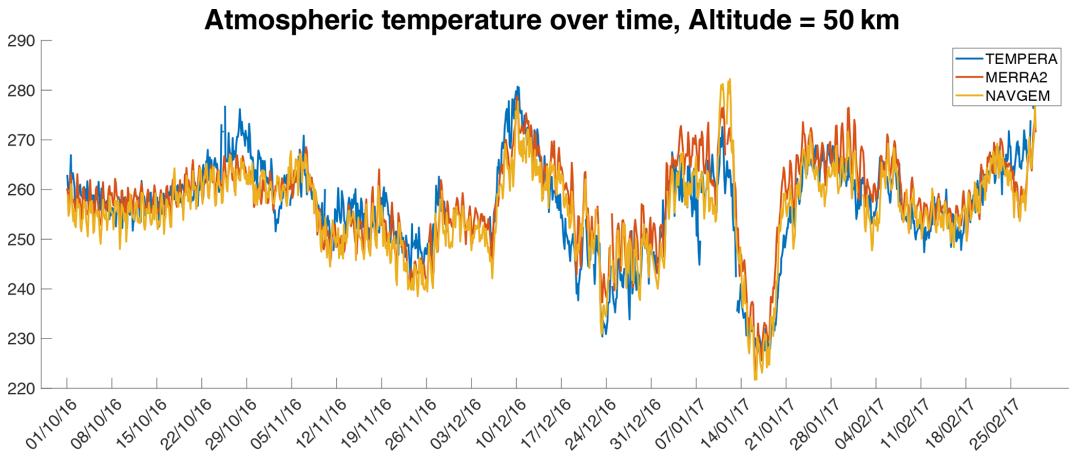

Figure 10. Comparison of TEMPERA, MERRA2, and NAVGEM temperatures on a larger timescale (months), at which planetary waves occur, and a smaller timescale (days), which is the timescale of atmospheric tides.

information source for data assimilation into MERRA2 and NAVGEM-HA at the stratosphere and mesosphere for the temperature and dynamical fields (Gelaro et al., 2017; Kuhl et al., 2013; Eckermann et al., 2018). Other meteorological observations such as radiosondes reach only altitudes of about 28–38 km and, thus, provide only temperature, wind, or chemical information at the lower and middle stratosphere. Furthermore, radiosondes are launched every 12 h, or at some stations occasionally every 6 h, which limits their impact to capture atmospheric tides at the stratosphere.

Navas-Guzmán et al. (2017) has already performed an intercomparison of the TEMPERA observations with MLS satellite data, lidar, and radiosondes, as well as WACCM simulations. The Pearson correlation coefficients obtained were between 0.9 to 0.94 for a 3-year-long time series and were interpolated to match the different temporal resolutions and emphasized altitudes between 22–43 km where the measurement response was larger than 0.8. In this study, we have already achieved this degree of correlation using median monthly profiles and for yearly observations for the altitude range from 20–55 km. However, the comparison to MERRA2 and NAVGEM-HA still exhibits a warm bias of TEMPERA for the altitude range between 20–30 and 35 km and a cold bias between 30(35)–48 km, which was already found in Navas-Guzmán et al. (2017). Some of the systematic biases at the lower altitudes as well as at the upper altitudes occur at heights with a low measurement response, and thus we investigated a potential a priori dependence by computing similar climatologies for MERRA2 and NAVGEM-HA as shown in Fig. 2 for ECMWF. A comparison of these a priori climatologies between all three reanalysis data sets revealed similar altitude-dependent offsets to the TEMPERA comparison and explains most of the upper stratospheric bias and at least partly the lower stratospheric offset.

9 Conclusions

In this study, we reprocessed observations of the TEMPERA radiometer conducted between 2014 and 2017 with a recently developed and updated temperature retrieval. The new algorithm accounts for the Zeeman effect in the line center for both oxygen emission lines and uses revised a priori information for the state vector and covariances. We demonstrate with the new retrievals that TEMPERA temperature soundings can be carried out nearly continuously and with an increased altitude coverage by leveraging the updated radiative transfer model (ARTS) and HITRAN quantum numbers, which were not available previously.

We validated the retrieved temperature against the MERRA2 reanalysis and the meteorological analysis NAVGEM-HA for the years 2014–2017. Seasonal Person correlations coefficients remained between 0.85–0.95 between 20–55 km altitude. Therefore, we conclude that considering the Zeeman effect in the line center together with the revised a priori information resulted in an extended altitude coverage of about 8–10 km compared to the previous algorithm applied to the same TEMPERA measurements while sustaining the temporal resolution (Stähli et al., 2013; Navas-Guzmán et al., 2017).

Furthermore, we assessed the correlation coefficients and mean biases for monthly median temperature profiles of TEMPERA and the validation data MERRA2 and NAVGEM-HA. We obtained correlation values between 0.8–0.96 throughout the course of the year. The smallest correlations are found in January and February during strong planetary wave activity or for stratospheric warming evens, which supports that high-quality local observations could still provide a benefit to studying dynamical processes in more detail. The months from April to September reached correlations between 0.94–0.96. The mean temperature bias between MERRA2 and the radiometric temperatures was

smaller than ±1 K and basically vanished for some months. However, the comparison to NAVGEM-HA resulted in a cold bias between 1–2 K for the TEMPERA temperatures.

Altitude-dependent differences were examined by computing temperature residuals of TEMPERA and both model data sets. We identified that the lower altitudes between 20–35 km tend to exhibit a warm bias of approximately 5 K for the radiometer, and from 35–50 km we found a systematic cold bias of approximately 5 K for TEMPERA compared to MERRA2 and NAVGEM-HA. Above 50 km altitude, MERRA2 and NAVGEM-HA also start to show some discrepancies in the vertical temperature structure. During strong planetary wave activity in the winter months the differences between MERRA2, NAVGEM-HA, and TEMPERA exceed ±10 K. However, it remains unclear whether these biases or differences are due to the instrument or due to the sparsity of the assimilated data in the models, which might be not sufficient to capture all dynamical details.

Appendix A

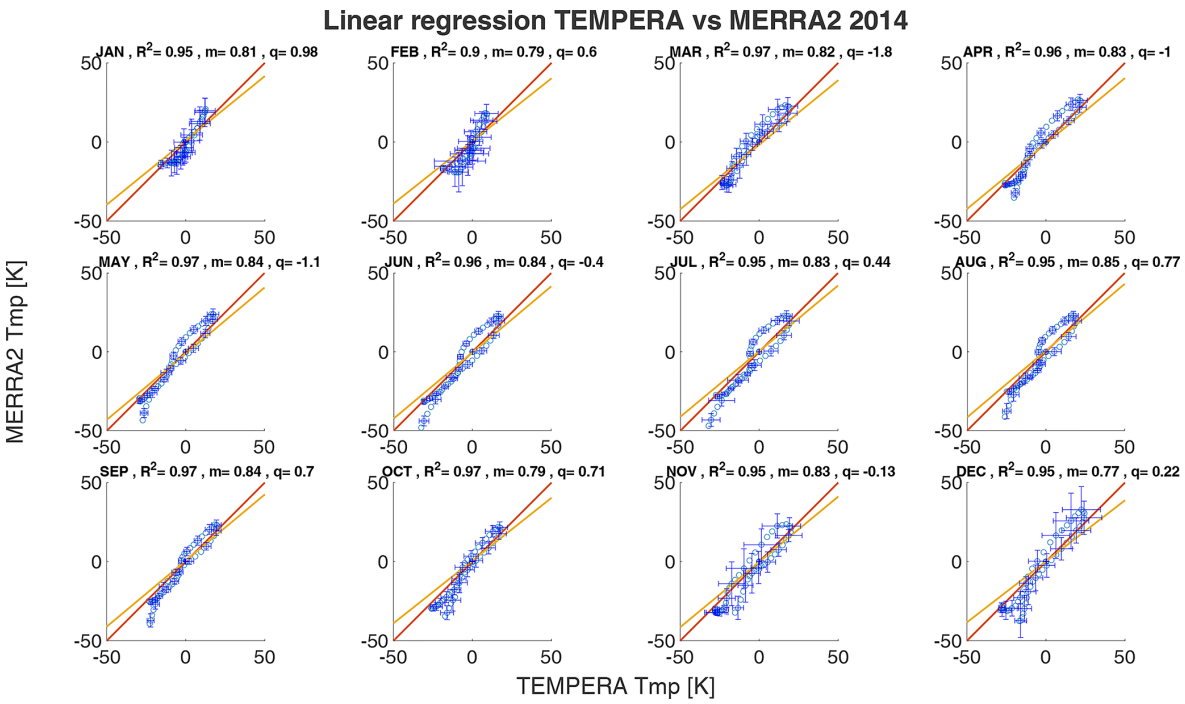

Figure A1. Linear regression of TEMPERA against MERRA2 temperatures for the year 2014.

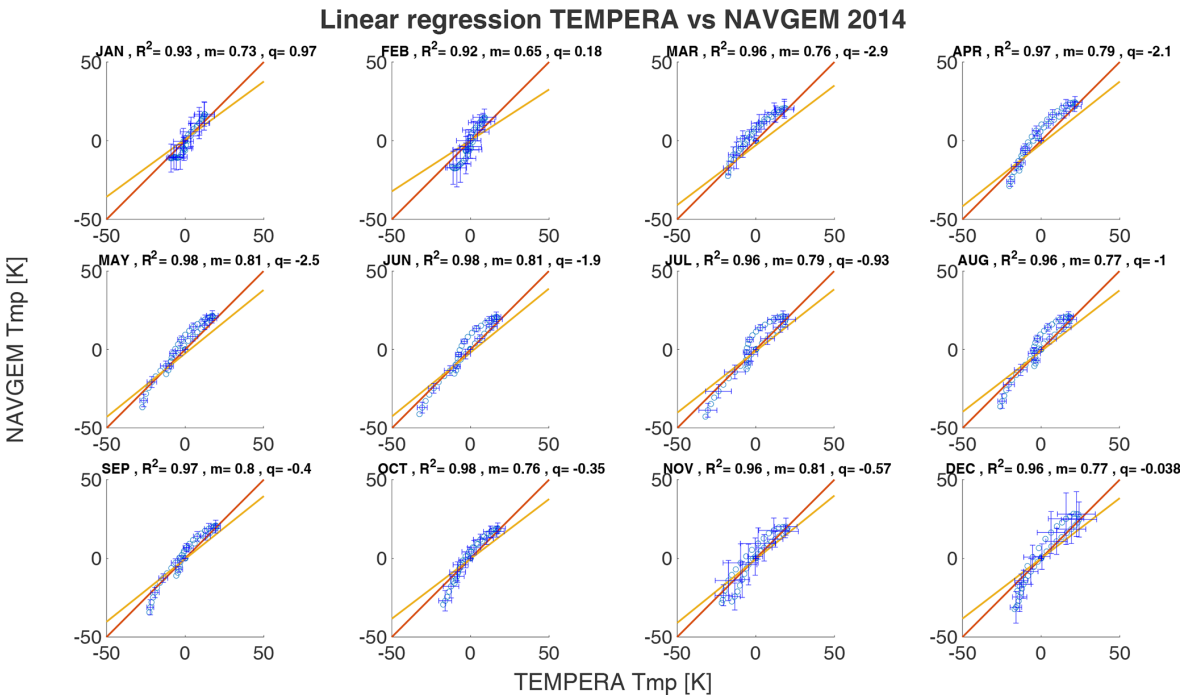

Figure A2. Linear regression of TEMPERA against NAVGEM temperatures for the year 2014.

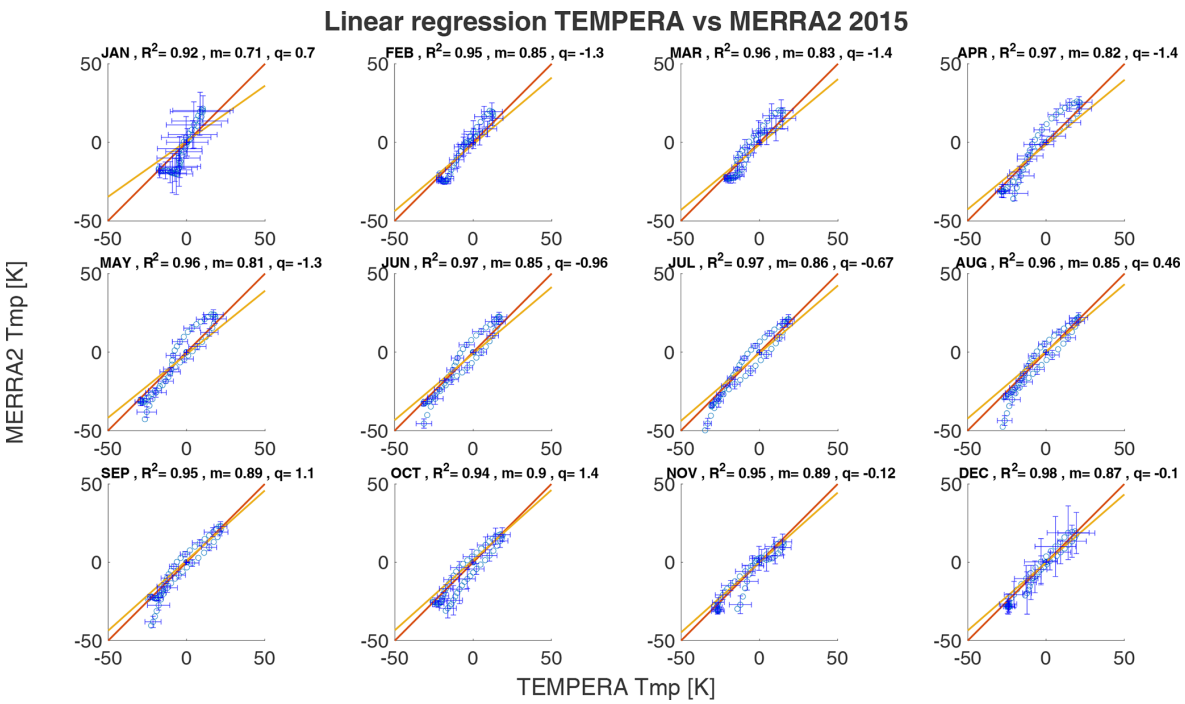

Figure A3. Linear regression of TEMPERA against MERRA2 temperatures for the year 2015.

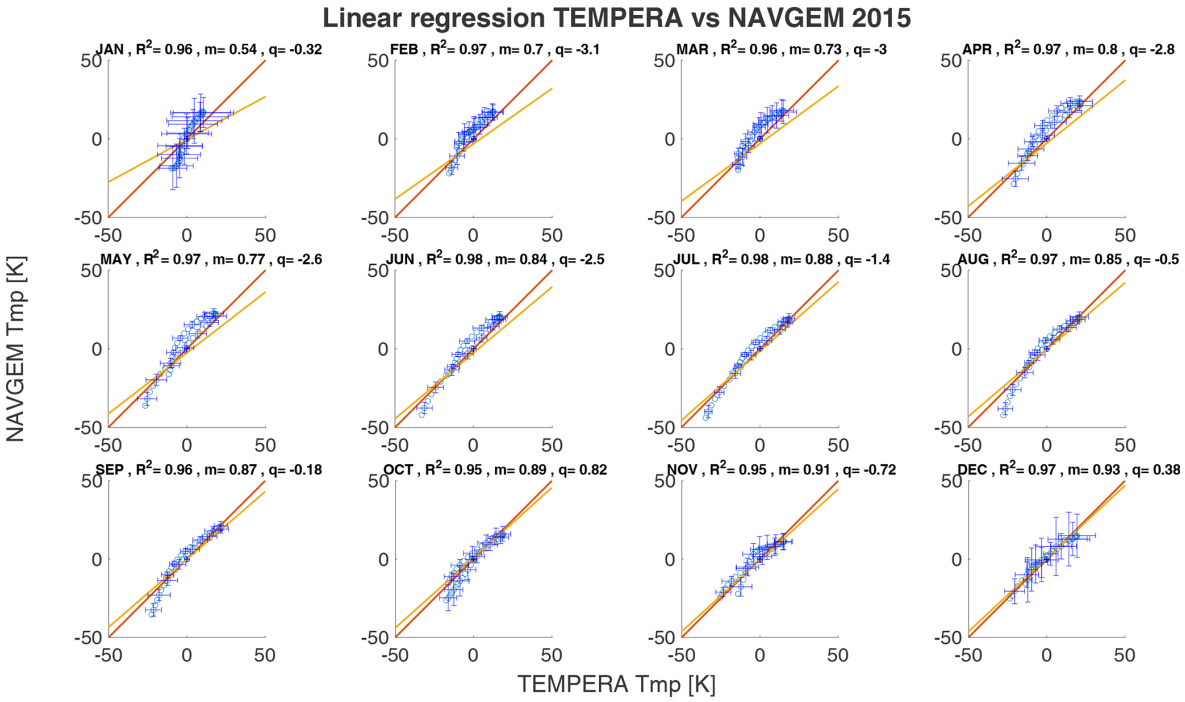

Figure A4. Linear regression of TEMPERA against NAVGEM temperatures for the year 2015.

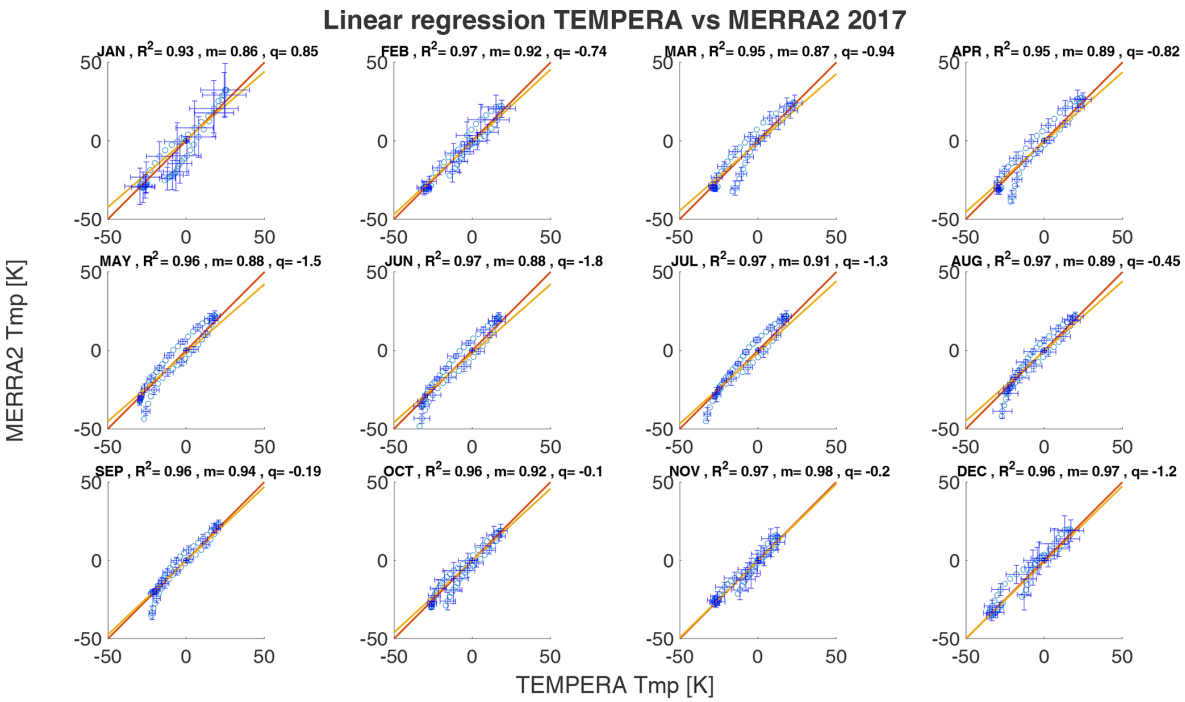

Figure A5. Linear regression of TEMPERA against MERRA2 temperatures for the year 2017.

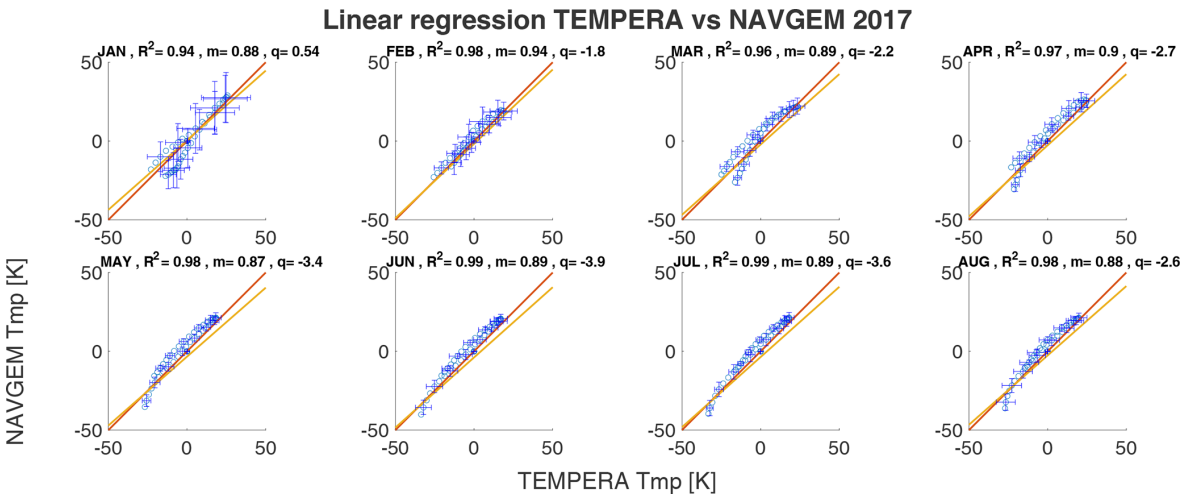

Figure A6. Linear regression of TEMPERA against NAVGE temperatures for the year 2017.

Appendix B: Comparison between MERRA2 and NAVGEM-HA

In Fig. B1 we show a differences between MERRA2 and NAVGEM-HA. Both models exhibit a very good agreement up to an altitude of 53 km. Above 53 km a systematic difference is obvious. NAVGEM-HA tends to show larger temperatures compared to MERRA2. However, we did not investigate the nature for the increasing discrepancy between both models above this altitude, which is beyond the scope of the paper. A detailed overview of the assimilated data sets and altitude range can be found in Eckermann et al. (2018) for NAVGEM-HA and for MERRA2 in Gelaro et al. (2017).

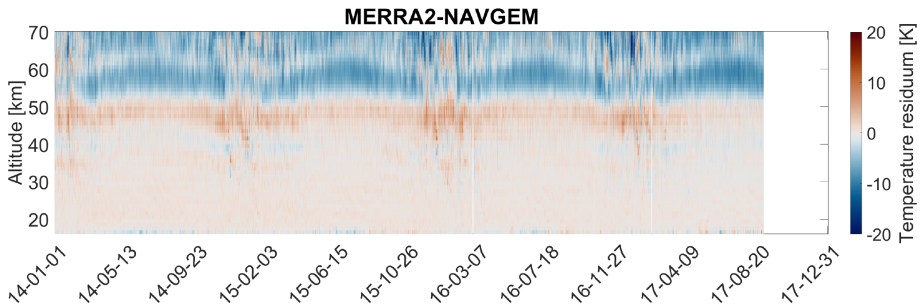

Figure B1. Absolute temperature difference between the MERRA2 and NAVGEM-HA datasets shows seasonal patterns above 45 km. The color scale is the same as in Fig. 9.

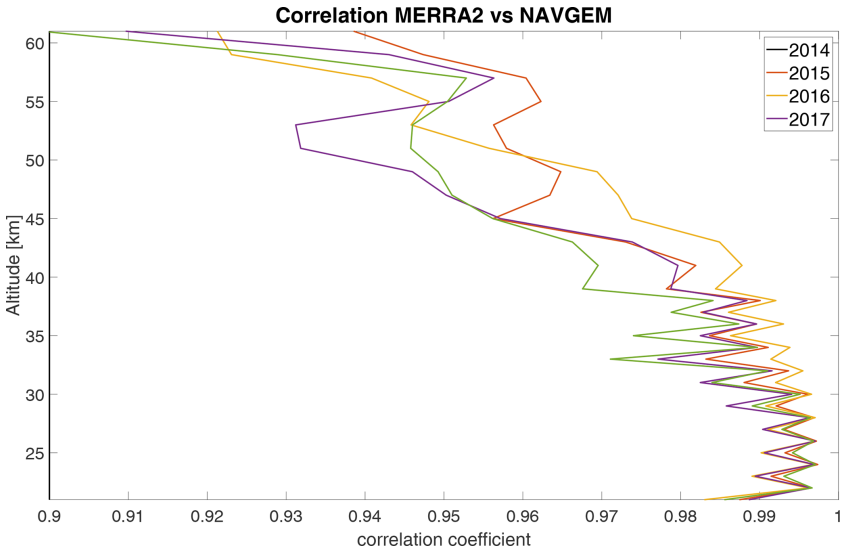

Figure B2. Correlation coefficients between the MERRA2 and NAVGEM-HA datasets. Correlation coefficients over all altitudes are above 0.9.

Data availability. MERRA-2 data are available at MDISC, managed by the NASA Goddard Earth Sciences (GES) Data and Information Services Center (DISC) https://doi.org/10.5067/QBZ6MG944HW0 (GMAO, 2015). TEMPERA temperatures are shared on request (gunter.stober@unibe.ch). The NAVGEM-HA data is available upon request from NRL (https://map.nrl.navy.mil/map/pub/nrl/navgem/, last access: 11 April 2022).

Author contributions. WK and GS conceptualized the content of the manuscript. WK implemented the retrieval and performed the data analysis of TEMPERA observations. GS reduced the MERRA2 and NAVGEM-HA data for the validation. AM, FNG, and DK guided and supported the preparation of the paper. All authors contributed to the editing of the paper.

Competing interests. The contact author has declared that neither they nor their coauthors have any competing interests

Disclaimer. Publisher's note: Copernicus Publications remains neutral with regard to jurisdictional claims in published maps and institutional affiliations.

Acknowledgements. The authors acknowledge the European Centre for Medium-Range Weather Forecasts (ECMWF) for the data supplied. This research has been supported by the Schweizerischer Nationalfonds zur Förderung der Wissenschaftlichen Forschung (grant no. 200021-200517/1), and the Swiss Polar Institute (SPI) supports the development of the TEMPERA-C radiometer. Francisco Navas-Guzma´n received funding from the Ramon y Cajal program (ref. RYC2019-027519-I) of the Spanish Ministry of Science and Innovation. We thank the ARTS developer team for their support in implementing the Zeeman effect into the retrievals. Scientific color maps (Crameri et al., 2020) are used in this study to prevent visual distortion of the data and exclusion of readers with color-vision deficiencies.

Financial support. This research has been supported by the Schweizerischer Nationalfonds zur Förderung der Wissenschaftlichen Forschung (grant no. 200021-200517/1), Swiss Polar Institute (SPI), and Ramon y Cajal program of the Spanish Ministry of Science and Innovation (grant no. RYC2019-027519-I).

Review statement. This paper was edited by Christian von Savigny and reviewed by two anonymous referees.

References

Anderson, J. G., Weisenstein, D. K., Bowman, K. P., Homeyer, C. R., Smith, J. B., Wilmouth, D. M., Sayres, D. S., Klobas, J. E., Leroy, S. S., Dykema, J. A., and Wofsy, S. C.: Stratospheric ozone over the United States in summer linked to observations of convection and temperature via chlorine and bromine catalysis, P. Natl. Acad. Sci. USA, 114, E4905–E4913, https://doi.org/10.1073/pnas.1619318114, 2017.

Baumgarten, K. and Stober, G.: On the evaluation of the phase relation between temperature and wind tides based on ground-based measurements and reanalysis data in the middle atmosphere, Ann. Geophys., 37, 581–602, https://doi.org/10.5194/angeo-37-581-2019, 2019.

Baumgarten, K., Gerding, M., Baumgarten, G., and Lübken, F.-J.: Temporal variability of tidal and gravity waves during a record long 10-day continuous lidar sounding, Atmos. Chem. Phys., 18, 371–384, https://doi.org/10.5194/acp-18-371-2018, 2018.

Buehler, S. A., Mendrok, J., Eriksson, P., Perrin, A., Larsson, R., and Lemke, O.: ARTS, the Atmospheric Radiative Transfer Simulator – version 2.2, the planetary toolbox edition, Geosci. Model Dev., 11, 1537–1556, https://doi.org/10.5194/gmd-11-1537-2018, 2018.

Crameri, F., Shephard, G. E., and Heron, P.: The misuse of colour in science communication, Nat. Commun., 11, 5444, https://doi.org/10.1038/s41467-020-19160-7, 2020.

Dhadly, M. S., Emmert, J. T., Drob, D. P., McCormack, J. P., and Niciejewski, R. J.: Short-Term and Interannual Variations of Migrating Diurnal and Semidiurnal Tides in the Mesosphere and Lower Thermosphere, J. Geophys. Res.-Space, 123, 7106–7123, https://doi.org/10.1029/2018JA025748, 2018.

Eckermann, S. D., Ma, J., Hoppel, K. W., Kuhl, D. D., Allen, D. R., Doyle, J. A., Viner, K. C., Ruston, B. C., Baker, N. L., Swadley, S. D., Whitcomb, T. R., Reynolds, C. A., Xu, L., Kaifler, N., Kaifler, B., Reid, I. M., Murphy, D. J., and Love, P. T.: High-Altitude (0-100 km) Global Atmospheric Reanalysis System: Description and Application to the 2014 Austral Winter of the Deep Propagating Gravity Wave Experiment (DEEPWAVE), Mon. Weather Rev., 146, 2639–2666, https://doi.org/10.1175/MWR-D-17-0386.1, 2018.

Eixmann, R., Matthias, V., Höffner, J., Baumgarten, G., and Gerding, M.: Local stratopause temperature variabilities and their embedding in the global context, Ann. Geophys., 38, 373–383, https://doi.org/10.5194/angeo-38-373-2020, 2020.

Eriksson, P., c. Jiménez, and Buehler, S.: Qpack, a general tool for instrument simulation and retrieval work, J. Quant. Spectrosc. Ra., 91, 47–64, 2005.

Gelaro, R., McCarty, W., Suárez, M. J., Todling, R., Molod, A., Takacs, L., Randles, C. A., Darmenov, A., Bosilovich, M. G., Reichle, R., Wargan, K., Coy, L., R., C., C., D., S., A., V., B., A., C., da Silva A. M., Gu, W., Kim, G., Koster, R., Lucchesi, R., Merkova, D., Nielsen, J. E., Partyka, G., Pawson, S., Putman, W., Rienecker, M., Schubert, S. D., Sienkiewicz, M., and Zhao, B.: The Modern-Era Retrospective Analysis for Research and Applications, Version 2 (MERRA-2), J. Climate, 30, 5419–5454, https://doi.org/10.1175/JCLI-D-16-0758.1, 2017.

Global Modeling and Assimilation Office (GMAO): MERRA-2 inst3_3d_asm_Np: 3d, 3-Hourly, Instantaneous, Pressure-Level, Assimilation, Assimilated Meteorological Fields V5.12.4, Greenbelt, MD, USA, Goddard Earth Sciences Data and Information Services Center (GES DISC) [data set], https://doi.org/10.5067/QBZ6MG944HW0, 2015.

Gordon, I., Rothman, L., Hill, C., Kochanov, R., Tan, Y., Bernath, P., Birk, M., Boudon, V., Campargue, A., Chance, K., Drouin, B., Flaud, J.-M., Gamache, R., Hodges, J., Jacquemart, D., Perevalov, V., Perrin, A., Shine, K., Smith, M.-A., Tennyson, J., Toon, G., Tran, H., Tyuterev, V., Barbe, A., Császár, A., Devi, V., Furtenbacher, T., Harrison, J., Hartmann, J.-M., Jolly, A., Johnson, T., Karman, T., Kleiner, I., Kyuberis, A., Loos, J., Lyulin, O., Massie, S., Mikhailenko, S., Moazzen-Ahmadi, N., Müller, H., Naumenko, O., Nikitin, A., Polyansky, O., Rey, M., Rotger, M., Sharpe, S., Sung, K., Starikova, E., Tashkun, S., Auwera, J. V., Wagner, G., Wilzewski, J., Wcisło, P., Yu, S., and Zak, E.: The HITRAN2016 molecular spectroscopic database, J. Quant. Spectrosc. Ra., 203, 3–69, https://doi.org/10.1016/j.jqsrt.2017.06.038, 2017.

Ingold, T. and Kämpfer, N.: Weighted mean tropospheric temperature and transmittance determination at millimeter-wave frequencies for ground-based applications, Radio Sci., 22, 905–918, 1998.

Kuhl, D., Rosmond, T., Bishop, C., McLay, J., and Baker, N.: Comparison of hybrid ensemble/4DVar and 4DVar within the NAVDAS-AR data assimilation framework, Mon. Weather Rev., 141, 2740–2758, https://doi.org/10.1175/MWR-D-12-00182.1, 2013.

Larsson, R., Lankhaar, B., and Eriksson, P.: Updated Zeeman effect splitting coefficients for molekular oxygen in planetary applications, J. Quant. Spectrosc. Ra., 224, 431–438, 2019.

Limpasuvan, V., Orsolini, Y. J., Chandran, A., Garcia, R. R., and Smith, A. K.: On the composite response of the MLT to major sudden stratospheric warming events with elevated stratopause, J. Geophys. Res.-Atmos., 121, 4518–4537, https://doi.org/10.1002/2015JD024401, 2015JD024401, 2016.

Liu, H.-L.: Variability and predictability of the space environment as related to lower atmosphere forcing, Adv. Space Res., 14, 634–658, https://doi.org/10.1002/2016SW001450, 2016.

Matsuno, T.: A Dynamical Model of the Stratospheric Sudden Warming, J. Atmos. Sci., 28, 1479–1494, 1971.

Matthias, V. and Ern, M.: On the origin of the mesospheric quasi-stationary planetary waves in the unusual Arctic winter 2015/2016, Atmos. Chem. Phys., 18, 4803–4815, https://doi.org/10.5194/acp-18-4803-2018, 2018.

Matthias, V., Hoffmann, P., Manson, A., Meek, C., Stober, G., Brown, P., and Rapp, M.: The impact of planetary waves on the latitudinal displacement of sudden stratospheric warmings, Ann. Geophys., 31, 1397–1415, https://doi.org/10.5194/angeo-31-1397-2013, 2013.

Matthias, V., Dörnbrack, A., and Stober, G.: The extraordinarily strong and cold polar vortex in the early northern winter 2015/2016, Geophys. Res. Lett., 43, 12287–12294, https://doi.org/10.1002/2016GL071676, 2016.

Matthias, V., Stober, G., Kozlovsky, A., Lester, M., Belova, E., and Kero, J.: Vertical Structure of the Arctic Spring Transition in the Middle Atmosphere, J. Geophys. Res.-Atmos., 126, e2020JD034353, https://doi.org/10.1029/2020JD034353, 2021.

McCormack, J., Hoppel, K., Kuhl, D., de Wit, R., Stober, G., Espy, P., Baker, N., Brown, P., Fritts, D., Jacobi, C., Janches, D., Mitchell, N., Ruston, B., Swadley, S., Viner, K., Whitcomb, T., and Hibbins, R.: Comparison of mesospheric winds

from a high-altitude meteorological analysis system and meteor radar observations during the boreal winters of 2009–2010 and 2012–2013, J. Atmos. Sol.-Terr. Phy., 154, 132–166, https://doi.org/10.1016/j.jastp.2016.12.007, 2017.

Navas-Guzmán, F., Kämpfer, N., Murk, A., Larsson, R., Buehler, S. A., and Eriksson, P.: Zeeman effect in atmospheric O_2 measured by ground-based microwave radiometry, Atmos. Meas. Tech., 8, 1863–1874, https://doi.org/10.5194/amt-8-1863-2015, 2015.

Navas-Guzmán, F., Kämpfer, N., and Haefele, A.: Validation of brightness and physical temperature from two scanning microwave radiometers in the 60 GHz O_2 band using radiosonde measurements, Atmos. Meas. Tech., 9, 4587–4600, https://doi.org/10.5194/amt-9-4587-2016, 2016.

Navas-Guzmán, F., Kämpfer, N., Schranz, F., Steinbrecht, W., and Haefele, A.: Intercomparison of stratospheric temperature profiles from a ground-based microwave radiometer with other techniques, Atmos. Chem. Phys., 17, 14085–14104, https://doi.org/10.5194/acp-17-14085-2017, 2017.

Oberheide, J., Forbes, J. M., Zhang, X., and Bruinsma, S. L.: Climatology of upward propagating diurnal and semidiurnal tides in the thermosphere, J. Geophys. Res.-Space, 116, A11306, https://doi.org/10.1029/2011JA016784, 2011.

Panka, P. A., Weryk, R. J., Bruzzone, J. S., Janches, D., Schult, C., Stober, G., and Hormaechea, J. L.: An Improved Method to Measure Head Echoes Using a Meteor Radar, Planet. Sci. J., 2, 197, https://doi.org/10.3847/psj/ac22b2, 2021.

Pokhotelov, D., Becker, E., Stober, G., and Chau, J. L.: Seasonal variability of atmospheric tides in the mesosphere and lower thermosphere: meteor radar data and simulations, Ann. Geophys., 36, 825–830, https://doi.org/10.5194/angeo-36-825-2018, 2018.

Remsberg, E. E., Marshall, B. T., Garcia-Comas, M., Krueger, D., Lingenfelser, G. S., Martin-Torres, J., Mlynczak, M. G., Russell III, J. M., Smith, A. K., Zhao, Y., Brown, C., Gordley, L. L., Lopez-Gonzalez, M. J., Lopez-Puertas, M., She, C.-Y., Taylor, M. J., and Thompson, R. E.: Assessment of the quality of the Version 1.07 temperature-versus-pressure profiles of the middle atmosphere from TIMED/SABER, J. Geophys. Res.-Atmos., 113, D17101, https://doi.org/10.1029/2008JD010013, 2008.

Rezac, L., Kutepov, A., Russell, J., Feofilov, A., Yue, J., and Goldberg, R.: Simultaneous retrieval of $T(p)$ and CO_2 VMR from two-channel non-LTE limb radiances and application to daytime SABER/TIMED measurements, J. Atmos. Sol.-Terr. Phy., 130-131, 23–42, https://doi.org/10.1016/j.jastp.2015.05.004, 2015.

Rodgers, C. D.: Inverse Methods for Atmospheric sounding Theory and Practice, World Scientific, https://doi.org/10.1142/3171, 2000.

Russell III, J. M., Mlynczak, M. G., Gordley, L. L., Tansock, J., and Esplin, R.: Overview of the SABER experiment and preliminary calibration results, in: Optical Spectroscopic Techniques and Instrumentation for Atmospheric and Space Research III, edited by: Larar, A. M., International Society for Optics and Photonics, SPIE, vol. 3756, 277–288, https://doi.org/10.1117/12.366382, 1999.

Scherhag, R.: Die explosionsartige Stratosphärenerwärmung des Spätwinters 1951/52, Ber. Deut. Wetterdienst, 38, 51–63, 1952.

Schoeberl, M., Douglass, A., Hilsenrath, E., Bhartia, P., Beer, R., Waters, J., Gunson, M., Froidevaux, L., Gille, J., Barnett, J., Levelt, P., and DeCola, P.: Overview of the EOS aura mission, IEEE T. Geosci. Remote, 44, 1066–1074, https://doi.org/10.1109/TGRS.2005.861950, 2006.

Shannon, C. E.: A Mathematical Theory of Communication, Bell Syst. Tech. J., 27, 379–423, https://doi.org/10.1002/j.1538-7305.1948.tb01338.x, 1948.

Shannon, C. E. and Weaver, W.: The Mathematical Theory of Communication, University of Illinois Press, Urbana, IL, https://doi.org/10.2307/3611062, 1949.

Sica, R. J. and Haefele, A.: Retrieval of temperature from a multiple-channel Rayleigh-scatter lidar using an optimal estimation method, Appl. Opt., 54, 1872–1889, https://doi.org/10.1364/AO.54.001872, 2015.

Stober, G., Matthias, V., Jacobi, C., Wilhelm, S., Höffner, J., and Chau, J. L.: Exceptionally strong summer-like zonal wind reversal in the upper mesosphere during winter 2015/16, Ann. Geophys., 35, 711–720, https://doi.org/10.5194/angeo-35-711-2017, 2017.

Stober, G., Baumgarten, K., McCormack, J. P., Brown, P., and Czarnecki, J.: Comparative study between ground-based observations and NAVGEM-HA analysis data in the mesosphere and lower thermosphere region, Atmos. Chem. Phys., 20, 11979–12010, https://doi.org/10.5194/acp-20-11979-2020, 2020.

Stober, G., Kuchar, A., Pokhotelov, D., Liu, H., Liu, H.-L., Schmidt, H., Jacobi, C., Baumgarten, K., Brown, P., Janches, D., Murphy, D., Kozlovsky, A., Lester, M., Belova, E., Kero, J., and Mitchell, N.: Interhemispheric differences of mesosphere–lower thermosphere winds and tides investigated from three whole-atmosphere models and meteor radar observations, Atmos. Chem. Phys., 21, 13855–13902, https://doi.org/10.5194/acp-21-13855-2021, 2021.

Stolarski, R. S., Douglass, A. R., Remsberg, E. E., Livesey, N. J., and Gille, J. C.: Ozone temperature correlations in the upper stratosphere as a measure of chlorine content, J. Geophys. Res.-Atmos., 117, D10305, https://doi.org/10.1029/2012JD017456, 2012.

Stähli, O., Murk, A., Kämpfer, N., Mätzler, C., and Eriksson, P.: Microwave radiometer to retrieve temperature profiles from the surface to the stratopause, Atmos. Meas. Tech., 6, 2477–2494, https://doi.org/10.5194/amt-6-2477-2013, 2013.

Waters, J., Froidevaux, L., Harwood, R., Jarnot, R., Pickett, H., Read, W., Siegel, P., Cofield, R., Filipiak, M., Flower, D., Holden, J., Lau, G., Livesey, N., Manney, G., Pumphrey, H., Santee, M., Wu, D., Cuddy, D., Lay, R., Loo, M., Perun, V., Schwartz, M., Stek, P., Thurstans, R., Boyles, M., Chandra, K., Chavez, M., Chen, G.-S., Chudasama, B., Dodge, R., Fuller, R., Girard, M., Jiang, J., Jiang, Y., Knosp, B., LaBelle, R., Lam, J., Lee, K., Miller, D., Oswald, J., Patel, N., Pukala, D., Quintero, O., Scaff, D., Van Snyder, W., Tope, M., Wagner, P., and Walch, M.: The Earth observing system microwave limb sounder (EOS MLS) on the aura Satellite, IEEE T. Geosci. Remote, 44, 1075–1092, https://doi.org/10.1109/TGRS.2006.873771, 2006.

Wing, R., Hauchecorne, A., Keckhut, P., Godin-Beekmann, S., Khaykin, S., McCullough, E. M., Mariscal, J.-F., and d'Almeida, É.: Lidar temperature series in the middle atmosphere as a reference data set – Part 1: Improved retrievals and a 20-year cross-validation of two co-located French lidars, Atmos. Meas. Tech., 11, 5531–5547, https://doi.org/10.5194/amt-11-5531-2018, 2018.

Publication III

Development of a Polarimetric 50-GHz Spectrometer for Temperature Sounding in the Middle Atmosphere

Witali Krochin, Gunter Stober, and Axel Murk

***Abstract*—This article addresses the further development of the ground-based temperature radiometer TEMPERA, which measures atmospheric microwave radiation in one linear polarization in order to retrieve temperature profiles up to an altitude of 50 km (Stähli *et al.*, 2013). The latest innovation is a new polarimetric receiver, which allows observing the atmosphere simultaneously in left- and right-circular polarization. In combination with an adapted inversion method, the fully polarimetric analysis can improve the accuracy and extends the vertical upper limit of retrieved temperature profiles. Comparisons between single polarization and fully polarimetric retrievals with simulated atmospheric spectra are presented, and the influence of the Earth's magnetic field is analyzed. In addition, we propose a simple calibration method for fully polarimetric radiometers and present first atmospheric spectra measured with the new TEMPERA-C instrument.**

***Index Terms*—Geomagnetism, microwave antennas, microwave radiometry, passive microwave remote sensing, radiometers, radiometry, remote sensing.**

I. Introduction

ATMOSPHERIC temperature observations at the stratosphere and lower mesosphere are crucial for numerical weather prediction and to understand the climatological behavior from the surface up to space. Tropospheric temperature profiles are derived routinely by remote sensing with spaceborne and ground-based microwave radiometers observing the wing of the oxygen absorption line complex in the 50–60-GHz band. The standard instruments for ground-based tropospheric temperature sounding use typically up to 15 channels with a frequency resolution between 10 MHz and 2 GHz [2]. Spaceborne instruments can have even more channels and a higher resolution [3], [4]. The addition of a high-resolution spectrometer allows us to resolve also several narrow line features, which can be used to retrieve temperature profiles in the middle atmosphere [1], [5]. Measurements in this altitude region between 12 and 80 km are important to understand the global atmospheric dynamics, such as planetary waves, atmospheric tides, and gravity waves, and dynamical induced processes such as sudden stratospheric warmings [6], [7]. In particular, atmospheric tides have become a vital science topic. These atmospheric waves cause periodic oscillations in temperature, which propagate/migrate over the whole globe and are present from the stratosphere up to the mesosphere and even the thermosphere. These waves carry energy and momentum from their source region to the altitude of their dissipation and, thus, are essential for the energetic coupling between the different vertical atmospheric layers.

Recently, an inversion algorithm for a ground-based single-polarization TEMPErature RAdiometer (TEMPERA) [1] was revised and extended to account for the Zeeman splitting (see Section IV) in the forward model [8]. This upgrade improved the upper altitude limit for temperature profile retrievals from single polarized spectra from 48 to 53 km. Furthermore, it was also demonstrated that temperatures at higher altitudes cannot be retrieved with single polarization due to the Zeeman effect in the line center resulting in an additional line broadening posing a natural limit for the former instrument.

In this article, it is demonstrated that the polarimetric decomposition of the atmospheric emission spectra provides a possibility to further enhance the altitude coverage to around 60 km and to study features of the Earth's magnetic field.

This article addresses the development of a fully polarimetric ground-based temperature radiometer, called TEMPERA-C. Based on simulated data, we compare the retrieval capabilities of a fully polarimetric instrument with one that observes only single linear polarization. In addition, we present first sensitivity investigations to analyze the magnetic field features. The last sections provide a description of the TEMPERA-C receiver and the first polarimetric observations of atmospheric emission lines.

II. Retrieval of Temperature Profiles

The method to retrieve atmospheric temperature profiles presented in this article is based on a numerical inversion of atmospheric microwave spectra with Atmospheric Radiative Transfer Simulator (ARTS) [9]. Atmospheric oxygen emits microwave radiation through rotational transitions. The shape of these emission lines is determined by pressure broadening. Fig. 1 shows a typical brightness temperature spectrum simulated with the ARTS. The red box highlights the frequency band covered by the high-resolution spectrometer of TEMPERA. The temperature profile in the stratosphere is retrieved from the pressure broadened lineshape of the two emission lines included in this spectral region. The mathematical formalism of the ARTS follows the optimal estimation method from Rodgers [10]. The measured spectrum $\mathbf{y}$ results from the atmospheric state $\mathbf{x}$ and the forward

Manuscript received 5 April 2022; revised 27 May 2022; accepted 19 June 2022. Date of publication 28 June 2022; date of current version 21 July 2022. This work was supported in part by the Schweizerischer Nationalfonds zur Förderung der Wissenschaftlichen Forschung under Grant 200021-200517/1 and in part by the Swiss Polar Institute. *(Corresponding author: Witali Krochin.)*

The authors are with the Institute of Applied Physics, University of Bern, 3012 Bern, Switzerland (e-mail: witali.krochin@iap.unibe.ch; gunter.stober@iap.unibe.ch; axel.murk@iap.unibe.ch).

Digital Object Identifier 10.1109/JSTARS.2022.3186796

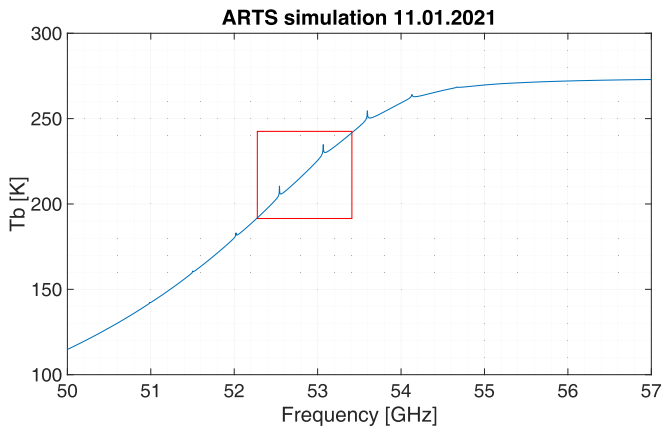

Fig. 1. Brightness temperature spectrum simulated for an elevation angle of 60°. The red box highlights the two stratospheric emission lines, which are observed with TEMPERA.

model F

$$\mathbf{y} = F(\mathbf{x}) + \boldsymbol{\epsilon} \tag{1}$$

where ϵ is the measurement error. The challenge is to retrieve $\mathbf{x}$ from the measurement $\mathbf{y}$. In our case, the inversion of the measured spectra into a vertical temperature profile leads to an inversion problem that is ill-posed. One of the reasons is that there are an infinite amount of solutions $\mathbf{x}$ for a given measurement $\mathbf{y}$. The optimal state $\tilde{\mathbf{x}}$ is the state that maximizes the probability $P(\mathbf{x}|\mathbf{y})$ for a given measurement $\mathbf{y}$. Using Bayes' theorem with the assumption that $\mathbf{x}$ and $\mathbf{y}$ have Gaussian probability density distributions, the optimization problem can be transformed into the problem of minimizing the cost function

$$\begin{aligned} J(\mathbf{x}) = & -2\ln P(\mathbf{x}|\mathbf{y}) = [\mathbf{y} - F(\mathbf{x})]^T \mathbf{S}_\epsilon^{-1} [\mathbf{y} - F(\mathbf{x})] \\ & + [\mathbf{x} - \mathbf{x}_a]^T \mathbf{S_a} [\mathbf{x} - \mathbf{x}_a]. \end{aligned} \tag{2}$$

Here, S_ϵ is the measurement error covariance matrix, $\mathbf{x}_a$ is the preknowledge background state of the atmosphere (apriori state), and $\mathbf{S}_a$ is its covariance matrix. The resulting matrix equation is solved by a Levenberg–Marquardt algorithm. Writing the optimal state as $\tilde{\mathbf{x}} = R(\mathbf{y}, \mathbf{x}_a)$, the averaging kernel matrix (AVK) is defined as

$$\mathbf{A} = \frac{\partial R}{\partial \mathbf{y}} \frac{\partial F}{\partial \mathbf{x}} = \mathbf{G}_y \mathbf{K}_x \tag{3}$$

that is basically the Jacobian matrix of the forward model $\mathbf{K}_x = \partial F/\partial \mathbf{x}$ weighted with the gain matrix $\mathbf{G}_y = \partial R/\partial \mathbf{y}$. The half-width of the rows of $\mathbf{A}$ can be regarded as a measure of the effective vertical resolution of the retrieval. The AVK is widely used to illustrate the performance of a retrieval. Another important quality control parameter is the measurement response vector (MR) defined as

$$\mathbf{MR}_i = \frac{\mathbf{A}_i \mathbf{x}_a}{\mathbf{x}_{ai}} \tag{4}$$

where $\mathbf{A}_i$ is the ith row of the AVK matrix and $\mathbf{x}_{ai}$ is the ith entry of the apriori vector. For an ideal retrieval, the entries $\mathbf{MR}_i$ are equal to 1, while values below 0.6 indicate that the retrieved state depends mostly on the apriori state.

A more detailed discussion of the retrieval algorithm can be found in [8] and is not repeated here. The only difference in the retrievals presented in this article is that simulated emission lines were used instead of observed emission lines and that the retrieval was performed with two left-circular-polarized (LCP)/right-circular-polarized (RCP) spectra instead of one linearly polarized spectrum.

III. Stokes Parameters

To describe the polarization states, we use the concept of Stokes parameters defined in the following way [11]. A monochromatic plane wave propagating in the z-direction in complex notation has the form

$$\mathbf{E}(t) = \mathbf{E}(0) e^{j(\omega t - \mathbf{kz} - \boldsymbol{\phi})}. \tag{5}$$

The directions orthogonal to the z-axis are denoted as h and v. The position of the receiver can be set to zero $z = 0$ so that the h and v components have the form

$$E_h(t) = E_h(0) e^{j(\omega t - \phi_h)} \tag{6}$$

$$E_v(t) = E_v(0) e^{j(\omega t - \phi_v)}. \tag{7}$$

The Stokes parameters for linear polarized field components are

$$I = |\langle E_h \rangle|^2 + |\langle E_v \rangle|^2 \tag{8}$$

$$Q = |\langle E_h \rangle|^2 - |\langle E_v \rangle|^2 \tag{9}$$

$$U = 2\Re\left(\langle E_h E_v^* \rangle\right) \tag{10}$$

$$V = 2\Im\left(\langle E_h E_v^* \rangle\right). \tag{11}$$

The brackets $\langle\rangle$ denotes the expectation value over a time period $\Delta t \gg {}^{2\pi}/_{\omega}$, E_α^* denotes the complex conjugation, $\Re$ is the real part, and $\Im$ is the imaginary part. We have ignored the prefactors in these equations, because these terms are determined after a total power calibration. To derive the LCP and RCP field components, the first and fourth Stokes parameters expressed with circular polarized fields will be used

$$I = |\langle E_{\text{LCP}} \rangle|^2 + |\langle E_{\text{RCP}} \rangle|^2 \tag{12}$$

$$V = |\langle E_{\text{LCP}} \rangle|^2 - |\langle E_{\text{RCP}} \rangle|^2. \tag{13}$$

IV. Altitude Limitation: Zeeman Effect

The observed emission lines are originated from rotational transitions of the oxygen molecule. The interaction with the Earth's magnetic field splits rotational energy levels into several sublevels. Therefore, one emission line splits into different lines, depending on the orientation of the angular momentum, magnetic moment, magnetic field, and polarization. For emission lines measured with a linearly polarized radiometer, this results in a broadening of the line center, which also depends on the orientation between the magnetic field lines and the line of sight of the instrument [12], [13].

Fig. 2 compares a measured emission line of the TEMPERA instrument with ARTS simulations. The simulations were performed with and without the Zeeman effect for the same linear

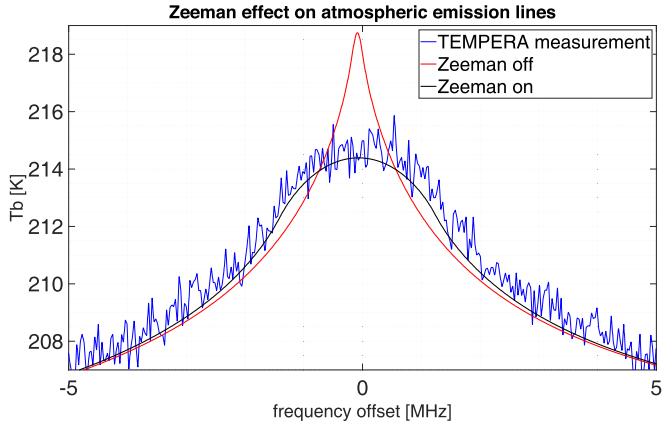

Fig. 2. Measurement with TEMPERA on the January 1, 2022 in Bern, and ARTS simulations with and without Zeeman effect. The line center is at 53.067 GHz.

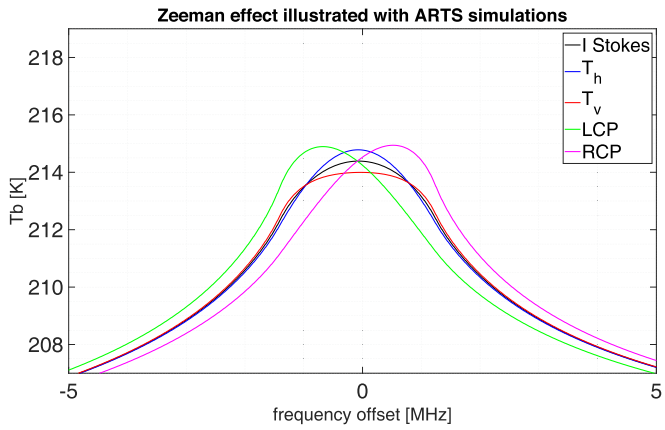

Fig. 3. Simulated line centers for vertical, horizontal, and left- and right-circular-polarized radiation in comparison to the total intensity. The line center is at 53.067 GHz.

polarization and observing geometry as in the observations with the line center at 53.067 GHz, an elevation of 60°, and an azimuth of 90°.

Above a certain altitude, this Zeeman broadening becomes larger than the pressure broadening. This limited the maximum height with significant measurement response of the retrieved temperature profiles of the first TEMPERA instrument to around 53 km.

V. Enhancing the Altitude Coverage of Temperature Retrievals by Polarimetric Decomposition

For observations in circular polarization, the Zeeman effect leads to a frequency shift of the line center with different signs for the left- and right-hand-circular polarization. Fig. 3 compares simulations of the line centers for LCP and RCP spectra with simulations in horizontal T_h and vertical T_v polarization. The observing geometry is the same as in Fig. 2. The LCP and RCP emission lines are narrower than the ones for linear polarization, and they will, thus, allow us to retrieve temperatures at higher altitudes. Furthermore, the frequency offset between

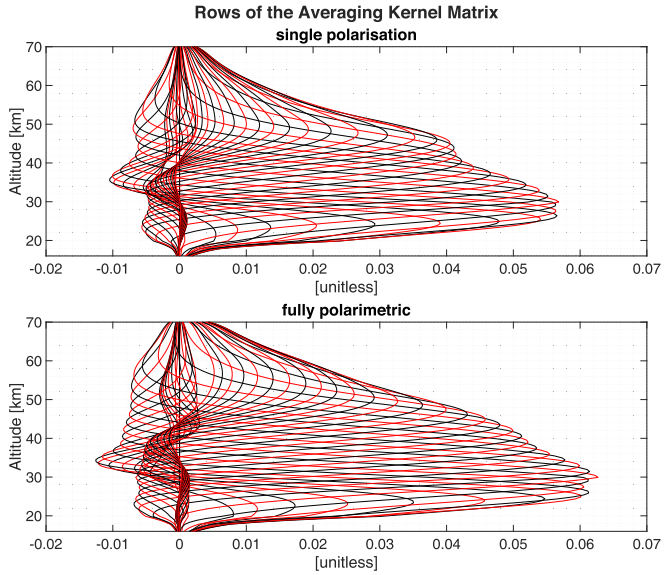

Fig. 4. Top: AVK for a retrieval with one simulated spectrum with total polarization. Bottom: AVK for a retrieval with two simulated spectra with RCP and LCP polarization.

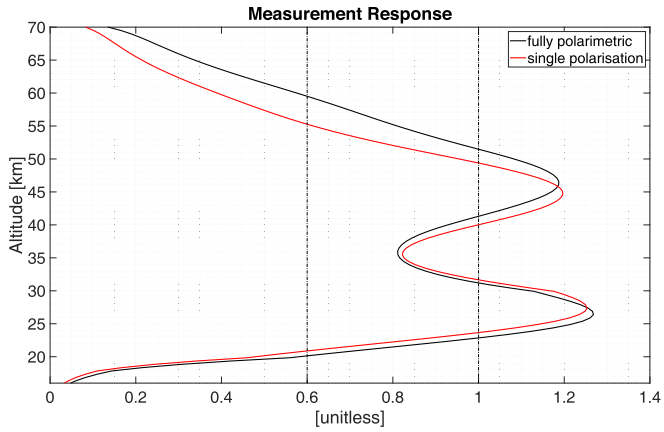

Fig. 5. Corresponding measurement response to the retrievals from Fig. 4. MR = 0.6 and MR = 1 are illustrated with the vertical dot-dashed lines.

them allows us to derive information on the magnetic field strength (MFS). Figs. 4 and 5 illustrate the improvement that can be achieved by a simultaneous retrieval of the left- and right-circular spectra, compared to the previous state-of-the-art retrievals using a single linear polarization. The plots show the rows of the AVK (see Fig. 4) and the measurement response vector (see Fig. 5) from both retrievals that were performed with simulated emission spectra. The conditions of the simulation are summarized in Table I. Our simulations exhibit an increased MR combining LCP and RCP spectra in the retrieval while keeping the width of the AVK resulting in a similar vertical resolution at almost all the altitudes. Only between 27 and 46 km, the MR of the newer retrieval version shows slightly lower values. This dip originates from negative values of the AVK matrix at these altitudes, which occurs due to an overestimation of the apriori error.

TABLE I
CONDITIONS FOR THE SIMULATED SPECTRA

Center 1	52.542 GHz
Center 2	53.067 GHz
Bandwidth	2×100 MHz
Resolution	20 kHz
Noise	2 K
Latitude	7.45 E
Longitude	46.95 N
Azimuth	6°
Elevation	60°

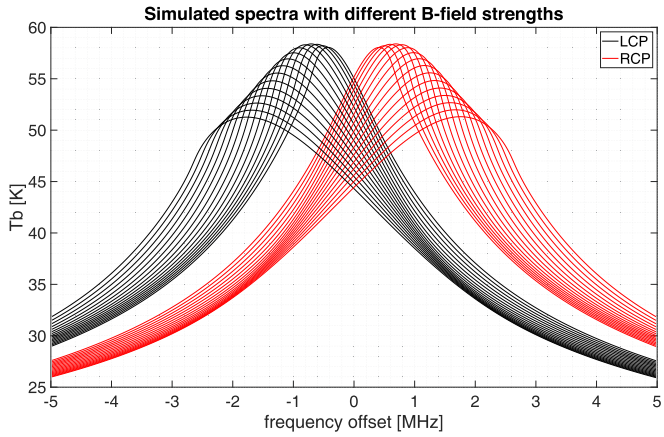

Fig. 6. Simulated spectra with the condition of Table I and different MFSs (see text). The line center is at 53.067 GHz. Radiative contribution from the troposphere was removed for this spectra.

VI. INFLUENCE OF THE MAGNETIC FIELD ON THE RETRIEVED PROFILE

The Zeeman-broadened lineshape depends on MFS, the polarization, and the angle between the line of sight of the instrument and the magnetic field lines. A study where linear polarized emission lines were measured for different azimuth angles, and hence with different angles between the line of sight and the magnetic field lines, is presented in [12]. In this section, the influence of the MFS is discussed. The Zeeman broadening gets stronger with increasing MFS. Fig. 6 shows simulated emission spectra at the line center of 53.067 GHz for LCP and RCP and different MFS. The reference magnetic field is the International Geometric Reference Field: 11th Generation, which is included in the ARTS. Contributions from the troposphere were removed in this case. The different MFSs were produced by multiplying the reference field with a factor between 0.5 and 2 with a step size of 0.1, yielding in total 16 different MFSs. The plot illustrates how the Zeeman broadening gets stronger with higher MFS. The line center offset is illustrated in Fig. 7. The relationship between this offset and the multiplication factor appears to be linear in this range of the magnetic field.

The influence of the MFS has to be considered in the retrieval because small deviations can produce large errors. If the MFS is underestimated, the measured emission line will be more Zeeman broadened as the forward model emission line. Therefore,

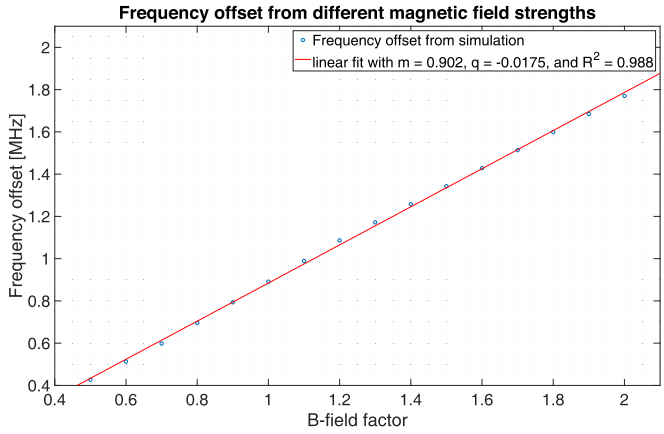

Fig. 7. Frequency offset from the line center at 53.067 GHz due to different MFS.

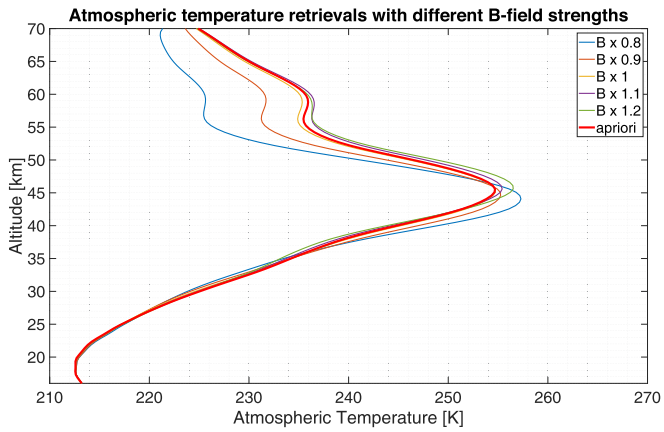

Fig. 8. Atmospheric temperature from retrievals with different MFSs, retrieved with the same emission line.

the pressure broadening (and with that the pressure as well) will be overestimated. This leads to an underestimation of the atmospheric temperature. That effect is illustrated in Fig. 8. It shows retrieved temperature profiles, where two emission spectra with LCP and RCP were simulated with the reference magnetic field and the conditions from Table I. From these spectra, temperature profiles were retrieved, using different MFSs by multiplying the reference magnetic field with factors between 0.8 and 1.2. Up to an altitude of about 35 km, the magnetic field has no significant influence on the retrieved profile. A cold bias occurs above 50 km in the profiles, which would result for an underestimated MFS. At the stratopause (45 km), a warm bias of around 2 K would be visible. We attribute this effect to decreased brightness temperatures of the line center due to the increased Zeeman broadening, which also results in a shift of a few megahertz of the line center for stronger MFS (see Fig. 6). Fig. 9 shows the difference between the retrieved profile and the apriori profile, which provides a better illustration of the resultant altitude-dependent biases and different MFSs. The retrieved temperature gets underestimated by around 5 K for the

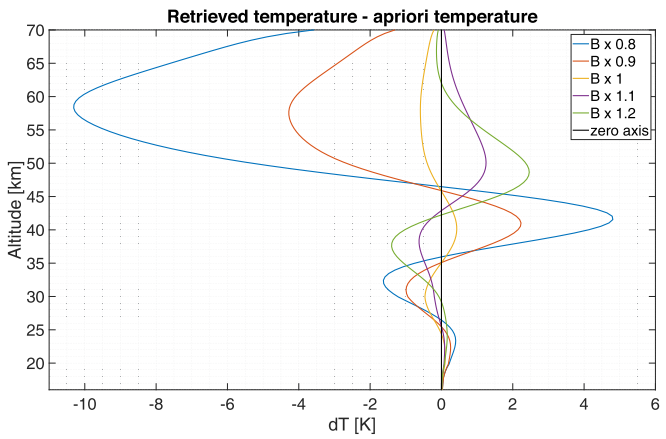

Fig. 9. Difference between retrieved temperature profiles with different MFSs and the apriori profile shows the expected behavior above 50 km.

factor 0.9 and 10 K for the factor 0.8, between an altitude of 50 and 60 km.

VII. Instrument Description

The novel TEMPERA-C instrument for atmospheric temperature sounding is based on our previous TEMPERA instrument, but it will perform simultaneous and fully polarimetric observations of two stratospheric emission lines. This will significantly improve the sensitivity and altitude range in the middle atmosphere compared to the current state of the art. The instrument uses an orthomode transducer (OMT) to split the two orthogonal polarization components, which are then processed by two identical receiver chains that share the same local oscillator (LO). The intermediate frequency bands are analyzed using a digital fast Fourier transform (FFT) spectrometer/correlator implemented on the "Universal Software Radio Peripheral" device (USRP X310).[1] A similar USRP with two UBX-160 daughterboards was first used for atmospheric Ozone measurements in [14]. For TEMPERA-C, we are using two TwinRX daughterboards. Each of them contains two coherent superheterodyne receivers. The two daughterboards are tuned to the line center of two different oxygen emission lines where they observe simultaneously the orthogonal polarizations. The baseband signals are digitized for each receiver with 200 MS/s and 14-bit resolution, and the on-board field-programmable gate array performs a real-time FFT analysis. The four complex spectra have a Nyquist bandwidth of 100 MHz and a resolution of 4096 channels each. These spectra are squared and accumulated independently to measure the total power in the two linear polarizations. In addition, they are correlated in real time, which allows us to derive the V-Stokes parameter and, hence, the left- and right-circular polarization spectra of the radiation. Similar digital spectrometers have been used previously for polarimetric observations in radio astronomy [15], but to our knowledge not for atmospheric remote sensing. Fig. 10 shows the schematic diagram of the TEMPERA-C polarimeter. The

[1]USRP X310 with TwinRX Daughterboard from www.ettus.com

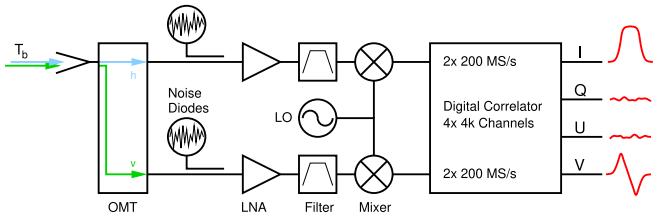

Fig. 10. Schematic diagram of the TEMPERA-C polarimeter.

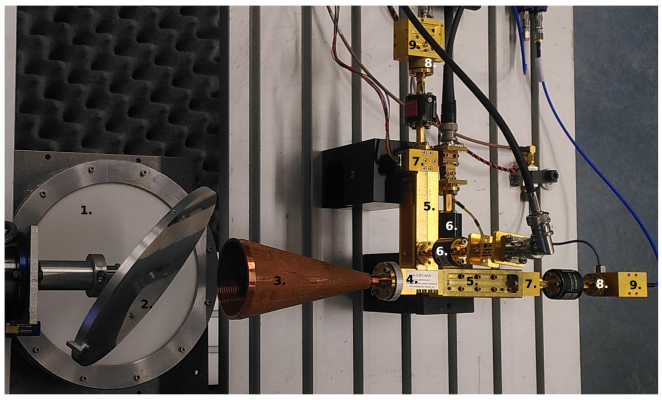

Fig. 11. Setup of the TEMPERA-C prototype with following components: *1) LN2 cold load; 2) rotating mirror; 3) feedhorn; 4) OMT; 5) coupler; 6) noise diodes; 7) low-noise amplifier (LNA); 8) bandpass filter; and 9) mixer.*

radiometric calibration of the instrument in operational use will be achieved by pointing the antenna at an ambient blackbody calibration target and injecting the signals of switchable noise diodes into the receivers through directional couplers. However, the prototype setup presented in this article was calibrated by switching the antenna between an ambient blackbody calibration target and a cold calibration target, consisting of a microwave absorber immersed in liquid nitrogen (LN2). Fig. 11 shows the setup of the initial TEMPERA-C prototype. The current prototype uses a simple Potter horn as feed and a flat rotating mirror for calibration. The final TEMPERA-C instrument will include a profiled corrugated feed, which is optimized to produce a symmetric ultra-Gaussian antenna pattern with low cross polarization, as well as a collimating quasi-optical network. More technical details are added in Table II.

VIII. Polarimetric Calibration

The digital correlator computes the square $|\langle E_h\rangle|^2, |\langle E_v\rangle|^2$ of both orthogonal polarized field components and its complex correlation $\langle E_h E_v^*\rangle$. In a first step, we assume an ideal and lossless receiver chain where the four output signals can be written in units of temperature as

$$A_h = |g_h\langle E_h\rangle|^2 + T_{Nh} \tag{14}$$

$$A_v = |g_v\langle E_v\rangle|^2 + T_{Nv} \tag{15}$$

$$A_U = 2\Re\left\{g_h g_v\langle E_h E_v^*\rangle\right\} \tag{16}$$

$$A_V = 2\Im\left\{g_h g_v\langle E_h E_v^*\rangle\right\}. \tag{17}$$

TABLE II
INSTRUMENT SPECIFICATIONS

OMT	
Manufacturer	AINFO
Port-to-Port Isolation	<–43 dB
Insertion Loss	<0.5 dB
LNA	
Manufacturer	LNF
Gain	>33dB
Noise Figure	2.4 dB
Bandpass filter	
Manufacturer	In house
3-dB Corner Fr	50.8-54.2 GHz
Insertion loss	<0.6 dB
Mixer	
Type	VDI
DSB conversion Loss	<6 dB
DSB Noise Temperature	<700 K
Digital Correlator	
Manufacturer	Ettus
Type	USRP X310
Daughterboards	2× TwinRX
Bandwidth	4×100 MHz
Channels	4×4096
Resolution	24.4 kHz

Here, g_h and g_v are the complex gains of the two receivers, and T_{Nh} and T_{Nv} are the corresponding receiver noise temperatures. With an analog correlator, the gain factors in (14)–(17) are not the same. With the digital spectrometer of TEMPERA-C, cross correlation is a completely numerical process, which allows the assumption that g_h and g_v in (14) and (15) are the same as in (16) and (17). The receiver noise is not included in the U and V components, because the radiometric noise of the two receiver chains is uncorrelated. It is common to use the Rayleigh–Jeans approximation; therefore, the relation between power and temperature units is linear. The gain, receiver noise, and brightness temperature are derived through a hot–cold load calibration, where the beam is switched alternately between the sky and two a known hot and cold blackbody source (see Fig. 11). The calibration equations for an ideal receiver are

$$T_h = A_h - T_{Nh} \tag{18}$$

$$T_v = A_v - T_{Nv} \tag{19}$$

$$T_V = A_V. \tag{20}$$

However, the breadboard receiver is far from ideal. Errors originate from multiple sources, which requires additional corrections, and thus, the simple approach from above is not suitable for practical implementation. Especially, the V-Stokes component is affected by even small errors, because its intensity is relatively low compared to the linear polarized components (see Fig. 12).

Possible error sources are the following.

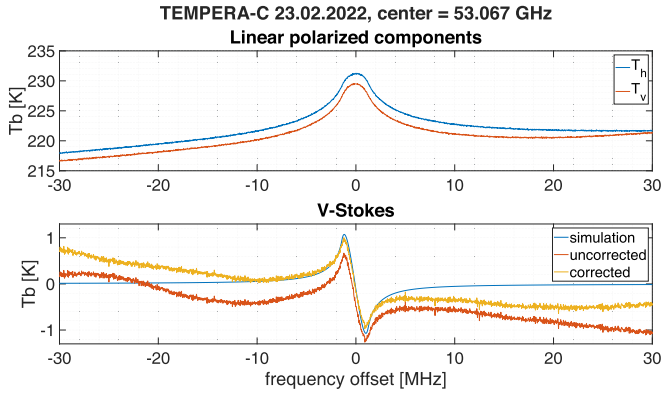

Fig. 12. Spectra of atmospheric microwave radiation, measured with the TEMPERA-C prototype setup.

1) The antenna pattern of the feedhorn is not the same for the two polarizations (asymmetry).
2) The OMT and feed do not ideally separate the polarization components (cross polarization).
3) Crosstalk between the two receiver chains after the OMT (crosstalk).

We assume that the main error source is cross polarization, which will be outlined in more detail in the following.

In a first step, we introduce frequency-dependent and complex cross-polarization terms c_h and c_v. The absolute value of c_h denotes the fraction of voltage leakage from the h-chain into the v-chain. The phase of c_h denotes the phase change of the leaked signal (and *vice versa* for c_v). With that, (14)–(17) can be rewritten in the following way:

$$A_h = |g_h\left(\langle E_h\rangle + c_v\langle E_v\rangle\right)|^2 + T_{Nh} \tag{21}$$

$$A_v = |g_v\left(\langle E_v\rangle + c_h\langle E_h\rangle\right)|^2 + T_{Nv} \tag{22}$$

$$A_U = 2\Re\left\{g_h g_v^*\left(\langle E_h\rangle + c_v\langle E_v\rangle\right)\left(\langle E_v\rangle + c_h\langle E_h\rangle\right)^*\right\} \tag{23}$$

$$A_V = 2\Im\left\{g_h g_v^*\left(\langle E_h\rangle + c_v\langle E_v\rangle\right)\left(\langle E_v\rangle + c_h\langle E_h\rangle\right)^*\right\}. \tag{24}$$

The goal is to derive c_h and c_v in order to correct the measurement by subtracting these terms. One approach to this problem is to use a fully polarimetric calibration target, consisting of hot and cold blackbodies, a polarizing wire grid, and a phase retardation plate [16]. In this article, we present a simpler alternative approach, which requires only unpolarized hot and cold blackbody targets. For these, we can assume that

$$\langle E_h E_v^*\rangle = 0 \quad \text{(black-body radiation)}. \tag{25}$$

Concerning the phases of the complex gains ϕ_h and ϕ_v, only their difference $\Delta\phi = \phi_h - \phi_v$ is of interest. Therefore, the following simplification can be made:

$$\phi_v = 0 \tag{26}$$

such that $\Delta\phi = \phi_h$, which was determined in a postprocess by a least-squares fit on the simulated spectrum. An additional simplification is to allow only for terms linear in c_h and c_v, which is justified by the assumption

$$|c_h c_v^*| \ll 1. \tag{27}$$

When the antenna beam is directed on the hot and cold target and with the assumptions (25) and (27), (23) and (24) become

$$A_U = 2\Re\left\{g_h g_v^*\left(c_h^*|\langle E_h\rangle|^2 + c_v|\langle E_v\rangle|^2\right)\right\} = 0 \tag{28}$$

$$A_V = 2\Im\left\{g_h g_v^*\left(c_h^*|\langle E_h\rangle|^2 + c_v|\langle E_v\rangle|^2\right)\right\} = 0. \tag{29}$$

With two targets, the above expression yields four equations to derive four unknowns contained in the two complex coefficients c_h and c_v. The complex gains g_h and g_v and the noise temperatures T_{Nh} and T_{Nv} can be derived beforehand by a hot/cold load calibration using (21) and (22).

Once the cross-polarization terms are known, the general correction term for the V-Stokes component reads as

$$C_V = 2\Im\left\{g_h g_v^*\left(c_h^*|\langle E_h\rangle|^2 + c_v|\langle E_v\rangle|^2\right)\right\}. \tag{30}$$

And the corrected V-Stokes component is simply the difference

$$T_V = A_V - C_V. \tag{31}$$

It has to be mentioned that the output signal consists of the partially cross-polarized field components with the receiver noise in addition $A_h/|g_h|^2$, $A_v/|g_v|^2$ [according to (23) and (24)], the pure fields $\langle E_h\rangle$ and $\langle E_v\rangle$ are not known. However, this appears to be of minor concern because considering the correction term [see (30)], cross-polarization terms cancels due to condition (27), and as mentioned above, the receiver noise is assumed to be uncorrelated. Therefore, it is reasonable to replace $\langle E_h\rangle$ and $\langle E_v\rangle$ with $A_h/|g_h|^2$ and $A_v/|g_v|^2$ in (23)–(30).

Fig. 12 shows the first polarimetric observations with the TEMPERA-C prototype after an integration time of about 12 h. The upper panel shows the brightness temperature around the 53.067-GHz emission line in the two orthogonal polarizations after a total power calibration with the hot and the cold target. We expect only a small difference between T_h and T_v at the line center, but not the observed offset on the line wings. Possible explanations for this calibration bias are the differences between the antenna pattern in the E- and H-planes of the feedhorn, the polarization dependence of the losses of the rotating calibration reflector, or a small nonlinearity of the receivers.

The lower panel of Fig. 12 shows the observed V-Stokes component of the correlator output with and without correction and compares it to the expected difference between the simulated LCP and RCP spectra. The observed signature close to the line center is very similar to the simulations in both the corrected and uncorrected spectra. The line wings, however, exhibit a slope of the baseline different from 0. This offset on the line wings is slightly improved by the corrections with (31), but a significant systematic bias remains. This means that apart from cross polarization, additional error sources affect the measurement. Fig. 13 illustrates the hot and cold load spectra of A_V and A_U before and after the correction. Condition (25) forces the corrected terms to zero. The measured LCP and RCP spectra after the correction are shown for the line center in Fig. 14.

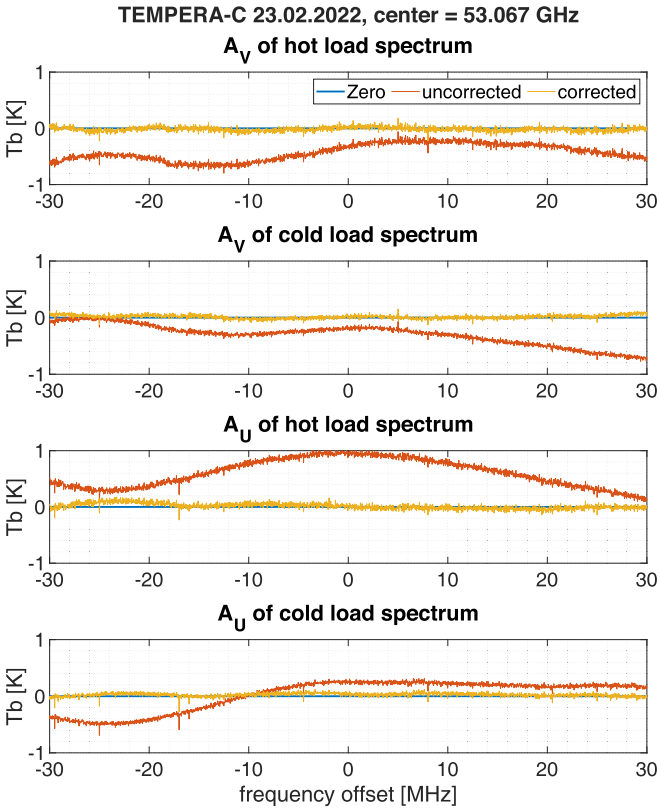

Fig. 13. Illustration of hot and cold load spectra before and after correction.

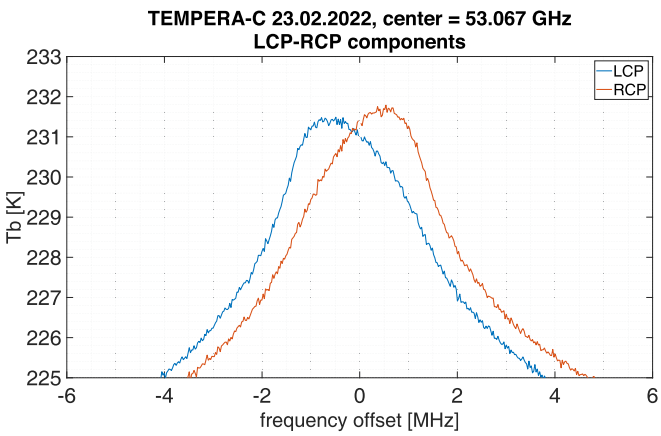

Fig. 14. Illustration of LCP and RCP components estimated with corrected data.

IX. Conclusion

In this article, we illustrated that observations of oxygen emission lines between 52 and 54 GHz can be used for temperature sounding in the middle atmosphere and how the vertical range of these retrievals is limited by the Zeeman effect. We further demonstrated by simulations that a simultaneous retrieval of LCP and RCP emission lines can improve the vertical range of the retrieval compared to the retrieval of a single emission line with linear polarization.

The increase in measurement response at 20–27 km can be explained by an increase of the signal-to-noise ratio by a factor of $\sqrt{2}$ by retrieving two instead of one spectra. The lower MR values between 27 and 46 km originate from a negative peak in the AVK at these altitudes, which is caused by an overestimation of the apriori error in this region. This small decrease, however,

does not affect the overall performance. In this study, we demonstrated that polarimetric observations of two oxygen emission lines and retrievals accounting for the Zeeman line splitting are beneficial to increase the MR at altitudes between 46 and 60 km. The improvement in the MR is about 12% (at 50 km) and 45% (at 60 km) higher than for the retrieval with single polarization. The effective upper altitude limit (altitudes with MR > 0.6) has increased from 55 km (with single polarization) to 59 km (fully polarimetric). The new TEMPERA-C instrument will provide fully polarimetric observations of the oxygen emission lines. Resolving the Zeeman splitting of the line center between the left- and right-circular polarization will extend the vertical range of the temperature retrievals into the lower mesosphere up to 60 km or above. First observations with a TEMPERA-C prototype receiver demonstrated the feasibility of the digital FFT spectrometer/correlator concept. Further work is needed to identify and correct additional error sources, such as a crosstalk between the receiver chains, to improve the polarimetric calibration of these observations.

Acknowledgment

Witali Krochin and Gunter Stober are members of the Oeschger Center for Climate Change Research.

References

[1] O. Stähli, A. Murk, N. Kämpfer, C. Mätzler, and P. Eriksson, "Microwave radiometer to retrieve temperature profiles from the surface to the stratopause," *Atmos. Meas. Techn.*, vol. 6, no. 9, pp. 2477–2494, Sep. 2013.

[2] T. Rose, S. Crewell, U. Löhnert, and C. Simmmer, "A network suitable microwave radiometer for operational monitoring of the cloudy atmosphere," *Atmos. Res.*, vol. 75, no. 3, pp. 183–200, 2005, doi: 10.1016/j.atmosres.2004.12.005.

[3] H. H. Auman *et al.*, "AIRS/AMSU/HSB on the aqua mission: Design, science objectives, data products, and processing systems," *IEEE T. Geosci. Remote Sens.*, vol. 41, no. 2, 2003, doi: 10.3390/atmos11050490.

[4] X. Fuzhong *et al.* "Calibration of suomi national polar-orbiting partnership advanced technology microwave sounder," *J. Geophysical Res. Atmos.*, vol. 118, no. 19, pp. 11,187–11,200, 2013.

[5] A. A. Shvetsov *et al.*, "Ground-based sounding of the middle-atmosphere thermal structure in the frequency range 50-60 GHz," *Radiophys. Quantum Electron.*, vol. 54, nos. 8/9, pp. 569–576, 2012.

[6] K. Baumgarten and G. Stober, "On the evaluation of the phase relation between temperature and wind tides based on ground-based measurements and reanalysis data in the middle atmosphere," *Ann. Geophys.*, vol. 37, no. 4, pp. 581–602, 2019.

[7] F. Schranz, J. Hagen, G. Stober, K. Hocke, A. Murk, and N. Kämpfer, "Small-scale variability of stratospheric ozone during the sudden stratospheric warming 2018/2019 observed at Ny-ålesund, Svalbard," *Atmos. Chem. Phys.*, vol. 20, no. 18, pp. 10791–10806, 2020.

[8] W. Krochin, F. Navas-Guzmán, D. Kuhl, A. Murk, and G. Stober, "Continuous temperature soundings at the stratosphere and lower mesosphere with a ground-based radiometer considering the Zeeman effect," *Atmos. Meas. Techn.*, vol. 2021, pp. 1–28, 2021.

[9] S. A. Buehler, J. Mendrok, P. Eriksson, A. Perrin, R. Larsson, and O. Lemke, "ARTS, the Atmospheric Radiative Transfer Simulator—version 2.2, the planetary toolbox edition," *Geosci. Model Dev.*, vol. 11, no. 4, pp. 1537–1556, Apr. 2018.

[10] C. D. Rodgers, *Inverse Methods for Atmospheric Sounding: Theory and Practice*, Singapore: World Scientific, 2000.

[11] J. Randa *et al.*, "Recommended terminology for microwave radiometry," Nat. Inst. Standards Technol., Gaithersburg, MD, USA, Tech. Note TN1551, 2008.

[12] F. Navas-Guzmán, N. Kämpfer, A. Murk, R. Larsson, S. A. Buehler, and P. Eriksson, "Zeeman effect in atmospheric O_2 measured by ground-based microwave radiometry," *Atmos. Meas. Techn.*, vol. 8, no. 4, pp. 1863–1874, Apr. 2015.

[13] R. Larsson, B. Lankhaar, and P. Eriksson, "Updated Zeeman effect splitting coefficients for molecular oxygen in planetary applications," *J. Quant. Spectrosc. Radiat. Transf.*, vol. 224, pp. 431–438, 2019.

[14] J. Hagen, A. Luder, A. Murk, and N. Kämpfer, "Frequency-agile FFT spectrometer for microwave remote sensing applications," *Atmosphere*, vol. 11, no. 5, 2020, Art. no. 490.

[15] A. Alvear *et al.*, "FPGA-based digital signal processing for the next generation radio astronomy instruments: Ultra-pure sideband separation and polarization detection," in *Proc. SPIE*, vol. 9914, pp. 332–345, 2016.

[16] J. Lahtinen, A. J. Gasiewski, M. Klein, and I. S. Corbella, "A calibration method for fully polarimetric microwave radiometers," *IEEE Trans. Geosci. Remote Sens.*, vol. 41, no. 3, pp. 588–602, Mar. 2003.

Witali Krochin received the bachelor.s degree in physics and the master's degree in theoretical physics, in 2017 and 2020, respectively, from the University of Bern, Bern, Switzerland, where he is currently working toward the Ph.D. degree in microwave physics with the Institute of Applied Physics.

Gunter Stober received the Diploma in physics and the Ph.D. degree in meteor physics from the University of Leipzig, Leipzig, Germany, in 2006 and 2009, respectively, and the Habilitation in microwave physics from the University of Bern, Bern, Switzerland, in 2020.

He is currently a Lecturer of meteor physics, microwave physics, and atmospheric dynamics with the University Bern. Since 2022, he has been the Head of the Atmospheric Processes and Radiometry Group.

Axel Murk received the master's degree from the Technical University of Munich, Munich, Germany, in 1995, and the Ph.D. degree from the University of Bern, Bern, Switzerland, in 1999, both in physics.

Since 2018, he has been the Head of the Microwave Physics Division.

Acknowledgements

I would like to thank my supervisor **Gunter Stober** for constant and passionate support in every issue. **Axel Murk** for the many patient consultations and providing bottomless technical and physical knowledge. **Andres Luder** and **André Amrein** from the electronic workshop for constructing and assembling TEMPERA-C. **Roland Albers** from the microwave group for designing the optic of TEMPERA-C and providing emotional support in difficult times. **Tobias Plüss** from the microwave group for designing the antenna horn and building electronic parts for TEMPERA-C. **Alexandra Brönnimann** from the microwave group for performing preliminary work and testing on the early TEMPERA-C prototype in her bachelor thesis. A special thank goes to **Richard Larsson** from the ARTS team who implemented the Zeeman broadening and line mixing algorithm. Also, I would like to thank **Daniela Bissig** and **Erich Furrer** from the Jungfraujoch high altitude research station for their passionate support. The last thank goes to **Thomas Käser** who kindly provided this nice latex layout.

References

Andrews, D. G., Holton, J. R., and Leovy, C. B. (1987). *Middle Atmosphere Dynamics*. Academic Press. ISBN: 978-0-12-058575-5.

Bailey, S. M. et al. (2021). "Trends in the polar summer mesosphere temperature and pressure altitude from satellite observations". In: *Journal of Atmospheric and Solar-Terrestrial Physics* 220, p. 105650. DOI: 10.1016/j.jastp.2021.105650.

Baumgarten, K. and Stober, G. (2019a). "On the evaluation of the phase relation between temperature and wind tides based on ground-based measurements and reanalysis data in the middle atmosphere". In: *Annales Geophysicae* 37.4, pp. 581–602. DOI: 10.5194/angeo-37-581-2019.

— (2019b). "On the evaluation of the phase relation between temperature and wind tides based on ground-based measurements and reanalysis data in the middle atmosphere". In: *Annales Geophysicae* 37, pp. 581–602. DOI: 10.5194/angeo-37-581-2019.

Becker, E. (2012). "Dynamical Control of the Middle Atmosphere". In: *Space Science Reviews* 168, pp. 283–314. DOI: 10.1007/s11214-011-9841-5.

— (2017). "Mean-Flow Effects of Thermal Tides in the Mesosphere and Lower Thermosphere". In: *Journal of the Atmospheric Sciences* 74.6, pp. 2043–2063. DOI: 10.1175/JAS-D-16-0194.1.

Bernet, L., Navas Guzmán, F., and N, K. (2017). "The effect of cloud liquid water on tropospheric temperature retrievals from microwave measurements". In: *Atmospheric Measurement Techniques* 10.11, pp. 4421–4437. DOI: 10.5194/amt-10-4421-2017.

Brewer, A. W. (1949). "Evidence for a world circulation provided by measurements of helium and water vapour distribution in the stratosphere". In: *Q. J. R. Meteorol. Soc.* 75.326, pp. 351–363. DOI: 10.1002/qj.49707532603.

Buehler, S. A. et al. (2018). "ARTS, the Atmospheric Radiative Transfer Simulator – version 2.2, the planetary toolbox edition". In: *Geoscientific Model Development* 11.4, pp. 1537–1556. DOI: 10.5194/gmd-11-1537-2018.

Buehler, S. et al. (2005). "ARTS, the atmospheric radiative transfer simulator". In: *Journal of Quantitative Spectroscopy and Radiative Transfer* 91.1, pp. 65–93. DOI: 10.1016/j.jqsrt.2004.05.051.

Butchart, N. (2014). "The Brewer-Dobson circulation". In: *Reviews of Geophysics* 52.2, pp. 157–184. DOI: 10.1002/2013RG000448.

Caspel, W. E. van et al. (2022). "The Mid- to High-Latitude Migrating Semidiurnal Tide: Results From a Mechanistic Tide Model and SuperDARN Observations". In: *Journal of Geophysical Research: Atmospheres* 127.1. DOI: 10.1029/2021JD036007.

Chang, L. et al. (2008). "Structure of the migrating diurnal tide in the Whole Atmosphere Community Climate Model (WACCM)". In: *Advances in Space Research* 41, pp. 1398–1407. DOI: 10.1016/j.asr.2007.03.035.

Chapman, S. and Lindzen, R. (1970). "Atmospheric Tides: Thermal and Gravitational". In: *D. Reidel Publishing company* New York. DOI: 10.1007/978-94-010-3399-2.

Dhadly, M. S. et al. (2018). "Short-Term and Interannual Variations of Migrating Diurnal and Semidiurnal Tides in the Mesosphere and Lower Thermosphere". In: *Journal of Geophysical Research: Space Physics* 123.8, pp. 7106–7123. DOI: 10.1029/2018JA025748.

Dobson, G. M. B. (1949). "Origin and distribution of polyatomic molecules in the atmosphere". In: *Proc. R. Soc. Lond* 236.1205, pp. 187–193. DOI: 10.1098/rspa.1956.0127.

Dobson, G. M. B., Harrison, D. N., and Lawrence, J. (1929). "Measurements of the amount of ozone in the Earth's atmosphere and its relation to other geophysical conditions". In: *Proc. R. Soc. Lond* 122.790, pp. 456–486. DOI: 10.1098/rspa.1929.0034.

Du, J. et al. (2007). "Semidiurnal tides from the extended Canadian Middle Atmosphere Model (CMAM) and comparisons with TIMED Doppler interferometer (TIDI) and meteor radar observations". In: *Journal of Atmospheric and Solar-Terrestrial Physics* 69.17, pp. 2159–2202. DOI: 10.1016/j.jastp.2007.07.014.

Eriksson, P. et al. (2011). "ARTS, the atmospheric radiative transfer simulator, version 2". In: *Journal of Quantitative Spectroscopy and Radiative Transfer* 112.10, pp. 1551–1558. DOI: 10.1016/j.jqsrt.2011.03.001.

Eriksson, P., Jiménez, C., and Buehler, S. A. (2005). "Qpack, a general tool for instrument simulation and retrieval work". In: *Journal of Quantitative Spectroscopy and Radiative Transfer* 91.1, pp. 47–64. DOI: 10.1016/j.jqsrt.2004.05.050.

Fong, W. et al. (2022). "Winter temperature tides from 30 to 110 km at McMurdo (77.8°S, 166.7°E), Antarctica: Lidar observations and comparisons with WAM". In: *Journal of Geophysical Research: Atmospheres* 119, pp. 2846–2863. DOI: doi:10.1002/2013JD020784.

Forbes, J. (1982). "Atmospheric Tides 1. Model Description and Results for the Solar Diurnal Componen". In: *Journal of Geophysical Research* 87.A7, pp. 5222–5240. DOI: doi:10.1029/2007JD008725.

Forbes, J. M. and Wu, D. (2006). "Solar Tides as Revealed by Measurements of Mesosphere Temperature by the MLS Experiment on UARS". In: *Journal of the Atmospheric Sciences* 63.7, pp. 1776–1797. DOI: 10.1175/JAS3724.1.

Gasiewski, A. and Kunkee, D. (1993). "Calibration and applications of polarization-correlating radiometers". In: *IEEE Transactions on Microwave Theory and Techniques* 41.5, pp. 767–773. DOI: 10.1109/22.234509.

Gille, S., Hauchecorne, A., and Chanin, M. (1991). "Semidiurnal and Diurnal Tidal Effects in the Middle Atmosphere as Seen by Rayleigh Lidar". In: *Journal of Geophysical Research* 96.D4, pp. 7579–7587. DOI: 10.1029/90JD02570.

Gordon, I. et al. (2017). "The HITRAN2016 molecular spectroscopic database". In: *Journal of Quantitative Spectroscopy and Radiative Transfer* 203. HITRAN2016 Special Issue, pp. 3–69. DOI: 10.1016/j.jqsrt.2017.06.038.

Grant, W. P. (2006). *A First Course in Atmospheric Radiation.* Sundog Publishing. ISBN: 978-0-9729033-1-8.

Hagan, M., Forbes, J., and F, V. (1995). "On modeling migrating solar tides". In: *Geophysical Research Letters* 22.8, pp. 893–896. DOI: 10.1029/95GL00783.

— (1999). "GSWM-98: Results for migrating solar tides". In: *Journal of Geophysical Research: Space Physics* 104.A4, pp. 6813–6827. DOI: 10.1029/1998JA900125.

Hagen, J. et al. (2020). "First measurements of tides in the stratosphere and lower mesosphere by ground-based Doppler microwave wind radiometry". In: *Atmospheric Chemistry and Physics* 20.4, pp. 2367–2386. DOI: 10.5194/acp-20-2367-2020.

Holton, J. R. et al. (1995). "Stratosphere-troposphere exchange". In: *Rev. Geophys* 33.4, pp. 403–439. DOI: 10.1029/95RG02097.

Holton, J. R. and Hakim, G. J. (2012). *An introduction to dynamic meteorology.—Fifth edition.* Academic Press. ISBN: 978-0-12-384866-6.

Hough, S. S. and Darwin, G. H. (1898). "V. On the application of harmonic analysis to the dynamical theory of the tides. Part II. On the general integration of Laplace's dynamical equations". In: *Philosophical Transactions of the Royal Society of London. Series A, Containing Papers of a Mathematical or Physical Character* 191, pp. 139–185. DOI: 10.1098/rsta.1898.0005.

Huang, F. T. et al. (2006). "Diurnal variations of temperature and winds inferred from TIMED and UARS measurements". In: *Journal of Geophysical Research: Space Physics* 111.A10. DOI: doi.org/10.1029/2005JA011426.

Ingold, T. and Kämpfer, N. (1998). "Weighted mean tropospheric temperature and transmittance determination at millimeter-wave frequencies for ground-based applications". In: *Radio Science* 22.4, pp. 905–918. DOI: 10.1029/98RS01000.

Kopp, M., Gerding, J., and Lübken, F.-J. (2015). "Tidal signatures in temperatures derived from daylight lidar soundings above Kühlungsborn". In: *Journal of Atmospheric and Solar-Terrestrial Physics* 127, pp. 37–50. DOI: 10.1016/j.jastp.2014.09.002.

Krochin, W., Murk, A., and Stober, G. (2024). "Thermal tides in the middle atmosphere at mid-latitudes measured with a ground-based microwave Radiometer". In: *Atmospheric Measurement Techniques Discussions* 2024, pp. 1–24. DOI: 10.5194/amt-2024-42.

Krochin, W. et al. (2022a). "Continuous temperature soundings at the stratosphere and lower mesosphere with a ground-based radiometer considering the Zeeman effect". In: *Atmospheric Measurement Techniques* 15, pp. 2231–2249. DOI: 10.5194/amt-15-2231-2022.

— (2022b). "Development of a Polarimetric 50-GHz Spectrometer for Temperature Sounding in the Middle Atmosphere". In: *IEEE Journal of selected topics in applied earth observations and remote sensing* 15. DOI: 10.48350/186172.

Lahtinen, J. et al. (2003). "A calibration method for fully polarimetric microwave radiometers". In: *IEEE Transactions on Geoscience and Remote Sensing* 41.3, pp. 588–602. DOI: 10.1109/TGRS.2003.810203.

Larsson, R., Lankhaar, B., and Eriksson, P. (2019). "Updated Zeeman effect splitting coefficients for molecular oxygen in planetary applications". In: *Journal of Quantitative Spectroscopy and Radiative Transfer* 224, pp. 431–438. DOI: 10.1016/j.jqsrt.2018.12.004.

Larsson, R. et al. (2014). "A treatment of the Zeeman effect using Stokes formalism and its implementation in the Atmospheric Radiative Transfer Simulator (ARTS)". In: *Journal of Quantitative Spectroscopy and Radiative Transfer* 133, pp. 445–453. DOI: 10.1016/j.jqsrt.2013.09.006.

Liebe, H., Rosenkranz, P., and Hufford, G. (1992). "Atmospheric 60-GHz oxygen spectrum: New laboratory measurements and line parameters". In: *Journal of Quantitative Spectroscopy and Radiative Transfer* 48.5. Special Issue Conference on Molecular Spectroscopic Databases, pp. 629–643. DOI: 10.1016/0022-4073(92)90127-P.

Lindzen (1990). *Dynamics in Atmospheric Physics*. Cambridge University Press.

Lindzen, R. S. (1979). "Atmospheric Tides". In: *Annual Review of Earth and Planetary Sciences* 7.1, pp. 199–225. DOI: 10.1146/annurev.ea.07.050179.001215.

— (1981). "Turbulence and stress owing to gravity wave and tidal breakdown". In: *Journal of Geophysical Research: Oceans* 86.C10, pp. 9707–9714. DOI: 10.1029/JC086iC10p09707.

Lindzen, R. S. and Chapman, S. (1969). "Atmospheric Tides". In: *Space Sci. Rev.* 10, pp. 3–188.

Liou, K. N. (2002). *An Introduction to Atmospheric Radiation*. Academic Press. ISBN: 978-0-12-451451-5.

Liu, H.-L. et al. (2007). "Comparative study of short-term diurnal tidal variability". In: *Journal of Geophysical Research: Atmospheres* 112.D18. DOI: 10.1029/2007JD008542.

Livesey, N. et al. (2006). "Retrieval algorithms for the EOS Microwave limb sounder (MLS)". In: *IEEE Transactions on Geoscience and Remote Sensing* 44.5, pp. 1144–1155. DOI: 10.1109/TGRS.2006.872327.

Lomb, N. (1976). "Least-squares frequency analysis of unequally spaced data". In: *Astrophysics and Space Science* 39, pp. 447–462.

Lu, X. et al. (2011). "Seasonal variability of the diurnal tide in the mesosphere and lower thermosphere over Maui, Hawaii (20.7°N, 156.3°W)". In: *Journal of Geophysical Research: Atmospheres* 116.D17. DOI: 10.1029/2011JD015599.

Lübken, F. J., Berger, U., and Baumgarten, G. (2018). "On the Anthropogenic Impact on Long-Term Evolution of Noctilucent Clouds". In: *Geophysical Research Letters* 45.13, pp. 1–28. DOI: 10.5194/egusphere-2024-65.

Makarov, D., Tretyakov, M., and Rosenkranz, P. (2011). "60-GHz oxygen band: Precise experimental profiles and extended absorption modeling in a wide temperature range". In: *Journal of Quantitative Spectroscopy and Radiative Transfer* 112.9, pp. 1420–1428. DOI: 10.1016/j.jqsrt.2011.02.018.

Matsuno, T. (1971). "A Dynamical Model of the Stratospheric Sudden Warming". In: *Journal of Atmospheric Sciences* 28(8), pp. 1479–1494.

Matthias, V. et al. (2021). "Vertical Structure of the Arctic Spring Transition in the Middle Atmosphere". In: *Journal of Geophysical Research: Atmospheres* 126.10. DOI: 10.1029/2020JD034353.

Mätzler, C., ed. (2006). *Thermal Microwave Radiation: Applications for Remote Sensing*. Electromagnetic Waves. Institution of Engineering and Technology.

Navas-Guzmán et al. (2015). "Zeeman effect in atmospheric O_2 measured by ground-based microwave radiometry". In: *Atmospheric Measurement Techniques* 8, pp. 1863–1874. DOI: 10.5194/amt-8-1863-2015.

Oberheide, J. et al. (2009). "Tropospheric tides from 80 to 400 km: Propagation, interannual variability, and solar cycle effects". In: *Journal of Geophysical Research: Atmospheres* 114.D1. DOI: 10.1029/2009JD012388.

Oberheide, J. et al. (2011). "Climatology of upward propagating diurnal and semidiurnal tides in the thermosphere". In: *Journal of Geophysical Research: Space Physics* 116.A11. DOI: 10.1029/2011JA016784.

Ortland, A. D. (2005). "A Study of the Global Structure of the Migrating Diurnal Tide Using Generalized Hough Modes". In: *JOURNAL OF THE ATMOSPHERIC SCIENCES* 62, pp. 2684–2702. DOI: 10.1016/j.jastp.2013.07.010.

Parkinson, C. L. (2022). "The Earth-Observing Aqua Satellite Mission: 20 Years and Counting". In: *Earth and Space Science* 9.9. e2022EA002481 2022EA002481, e2022EA002481. DOI: 10.1029/2022EA002481.

Pokhotelov, D. et al. (2018). "Seasonal variability of atmospheric tides in the mesosphere and lower thermosphere: meteor radar data and simulations". In: *Annales Geophysicae* 36.3, pp. 825–830. DOI: 10.5194/angeo-36-825-2018.

Press, W. et al. (1992). "Numerical Recipes in C: the Art of Scientific Computing". In: *Cambridge Univ. Press*, pp. 575–584.

Riggin, D. M. et al. (2002). "Jicamarca radar observations of the diurnal and semidiurnal tide in the troposphere and lower stratosphere". In: *Journal of Geophysical Research: Atmospheres* 107.D8, ACL 5-1-ACL 5–10. DOI: 10.1029/2001JD001216.

Rodgers, C. D. (2000). *Inverse Methods for Atmospheric sounding Theory and Practice*. World Scientific. DOI: doi.org/10.1142/3171.

Rosenkranz, P. (1975). "Shape of the 5 mm oxygen band in the atmosphere". In: *IEEE Transactions on Antennas and Propagation* 23.4, pp. 498–506. DOI: 10.1109/TAP.1975.1141119.

Russell III, J. et al. (1999). "Overview of the SABER experiment and preliminary calibration results". In: *Proceedings of SPIE - The International Society for Optical Engineering* 3756.

Sakazaki, T. et al. (2012). "Diurnal tides from the troposphere to the lower mesosphere as deduced from TIMED/SABER satellite data and six global reanalysis data sets". In: *Journal of Geophysical Research* 117.D13108. DOI: doi:10.1029/2011JD017117.

Sauvageat, E. et al. (2023). "Microwave radiometer observations of the ozone diurnal cycle and its short-term variability over Switzerland". In: *Atmospheric Chemistry and Physics* 23.13, pp. 7321–7345. DOI: 10.5194/acp-23-7321-2023.

Scargle, J. D. (1982). "Studies in astronomical time series analysis. II. Statistical aspects of spectral analysis of unevenly spaced data." In: 263, pp. 835–853. DOI: 10.1086/160554.

Schranz, F. et al. (2019). "Investigation of Arctic middle-atmospheric dynamics using 3 years of H_2O and O_3 measurements from microwave radiometers at Ny-Ålesund". In: *Atmospheric Chemistry and Physics* 19.15, pp. 9927–9947. DOI: 10.5194/acp-19-9927-2019.

Schranz, F. et al. (2020). "Small-scale variability of stratospheric ozone during the sudden stratospheric warming 2018/2019 observed at Ny-Ålesund, Svalbard". In: *Atmospheric Chemistry and Physics* 20.18, pp. 10791–10806. DOI: 10.5194/acp-20-10791-2020.

She, C. Y. et al. (2002). "Tides in the mesopause region over Fort Collins, Colorado (41°N, 105°W) based on lidar temperature observations covering full diurnal cycles". In: *Journal of Geophysical Research: Atmospheres* 107.D18, ACL 4-1-ACL 4–12. DOI: 10.1029/2001JD001189.

Shi, G. et al. (2023). "Ozone and water vapor variability in the polar middle atmosphere observed with ground-based microwave radiometers". In: *Atmospheric Chemistry and Physics* 23.16, pp. 9137–9159. DOI: 10.5194/acp-23-9137-2023.

Smith, A. K. (2012). "Global Dynamics of the MLT". In: *Surveys in Geophysics* 33, pp. 1177–1230. DOI: 10.1007/s10712-012-9196-9.

Stähli, O. et al. (2013). "Microwave radiometer to retrieve temperature profiles from the surface to the stratopause". In: *Atmospheric Measurement Techniques* 6, pp. 2477–2494. DOI: 10.5194/amt-6-2477-2013.

Stamnes, K., Thomas, G. E., and Stamnes, J. J. (2017). *Radiative transfer in the atmoshphere and ocean.* Cambridge University Press. ISBN: 978-1-107-09473-4.

Stevens, M. H. et al. (2022). "Northern Mid-Latitude Mesospheric Cloud Frequencies Observed by AIM/CIPS: Interannual Variability Driven by Space Traffic". In: *Earth and Space Science* 9.6. DOI: 10.1029/2022EA002217.

Stober, G. et al. (2020). "Comparative study between ground-based observations and NAVGEM-HA analysis data in the mesosphere and lower thermosphere region". In: *Atmospheric Chemistry and Physics* 20, pp. 11979–12010. DOI: 10.5194/acp-20-11979-2020.

Stober, G. et al. (2021). "Interhemispheric differences of mesosphere–lower thermosphere winds and tides investigated from three whole-atmosphere models and meteor radar observations". In: *Atmospheric Chemistry and Physics* 21.18, pp. 13855–13902. DOI: 10.5194/acp-21-13855-2021.

Thébault, E. et al. (2015). "International Geomagnetic Reference Field: the 12th generation". In: *Earth, Planets and Space* 67.1, pp. 1880–5981. DOI: 10.1186/s40623-015-0228-9.

Torrence, C. and Compo, G. P. (1998). "A Practical Guide to Wavelet Analysis". In: *Bulletin of the American Meteorological Society* 79.1, pp. 61–78. DOI: 10.1175/1520-0477(1998)079<0061:APGTWA>2.0.CO;2.

Tretyakov, M. et al. (2005). "60-GHz oxygen band: precise broadening and central frequencies of fine-structure lines, absolute absorption profile at atmospheric pressure, and revision of mixing coefficients". In: *Journal of Molecular Spectroscopy* 231.1, pp. 1–14. DOI: 10.1016/j.jms.2004.11.011.

Van Vleck, J. H. and Weisskopf, V. F. (1945). "On the Shape of Collision-Broadened Lines". In: *Rev. Mod. Phys.* 17 (2-3), pp. 227–236. DOI: 10.1103/RevModPhys.17.227.

Vincent, R. A., Tsuda, T., and Kato, S. (1988). "A comparative study of mesospheric solar tides observed at Adelaide and Kyoto". In: *Journal of Geophysical Research: Atmospheres* 93.D1, pp. 699–708. DOI: 10.1029/JD093iD01p00699.

Vleck, J. H. van (1934). "Magnetic Dipole Radiation and the Atmospheric Absorption Bands of Oxygen". In: 80, p. 161. DOI: 10.1086/143594.

— (1947). "The Absorption of Microwaves by Oxygen". In: *Phys. Rev.* 71 (7), pp. 413–424. DOI: 10.1103/PhysRev.71.413.

Ward, W. E. et al. (2010). "On the consistency of model, ground-based, and satellite observations of tidal signatures: Initial results from the CAWSES tidal campaigns". In: *Journal of Geophysical Research: Atmospheres* 115.D7. DOI: 10.1029/2009JD012593.

Waters, J. et al. (2006). "The Earth observing system microwave limb sounder (EOS MLS) on the aura Satellite". In: *IEEE Transactions on Geoscience and Remote Sensing* 44.5, pp. 1075–1092. DOI: 10.1109/TGRS.2006.873771.

Xu, J. et al. (2009). "Seasonal and quasi-biennial variations in the migrating diurnal tide observed by Thermosphere, Ionosphere, Mesosphere, Energetics and Dynamics (TIMED)". In: *Journal of Geophysical Research: Atmospheres* 114.D13. DOI: doi.org/10.1029/2008JD011298.

Yuan, T. et al. (2021). "Temperature Tides Across the Mid-Latitude Summer Turbopause Measured by a Sodium Lidar and MIGHTI/ICON". In: *Journal of Geophysical Research: Atmospheres* 126.16. DOI: 10.1029/2021JD035321.

Yuan, T. et al. (2008). "Seasonal variations of semidiurnal tidal perturbations in mesopause region temperature and zonal and meridional winds above Fort Collins, Colorado (40.6°N, 105.1°W)". In: *Journal of Geophysical Research: Atmospheres* 113.D20. DOI: 10.1029/2007JD009687.

Yuan, T. et al. (2014). "Vertical tidal wind climatology from full-diurnal-cycle temperature and Na density lidar observations at Ft. Collins, CO (41N, 105W)". In: *J. Geophys. Res. Atmos.* 119.8, pp. 4600–4615. DOI: 10.1002/2013JD020338.

Zhang, X., Forbes, J., and Hagan, M. (2010). "Longitudinal variation of tides in the MLT region: 1. Tides driven by tropospheric net radiative heating". In: *Journal of Geophysical Research* 115.A06316. DOI: doi:10.1029/2009JA014897.

Zhang, X. et al. (2006). "Monthly tidal temperatures 20–120 km from TIMED/SABER". In: *Journal of Geophysical Research: Space Physics* 111.A10. DOI: 10.1029/2005JA011504.

Erklärung

gemäss Art. 18 PromR Phil.-nat. 2019

Name/Vorname:

Matrikelnummer:

Studiengang:

Bachelor ☐ Master ☐ Dissertation ☑

Titel der Arbeit:

LeiterIn der Arbeit:

Ich erkläre hiermit, dass ich diese Arbeit selbständig verfasst und keine anderen als die angegebenen Quellen benutzt habe. Alle Stellen, die wörtlich oder sinngemäss aus Quellen entnommen wurden, habe ich als solche gekennzeichnet. Mir ist bekannt, dass andernfalls der Senat gemäss Artikel 36 Absatz 1 Buchstabe r des Gesetzes über die Universität vom 5. September 1996 und Artikel 69 des Universitätsstatuts vom 7. Juni 2011 zum Entzug des Doktortitels berechtigt ist. Für die Zwecke der Begutachtung und der Überprüfung der Einhaltung der Selbständigkeitserklärung bzw. der Reglemente betreffend Plagiate erteile ich der Universität Bern das Recht, die dazu erforderlichen Personendaten zu bearbeiten und Nutzungshandlungen vorzunehmen, insbesondere die Doktorarbeit zu vervielfältigen und dauerhaft in einer Datenbank zu speichern sowie diese zur Überprüfung von Arbeiten Dritter zu verwenden oder hierzu zur Verfügung zu stellen.

Ort/Datum

Unterschrift